Title
Many-Body Quantum Dynamics and Non-Equilibrium Phases of Matter

Author
Potirniche, Ionut-Dragos

Publication Date
2019

Many-Body Quantum Dynamics and Non-Equilibrium Phases of Matter

by

Ionut Dragos Potirniche

A dissertation submitted in partial satisfaction of the

requirements for the degree of

Doctor of Philosophy

in

Physics

in the

Graduate Division

of the

University of California, Berkeley

Committee in charge:

Professor Ehud Altman, Chair
Professor Dan Stamper-Kurn
Associate Professor David Limmer

Summer 2019

Many-Body Quantum Dynamics and Non-Equilibrium Phases of Matter

Abstract

Many-Body Quantum Dynamics and Non-Equilibrium Phases of Matter

by

Ionut Dragos Potirniche

Doctor of Philosophy in Physics

University of California, Berkeley

Professor Ehud Altman, Chair

Isolated, many-body quantum systems, evolving under their intrinsic dynamics, exhibit a multitude of exotic phenomena and raise foundational questions about statistical mechanics. A flurry of theoretical work has been devoted to understanding how these systems reach thermal equilibrium in the absence of coupling to an external bath and, when thermalization does not occur, investigating the emergent non-equilibrium phases of matter. With the advent of synthetic quantum systems, such as ultra-cold atoms in optical lattices or trapped ions, these questions are no longer academic and can be directly studied in the laboratory. This dissertation explores the non-equilibrium phenomena that stem from the interplay between interactions, disorder, symmetry, topology, and external driving.

First, we study how strong disorder, leading to many-body localization, can arrest the heating of a Floquet system and stabilize symmetry-protected topological order that does not have a static analogue. We analyze its dynamical and entanglement properties, highlight its duality to a discrete time crystal, and propose an experimental implementation in a cold-atom setting.

Quenched disorder and the many-body localized state are crucial ingredients in protecting macroscopic quantum coherence. We explore the stability of many-body localization in two and higher dimensions and analyze its robustness to rare regions of weak disorder.

We then study a second example of non-thermal behavior, namely integrability. We show that a class of random spin models, realizable in systems of atoms coupled to an optical cavity, gives rise to a rich dynamical phase diagram, which includes regions of integrability, classical chaos, and of a novel integrable structure whose conservation laws are reminiscent of the integrals of motion found in a many-body localized phase.

The third group of disordered, non-ergodic systems we consider, spin glasses, have fascinating connections to complexity theory and the hardness of constraint satisfaction. We define a statistical ensemble that interpolates between the classical and quantum limits of such a problem and show that there exists a sharp boundary separating satisfiable and unsatisfiable phases.

To my family.

Contents

Acknowledgments

It takes a village to educate a physicist.

First and foremost, I am forever grateful to my adviser Ehud Altman. It has been a great pleasure and honor to witness Ehud's staggering phenomenological instinct and boundless creativity. He has an incredible knack for picking the right problem, asking the most enlightening questions, and then reducing everything to a simple toy model that captures the essentials. His style of doing physics has greatly shaped my own way of thinking and I am deeply thankful for it. Moreover, Ehud has been a wonderful mentor outside of the physics realm. Through his patience, calm, and unwavering optimism, he has taught me to focus only on what truly matters and he has given me limitless encouragement when I most needed it. Without his generous support and kind words through the tougher times, this dissertation would not exist.

Two other people have provided me with incredibly valuable mentorship throughout the years. I would like to thank Ashvin Vishwanath for helping me navigate the confusing first years of graduate school. He has encouraged me to find the sort of questions I am interested in and he has supported me during every big decision I had to make. It has also been a great privilege to learn from Ashvin and to collaborate on a few problems contained therein. Secondly, I am very grateful to Shivaji Sondhi for his guidance and for introducing me to the beautiful world of condensed matter theory. He has taught me a great deal of physics during my time at Princeton and I am very happy and proud that we did some good science together. I would also like to thank him for his thoughtful support in helping me figure out my next steps and for the many delightful conversations punctuated by his wit and dry sense of humor.

I thank Dan Stamper-Kurn and David Limmer for their generosity and for agreeing to serve on my dissertation committee. From the Birge universe, I also thank Michael Zaletel for serving on my qual committee and Joel Moore for his very broad and fascinating condensed matter classes. And nothing would have been possible without the magic of Anne Takizawa and Joelle Miles.

I am incredibly grateful to a group of phenomenal physicists with whom I have had the honor to collaborate or have really interesting conversations. In particular, it has been a pleasure to benefit from the expertise and learn from Monika Schleier-Smith, Xiangyu Cao, Thomas Scaffidi, Sumilan Banerjee, Snir Gazit, Drew Potter, Maksym Serbyn, Dima Abanin, Chris Laumann, Joseph Maciejko, and Rahul Nandkishore.

I would also like to thank my fellow graduate students and friends for making these past five years pass by in a flash. In particular, the long lunches or coffee runs with Stephen, Vir, and Will B. have always added color to a long day in the office. The dinners, drinks, and

banter with Jeffrey, Carlos, and the chemistry posse have been a pleasure and a weekend highlight. And my college friends Jared, Chris, Will S., and Ben have provided me with a much-needed respite from the physics bubble.

I do not know where I would be without the support of my close friends. I am incredibly grateful and happy to have shared so many wonderful memories with Gabi, Bridget, and Jeffrey so a heartfelt 'Mulțumesc!' is the least I owe them. I am looking forward to the next chapters in our journey.

This dissertation is dedicated to my family. Their selfless and unconditional love has made everything possible and has always emboldened me. To my mother for her many sacrifices and boundless love throughout my entire life and for sparking my curiosity for math and science. To the loving memory of my father who has always inspired me to read, learn, and never stop wondering how the world works. To my sister Anca and my brother-in-law Laurențiu for their love, wise pieces of advice, and the many Skype calls that have always filled me with joy and kept me going, especially through the cloudy times. To my nephew and new best friend Ștefan: I am already in awe at how much he has grown up and learned these past couple of years and I am incredibly excited to see what's next.

Chapter 1

Introduction

One of the most fascinating themes in condensed matter physics, often invoked using Anderson's dictum [16] 'More is different,' is the emergence of collective (macroscopic) phenomena from the microscopic details of a complex, many-body system.

A fruitful approach to investigating this mechanism starts by assuming that the system is in thermal equilibrium and relies on the powerful tools of equilibrium statistical mechanics. In particular, the renormalization group (RG) program allows the systematic exploration of the physics at different energy scales by generating and analyzing effective theories. Although these theories ignore most of the underlying microscopic details of the system by considering only a few relevant operators, they capture the correct behavior at macroscopically long distances. Strikingly, the RG approach sheds light on the underlying structure of *equilibrium* phases of matter and explains the universality of the transitions between them: many-body systems that are very different at the microscopic level may exhibit the same thermodynamic properties if they are governed by the same RG fixed points. In this sense, the RG philosophy provides the theoretical underpinning for the phenomenological Ginzburg-Landau theory of broken symmetry phases [6], as well as the Fermi Liquid theory of weakly interacting electrons [212].

These venerable considerations can be extended to the more general problem of *out of equilibrium*, many-body systems via the Martin–Siggia–Rose-Janssen–De Dominicis (MSRJD) formalism [11]. The standard approach therein is to re-cast the Langevin stochastic differential equation governing the time evolution of the system into a functional path integral, which, in turn, enables the use of RG to uncover universal properties of the dynamics. This has lead to a plethora of work on problems varying from surface growth models, including the famous Kardar-Parisi-Zhang (KPZ) theory [53], to exotic phenomena in active matter systems, such as the flocking of birds [236].

However, all of these studies focus on many-body *classical* systems out-of-equilibrium. A natural question to ask, then, is what happens in the case of many-body *quantum* systems out-of-equilibrium? And, more specifically, how do *isolated* many-body quantum systems, prepared in a non-equilibrium initial state, thermalize? These two intimately related questions are more complicated than their classical analogues for several reasons.

First, one must explain how the microscopic dynamics leads to thermal equilibration. In classical physics, this is a foundational problem in statistical mechanics: even though the physical laws describing the microscopics are invariant under time reversal, there is an 'arrow of time' governing the macroscopics, as indicated by the second law of thermodynamics. This source of tension in classical statistical mechanics is often reconciled by invoking the ergodic hypothesis, whereby, at long times, a trajectory in phase space uniformly explores the manifold of accessible states and time averages become equal to ensemble averages. This latter statement is then used to argue that microstates are accessed with equal probability, which enables the use of the microcanonical ensemble. However, it is not *a priori* clear how to generalize this reasoning to quantum statistical mechanics, as phase space trajectories are ill-defined due to the uncertainty principle.

Second, the ergodic hypothesis itself is often justified by arguing that the coupled nonlinear differential equations governing the microscopic degrees of freedom lead to chaotic dynamics, characterized by exponentially diverging trajectories in phase space, and, thus, to a decay of correlations and ergodicity. But since in quantum mechanics the Schrodinger equation is linear and the spectrum is discrete (for a finite-size system), defining quantum chaos is also a non-trivial task.

This brings us to the third—and related—complication. While many materials may be described as a many-body quantum system coupled to a thermal bath [1], which reduces the problem to effectively classical dynamics, that crutch does not exist in the case of *isolated* quantum systems. The latter evolve under their intrinsic unitary dynamics and this time evolution may be coherent for much longer time scales. In fact, this may actually inhibit the system from reaching thermal equilibrium. Therefore, it is crucial to understand the roles that entanglement and the scrambling of quantum information play in the thermalization of isolated quantum systems.

Lastly, tackling any of these questions is computationally hard. In general, simulating the dynamics of a closed quantum system comprised of N physical degrees of freedom requires keeping track of exponentially many eigenstates, i.e. storing $e^{\mathcal{O}(N)}$ data on a classical computer.

Nonetheless, over the past decade there has been an exciting flurry of experimental and theoretical advances on engineering the dynamics directly on a quantum simulator, as envisioned by Feynman [83]. Two prominent examples of such *synthetic quantum systems* [2] are ultra-cold atoms in optical lattices [42] and trapped ions [41]. Both of these platforms are natural playgrounds for addressing all of the aforementioned questions: as opposed to conventional solid state systems, they are truly isolated from the environment [2]; they are characterized by long coherence time scales [3]; and there exists an impressive array of con-

---

[1] For instance, phonons characterizing the vibrations in the crystal lattice.

[2] On the flip side, this also makes the cooling of these systems much harder because there is nowhere else to move the excess entropy [224].

[3] Typical frequencies are kHz, whereas the dynamics of solid state systems occurs in the GHz range (or higher).

trolling techniques and tunability, such as the preparation of highly non-equilibrium states, the ability to perform time of flight experiments, and single-site resolution imaging.

The main goal of this dissertation is to explore the dynamics of closed, many-body quantum systems and their thermalization, or lack thereof, with an eye towards possible applications to synthetic quantum matter. The rest of this chapter introduces the fundamental ideas that shall be used throughout the thesis.

In Section 1.1 we will discuss the basics of quantum statistical mechanics: the Eigenstate Thermalization Hypothesis (ETH), its relation to random matrix theory, and the connections to quantum chaos.

In section 1.2 we will discuss the spin glass phase occurring in many-body systems with quenched disorder. Since we are ultimately interested in ensembles of classical and quantum optimization problems (Chapter 5) and their connections to glasses, we will focus solely on the relevant case of models with *infinite-range* interactions. The added benefit of this restriction is that these models are well described by solvable mean-field theories and have an equilibrium, *thermodynamic* spin glass phase at low temperatures, exhibiting a special type of non-ergodic dynamics.

We then introduce two classes of many-body quantum systems that do not thermalize and violate ETH. In Section 1.3 we study the phenomenology of integrable systems, characterized by the existence of an extensive number of conserved quantities. This property leads to very constrained (regular) dynamics, the violation of ETH, ballistic transport, and the failure of thermalization. We analyze such an integrable model in Chapter 4.

One may argue that the integrability of many-body quantum systems is a fine-tuned phenomenon that is not robust to weak perturbations. Therefore, in Section 1.4 we discuss a second form of non-ergodicity, which is robust to perturbations: the many-body localized (MBL) state. We will present how the interplay between quenched disorder and interactions is responsible for the failure of thermalization, violation of ETH, and coherent, non-ergodic dynamics. We will overview two criteria for the stability of many-body localization, and investigate one of them in Chapter 3. Lastly, we will explain how MBL can stabilize exotic order in highly excited states of a many-body quantum system.

Building upon this description of localization-protected order, we will turn to *driven* (Floquet) quantum systems. In the last section (1.5) of this chapter we will introduce the building blocks of Floquet theory and, more specifically, of Floquet-MBL systems. We will argue that MBL can arrest the heating of a driven quantum system and stabilize order in the Floquet eigenstates. In particular, we will discuss the example of symmetry-protected topological (SPT) order. Then we will investigate the properties of two types of Floquet SPT's in Chapter 2.

1.1 Thermalization, random matrix theory, and quantum chaos

Classical thermalization and the ergodic hypothesis

Let us briefly review the intuition behind the ergodic hypothesis, invoked in classical statistical mechanics to justify using the microcanonical ensemble to predict the long-time behavior of a many-body system. Consider such an isolated system consisting of N particles that has been prepared in a non-generic initial state of total energy E [4]. The state of the system is fully determined by a $6N$ vector in phase space, i.e. $(\mathbf{q}, \mathbf{p}) \equiv (\mathbf{q}_1, \ldots, \mathbf{q}_N, \mathbf{p}_1, \ldots, \mathbf{p}_N)$, where $\mathbf{q}_i$ and $\mathbf{p}_i$ are the canonical variables of the i^{th} particle.

If we restrict ourselves to Hamiltonian dynamics, then the behavior at later times t is described by trajectories $(\mathbf{q}(t), \mathbf{p}(t))$ in phase space, according to Hamilton's equations. Moreover, the total energy E and the number of particles N will be conserved. If we assume that the equations of motion are non-linear, leading to dynamical chaos, then the system will ultimately visit all the microstates $(\mathbf{q}, \mathbf{p})_{E,N}$ consistent with the conservation of E and N[5]. An important consequence of this chaotic assumption is that the time spent in a given region of phase space will be proportional to its volume. And, in turn, this determines the long-time behavior of observables.

To make this more precise, we define the infinite-time average of an observable $O(\mathbf{q}, \mathbf{p})$ as

$$\overline{O} \equiv \lim_{\tau \to \infty} \frac{1}{\tau} \int_0^\tau dt \, O\left(\mathbf{q}(t), \mathbf{p}(t)\right). \tag{1.1}$$

Secondly, let $\mathcal{M}$ designate the manifold of constant energy and particle number in phase space, $V_\mathcal{M}$ denote its volume, and $\rho(\mathbf{q}, \mathbf{p})$ represent the density of states is (which is constant in time, according to Liouville's theorem). Thus, if the amount of time the system spends in a phase space region is proportional to the volume of that region, then the infinite-time average must obey

$$\overline{O} = \langle O \rangle_{\text{MC}} \equiv \frac{1}{V_\mathcal{M}} \int_\mathcal{M} d^{3N}q d^{3N}p \; \rho(\mathbf{q}, \mathbf{p}) O(\mathbf{q}, \mathbf{p}), \tag{1.2}$$

where $\langle \ldots \rangle_{\text{MC}}$, defined by the latter part of the equation, denotes an average over the microcanonical ensemble. The equality between infinite-time averages and microcanonical averages is the definition of *ergodicity* and it represents the bridge between the microscopic *chaotic* dynamics and the thermal description of the macroscopic system [6]. This statement

---

[4] Imagine the following classical quench protocol: we place a balloon in a room and, at time $t = 0$, we pop it.

[5] In fact, by the Poincaré recurrence theorem, the trajectory will eventually get arbitrarily close to the initial state $(\mathbf{q}, \mathbf{p})$. However, the time scale of this process is exponential in N so we ignore this "revival."

[6] This type of ergodicity is also known as *weak ergodicity* because it is a statement about the long-time *averages* of observables—in contradistinction, *strong ergodicity* refers to the *values* of observables at late times.

is, for the most part, a hypothesis and it has been proved for a few specific systems, such as the Sinai Billiards or the Bunimovich stadium [68].

Thus far, we have sketched how dynamical chaos leads to ergodicity [7]. A second consequence of the chaotic assumption is that, at late times, the state of the system is fully captured by an $\mathcal{O}(1)$ number of conserved quantities, such as E and N. This is the full extent of the "memory" of initial conditions present in the system as $t \to \infty$. In more precise terms, the auto-correlation functions of observables decay as a function of time [8], i.e. the details of the initial state are scrambled.

Quantum thermalization and the Eigenstate Thermalization Hypothesis

Generalizing the above arguments to explain the thermalization of many-body quantum systems poses a few challenges. First, due to the uncertainty principle, trajectories in the phase space of a quantum system are not well-defined. Second, since classical chaos is defined in terms of the exponential divergence of trajectories in phase space, we also need a different interpretation of quantum chaos (see the next section). Third, for similar reasons, it is not clear what should take the place of the classical ergodic hypothesis in explaining how thermal equilibrium emerges from the microscopic dynamics. As detailed below, that role is fulfilled by the Eigenstate Thermalization Hypothesis (ETH).

ETH: Srednicki-Deutsch interpretation

Following Refs. [72, 222], we now present one interpretation of ETH, which we call the "Srednicki-Deutsch interpretation," that is inspired by the classical picture. The goal is to show how the *expectation values* of local observables behave at late times.

Consider an isolated, many-body quantum system described by a local Hamiltonian H, whose eigenstates are $H\left|n\right\rangle = E_n \left|n\right\rangle$, with energies E_n. We prepare this system in an initial state

$$\left|\Psi(0)\right\rangle = \sum_n c_n \left|n\right\rangle , \tag{1.3}$$

such that the total energy is $\overline{E} = \sum_n |c_n|^2 E_n$. We assume that the c_n's are chosen as a narrow distribution over energy eigenstates centered on $\overline{E}$ and of width $\delta E \ll \overline{E}$, where

$$(\delta E)^2 = \sum_n |c_n|^2 \left(E_n - \overline{E}\right)^2 . \tag{1.4}$$

---

[7] Although chaos implies ergodicity, there are systems that are ergodic, but not chaotic: for instance, the simple harmonic oscillator. However, most generic *many-body* systems are both chaotic and ergodic so we will use these two terms interchangeably.

[8] This property is known as *mixing* in the mathematical literature. It also admits a weak-strong dichotomy, characterizing the role of fluctuations: strong mixing entails that the auto-correlation function goes to zero as $t \to \infty$, whereas weak mixing means that the long-time average of the correlation function decays to zero. Lastly, note that chaos implies mixing and mixing implies ergodicity.

This assumption holds for most generic states, including those that can be prepared in an ultra-cold atom setting, for instance. The state at later times acquires a phase factor [9], namely $|\Psi(t)\rangle = \sum_n c_n e^{-iE_n t} |n\rangle$. Thus, the expectation value of a generic (local) operator O at a time t is

$$\langle O(t)\rangle = \sum_{n,m} c_n^* c_m e^{-i(E_m - E_n)t} O_{nm}, \tag{1.5}$$

where $O_{nm} \equiv \langle n| O |m\rangle$. Then we can define the infinite-time average of the observable O as

$$\overline{O} \equiv \lim_{\tau\to\infty} \frac{1}{\tau} \int_0^\tau dt \; \langle O(t)\rangle. \tag{1.6}$$

If we assume that the spectrum of H is non-degenerate, we can write the above expression as

$$\overline{O} = \sum_n |c_n|^2 O_{nn} + \lim_{\tau\to\infty} \sum_{n\neq m} c_n^* c_m O_{nm} \frac{1 - e^{-i(E_m - E_n)\tau}}{i(E_m - E_n)\tau}. \tag{1.7}$$

If we further assume that there is *dephasing* in the dynamics, namely that there is no large-scale interference between the above phase factors $e^{-i(E_m - E_n)t}$, then the second term will vanish in the $\tau \to \infty$ limit. Thus, the infinite-time average of a local observable can be written as

$$\overline{O} = \sum_n |c_n|^2 O_{nn}. \tag{1.8}$$

If the system is thermalizing then, mirroring the discussion in the classical problem, this value $\overline{O}$ should equal the one predicted by a microcanonical ensemble.

However, we can make the following important observation: the infinite-time average appears to retain a lot of information about the initial state due to the $|c_n|^2$ coefficients. This large amount of information should be contrasted with the expectation that, in thermal equilibrium, only an $\mathcal{O}(1)$ number of parameters, such as $\overline{E}$ or N, are set by the initial state.

The resolution to this apparent paradox is the Eigenstate Thermalization Hypothesis which makes an assumption (justified in the next sections) about O_{nn}. In particular, if we take these diagonal matrix elements to be a smoothly varying function of the energy $\overline{E}$, i.e. $O_{nn} = \langle O\rangle(\overline{E})$ for all eigenstates $|n\rangle$ in an energy window around $\overline{E}$, then we immediately find that

$$\overline{O} = \sum_n |c_n|^2 O_{nn} \approx \sum_{|E_n - \overline{E}| < \delta E} |c_n|^2 O_{nn} = \langle O\rangle(\overline{E}) \sum_{|E_n - \overline{E}| < \delta E} |c_n|^2 = \langle O\rangle(\overline{E}). \tag{1.9}$$

Note that we have used the fact that the distribution of $|c_n|^2$ is centered on $\overline{E}$, has a width $\delta E \ll \overline{E}$, and is normalized to $\sum_n |c_n|^2 = 1$. If we re-write the ETH ansatz $O_{nn} = \langle O\rangle$ as

$$\langle O\rangle(\overline{E}) \approx \frac{1}{\mathcal{N}_{\overline{E}}} \sum_{|E_n - \overline{E}| < \delta E} O_{nn}, \tag{1.10}$$

---

[9] For the rest of this dissertation, we set $\hbar = 1$.

where $\mathcal{N}_{\overline{E}}$ is the number of energy eigenstates in the window $\left[\overline{E} - \delta E, \overline{E} + \delta E\right]$, then we find that the infinite-time average of the expectation value is equal to the microcanonical average: $\overline{O} = \langle O \rangle$.

We emphasize that the ETH ansatz has a very powerful implication: a single eigenstate is sufficient to predict the value of the observable O in thermal equilibrium. In other words, each eigenstate of energy E_n such that $|E_n - \overline{E}| < \delta E$ is thermal in the sense that $\overline{O} = \langle O \rangle(\overline{E}) = \langle n| O |n\rangle$. Secondly, quantum ergodicity is a property of the Hamiltonian eigenstates, and not of the unitary time evolution *per se*. The dynamics does not construct the thermal state (as it happens in a classical system), but it only reveals it via the dephasing the off-diagonal terms $e^{-i(E_m - E_n)t}$.

ETH: quantum interpretation

The above discussion, termed the "Srednicki-Deutsch interpretation," is illuminating due to its analogy with the classical problem and the ergodic hypothesis: it shows how long-time averages of expectation values are equal to microcanonical averages over eigenstates. We now present a more quantum interpretation of ETH that sheds light on the structure of many-body quantum entanglement, decoherence, and the role of reservoirs [175].

Note that, thus far, we have used the ETH ansatz to explain how only an $\mathcal{O}(1)$ amount of information about the initial (pure) state $|\Psi(0)\rangle$ of the system can be recovered from the behavior of *local* observables at late times. However, one may immediately point out that the full system will always be in a pure state $|\Psi(t)\rangle$ and no quantum information may be erased. In principle, this means that we can always recover $e^{\mathcal{O}(N)}$ information about the initial state. The resolution to this paradox is that, while true, this process would entail measuring *global* (i.e. N-local in the complexity theory sense) operators or N-point correlation functions, which is unphysical. In other words, the quantum information is scrambled globally and the entanglement is spread throughout the full system.

This intuition behind the decoherence process leads us to the following insight. Suppose that we partition the full, isolated system of size N into two pieces, A and B, such that the size of A is much smaller than the size of B, i.e. $|A| \ll |B|$ and $|A| + |B| = N$. Since A can exchange energy and particles with B and the two can also get entangled, then B acts like a bath for A, the much smaller sub-system. Therefore, at late times, A will be in a thermal, Gibbs state.

Let us make this argument more precise. We define the initial reduced density matrix of the full system as

$$\rho(0) = |\Psi(0)\rangle \langle \Psi(0)| \,, \tag{1.11}$$

corresponding to an energy $\overline{E} = \sum_n |c_n|^2 E_n = \mathrm{Tr}\left[\rho H\right]$. If this system thermalizes, then we assume that it equilibrates to a temperature T and thermal energy given by

$$E^{\mathrm{eq}}(T) = \frac{1}{\mathrm{Tr}\left[e^{-H/k_b T}\right]} \mathrm{Tr}\left[H e^{-H/k_b T}\right] . \tag{1.12}$$

For notational simplicity, let $Z(T) = \mathrm{Tr}\left[e^{-H/k_bT}\right]$. Note that the energy fluctuations $(\delta E)^2 = \langle\left(\overline{E} - E^{\mathrm{eq}}\right)^2\rangle$, related to the specific heat by a fluctuation-dissipation theorem, must scale as $(\delta E)^2 \sim N$, ensuring that $\frac{\delta E}{E^{\mathrm{eq}}} \sim N^{-1/2}$ vanishes in the thermodynamic limit.

The state of the full system at later times is given by the von Neumann equation [10]

$$i\frac{d\rho}{dt} = [H, \rho]\,, \tag{1.13}$$

whose solution is $\rho(t) = e^{-iHt}\rho(0)e^{iHt}$. With this in hand, we can compute the state of the sub-system A at late times by tracing out the degrees of freedom in B, namely

$$\rho_A(t) = \underset{B}{\mathrm{Tr}}\left[\rho(t)\right]. \tag{1.14}$$

If the bath B manages to thermalize A, then we can write the equilibrium state of A at temperature T as

$$\rho_A^{\mathrm{eq}}(T) = \underset{B}{\mathrm{Tr}}\left[\frac{1}{Z(T)}e^{-H/k_bT}\right]. \tag{1.15}$$

Thus, we say that the *full system* is thermal if

$$\lim_{\substack{t\to\infty \\ N\to\infty}} \rho_A(t) = \lim_{N\to\infty} \rho_A^{\mathrm{eq}}(T), \tag{1.16}$$

for any sub-system A such that $\frac{|A|}{N} \to 0$ as $N \to \infty$. We take both limits to ensure that diffusive transport covers the full system (infinite time) and to avoid issues such as Poincaré recurrences (infinite size).

We are now ready to state the ETH in this second interpretation. If the initial state were an energy eigenstate, i.e. $\rho(0) = |n\rangle\langle n|$, then $\rho(t) = \rho(0)$ and $\rho_A^n = \mathrm{Tr}_B\left[|n\rangle\langle n|\right]$ so the above condition becomes

$$\rho_A^n = \rho_A^{\mathrm{eq}}(T_n), \tag{1.17}$$

where T_n is the temperature corresponding to the energy E_n. This is just another way of re-stating our previous observation that each eigenstate is thermal. However, our previous analysis revealed that the prediction of an energy eigenstate agrees with the one of a microcanonical ensemble—Eq. 1.17 now shows how it can also be stated in terms of a Gibbs ensemble, thus emphasizing the *equivalence of ensembles* in quantum statistical mechanics.

Moreover, this interpretation of ETH makes another powerful prediction. The entanglement entropy in sub-system A can be written as $S_A^n = -k_b\,\mathrm{Tr}\left[\rho_A^n \log \rho_A^n\right]$ and, by Eq. 1.17, it equals

$$S_A^n = -k_b\,\mathrm{Tr}\left[\rho_A^{\mathrm{eq}}(T_n)\log\rho_A^{\mathrm{eq}}(T_n)\right], \tag{1.18}$$

the thermodynamic entropy at temperature T_n. Since the latter obeys a volume law, then we find that any energy eigenstate also obeys a volume law, i.e. $S_A^n = s|A|$, where s is a non-zero entropy density.

---

[10] Note that this equation has a classical counterpart, the Liouville equation. Thus, strictly speaking, the classical time evolution is as linear as the quantum evolution.

ETH and Random Matrix Theory

So far we have provided two phenomenological interpretations of ETH: the first allowed us to connect the late-time behavior of local observables to the microcanonical ensemble; the second allowed us to connect the properties of many-body energy eigenstates to the Gibbs state (ensemble). We now introduce a few important results about random matrices and we will use them to justify the ETH ansatz and to define quantum chaos [68].

While studying complex nuclei consisting of many electrons, E. Wigner [240] and, later, F. Dyson [74] realized that computing the spectra of generic, complex, many-body quantum systems is an almost intractable problem. However, one can make significant progress if the question is restricted to the *statistical* properties of the spectrum. This paradigmatic shift is similar in spirit to the one pioneered by Boltzmann in the many-body classical problem.

The fundamental insight originating from Wigner is that, in a narrow energy window such as the one considered above, the eigenvalues of a generic and complex Hamiltonian H are well described by a random matrix theory (RMT). In particular, the energies E_n of such an RMT repel each other according to the Wigner-Dyson surmise and the eigenstates $|n\rangle$ are random orthonormal vectors in the Hilbert space.

Level repulsion and Gaussian ensembles

Let us investigate the first property mentioned above, namely the Wigner-Dyson level statistics. For simplicity, we focus on a 2×2 matrix H, whose entries are drawn from a Gaussian distribution:

$$H = \begin{pmatrix} e_1 & \frac{V}{\sqrt{2}} \\ \frac{V}{\sqrt{2}} & e_2 \end{pmatrix}, \tag{1.19}$$

where $e_1, e_2, V \sim \mathcal{N}(0,1)$. Note that we have assumed that H is a real matrix, i.e. it is invariant under time-reversal symmetry. The eigenvalues of H are

$$E_{1,2} = \frac{e_1 + e_2}{2} \pm \frac{1}{2}\sqrt{(e_1 - e_2)^2 + 2V^2} \tag{1.20}$$

and the separation between them is

$$s = \sqrt{(e_1 - e_2)^2 + 2V^2}. \tag{1.21}$$

Using the fact that all three numbers are drawn from the standard normal distribution, we find that the probability density

$$P(s) = \frac{1}{(2\pi)^{3/2}} \int_{-\infty}^{+\infty} de_1 de_2 dV \exp\left(-\frac{e_1^2 + e_2^2 + V^2}{2}\right) \delta\left(s - \sqrt{(e_1 - e_2)^2 + 2V^2}\right). \tag{1.22}$$

After doing the integrals, we obtain the following simple expression:

$$P(s) = \frac{1}{2} s e^{-\frac{s^2}{4}}, \tag{1.23}$$

known as the Wigner-Dyson distribution. Note that the probability vanishes as a Gaussian at large spacings $s \gg 1$ and, most importantly, it also vanishes as $s \to 0$ for small spacings. The fact that the probability of having an accidental degeneracy ($s = 0$) is exactly zero is known as *level repulsion*.

While this result may seem trivial and an artifact of the small matrix size, it is remarkably general! Let A be a real $N \times N$ matrix such that its elements A_{ij} are i.i.d. from $\mathcal{N}(0, \frac{1}{N})$ [11]. Then $H = (A + A^T)/\sqrt{2}$ is called a Gaussian Orthogonal Ensemble (GOE) matrix and we can immediately show [12] that its density is given by

$$P(H) = \frac{1}{Z_N^{\mathrm{GOE}}} \exp\left[-\frac{N}{4} \operatorname{Tr}\left(H^2\right)\right]. \tag{1.24}$$

The name stems from the fact that the matrix elements are Gaussian (or that $\operatorname{Tr} H^2$ is a Gaussian random variable by the Central Limit Theorem) and that the measure is invariant under Orthogonal transformations, i.e. $\operatorname{Tr}\left[OHO^TOHO^T\right] = \operatorname{Tr}\left[H^2\right]$ for any orthogonal matrix O. While the distribution $P(s)$ of level spacings for such GOE matrices does not have a close-form expression, the Wigner-Dyson distribution (1.23) is not only qualitatively, but also *quantitatively* accurate [73]. We note, in passing, that there exist other ensembles, the Gaussian Unitary (GUE) and Gaussian Simplectic (GSE) ensembles, which correspond to different symmetry classes for the Hamiltonian H, but their level spacings behave similarly: $P(s) = Z_\beta s^\beta \exp\left(-c_\beta s^2\right)$, where $\beta = 1, 2, 4$ for GOE, GUE, and GSE, respectively.

Therefore, the current working assumption is that, for a generic and complex Hamiltonian H with time-reversal symmetry, the eigenenergies $E_n \in [E - \delta E, E + \delta E]$ behave like the eigenvalues of a GOE random matrix.

Random eigenvectors and the ETH ansatz

Let us now explore what the RMT assumption entails in terms of the eigenstates $|n\rangle$ of H. Intuitively, *in a generic basis*, the eigenvectors of a GOE matrix will look like random unit vectors. Of course, these vectors are not strictly independent since they must be orthogonal to each other. However, if we restrict ourselves to a sufficiently small energy window, then we can ignore the correlations between the corresponding eigenstates since a few uncorrelated random vectors in a very high-dimensional (for instance 2^N) Hilbert space would be essentially orthogonal.

Thus, focusing on a narrow energy window centered on E, the components $v_i^{(n)} = \langle i|n\rangle$ of an eigenvector $|n\rangle$ in a generic basis $\{|i\rangle : i = 1, \ldots, \mathcal{D}\}$ are uncorrelated Gaussian random variables with mean 0 and variance $\frac{1}{\mathcal{D}}$, where $\mathcal{D}$ is the dimension of the Hilbert space. Averaging over eigenstates in the $[E - \delta E, E + \delta E]$ window, we can write

$$\overline{v_i^{(n)} v_j^{(m)}} = \delta^{nm} \delta_{ij} \frac{1}{\mathcal{D}}. \tag{1.25}$$

---

[11] The $\frac{1}{N}$ scaling of the variance is needed for a suitable thermodynamic limit.

[12] We write the joint density as a product of each individual Gaussian density and group the terms in the exponent summation to obtain the stated result.

If we take the states $\{|i\rangle\}$ to be the eigenstates of the observable O, i.e. $O = \sum_i O_i |i\rangle \langle i|$, then we find that the average matrix element is

$$\overline{O_{nm}} = \sum_i O_i \overline{v_i^{(n)} v_i^{(m)}} = \delta_{nm} \overline{O}(E), \tag{1.26}$$

where $\overline{O}$ is the microcanonical average at energy E. Note that this is precisely the ETH ansatz used in the Srednicki-Deutsch interpretation!

We can also study the fluctuations of the matrix element around this average value:

$$\begin{aligned}
\overline{|O_{nm}|^2} - \left|\overline{O_{nm}}\right|^2 &= \overline{\langle n| O |m\rangle \langle m| O |n\rangle} - \left|\overline{\langle n| O |m\rangle}\right|^2 \qquad (1.27)\\
&= \sum_{ij} O_i O_j \overline{v_i^{(n)} v_i^{(m)} v_j^{(m)} v_j^{(n)}} - \sum_{ij} O_i O_j \overline{v_i^{(n)} v_i^{(m)}} \cdot \overline{v_j^{(n)} v_j^{(m)}} \\
&= \sum_{ij} O_i O_j \overline{v_i^{(n)} v_j^{(n)}} \cdot \overline{v_j^{(m)} v_j^{(m)}} + \sum_{ij} O_i O_j \overline{v_i^{(n)} v_j^{(m)}} \cdot \overline{v_i^{(m)} v_j^{(n)}} \\
&= \frac{\overline{O^2}}{\mathcal{D}} + \delta_{nm} \frac{\overline{O^2}}{\mathcal{D}}.
\end{aligned}$$

In the third line we expressed the four-point function in terms of Wick contractions (since the components v_i are normal random variables) and, in the fourth line, we used the orthonormality relation (1.25).

Putting everything together for the mean and variance of the matrix elements, we find that

$$O_{nm} = \overline{O}(E)\delta_{nm} + \sqrt{\frac{\overline{O^2}}{\mathcal{D}}} \eta_{nm}, \tag{1.28}$$

where η_{nm} is a random variable of zero mean and unit variance for $n \neq m$ and variance two for $n = m$. Note that the off-diagonal matrix elements are much smaller (by a factor of $\mathcal{D}^{-1/2}$) than the diagonal ones.

This equation represents a refinement of the ETH ansatz, in that it takes into account the fluctuations of the matrix element via the second term. In particular, $\overline{O^2}(E, \omega)$, where $\omega = E_n - E_m$, is approximately equal to the average spectral function $\rho(\omega)$ for states at energy E. This quantity can be measured in tunneling or absorption experiments. Secondly, $\rho(\omega)$ is the Fourier transform of the $\langle O(t)O(0)\rangle_E$ correlation function at energy E:

$$\rho(\omega) = \int dt e^{-i\omega t} \langle O(t)O(0)\rangle_E, \tag{1.29}$$

which can be related to the quantum generalization of the Fluctuation-Dissipation theorem [68, 209].

Finally, using this observation, the ETH ansatz can be put into the following form, which we will use in later chapters:

$$O_{nm} = \overline{O}(E)\delta_{nm} + \sqrt{\frac{\rho(\omega, E)}{\mathcal{D}}} \eta_{nm}, \tag{1.30}$$

for Hamiltonian eigenstates in the energy window $[E - \delta E, E + \delta E]$. We emphasize that this expression goes beyond RMT by incorporating the frequency dependence of the spectral function. Within ETH, we expect the spectral function to be a constant and the behavior to be captured by RMT only for $\omega \leq E_{\mathrm{TH}}$, where E_{TH} is called the Thouless energy.

To recapitulate, we justified this ansatz by assuming that, in the above energy window, H is well described by RMT. With this powerful result in hand, we showed that the expectation value of observables at late times is dictated by the microcanonical ensemble, i.e. the first term on the right-hand side. We also sketched how to quantify the thermal equilibration process by using the second term in Eq. 1.30, which measures time auto-correlation functions and captures decoherence (dephasing) phenomena. Third, since every eigenstate is thermal, we argued that the reduced density matrix obtained by tracing out an extensive part of the system is equal to the one obtained by starting from a Gibbs state—an immediate consequence is that thermal eigenstates obey a volume law for the entanglement entropy. Fourth, we showed that, if the RMT assumption holds, then the energy levels of a thermalizing quantum systems will repel each other.

Quantum chaos

The level repulsion property of GOE random matrices is often used as an operational definition of quantum chaos. Since the Wigner-Dyson RMT was numerically and experimentally confirmed in the case of different complex nuclei, it was then thought that it may be generally applicable to any "complex" many-body quantum systems. However, it was not completely clear what are the requirements for this complexity. This was put on a more solid footing by the work of Bohigas, Giannoni, and Schmit (BGS) [43] on the semiclassical version of the Sinai billiards problem, whose classical limit has a strongly chaotic behavior. They found that the level statistics of the quantum problem is in very good agreement with the GOE predictions and they conjectured that *any* quantum system with a classically chaotic counterpart will exhibit Wigner-Dyson level statistics. This BGS conjecture has been tested and confirmed in many cases, although there exist non-generic counterexamples [68].

This is why the GOE prediction for the behavior of levels has become a definition of quantum chaos in and of itself, regardless of whether there exists a classical limit. A subtle point worth emphasizing is the connection between level repulsion and the sensitivity to perturbations, similar to the butterfly effect in classical systems. Imagine a many-body Hamiltonian H_0 that is quantum chaotic, according to the above definition. If we add a weak perturbation λV $(\lambda \ll 1)$ such that the full Hamiltonian $H = H_0 + \lambda V$ is also chaotic, then the energy levels E_n in a narrow window will have Wigner-Dyson statistics. Moreover, the full eigenstates $|n\rangle$ will look like random vectors in the basis $\{|n^{(0)}\rangle\}$ of the *unperturbed* Hamiltonian H_0. This means that the perturbed Hamiltonian, written in the unperturbed basis, will effectively look like a GOE random matrix.

We can actually provide a more straightforward definition of the butterfly effect in quantum systems by starting from the classical definition. The divergence of (classical) trajectories can be captured via the sensitivity $d(t)$ to initial conditions:

$$d(t) = \left(\frac{\partial q_i(t)}{\partial q_j(0)}\right)^2, \tag{1.31}$$

i.e. we imagine applying a perturbation at site j and time $t = 0$ and study its impact at a different site i and later time $t > 0$. The system is chaotic if $d(t) \propto e^{2\lambda t}$, with a positive Lyapunov exponent $\lambda > 0$. Using the Poisson bracket structure of classical mechanics, we can easily show that the sensitivity is equivalent to

$$d(t) = \left(\{q_i(t), p_j\}\right)^2. \tag{1.32}$$

Following a standard approach to quantizing classical systems whereby we replace Poisson brackets $\{A, B\}$ by commutators $-\frac{i}{\hbar}\left[\hat{A}, \hat{B}\right]$ of Hermitian operators $\hat{A}$ and $\hat{B}$, we can introduce a generalization of the sensitivity, known as the out-of-time-order correlator (OTOC):

$$C(t) \equiv -\langle [\hat{x}_i(t), \hat{p}_j]^2 \rangle_T, \tag{1.33}$$

where the brackets $\langle \dots \rangle_T$ denote an average over the thermal ensemble at temperature T. The claim is that the system is quantum chaotic if $C(t) \propto \hbar^2 e^{2\lambda t}$ with $\lambda > 0$.

The OTOC characterizes the decoherence phenomena occurring in a thermal system, measuring how fast the quantum information is scrambled. In fact, in the context of scrambling near the event horizon of a black hole, Maldacena et al. [162] argued that there exists a *universal* bound on the rate λ:

$$\lambda \leq \frac{2\pi k_b T}{\hbar}. \tag{1.34}$$

In a related development, Kitaev proposed an example of a many-body quantum system that saturates this bound on chaos [137, 163]. This model, known as the Sachdev-Ye-Kitaev (SYK) model [200], was shown to be dual to a black hole in AdS_2 [200, 123, 225].

Having overviewed the properties and consequences of thermalization, we are now ready to analyze different possibilities of non-ergodic behavior.

1.2 Spin glasses

As a warm-up, in this section we will discuss the spin glass phase occurring in many-body systems with quenched disorder. Since we are ultimately interested in ensembles of classical and quantum optimization problems (Chapter 5) and their connections to glasses, we will focus solely on the relevant case of models with *infinite-range* interactions. The added benefit of this restriction is that these models are well described by solvable mean-field theories and have an equilibrium, *thermodynamic* spin glass phase at low temperatures, exhibiting a special type of non-ergodic dynamics.

The fundamental ingredient of spin glasses is the presence of *quenched disorder*. An example of a real physical system which is often discussed in the context of spin glasses [87] is a dilute solution of magnetic impurities in a noble metal host. An impurity magnetic moment at a site $\mathbf{r}_i$ will magnetize the nearby host conduction electrons, such that this polarization is negative at some distances and positive at others. Then another impurity moment at a site $\mathbf{r}_j$ will feel this electronic magnetization and will try to lower the overall energy by aligning along it. However, assuming that the impurities are randomly placed, these magnetic interactions J_{ij} will effectively have random signs, i.e. will be either ferromagnetic ($J_{ij} < 0$) or anti-ferromagnetic ($J_{ij} > 0$) with some non-zero probability. If the time scale over which the impurity moments (spins) fluctuate is much shorter than the time scale over which the J_{ij}'s change (the time scale of the electronic magnetization), then the disorder is quenched (frozen) from the spins' perspective.

A classical and solvable [180] toy model for this is due to D. Sherrington and S. Kirkpatrick [214] and can be easily written as

$$H = -\sum_{i,j=1}^{N} J_{ij}\sigma_i\sigma_j, \tag{1.35}$$

where $\sigma_i = \pm 1$ denote Ising variables [13] and the couplings J_{ij} are drawn from a Gaussian distribution. We emphasize that, since we are interested in the connections to classical and quantum optimization problems, we focus only on the case of infinite-range interactions, as defined above.

Moreover, in these models the spin glass is an equilibrium thermodynamic phase that occurs at low temperatures, and is also characterized by a sharp dynamical signature and non-ergodicity (see the next sections for details). Crucially, the quenched disorder leads to *frustration*: the spins will find it impossible to satisfy all of the ferromagnetic and anti-ferromagnetic constraints and there will exist many configurations with a similar degree of frustration (number of bonds where there is an energy penalty). From the point of view of the system's thermodynamic properties, this translates into a rugged free energy landscape with many local minima separated by large barriers. Although it is believed that this "idealized" spin glass phase does not exist in systems with short-range interactions [84, 86, 85], such systems nonetheless exhibit very slow dynamics whereby autocorrelation functions decay logarithmically in time.

Consequently, there are three fruitful ways to think about the phenomenology of infinite-range, ideal spin glasses: in terms of statics, dynamics, and complexity.

Statics

Ideal glasses form a distinct equilibrium thermodynamic phase. A mean field theory has been developed to calculate the disorder-averaged free energy within the framework of

---

[13] The Sherrington-Kirkpatrick model can also be used to discuss quantum spin glasses, provided that we promote the variables σ to Pauli matrices ($\sigma_i \to \hat{\sigma}_i^z$) and include another *non-commuting* term in the Hamiltonian, such as a transverse field $\sum_i \Gamma_i \hat{\sigma}_i^x$. The following discussion, focusing on phenomena driven by thermal fluctuations at non-zero temperatures ($T > 0$), will apply to both the classical and quantum problems.

equilibrium statistical mechanics.

If we define the local magnetization as $m_i = \langle \sigma_i \rangle$, where $\langle \dots \rangle$ denotes an average over the thermal ensemble or an energy eigenstate, then the average magnetization can be written as $m = \frac{1}{N}\sum_i m_i$. Note that the quenched disorder may favor a state with non-zero m_i, namely a glassy state, even though m is zero at all temperatures due to the random spin directions preferred at each site i. This means that the onset of glassy physics can be captured from the establishment of a non-zero value of

$$q_{\mathrm{EA}} = \frac{1}{N}\sum_i m_i^2, \tag{1.36}$$

known as the Edwards-Anderson order parameter.

We can also define the local susceptibility χ_{ii} as the response function to an applied magnetic field h_i [14], $\chi_{ii} = \frac{\partial m_i}{\partial h_i}$. From the fluctuation-dissipation theorem, we get that the average local susceptibility $\chi = \frac{1}{N}\sum_i \chi_{ii}$ is equal to

$$\chi = \frac{1 - q_{\mathrm{EA}}}{T}, \tag{1.37}$$

which is a quantity that can be measured in an experiment [87]. Thus, the Edwards-Anderson order parameter quantifies the reduction of the local susceptibility from the Curie-Weiss expectation of free moments and the putative (static) glass transition, occurring at a temperature T_s, can be identified as a cusp in $\chi(T)$.

Secondly, the low-temperature ($T < T_s$) phase is also characterized by *non-ergodicity*, in that the system only explores a subset of the phase space: the microstates (configurations) become clustered into *many* pure states and the Gibbs measure splits into sub-components. And, most interestingly, there is a deep connection between the hierarchical (ultrametric) structure of pure states, their overlaps, the Edwards-Anderson order parameter, and the phenomenon known as *replica symmetry-breaking* [87, 54].

We emphasize that this only holds for mean-field, ideal spin glasses. In short-range Ising spin glasses, Huse and Fisher [84, 86, 85] have argued that there exist only two pure states (clusters) below T_s, which are related by a global spin flip. Moreover, an external magnetic field would select one of these pure states and the spin glass phase is destroyed! This stands in stark contrast to ideal spin glasses wherein the multitude of pure states are responsible for a thermal phase transition even at finite magnetic fields, known as the Almeida-Thouless line [10].

Dynamics

The second avenue to understanding glassiness is dynamics. From an experimental perspective, it turns out that the a.c. susceptibility depends also on the frequency of the applied

---

[14] Note that this is a reason why the spin glass problem is much more complicated than the “clean” (non-disordered) Ising problem: in the latter case, we can select a particular low-temperature state since we can apply a local magnetic field. However, in the disordered case, these directions are random and we do not know them *a priori*.

magnetic field: $\chi(T) = \chi(T, \omega)$ and both the real and imaginary parts of $\chi(T, \omega)$, related by a Kramers-Kronig relation, can be measured independently. Moreover, the dependence persists even at very low frequencies, corresponding to time scales much larger than those characteristic of the experiments. This behavior should be contrasted with that of conventional magnets where there is no such dependence on frequencies below some Ω_0 inherent to the physical system.

The slow (glassy) dynamics suggests that there exist many metastable states with very large lifetimes, or large energy barriers separating them. Not only that the system can be non-ergodic in the sense that it does not fully explore all of the available phase space—strictly speaking, it may also be ergodic, yet get trapped for very long times into *unstable saddle points* of the rugged energy landscape.

In fact, it is possible that there exists a dynamical phase transition occurring at a temperature T_d that is different from the thermodynamic (static) phase transition occurring at T_s. This happens, for instance, in another infinite-range model, namely the p-spin spherical model [54]. For such a system, at very large temperatures and deep in the paramagnetic phase, the dynamics is ergodic and correlation functions decay very fast. Closer to T_d (but still above this temperature), the dynamics is still ergodic, but the system slowly explores a small region of the phase space close to the initial state, by getting trapped into a successive series of metastable states, which are saddles. Exactly at T_d, at the dynamical transition, the relaxation time diverges, the dynamics becomes non-ergodic, and the saddles turn into trapping minima. Interestingly, the static (equilibrium) transition occurs at an even lower temperature, $T_s < T_d$, and thermodynamics cannot detect the existence of the long-lived metastable states. Lastly, below T_s, the microscopic spin configurations cluster into many different pure states and the lowest lying ones dominate the Gibbs measure, leading to replica symmetry-breaking.

Therefore, not only that ideal glasses exhibit very exotic phenomena in a mean-field, equilibrium description, but their dynamics is also very rich [15], which, ultimately, is due to a complex hierarchical organization of length scales and metastable states.

Complexity

As alluded to above, the third way to think about glasses is in terms of complexity, which is the predominant route we will take in Chapter 5. In this section, we introduce an optimization problem studied in computer science, the 3-Satisfiability problem, and show how the constraint satisfaction can be recast into finding a zero total energy ground-state for a spin glass Hamiltonian. Moreover, the satisfiability problem is "hard" (to be defined below) for both classical and quantum computers. We can understand this hardness as a consequence of the thermodynamic and dynamical properties of an ideal glass, as discussed in the previous two sections: quenched disorder, leading to frustration, creates a rugged

---

[15] We have not even mentioned fascinating phenomena such as hysteresis, aging, or other memory effects in glasses.

energy landscape of many sub-optimal states and any algorithm will take a very long time to explore these local minima and to converge to a solution.

To make things more precise and narrow, we will focus strictly on complexity as it is understood in the theory of computation. The goal therein is to classify problems based on the asymptotic scaling of the resources—time or memory required by a computer to solve the problem—with the input size N. Focusing on decision problems (i.e. problems whose solution entails outputting 'yes' or 'no'), an algorithm purported to solve them *efficiently* will only need a polynomial in N amount of resources. Similarly, a problem is tractable if there exists an efficient algorithm that can solve it. Roughly speaking, for a classical computer, this defines the complexity class P.

A generalization of this class is NP, corresponding to the class of decision problems whose 'yes' instances can be efficiently verified—note that it does not make any assumptions about 'no' instances and, in fact, these need not have verifiable proofs. Intuitively, this class includes problems where if there exists a solution, then it is easy to check whether an adversary claiming to have a solution is lying. Conversely, it can be very hard (i.e. it cannot be done in polynomial time) to verify that there is no solution. It is easy to see that P is a subset of NP, but it is a fundamental and unsolved problem in computer science whether P = NP.

Lastly, there exist problems that are NP-complete, namely they capture the hardness of the entire class NP. More precisely, a problem A is NP-complete if $A \in$ NP and *any* other problem $B \in$ NP can be mapped into A with at most a polynomial overhead. Thus, A is at least as hard as hard as any other problem in NP. We are now ready to establish the connection to spin glasses.

A famous example of an NP-complete problem is the 3-Satisfiability problem (3-SAT). We are given a Boolean expression $\mathcal{C}$ consisting of M clauses on an N-bit string $(\sigma_1, \ldots, \sigma_N)$ of the form

$$\mathcal{C} = \bigwedge_{m=1}^{M} \mathcal{C}_m, \tag{1.38}$$

where $\mathcal{C}_m = \sigma_{i_m} \vee \overline{\sigma_{j_m}} \vee \sigma_{k_m}$ is a clause on exactly 3 bits and $i_m, j_m, k_m \in \{1, \ldots, N\}$. Note that $\overline{\sigma} \equiv 1 - \sigma$ is the logical negation of a bit and we allow any number of such negations in the clauses $\mathcal{C}_m$. The 3-SAT problem is the following: given $\mathcal{C}$, can we assign values to $(\sigma_1, \ldots, \sigma_N)$ such that $\mathcal{C}$ evaluates to 1? Clearly, 3-SAT is in NP since 'yes' instances (also called SAT instances) are easily verifiable. However, note that proving that $\mathcal{C}$ is a 'no' instance (also called UNSAT) may require checking all 2^N configurations! Lastly, showing that 3-SAT is NP-complete is a non-trivial step and it is the object of the famous Cook-Levin theorem.

Now suppose that we map the bits taking values in $\{0, 1\}$ to Ising variables taking values in $\{-1, 1\}$ and the formula $\mathcal{C}$ to a Hamiltonian $H(\sigma_1, \ldots, \sigma_N) = \sum_{m=1}^{M} H_m$, where the 3-body terms are given by

$$H_m = (1 \pm \sigma_{i_m})(1 \pm \sigma_{j_m})(1 \pm \sigma_{k_m}). \tag{1.39}$$

Note that the ± signs depend on the negations in $\mathcal{C}_m$. Therefore, the question posed by the 3-SAT problem can be framed as: does H have a ground state of energy *exactly* zero?

At this point, the connection to spin glasses should be evident upon introducing an appropriate measure on the instances of 3-SAT to generate a question in statistical physics. We can then attempt to understand the structure of problems that are typical with respect to the measure. For example, a SAT-UNSAT phase transition, arising as function of the parameters controlling the measure, would signal the regimes where the most complicated problems may be found [109]. Close to the critical point, where there is a very large degree of frustration and a proliferation of states close to being solutions (i.e. metastable states), this statistical problem becomes very glassy. We analyze a simplified example of this in Chapter 5, where we study an interpolation between the classical and quantum problems.

This third way of thinking about spin glasses (in terms of complexity) builds on the seminal insight of Fu and Anderson [91] that the intractability of NP-complete problems is a form, indeed an extreme one, of spin glassiness. More philosophically, one may argue that physical processes occurring in nature are also a form of computation [16]. Thus, the glassy dynamics and all the exotic phenomena associated with it are manifestations of the intractability of that computation.

1.3 Integrable systems

Although an ideal spin glass is characterized by special non-ergodic dynamics due to the existence of many metastable states at low temperatures, it is an *equilibrium* phase of matter. In contradistinction, we now discuss non-ergodicity in *non-equilibrium* quantum systems, i.e. systems where ETH is violated and the canonical ensemble does not provide a correct description. In this section we introduce integrability, and in the next section (1.4) we present many-body localization.

We now overview the basic phenomenology of integrable systems and describe how the existence of many conserved quantities places a strong constraint on ergodicity, leading to very regular dynamics, to coherent transport properties of the system, and to the absence of thermalization in the sense of Section 1.1. We will also briefly discuss how these systems, in fact, manage to thermalize, albeit in a special way, to a Generalized Gibbs Ensemble (GGE) [55]. These results will be used and further explored in Chapter 4, describing a specific and novel type of quantum integrability.

Classical integrability

Let us begin by reviewing the precise definition of Liouville integrability used in classical physics. A Hamiltonian $H(\mathbf{q}, \mathbf{p})$ with N physical degrees of freedom, i.e. $\mathbf{q} = (q_1, \ldots, q_n)$ and $\mathbf{p} = (p_1, \ldots, p_N)$, is integrable if there exist N functionally independent integrals of

---

[16] Variants of this idea are sometimes called the Physical Church-Turing thesis.

motion in involution, $\mathbf{I} = (I_1, \ldots, I_N)$, such that

$$\{I_i, H\} = 0 \quad \text{and} \quad \{I_i, I_j\} = 0, \quad \forall i, j = 1, \ldots, N. \tag{1.40}$$

If H has N such integrals of motion, then the Liouville-Arnold theorem guarantees that there exists a mapping between the variables $(\mathbf{q}, \mathbf{p})$ and the action-angle variables $(\mathbf{I}, \boldsymbol{\theta})$ such that the canonical Hamiltonian $\tilde{H}$ depends solely on $\mathbf{I}$, $H(\mathbf{q}, \mathbf{p}) \to \tilde{H}(\mathbf{I})$, and the Hamilton equations of motion become

$$\begin{aligned} \frac{d\mathbf{I}}{dt} &= 0 \\ \frac{d\boldsymbol{\theta}}{dt} &= \frac{\partial \tilde{H}(\mathbf{I})}{\partial \mathbf{I}} \equiv \boldsymbol{\omega}, \end{aligned} \tag{1.41}$$

for some frequencies $\boldsymbol{\omega}$. We can integrate (thus the name *integrability*) these differential equations to obtain

$$\begin{aligned} I_i &= I_{0,i} \\ \theta_i(t) &= \omega_i t + \theta_{0,i}. \end{aligned} \tag{1.42}$$

The above equations show that the integrals of motion $\mathbf{I}$ are time-independent (i.e. conserved $\mathbf{I} = \mathbf{I}_0$) and the angles $\boldsymbol{\theta}$ vary linearly in time with fixed angular frequencies. Therefore, the trajectories of this integrable system are confined to an N-dimensional torus, fully determined by the initial conditions $\mathbf{I}_0$, and the motion is quasiperiodic.

A fundamental result of classical integrability is the Kolmogorov-Arnold-Moser (KAM) theorem which states, roughly speaking, that under some assumptions about regularity and non-degeneracy, most of the invariant tori that foliate the phase space of an integrable system will be deformed and survive under weak Hamiltonian perturbations. The motion on these deformed tori will still be quasiperiodic orbits, yet the dynamics will smoothly cross over into chaotic dynamics for strong enough perturbations. Thus, we can think of the KAM theory as a result showing the robustness of the regular, non-ergodic dynamics of *classically* integrable systems to weak perturbations.

However, the important caveat to KAM is the non-degeneracy assumption: as soon as this condition is relaxed, there may occur an uncontrolled proliferation of resonances and small denominators in the perturbative expansions, which will threaten the convergence of the perturbation theory. For the same reason, KAM only applies to *few-body* classical systems and there is no known generalization for many-body, $N \to \infty$, classical systems. Finally, as detailed in the sections on localization, resonances will also play a key role in the thermalization of many-body *quantum* systems.

Quantum integrability

Defining integrability for a *quantum* system is hard [17]. First of all, there is no known quantum analogue of the KAM theorem so even if there exists a proper definition for few-body

---

[17] For a review of all the problems associated with such a definition, see Ref. [55].

quantum systems, let alone many-body quantum systems, then there are no guarantees that this form of non-ergodicity is robust (i.e. not fine-tuned). Secondly, naively extending the above requirement that there exist extensively many conserved quantities is somewhat trivial: any Hamiltonian H can be diagonalized and the energy eigenstate projectors, $\{|n\rangle\langle n|\}$, form a fully commuting set. We can circumvent this issue by insisting that the conserved quantities be *local*.

Let us restrict the discussion to a one-dimensional, *local*, many-body quantum Hamiltonian $H = \sum_{i=1}^{N} h_i$ on N sites, where the support of each operator h_i is localized around site i [18]. We say that H is integrable if there exist $N-1$ functionally independent and *local* operators $I^{(n)}$, namely

$$I^{(n)} = \sum_{i=1}^{N} q_i^{(n)}, \tag{1.43}$$

such that

$$[I^{(n)}, I^{(m)}] = 0 \quad \text{and} \quad [I^{(n)}, H] = 0 \quad \forall\, n, m = 1, \ldots, N-1. \tag{1.44}$$

Note that we can define $I^{(0)}$ to be the Hamiltonian, $I^{(0)} \equiv H$, such that the full set of local and commuting quantities is N-dimensional and indexed by $n = 0, \ldots, N-1$.

We now argue that this definition significantly restricts the dynamics of the quantum system, is responsible for a failure of thermalization, and it leads to non-diffusive (coherent) transport.

Dynamics

We start by showing why the naive thermalization defined in Section 1.1 fails and the ETH is violated. As before, suppose we initialize the system in a non-equilibrium state $|\Psi(0)\rangle$ which can be written as $|\Psi(0)\rangle = \sum_n c_n |n\rangle$ in terms of the energy eigenstates, and the $|c_n|^2$ are narrowly distributed around an energy $\overline{E}$. Then the long-time average expectation value of an operator O is

$$\overline{O} = \lim_{\tau\to\infty} \frac{1}{\tau} \int_0^{\tau} dt \langle O(t)\rangle = \sum_n |c_n|^2 O_{nn}. \tag{1.45}$$

However, in general, this long-time average will *not* equal the canonical average if H is integrable. This is because the canonical ensemble does not take into account the fact that there are an additional $N-1$ conserved quantities set by the initial state:

$$\langle\Psi(0)|\, I^{(n)} \,|\Psi(0)\rangle \quad \text{for } n = 1, \ldots, N-1, \tag{1.46}$$

in addition to the energy $\overline{E}$.

---

[18] For a spin-$\frac{1}{2}$ system, imagine that h_i can be written as a tensor product over Pauli matrices on a few (not a fraction of N as $N \to \infty$) sites and identity everywhere else.

However, if we account for all of these conserved quantities, then the system thermalizes to a Generalized Gibbs Ensemble (GGE) defined as [55]:

$$\begin{aligned} \langle O \rangle_{\mathrm{GGE}} &= \frac{1}{Z_{\mathrm{GGE}}} \operatorname{Tr}\left[O e^{-\sum_{m=0}^{N-1} \beta_m I^{(m)}} \right] && (1.47) \\ Z_{\mathrm{GGE}} &= \operatorname{Tr}\left[e^{-\sum_{m=0}^{N-1} \beta_m I^{(m)}} \right]. && (1.48) \end{aligned}$$

Note that β_0 corresponds to the standard inverse temperature $\beta_0 = 1/(k_b T)$ and β_m, for $m = 1, \ldots, N-1$, are the Lagrange multipliers enforcing the conservation of each $I^{(m)}$. They are defined implicitly via

$$\langle \Psi(0) | I^{(n)} | \Psi(0) \rangle = \frac{1}{Z_{\mathrm{GGE}}} \operatorname{Tr}\left[I^{(n)} e^{-\sum_{m=0}^{N-1} \beta_m I^{(m)}} \right]. \tag{1.49}$$

Therefore, a quantum integrable system thermalizes to a special Gibbs ensemble with an infinite number of "temperatures" as $N \to \infty$. However, it does not thermalize in the sense of Section 1.1 and the ETH, as defined there, is violated. It has been argued [9] that integrable systems satisfy a *weak* version of ETH, whereby it holds for typical eigenstates, but not for *all* of them: there exist "rare" eigenstates which violate ETH.

Non-ergodic dynamics

The fact that a non-equilibrium initial state $|\Psi(0)\rangle$ sets the values for N conserved quantities, $\langle \Psi(0) | I^{(n)} | \Psi(0) \rangle$, means that there is a lot of memory, $\mathcal{O}(N)$, of the initial conditions, leading to *non-ergodic* dynamics. We now make this quantum non-ergodicity more precise by using Mazur's inequality [166, 228, 55] for time auto-correlation functions in a generic system characterized by a Hamiltonian H (not necessarily integrable) on N physical degrees of freedom.

For simplicity, suppose that the *canonical* average of a generic local operator O is zero:

$$\langle O \rangle \equiv \frac{1}{Z} \operatorname{Tr}\left[O e^{-\beta H} \right] = 0. \tag{1.50}$$

Then this operator is ergodic if the average auto-correlation function (or the zero frequency spectral function $\rho(\omega = 0)$ defined in Eq. 1.29) vanishes:

$$\lim_{\tau \to \infty} \frac{1}{\tau} \int_0^\tau dt \langle O(t) O(0) \rangle = 0. \tag{1.51}$$

If there exists a set of conserved quantities $\{Q_i\}$ such that they are orthonormal with respect to the canonical average

$$\langle Q_i Q_j \rangle \equiv \frac{1}{Z} \operatorname{Tr}\left[e^{-\beta H} Q_i Q_j \right] = \delta_{ij}, \tag{1.52}$$

then Mazur's inequality states that

$$\lim_{\tau \to \infty} \frac{1}{\tau} \int_0^\tau dt \langle O(t) O(0) \rangle \geq \sum_i \left| \langle O Q_i \rangle \right|^2. \tag{1.53}$$

The above equation becomes an equality when the orthonormal set $\{Q_i\}$ is maximal, namely when it contains N elements. This is precisely the case for an integrable system where that set is $\{I^{(n)} : n = 0, \ldots, N-1\}$—note, however, that the $I^{(n)}$'s are not necessarily orthonormal with respect to the canonical ensemble (1.52) so we would have to Gram-Schmidt them.

Assuming that the conserved quantities are local, then the overlap between a generic operator O and each Q_i scales as $\mathcal{O}(\frac{1}{N})$. Moreover, if the set $\{Q_i\}$ is maximal, then there are N such overlaps and the summation on the right-hand side of Eq. 1.53 will lead to an $\mathcal{O}(1)$ lower bound for the long-time average of the autocorrelation function of O. Therefore, the dynamics of generic local operators in many-body quantum integrable systems, exhibiting a maximal set of conserved quantities, is non-ergodic.

Conversely, in a thermalizing system, the overlap between a generic local operator O and the *few* $[\mathcal{O}(1)]$ conserved quantities will be $\mathcal{O}(\frac{1}{N})$, which vanishes in the thermodynamic limit.

Transport

Not only that the Mazur inequality shows how the dynamics is non-ergodic, but it also has an interesting consequence in terms of the transport properties of the system. Let us show how we can use it to prove that an integrable system exhibits ballistic, i.e. *coherent*, transport.

Using Kubo's formula for linear response, the real part of the optical conductivity at temperature T and frequency ω can be written as

$$\sigma'(\omega, T) = 2\pi D_T \delta(\omega) + \sigma^{\text{reg}}(\omega), \tag{1.54}$$

and the Drude weight is given by

$$D_T = \lim_{\tau\to\infty} \lim_{N\to\infty} \frac{1}{NT\tau} \int_{-\tau}^{\tau} dt \langle J(t)J(0)\rangle. \tag{1.55}$$

The current operator is a sum of local terms: $J = \sum_{i=1}^{N} j_i$. Using Mazur's inequality defined above, we find that [228]

$$D_T \geq \frac{1}{T} \lim_{N\to\infty} \frac{1}{N} \sum_i |\langle JQ_i\rangle|^2 . \tag{1.56}$$

First, let us see what this entails for a thermalizing system. If there is a single conserved quantity (the energy) and the Hamiltonian H has time-reversal symmetry (TRS), then the overlap between H and the energy current J is zero since the current is odd under TRS. Note that this also holds for systems with particle-hole symmetry [215]. Moreover, if the overlap between J and H is zero, then the current operator is ergodic (vanishing current-current correlation function) and that leads to a zero Drude weight, $D_T = 0$ at all temperatures. The delta function in the real part of the optical conductivity (1.54) is broadened (conventionally into a Lorentzian), which means that the zero frequency (DC) conductivity is finite.

Therefore, transport in a thermal system is *diffusive* since a finite $\sigma_{\mathrm{DC}} \neq 0$ implies a non-zero diffusion constant by an Einstein relation.

On the other hand, in an integrable system, the current operator J will generically have a non-zero overlap with the N conserved quantities [19], i.e. $\langle JQ_i \rangle \neq 0$, which leads to a non-zero Drude weight, $D_T > 0$, by Eq. 1.56. Therefore, the DC conductivity of an integrable system is *infinite* (due to the delta function in Eq. 1.54), there exists a persistent (non-decaying) current, and the transport is *ballistic*. This holds for spin transport in the XXZ chain or for charge transport in the Hubbard model away from half-filling [251]. In other words, as opposed to a thermal system, an integrable system will exhibit non-vanishing correlation functions (coherence) and ballistic, rather than diffusive, transport.

Level statistics

In Section 1.1, we found that quantum chaos is intimately related to level repulsion and to Wigner-Dyson level statistics. Moreover, the BGS conjecture states that quantum systems that have a classically chaotic limit will exhibit such level statistics.

A similar set of results exists for integrable systems. In particular, the Berry-Tabor conjecture [37] states that quantum systems with a classically integrable limit will exhibit Poissonian level statistics. Analytical and numerical studies have confirmed this conjecture in many cases, including for quantum integrable systems that do not have a classical limit [226, 182, 192, 178, 202].

Let us provide some intuition for the Poissonian statistics by analyzing a trivially integrable quantum system, namely a set of *uncoupled* (non-interacting) simple harmonic oscillators with incommensurate frequencies ω_i. The many-body energy levels can be written in terms of the occupation numbers n_i of each single-particle level i:

$$E = \sum_i n_i \omega_i. \tag{1.57}$$

At high energies where the occupation numbers are also large, adjacent many-body levels may come from very different sets of occupation numbers $\{n_i\}$, provided that the frequencies are incommensurate [37]. Intuitively, this means that nearby levels are uncorrelated (unlike those of a thermalizing system, which exhibits level repulsion) and can be modelled as a Poisson process. If the average density of states at high energies is roughly constant and equal to ρ, then the average number of levels in an energy window $[E - \delta E, E + \delta E]$ is $\lambda \equiv 2\delta E \rho$. The probability of finding n levels in this window is, therefore,

$$P_n = \frac{\lambda^n e^{-\lambda}}{n!}. \tag{1.58}$$

---

[19] In fact, the current operator can itself be a conserved quantity. This is the case with the energy current in the XXZ chain [38].

Since the “time of arrival” for a Poisson point process is exponentially distributed, then the probability distribution of adjacent level spacings $s = E_{k+1} - E_k$ is given by

$$P(s) = \lambda e^{-\lambda s}, \tag{1.59}$$

which is very different from the Wigner-Dyson surmise (1.23)! Qualitatively, there is no level repulsion, and there are many degeneracies.

Thus, level repulsion or the lack thereof and the Wigner-Dyson versus Poisson level statistics provide a natural way to test whether an unknown many-body quantum system is thermal or non-thermal, respectively. The latter holds for integrable systems and, as we will discuss next, to localized systems as well.

1.4 Many-Body Localization

Although integrability represents a standard example of the failure of thermalization (violation of ETH) and non-ergodic dynamics in many-body quantum systems, it is not robust to naturally-occurring generic perturbations. In fact, it is generally believed that weak integrability-breaking will ultimately lead to the thermalization of the system.

We introduce localized systems as another class of non-ergodic, many-body systems where quenched disorder plays a crucial role in the failure of thermalization and, most importantly, to its robustness to generic perturbations. In this section we focus on two aspects of many-body localized systems that will be important for different parts of this dissertation.

First, we discuss criteria for the regimes of stability of the MBL phase. This analysis will be essential to Chapter 3, where we will address a controversy *vis-à-vis* the existence of many-body localization $d > 1$ spatial dimensions. As a warm-up, we present the well-known problem of single-particle Anderson localization, in the way Anderson first conceived it: to wit, as the stability of localized single-particle states to the addition of hopping between them. As detailed below, we find that resonances play an important role and we lever this observation to derive a criterion for the stability of Anderson localization. This criterion will depend on the number d of spatial dimensions and we will briefly comment on the role of dimensionality.

We then ask about the stability of localization to the inclusion of interactions between particles and whether there exists a many-body localized (MBL) state. We introduce and contrast two criteria, both of which are based on the counting of many-body resonances. On the one hand, following the work of Basko, Aleiner, and Altshuler [29] (BAA), we can think about the interactions between particles as causing hops in the space of single-particle states. Describing MBL as Anderson localization in *Fock space* allows us to derive a criterion for the existence of many-body localization in any dimension d. On the other hand, following the work of De Roeck and Huveneers [70], we study the role of interactions directly in real space and obtain a second criterion for the stability of MBL. We find that this De Roeck-Huveneers criterion is in tension with the BAA one even in $d = 1$. A striking prediction of this second approach is that MBL is unstable in higher dimensions, $d > 1$, due to rare regions of weak disorder—we carefully explore this implication in Chapter 3.

The second aspect of MBL, which we review in this section, is the role of localization in stabilizing exotic order that would be forbidden in equilibrium systems. To this end, we introduce a phenomenological description of a system deep in the MBL phase. This enables us to explain how disorder localizes bulk excitations, circumventing the restrictions of Landau-Peierls-type arguments, and protects order in highly excited states.

We deploy this second crucial property of MBL in Section 1.5 where we discuss driven (Floquet) systems, and, more specifically, in Chapter 2 where we present how many-body localization arrests the heating of a Floquet system and stabilizes symmetry-protected topological order in Floquet eigenstates.

Anderson localization

The simplest version of localization was first introduced by P.W. Anderson [15] in the context of non-interacting quantum systems with quenched disorder. As the title of the original paper suggests, the salient feature of single-particle localization (SPL) is the absence of diffusive transport characteristic of thermal systems and, consequently, zero DC conductivity ($\sigma_{\text{DC}} = 0$).

Let us present the main results of Anderson localization, with an emphasis on the role of resonances. On the one hand, this allows us to obtain a very coarse criterion for the stability of Anderson localization to hopping in real space. On the other hand, we will generalize this approach to study the stability of many-body localization to interactions between particles and rare regions of weak disorder.

The model used by Anderson describes a *single electron* hopping ($t \neq 0$) on an infinite lattice with on-site quenched disorder via the Hamiltonian

$$H = t \sum_{\langle ij \rangle} \left(c_i^\dagger c_j + c_j^\dagger c_i \right) + \sum_i \mu_i c_i^\dagger c_i, \tag{1.60}$$

where μ_i is a random variable drawn from some distribution of width W. In the $t = 0$ limit, the eigenstates of H are of the form $|\phi_i\rangle \equiv c_i^\dagger |0\rangle$ and are trivially localized on single sites $\mathbf{R}_i$.

Using a perturbative "locator" expansion in $\frac{t}{W} \ll 1$, Anderson [15] showed that in $d = 1, 2$ and for *arbitrarily weak* disorder, *all* eigenstates $|\psi_a\rangle$ are localized around sites $\mathbf{R}_a$, such that $|\psi_a(\mathbf{r})|^2 \propto e^{-\frac{|\mathbf{r}-\mathbf{R}_a|}{\xi}}$, where ξ is some localization length dependent on energy and W. And in $d = 3$, there exists a critical value t_c such that eigenstates are localized for $t < t_c$ and there exist delocalized states for $t > t_c$ (i.e. $|\psi_a(\mathbf{r})|^2 \propto V^{-1}$, where V is the volume). In the latter case, not all eigenstates are extended: there are both localized and delocalized states and these two groups are separated by a *mobility edge*, i.e. they do not co-exist at the same energy.

As advertised, instead of presenting Anderson's *tour de force* in perturbation theory, we introduce a simple criterion for a localization-delocalization transition based on the counting on resonances.

The role of resonances

First, let us define the meaning of a hopping resonance and understand its role in the stability of Anderson localization.

Suppose that we are in the weakly hopping limit $t \ll W$ and we want to express the eigenstates $|\psi_a\rangle$ of the Hamiltonian in terms of the single-site, *unperturbed* eigenstates $|\phi_i\rangle = c_i^\dagger |0\rangle$. For illustrative purposes, consider the two-site problem. The Hamiltonian can be written as

$$H = \begin{pmatrix} \mu_1 & t \\ t & \mu_2 \end{pmatrix}, \tag{1.61}$$

and we have encountered it while discussing the Wigner-Dyson surmise. The bare energy separation is $|\mu_1 - \mu_2| \sim W$ and, in the limit $\frac{t}{W} \ll 1$, the eigenstates can be written as $|\psi_{1,2}\rangle \approx |\phi_{1,2}\rangle + \frac{t}{W} |\phi_{2,1}\rangle$ and they are close to the unperturbed states $|\phi_a\rangle$ where fermion is localized on one of the sites. In the opposite case, the *resonant* limit $\frac{t}{W} \gg 1$, the hopping t strongly hybridizes the eigenstates such that $|\psi_{1,2}\rangle \propto |\phi_1\rangle \pm |\phi_2\rangle$ and the fermion is delocalized, i.e. it is equally likely to be on either site.

The two-site toy problem suggests the following intuition for the Anderson localization: in the insulating (localized) phase there are only a few resonances in the system and the eigenstates $|\psi_a\rangle$ are "close" to the on-site (unperturbed) eigenstates $|\phi_a\rangle$, whereas in the metallic (delocalized) phase there exist a proliferation of resonances and the $|\phi_a\rangle$'s are strongly hybridized.

Counting resonances and criterion for the stability of Anderson localization

We now turn back to the full lattice problem and establish a criterion for the stability of Anderson localization by counting resonances: the localization is destroyed once resonances proliferate and single-site states are strongly mixed.

On a lattice in d spatial dimensions, each site has $2d$ neighbors and the energy for a nearest-neighbor hop is $2dt$. The energy mismatch between two neighboring sites is, as before, $|\mu_{\mathbf{R}_i} - \mu_{\mathbf{R}_i+\mathbf{e}}| \sim W$. As shown above, the mixing between single-site states is controlled by the hybridization ratio

$$g = \frac{2dt}{W}. \tag{1.62}$$

Note that, with nearest-neighbor hopping, a fermion can travel a distance r at the r^{th} order in perturbation theory and the matrix element of this hop is approximately tg^r. In the locator limit, $t \ll W$, we have that $g \ll 1$, and the matrix element for a long-range hop decreases exponentially with the distance r. Therefore, for a long-range incoherent transition to be possible, the energy spacing between the initial and final states has be exponentially small as well: $\delta \lesssim tg^r$.

Therefore, our naive criterion for the delocalization transition is

$$g_c = \frac{2dt_c}{W} \sim 1, \tag{1.63}$$

ensuring that single-site states are strongly hybridized and resonances proliferate. In fact, a more careful analysis that takes into account the probability long-range resonances [15] would refine the above criterion to

$$\frac{t_c}{W} \approx \frac{1}{2d \log d}. \tag{1.64}$$

This prediction is incorrect in $d = 1$ and $d = 2$ where there is *no* transition ($t_c \to \infty$). In $d = 2$, this is due to the fact that the localization is caused by quantum interference effects: an electron will visit the same site infinitely many times [20], leading to a loop. However, there are two oriented loops, and these two interfere constructively in the path integral, leading to an enhancement of the localization probability. This phenomenon is also known as *weak localization.*

Nevertheless, our naive criterion (1.64) works increasingly well in higher dimensions for $d > 2$. In fact, it is exact for the "infinite" dimensional case of the Cayley tree (Bethe lattice) of coordination z: the transition occurs at $t_c/W = 1/(z \log z)$, as shown in the pioneering work of Abou-Chacra, Thouless, and Anderson [4].

Stability to interactions

The fundamental message of the previous sections is twofold. First, the stability of Anderson localization to hopping in real space is controlled by resonances and their proliferation leads to delocalization. Second, the spatial dimension d plays an important role [21]. These two observations will have counterparts in our analysis of the stability of localization to adding interactions between particles, which we now discuss.

Let us start by writing Anderson's Hamiltonian (1.60) in second quantized form in the basis of the single-particle localized states:

$$H = \sum_a \epsilon_a \gamma_a^\dagger \gamma_a, \tag{1.65}$$

where $\gamma_a^\dagger$ creates a fermion with energy ϵ_a and state $|a\rangle$, localized around the site $\mathbf{R}_a$. Framing the problem in this second quantized form allows us to naturally extend it to

---

[20] This discussion is very similar (and intimately related) to Polya's recurrence theorem for random walks: an unbiased random walk on $\mathbb{Z}^d$ is recurrent for $d = 1, 2$ and transient for $d > 2$.

[21] An even richer picture emerges from the beautiful scaling theory of Abrahams, Anderson, Licciardello, and Ramakrishnan [5], which we omit here for brevity.

the many-particle, *non-interacting* case. The many-body eigenstates are just Fock states (tensor products of single-particle states) labeled by the occupation numbers $\{n_a\}$.

Based on this formulation, we can make a few last observations *vis-à-vis* the properties of *many-body* Anderson localized systems. First, the level statistics is Poissonian, as discussed above in the case of non-interacting simple harmonic oscillators (Section 1.3). Second, if we start with a spatially non-uniform density of particles in the localized states over a large length scale, this initial density survives at all times because each particle is localized. Thus, the ETH is violated and the system does not thermalize. Third, since the system is non-interacting, there is no spreading of entanglement, no dephasing, and no dissipation.

Therefore, if localization is stable to fermionic hops, then a natural question to ask is whether it is also robust to adding generic fermion-fermion interactions: $\sum_{abcd} V_{abcd}\gamma_a^\dagger\gamma_b^\dagger\gamma_c\gamma_d$. In other words, is *many-body* localization (MBL) possible?

The problem whether Anderson localization is stable to fermionic interactions was first studied by Fleishman and Anderson [89], who found that the answer crucially depends on the dimensionality d of the system and the range of the interactions. The first non-perturbative approach was undertaken by Altshuler, Gefen, Kamenev, and Levitov [13] for a *quantum dot* (i.e. a system without spatial structure) and it had two crucial insights: i) the problem of many-body localization (MBL) can be recast as Anderson localization in the Fock space of single-particle states (a Cayley tree) and ii) the stability of the phase can be investigated using a Fermi's Golden Rule criterion. This second approach (of Altshuler *et al.*) has culminated with the seminal perturbative analysis of Basko, Aleiner, and Altshuler [29] (BAA): they have found that there exists a metal-insulator transition between an MBL state and a delocalized state at a finite temperature T_c and in any spatial dimension d (see also the contemporaneous work of Gornyi, Mirlin, and Polyakov [103]).

More recently, several works have attempted to go beyond the perturbative arguments of BAA. In particular, Imbrie [120] has given a proof for the existence of MBL in spin chains with short-range interactions [22]. Secondly, De Roeck and Huveneers [71, 70] have proposed a non-perturbative mechanism, based on rare regions of weak disorder, that can destabilize many-body localization by triggering a thermalization avalanche. We will present the De Roeck-Huveneers criterion in the remaining part of this section, and we will contrast it to the BAA prediction. Then, in Chapter 3, we will study its most striking consequence: contrary to the BAA prediction, the MBL state is unstable in $d > 1$ or in $d = 1$ with sub-exponentially decaying interactions.

BAA criterion for the stability of MBL

Let us now introduce the BAA criterion and explain how it maps the stability of MBL into a question about Anderson localization in the Fock space of single-particle states.

---

[22] The caveat is that the proof relies on a reasonable assumption, namely that the energy levels do not show level *attraction*.

Following the BAA work [29], we start from the second quantized Hamiltonian

$$H = \sum_a \epsilon_a \gamma_a^\dagger \gamma_a + \sum_{abcd} V_{abcd} \gamma_a^\dagger \gamma_b^\dagger \gamma_c \gamma_d, \tag{1.66}$$

where the interaction V is taken to be "weak," as we will define shortly. Strictly speaking, we have already seen that the non-interacting model ($V = 0$), i.e. the Anderson insulator, has a zero DC conductivity. For the interacting ($V \neq 0$) model, BAA found that there exists a *many-body mobility edge* [23]: there exists a finite energy density $\epsilon_c = \frac{E_c}{N}$ such that $\sigma(\epsilon) = 0$ for $\epsilon < \epsilon_c$ and $\sigma(\epsilon) > 0$ for $\epsilon > \epsilon_c$. This represents a critical point for an insulator-metal transition, separating the insulating MBL phase wherein *many-body* eigenstates are localized, from the metallic phase wherein the eigenstates are extended.

As advertised, the key phenomenological insight of BAA is that many-body localization can be understood as *Anderson localization in the Fock space* of single-particle states. Since the electron-electron interaction is assumed to be short-ranged and the unperturbed eigenstates are exponentially localized around sites $\mathbf{R}_a, \mathbf{R}_b$, etc., then the interaction will only couple a single-particle state $|a\rangle$ to other single-particle states $|b\rangle$ located inside a *localization volume* ξ^d around $\mathbf{R}_a$. For these states, the energy separation between two adjacent levels is typically

$$\delta_\xi^{-1} = \nu \xi^d, \tag{1.67}$$

where ν is the single-particle density of states.

Secondly, we assume that the matrix element takes the form $V_{abcd} = \lambda \delta_\xi$ for states a, b, c, d in the same ball ξ^d centered on $\mathbf{R}_a$ in real space. The fundamental question addressed by BAA is the following: if we start with an electron localized in the single particle state $|a\rangle$, can this electron decay incoherently to a continuum of many-body states?

If we apply the interaction V_{abcd} to an initial state whereby a fermion is located on site a, then this will lead to the decay of this excited state into a three-particle excitation, consisting of a hole on nearby site b and two particles on nearby sites c and d. The energy mismatch between the single-particle excitation and the three-particle excitation is $|\epsilon_a + \epsilon_b - \epsilon_c - \epsilon_d| \sim \delta_\xi$. Further applications of V will lead to five-particle excitations, seven-particle excitations, etc. Therefore, the question becomes whether a single-particle state can lead to a cascade process and ultimately decay into all possible many-body eigenstates.

Inspired by the counting of resonances for Anderson localization, we want to compare the hopping energy $V = \lambda \delta_\xi$ to the energy mismatch δ_ξ and use their ratio as a criterion for the transition: if the hopping energy is much larger than the mismatch, then a single-particle excitation will lead to a proliferation of resonances (excitations). Recalling that the criterion for Anderson localization [15] is

$$\frac{2dt_c}{W} \log \frac{W}{t_c} \sim 1, \tag{1.68}$$

---

[23] More recently, the existence of a many-body mobility edge in a thermodynamic system has been disputed [71], also based on a rare regions mechanism.

we can identify the hopping term with $t \to V = \lambda\delta_\xi$ and the mismatch with $W \to \delta_\xi$. The temperature T sets the number of excited quasi-particles that can scatter with the electron initiated on site a and, through this, it controls the effective connectivity in Fock space $2d \to \frac{T}{\delta_\xi}$.

By identifying the stability of localization to electron-electron interactions with the stability of Anderson localization in Fock space, BAA obtained that a metal-insulator transition occurs at a critical temperature T_c [24] given by

$$T_c \sim \frac{\delta_\xi}{\lambda \log \frac{1}{\lambda}}. \tag{1.69}$$

This mobility edge at T_c separates localized many-body eigenstates of the insulating phase, characterized by $\sigma_{\mathrm{DC}} = 0$, from extended many-body eigenstates of the metallic phase, characterized by diffusive transport $\sigma_{\mathrm{DC}} > 0$.

We emphasize that the above criterion is valid at sufficiently low temperatures. In the limit of high temperatures, the number of available scattering process for $|a\rangle$ is given by $\frac{w}{\delta_\xi}$, where w is the single-particle bandwidth. In $d = 1$ the bandwidth scales as

$$w \approx \frac{1}{\nu a}, \tag{1.70}$$

where a is the lattice constant and ν, as before, is the single-particle density of states. Then the effective connectivity at high temperatures becomes $2d \to \frac{\nu\xi}{\nu a} = \frac{\xi}{a}$.

Therefore, the BAA criterion for the stability of MBL in $d = 1$ and at high temperatures is:

$$\xi_c \sim \frac{a}{\lambda \log \frac{1}{\lambda}}. \tag{1.71}$$

The main prediction of this criterion, which we will contrast with the one due to De Roeck and Huveneers, is that MBL is stable in $d = 1$ for *arbitrarily large* localization lengths ξ, provided that the interaction λ is sufficiently weak.

A phenomenological theory of MBL

In order to present the second criterion for the stability of MBL to rare regions of weak disorder, we have to first introduce a phenomenological description of the system deep in the MBL phase in terms of local integrals of motion (LIOM). Historically, this picture emerged from an early dynamical renormalization group study [238, 12], was expanded by a series of phenomenological arguments [117, 211, 210, 56], and culminated in a rigorous proof [120]. After explaining the origin and main features of this emergent integrability, we review the De Roeck-Huveneers criterion and compare it to the BAA predictions. Subsequently, we shift gears and use the phenomenological theory to explain localization-protected order.

---

[24] Strictly speaking, the temperature is ill-defined for a non-thermal system and we should use energy densities instead.

Since most of this dissertation is concerned with spin chains, let us focus on analyzing MBL in spin systems. First, using a Jordan-Wigner transformation, we can re-cast the Anderson Hamiltonian (1.60) for single-particle localization as a spin Hamiltonian:

$$H = \sum_i J(\sigma_i^x \sigma_{i+1}^x + \sigma_i^y \sigma_{i+1}^y) + \sum_i h_i \sigma_i^z. \tag{1.72}$$

The $\sigma^{x,y,z}$ are Pauli matrices and we have re-labelled the hopping $t \to J$ and the random local fields, drawn from a distribution of width W, $\mu_i \to h_i$. Note that, in this spin picture, $|{\uparrow_i}\rangle$ corresponds to a fermion on site i, whereas $|{\downarrow_i}\rangle$ corresponds to a hole on site i. Secondly, the interactions take the form of an additional term, $\sum_i V_i \sigma_i^z \sigma_{i+1}^z$, leading to the Pal-Huse model [179]:

$$H = \sum_i h_i \sigma_i^z + \sum_i V_i \sigma_i^z \sigma_{i+1}^z + \sum_i J(\sigma_i^x \sigma_{i+1}^x + \sigma_i^y \sigma_{i+1}^y). \tag{1.73}$$

A few remarks are in order. First, this model has a $\mathbb{Z}_2$ symmetry generated by $\Theta = \prod_i \sigma_i^z$. Secondly, in the limit $J = 0$, all of the local spin operators σ_i^z commute with each other, $[\sigma_i^z, \sigma_j^z] = 0$, and with the Hamiltonian, $[\sigma_i^z, H] = 0$. In other words, each local σ_i^z is conserved and the system is trivially localized. To understand why, note that there are N conserved quantities and each one has eigenvalues $\sigma_i^z = \pm 1$. Therefore, *all* 2^N many-body eigenstates of the Hamiltonian H can be labelled by a collection $\{\sigma_i^z\}$ of the quantum numbers, i.e. the eigenstates are product states of the form $|\sigma_1^z\rangle \otimes \cdots \otimes |\sigma_N^z\rangle$.

Turning on a hopping term, $0 < J \ll W$, we can imagine constructing the eigenstates perturbatively à la BAA. The typical level splittings between nearest-neighboring sites $|h_i - h_{i+1}| \sim W$ are much larger than the strength J and the states on different sites are only weakly hybridized. Thus, a conventional BAA analysis would reveal that there exists an energy density ϵ_c such that many-body eigenstates corresponding to $\epsilon > \epsilon_c$ obey ETH, whereas those below ϵ_c violate ETH. This is, indeed, the case for *weak* disorder.

However, extensive numerical evidence [159, 175, 12] and Imbrie's proof [120] reveal an even more complex phenomenology for *strong disorder*. There also exists a critical value for the disorder strength W_c such that, for $W > W_c$, *all* eigenstates are MBL and this occurs even for strong interactions, *well outside the perturbative regime* [25]. This scenario where there is no mobility edge and all many-body eigenstates are localized is known as full-MBL or infinite-temperature MBL.

We are now ready to introduce the phenomenological description [175, 12] of the full-MBL state in one spatial dimension, $d = 1$. For $J \neq 0$, it was argued [210, 211] that the bare physical degrees of freedom σ_i^z, known as *p-bits*, acquire a quasi-local dressing and they can be adiabatically connected to a new set of localized degrees of freedom τ_i^z, known as *l-bits*

---

[25] We emphasize that this transition between thermal (all eigenstates obey ETH) and MBL (all eigenstates violate ETH) phases is an *eigenstate phase transition*, which is marked by sharp changes in the properties of the many-body eigenstates and, thus, the dynamics of the system (i.e. also a *dynamical phase transition*). Clearly, this is visible solely if one employs single-eigenstate ensembles. Otherwise, averaging over many eigenstates as is customary in traditional statistical mechanics would wash away this physical phenomenon.

or LIOMs. This is very similar to the phenomenology of the Fermi Liquid Theory and its quasi-particle description, which we emphasize shortly. Therefore, we can write the p-bits as

$$\sigma_i^z = ... + A_{-1}\tau_{i-1}^z + A_0\tau_i^z + A_1\tau_{i+1}^z + ... + \text{tail}, \tag{1.74}$$

where the tail contains higher-body terms such as $\tau_l^z\tau_m^z\tau_n^z$ etc. The A_r's describe the dressing tail and the LIOMs are quasi-local because this dressing falls off exponentially with the distance r, namely $A_r \propto e^{-r/\xi}$, with a localization length ξ. Note that A_0, known as the quasi-particle residue in Fermi Liquid Theory (FLT), controls the overlap between the renormalized, quasi-local, integrals of motion τ_i^z and the bare (strictly local) σ_i^z.

Most importantly, the quasi-local unitary [26] that maps p-bits to l-bits (LIOMs) also *diagonalizes* the Hamiltonian into

$$H = E_0 + \sum_i \tau_i^z + \sum_{i,j} J_{ij}\tau_i^z\tau_j^z + \sum_{n=1}^{\infty}\sum_{i,\{k\},j} K_{i\{k\}j}^{(n)}\tau_i^z\tau_{k_1}^z...\tau_{k_n}^z\tau_j^z. \tag{1.75}$$

Let us make a few important observations based on this result. First, $J = 0$ and $K = 0$ corresponds to the Anderson insulating limit.

Second, similar to FLT, note that this transformation diagonalizes the Hamiltonian in the quasi-particle basis: the LIOMs τ_i^z commute with each other, $[\tau_i^z, \tau_j^z] = 0$, and with the Hamiltonian $[\tau_i^z, H] = 0$; they are Hermitian and $(\tau_i^z)^2 = 1$, which means that they also have eigenvalues $\tau_i^z = \pm 1$. Therefore, the eigenstates of H are fully determined by specifying a collection $\{\tau_i^z\}$, and they are product states of the form $|\tau_1^z\rangle \otimes \cdots \otimes |\tau_N^z\rangle$.

Third, the dressing tail of each LIOM leads to an effective LIOM-LIOM interaction of the form

$$\sigma_i^z\sigma_{i+1}^z \to Je^{-|i-j|/\xi}\tau_i^z\tau_j^z, \tag{1.76}$$

where J is the bare interaction strength and ξ is the localization length. Thus, the effective interactions J_{ij} in Eq. 1.75 fall off exponentially with distance, as do their probabilities of being large.

Fourth, similar to the emergence of the phenomenological Fermi Liquid Theory as a fixed point in an RG treatment of interacting electrons [212], the phenomenological l-bit Hamiltonian (1.75) emerges as a fixed point in a dynamical RG treatment [238, 12] of the spin model (1.73). This is the reason why full-MBL in $d = 1$, characterized by N local integrals of motion, is sometimes referred to as *emergent integrability*. Nonetheless, note that the quasi-locality of the LIOMs is a crucial aspect since, otherwise, an integrable system *per se* would exhibit ballistic transport (Section 1.3), as opposed to no transport ($\sigma_{\text{DC}} = 0$).

Finally, the dynamics of a single l-bit is trivial: it precesses around the z-axis at a rate given by the strength of the interactions with all the other l-bits. In contradistinction with the Anderson insulating phase, this interaction between the localized degrees of freedom produces both entanglement and dephasing! However, there is no dissipation since there are no spin-flip operators in Eq. 1.75.

---

[26] LIOMs are usually constructed perturbatively and this unitary is generally not unique.

De Roeck-Huveneers criterion for the stability of MBL

We now have the necessary background to introduce the De Roeck-Huveneers [70] criterion for the stability of MBL. We will describe how a rare region of weak disorder, naturally occurring in any disordered and thermodynamic system, may trigger a thermalization avalanche that renders MBL unstable in $d > 1$. Secondly, the De Roeck-Huveneers criterion also implies that there exists a true localization-delocalization transition in $d = 1$, controlled by the localization length ξ, for systems with short-range interactions. This is in stark contrast with the BAA analysis (1.71), which found that MBL is stable in $d = 1$ for arbitrarily large ξ, provided that the interaction is sufficiently weak. We will further explore the thermalization avalanche in Chapter 3, where we will analyze the $d = 1$ problem with exponentially decaying interactions, as well as the cases of $d > 1$ and $d = 1$ with sub-exponential interactions.

Consider a strongly disordered insulator, deep in the putative MBL phase, and let us described it using the phenomenological Hamiltonian from Eq. 1.75, with a localization length ξ. In a thermodynamic system in d spatial dimensions, there will always exist rare regions of abnormally weak disorder. Furthermore, the disorder strength in such a "bubble" may be so weak that this region, in isolation, is thermalizing. Note that thermal bubbles of size ℓ are an extremely rare fluctuation, and they occur with a frequency that decays at least as $\exp(-A\ell^d)$, where A is an $\mathcal{O}(1)$ number.

Let us focus on a single thermal region. If the linear size is ℓ, then it has a many-body level spacing $\delta_b \sim \exp(-A_d\ell^d)$. Secondly, the matrix elements of a local operator σ_i^x acting in the ergodic region are given by the ETH ansatz (1.30):

$$\langle n| \sigma_i^x |m\rangle \approx \sqrt{\delta_b \rho(\omega)}\eta_{nm}, \tag{1.77}$$

where $|n\rangle$ and $|m\rangle$ are eigenstates of the local Hamiltonian characterizing the thermal bubble and correspond to energies E_n and E_m, respectively. The frequency is $\omega = E_n - E_m$. And, for simplicity, we have assumed that the diagonal matrix element $\langle n| \sigma_i^x |n\rangle$ is zero. Lastly, the thermal region is also characterized by a spectral function $\rho(\omega)$, as described in Section 1.1.

We assume that, except for this rare thermal bubble, the rest of the system is deep in the MBL regime and it is characterized by LIOMs τ_α^z. Furthermore, we consider that the LIOMs interact with the ergodic region through their exponentially-decaying dressing tails. Taking the bubble to be located at the origin, the effective coupling between the bubble and the insulator is given by

$$H_{\text{coupling}} = \sum_{i,\alpha} V e^{-r_\alpha/\xi} \sigma_i^x \tau_\alpha^x, \tag{1.78}$$

where σ_i^x is a local operator acting on the bubble, and τ_α^x is a local operator acting on the LIOM located at distance r_α from the origin.

The first step in the thermalization avalanche argument [70] is to consider whether the LIOM closest to the bubble, namely the localized site with the strongest coupling V_α, gets hybridized with the bubble. The criterion for this is given by the following condition for the matrix element $\mathcal{T}$:

$$\mathcal{T} \propto V |\langle n| \sigma_i^x |m\rangle| \approx V\sqrt{\delta_b \rho(W)} \gg \delta_b, \tag{1.79}$$

where $|E_n - E_m| \approx W$ and W is the disorder strength. Crucially, this entails a non-zero Fermi Golden Rule (FGR) decay rate $\sim \mathcal{T}^2/\delta_b$ for the LIOM. If this is the case then the site can be considered as part of the bubble and, once again, we assume the ETH ansatz for the matrix elements. Since the LIOM is absorbed into the ergodic region then the Hilbert space dimension of the combined system increases by a factor of 2, i.e. the level spacing gets reduced to $\delta_E \simeq \delta_b/2$. However, in the process, the spectral function of the ergodic grain also gets modified from $\rho(\omega)$ to $\tilde{\rho}(\omega)$. Based on certain assumptions about the eigenfunctions $|\widetilde{n}\rangle$ of the combined system as a linear superposition of product states $\{|n\rangle \otimes |\tau_\alpha^z\rangle\}$ of the initial bubble and the LIOM, Ref. [70] argues that $\tilde{\rho}(\omega) \simeq \rho(\omega)$, i.e. that the spectral function remains essentially the same after the LIOM becomes a *bona fide* member of the bubble.

If we iterate this argument multiple times such that the bubble grows to a total radius R, then the level spacing becomes $\delta_E(R) \sim \delta_b e^{-A_d R^d}$, where $A_d \sim \mathcal{O}(1)$. The matrix element to absorb an additional LIOM at distance R is $\mathcal{T}_R \sim V\sqrt{\delta_E(R)\rho(W)}e^{-R/\xi}$, leading to the following condition for the hybridization of the site into the bubble:

$$\frac{\mathcal{T}_R}{\delta_E(R)} \sim V\sqrt{\frac{\rho(W)}{\delta_b}} e^{A_d R^d/2 - R/\xi} \gg 1. \tag{1.80}$$

Evidently, the above condition can always be satisfied for $R \to \infty$ in $d > 1$, rendering the localized state unstable in any dimension higher than one! This is in stark contrast with the BAA criterion, which found that MBL is stable in any dimension d at low temperatures—in fact, the BAA prediction should work better in higher dimensions. We emphasize that the De Roeck-Huveneers criterion is based on a non-perturbative effect, whereas the BAA criterion is based on a perturbative analysis, albeit *at all orders*.

A second consequence of Eq. 1.80 is that the exponential has a minimum at

$$R^* = [2/(dA_d\xi)]^{1/(d-1)} \tag{1.81}$$

when $d > 1$. For the avalanche to continue indefinitely, it must survive around R^*. Thus, a necessary and sufficient condition for the LIOM at an arbitrary distance $R > R^*$ to be hybridized with the ergodic region is that $\mathcal{T}_{R^*}/\delta_E(R^*) \gg 1$. This immediately holds if the initial bubble size $N > N^*$, where

$$N^* \sim (1/\xi)^{d/(d-1)}. \tag{1.82}$$

In Chapter 3, we will further analyze this requirement for critical bubble sizes needed to sustain an avalanche.

Lastly, we emphasize that the De Roeck-Huveneers criterion has a striking consequence also in one spatial dimension. For $d = 1$, the function in Eq. 1.80 is monotonically increasing or decreasing if $\xi > \xi_c$ or $\xi < \xi_c$, respectively, where $\xi_c = \frac{2}{A_d}$. This means that the MBL state is stable only below a critical localization length ξ_c! This is in stark contrast with the BAA prediction from Eq. 1.71 whereby MBL is stable in $d = 1$ at *arbitrarily large* localization lengths ξ, provided that the interaction strength is sufficiently small. We will explore this controversy in Chapter 3.

Localization-protected quantum order

We shift gears and present how many-body localization can stabilize quantum order that would otherwise not exist in equilibrium systems. Specifically, we start by discussing the notion of *eigenstate order* whereby certain correlation functions exhibit long-range order in many-body eigenstates. This idea agrees with our conventional understanding of phases of matter for equilibrium systems due to ETH: averaging over a single energy eigenstate is equivalent to a canonical ensemble average. But, most importantly, eigenstate order allows us to generalize the notion of long-range order to *non-equilibrium*, many-body quantum systems, where thermal ensemble averaging provides an incorrect description.

In this section, we will focus on the specific case of spontaneous-symmetry breaking (SSB). From Landau-Peierls-type arguments, we know that such order does not exist at finite temperatures in $d = 1$ for *equilibrium* quantum systems. Taking advantage of the phenomenological theory of MBL introduced in the previous section, we will discuss how strong disorder localizes thermal excitations, leading to SSB order at high energy densities (since temperature is ill-defined) for *non-equilibrium* quantum systems.

In addition to SSB, this “localization-protected” order [118] has also been studied for long-range topological order and for symmetry-protected topological order [175, 12, 118]. We will discuss the latter in the next section, in the context of driven quantum systems, as well as in Chapter 2.

Spontaneous symmetry-breaking below the critical dimension

Let us explain the notion of eigenstate SSB order and how MBL protects it in $d = 1$ by analyzing a transverse-field Ising model:

$$H = -\sum_{i=1}^{N} h_i \sigma_i^x - \sum_{i=1}^{N-1} \left(J_i \sigma_i^z \sigma_{i+1}^z + V_i \sigma_i^x \sigma_{i+1}^x \right), \tag{1.83}$$

where $h_i, J_i, V_i > 0$ are random and drawn from log-normal distributions with means $\overline{h}$, $\overline{J}$, and $\overline{V}$. This model has a $\mathbb{Z}_2$ symmetry generated by the global spin-flip operator $\Theta = \prod_i \sigma_i^x$. Consequently, eigenstates of H must also be eigenstates of Θ.

The clean ($h_i = h$ and $J_i = J$) and non-interacting ($V_i = 0$) model has a zero-temperature phase transition, occurring when $h = J$. Since this is a quantum ($T = 0$) phase transition, it is characterized by different Hamiltonian ground-state properties. To wit, when $h > J$, the system is in a paramagnetic phase: the ground-state is a trivial product state of the form

$|{\rightarrow}{\rightarrow}\cdots{\rightarrow}\rangle$, where $|{\rightarrow_i}\rangle$ is an eigenstate of $\sigma_i^x\,|{\rightarrow_i}\rangle = |{\rightarrow_i}\rangle$. When $h < J$, the system is in a ferromagnetic, *ordered* phase: the ground-states are "cat states" $|\pm\rangle = \frac{|\Uparrow\rangle \pm |\Downarrow\rangle}{\sqrt{2}}$, where $|\Uparrow\rangle = |\uparrow\uparrow\ldots\uparrow\rangle$ and $|\Uparrow\rangle = \Theta\,|\Downarrow\rangle$. These eigenstates are degenerate in the thermodynamic limit and they exhibit *long-range order*:

$$\lim_{r\to\infty}\lim_{N\to\infty}\left(\langle\pm|\,\sigma_0^z\sigma_r^z\,|\pm\rangle - \langle\pm|\,\sigma_0^z\,|\pm\rangle\,\langle\pm|\,\sigma_r^z\,|\pm\rangle\right) = c > 0. \tag{1.84}$$

Crucially, no such order exists at $T > 0$ in $d = 1$, based on Landau-Peierls-type arguments. The intuition is that thermal fluctuations will lead to a proliferation of defects (in this case, domain walls) which will destroy order. We emphasize that eigenstate order, as defined above, reduces to the standard definition of phases of matter for a system in thermal equilibrium: according to ETH, averages in energy eigenstates (1.84) are equivalent to a thermal ensemble average.

Let us now consider the full (disordered and interacting) model from Eq. 1.83. If the disorder is strong enough such that the system is fully-MBL, then we can take advantage of the phenomenological picture from Eq. 1.75. As discussed before, all the eigenstates of the Hamiltonian can be labelled by specifying the quantum numbers of each LIOM τ_i^z. However, depending on the relative strength of the averages $\overline{J}$ and $\overline{h}$, the dependence between LIOMs and the physical degrees of freedom changes dramatically.

In the ordered phase, $\overline{J} \gg \overline{h}$, the LIOMs stem from the local operators σ_i^z: to wit, $\tau_i^z = Z_i\sigma_i^z + \ldots$ and they are *odd* under the $\mathbb{Z}_2$ symmetry generated by Θ. Therefore, if we consider a state $|\tau_1^z\ldots\tau_N^z\rangle$ specified by the LIOM quantum numbers, then we can generate pairs of Hamiltonian eigenstates:

$$|n,\pm\rangle = \frac{|\tau_1^z\ldots\tau_N^z\rangle \pm \left|\overline{\tau_1^z}\ldots\overline{\tau_N^z}\right\rangle}{\sqrt{2}}, \tag{1.85}$$

where $\left|\overline{\tau_1^z}\ldots\overline{\tau_N^z}\right\rangle = \Theta\,|\tau_1^z\ldots\tau_N^z\rangle$. Note that the states $|n,\pm\rangle$ are also eigenstates of Θ, with parity ±1. The number n in $|n,\pm\rangle$ is an index that labels the collection of LIOM quantum numbers $\{\tau_i^z\}$. We immediately see that $\langle n,\pm|\,\tau_i^z\,|n,\pm\rangle = 0$ since the LIOMs are odd under the $\mathbb{Z}_2$ symmetry. Secondly, these Hamiltonian eigenstates exhibit long-range order:

$$\lim_{r\to\infty}\lim_{N\to\infty}\langle n,\pm|\,\sigma_0^z\sigma_r^z\,|n,\pm\rangle \approx \lim_{r\to\infty}\lim_{N\to\infty} Z_0 Z_r\,\langle n,\pm|\,\tau_0^z\tau_r^z\,|n,\pm\rangle \sim Z_0^2 > 0, \tag{1.86}$$

where Z_0^2 represents the overlap between l-bits and p-bits. Note that we have not made any assumptions about the energies of these eigenstates (other than assuming that the system is full-MBL). Thus, we see that MBL stabilizes SSB order in highly-excited eigenstates, i.e. at arbitrarily-high energy densities, which is impossible in thermal equilibrium!

Lastly, to complete the story, note that in the paramagnetic phase ($\overline{J} \ll \overline{h}$) the LIOMs stem from the local operators σ_i^x: $\tau_i^x = \tilde{Z}_i\sigma_i^x + \ldots$ and they are *even* under the $\mathbb{Z}_2$ symmetry generated by Θ. Thus, the eigenstates of the Hamiltonian H are trivial product states of the form $|\tau_1^x\rangle \otimes \cdots \otimes |\tau_N^x\rangle$, and they are also eigenstates of Θ with parity ±1. Since the eigenstates are product states, then it immediately follows that there is *no long-range order* in the $\langle \sigma_0^z \sigma_r^z \rangle$ correlation function.

To summarize, we have found that strong disorder, leading to MBL, localizes the thermal excitations (domain walls) which are responsible for the destruction of long-range, symmetry-breaking order in equilibrium systems below the upper critical dimension.

1.5 Driven systems

Thus far, we have only considered *isolated* many-body systems described by static Hamiltonians. It is natural to wonder whether time-dependent systems, characterized by Hamiltonians $H(t)$, can exhibit exotic and stable phases of matter that do not exist in static systems. To investigate this question, we analyze driven (Floquet) quantum systems, where the Hamiltonian obeys $H(t) = H(t+T)$ with a period T. This basic time dependence can be naturally engineered in cold-atom experiments via an *external* periodic drive field, as we will discuss in Chapter 2.

The remainder of this chapter is organized as follows. We will overview the Floquet formalism, with an emphasis on two fundamental behaviors. First, we will present Floquet-thermalization and draw parallels to our discussion from Section 1.1: the quasi-energies will exhibit level repulsion and the Floquet eigenstates will obey ETH. Such a system will absorb energy indefinitely from the external drive field and eventually heat up to a featureless "infinite-temperature" state. Second, we will introduce Floquet-MBL and explain how the unitary time evolution over a period T can be effectively described using a static, local, and many-body localized (in the sense of Section 1.4) Floquet Hamiltonian: the quasi-energies will obey Poissonian statistics and the Floquet eigenstates will violate ETH. Most importantly, this Floquet Hamiltonian can be diagonalized in terms of local integrals of motion, which explains the absence of heating in a Floquet-MBL system. Finally, we will describe how one can lever the arresting of heating to protect quantum order in Floquet eigenstates. We will concentrate on the case of symmetry-protected topological (SPT) order and briefly describe how to engineer intrinsically-Floquet SPT's that do not have static counterparts, which will be the focus of Chapter 2.

Let us now introduce the building blocks of Floquet theory. Suppose we initialize a Floquet system, described by a periodic Hamiltonian $H(t+T) = H(t)$, in a state $|\Psi(0)\rangle$. The Floquet theorem ensures that Schrodinger's equation

$$i\frac{d\,|\Psi(t)\rangle}{dt} = H(t)\,|\Psi(t)\rangle \tag{1.87}$$

has a solution of the form

$$|\Psi(t)\rangle = e^{-i\epsilon_n t}\,|\phi_n(t)\rangle\,, \tag{1.88}$$

where the Floquet states $|\phi_n\rangle$ are also periodic, i.e. $|\phi_n(t)\rangle = |\phi_n(t+T)\rangle$. This result is the equivalent of Bloch's theorem for spatially-periodic crystals, and the counterparts of the states $|\phi_n\rangle$ are the Bloch waves. Similarly, since in a periodic crystal the momentum is defined in a Brillouin zone, the Floquet *quasi-energies* ϵ_n are also defined modulo 2π, namely $-\frac{\pi}{T} \leq \epsilon_n \leq \frac{\pi}{T}$. Note that they are called *quasi*-energies since the energy, in its traditional understanding, is no longer conserved.

Secondly, a fruitful way to think about these driven systems is to consider the time evolution unitary $U(T)$ over a period T. Solving the linear differential equation in the standard way, we can write

$$U(T) = \mathcal{T} \exp\left(-i \int_0^T dt H(t)\right), \tag{1.89}$$

where $\mathcal{T}$ is the time-ordering operator. Then it becomes evident that the Floquet states $|\phi_n\rangle$ are eigenstates of $U(T)$:

$$U(T) |\phi_n\rangle = e^{-i\epsilon_n T} |\phi_n\rangle . \tag{1.90}$$

In certain cases and under some restrictions for $U(T)$, it is possible to take its logarithm in a controlled way, namely to write it as

$$U(T) = e^{-iH_F T}, \tag{1.91}$$

such that all the information about the driven system is encoded in *a local* Floquet Hamiltonian H_F. In particular,

$$H_F |\phi_n\rangle = \epsilon_n |\phi_n\rangle . \tag{1.92}$$

Note that, since the quasi-energies ϵ_n are not uniquely defined (only modulo 2π), this holds for H_F as well and one needs to specify a branch for the log.

Floquet-thermalization

The existence of *a local* Floquet Hamiltonian is intimately related to the thermalization and heating of the system [1, 184, 185]. In practice, as we will show in Chapter 2, we can attempt to find a local H_F by moving into a rotating frame and then performing a perturbative (Magnus) expansion in the driving frequency ω: we construct $H_F = \sum_n H_F^{(n)}$ and the n^{th} order term is $\mathcal{O}(\omega^{-n})$. This approach fails in *thermalizing* Floquet systems, leading to either a series that does *not* converge or to a Floquet Hamiltonian that is non-local and, therefore, unphysical.

Nevertheless, the term Floquet-thermalizing is warranted since the quasi-energies ϵ_n will exhibit level repulsion and the level statistics will be described by the Circular Orthogonal Ensemble (COE) [27]. Secondly, the Floquet eigenstates $|\phi_n\rangle$ will obey a volume law for the entanglement entropy and satisfy ETH. Finally, in this thermalizing case, the Floquet system will absorb energy indefinitely from the external drive and, provided that the Hilbert space is bounded, heat up to an "infinite-temperature" state whereby the reduced density matrix of a sub-system is $\rho \propto \mathbb{1}$. We emphasize that, as argued in Ref. [185], the heating to an infinite-temperature state guarantees that the Magnus expansion does *not* converge.

---

[27] This ensemble is the generalization of GOE for the case where the ϵ_n's are defined on the circle (i.e. modulo 2π).

Floquet-MBL

We now discuss the second possibility, namely that the Floquet unitary $U(T)$ admits a decomposition in terms of a local Floquet Hamiltonian. In particular, we will explain how, for sufficiently strong disorder, it is possible to obtain a Floquet-MBL phase where H_F is local and it can be diagonalized in terms of local integrals of motion *à la* Section 1.4.

In recent years, there has been a flurry of work [185, 131, 132, 77, 76, 133, 244, 186] on driven systems with a binary protocol whereby one dynamically toggles between a localized Hamiltonian H_1 and a delocalized Hamiltonian H_2. For illustrative purposes, let us focus on the following example [185]:

$$H(t) = \begin{cases} H_1 = \sum_i h_i \sigma_i^z + J_z \sigma_i^z \sigma_{i+1}^z & \text{if } 0 \leq t < T_1 \\ H_2 = \sum_i J_x (\sigma_i^x \sigma_{i+1}^x + \sigma_i^y \sigma_{i+1}^y) & \text{if } T_1 \leq t < T_1 + T_2 \end{cases} ,$$

where h_i is drawn from a distribution of width W [28]. Suppose that we fix the interaction strengths J_z and J_x, the disorder strength W, and the first period T_1. We then vary the second period T_2 and study the behavior of the Floquet unitary:

$$U(T_2) = \exp\left(-iH_2T_2\right) \exp\left(-iH_1T_1\right). \tag{1.93}$$

For large T_2 (i.e. small driving frequencies), the system is thermalizing: the eigenstates of $U(T_2)$ obey ETH and the quasi-energies are well-described by the COE [185]. For large enough driving frequencies, namely for $T_2 < T_2^*$, where T_2^* does *not* scale with system size and it is a true critical point, the system is localized: the Floquet eigenstates violate ETH and the quasi-energies obey Poissonian statistics. Moreover, in the Floquet-MBL regime, the system exhibits coherent dynamics at infinite times. For instance, if we prepare the system (1.93) in a Nèel initial state $|\Psi(0)\rangle = |\uparrow\downarrow\uparrow\downarrow \ldots\rangle$ and let it evolve for infinitely-many Floquet periods, then the infinite-time average of a local operator $\langle \sigma_0^z(\infty) \rangle$ will *not* decay [185]. Conversely, in the Floquet-thermalizing phase at small driving frequencies, this time-averaged expectation value will vanish.

All of the above features of the Floquet-MBL state can be understood by using the phenomenological picture of many-body localization. In particular, the Floquet Hamiltonian H_F is quasi-local and it can be diagonalized in terms of LIOMs:

$$H_F = E_0 + \sum_i \tau_i^z + \sum_{ij} J_{ij} \tau_i^z \tau_j^z + \ldots \tag{1.94}$$

In other words, the dynamical properties of the Floquet-MBL phase are described by an effective *static* Hamiltonian H_F that is many-body localized in the sense of Section 1.4. If localization can arrest the heating of the system, then an immediate question is whether it is possible to obtain stable phases of matter in a driven system and, more ambitiously, whether we can find *novel* phases that do not exist in static systems.

---

[28] The clean model, $h_i = h$, heats up to infinite temperature and the Floquet Hamiltonian is non-local [67].

Floquet-SPT order

We now briefly investigate order in Floquet systems. In Chapter 2, we will see that the interplay between interactions, periodic driving, and disorder leads to exotic phases of matter, such as discrete time-translation symmetry-breaking phases (i.e. the discrete time crystals observed in Refs. [250, 61]) and symmetry-protected topological phases that do *not* have analogues in static Hamiltonians. In this section, we will present the latter. First, we will define SPT order in the context of equilibrium, static systems. Then we will introduce the notion of driven SPT's and describe how there exist intrinsically-Floquet SPT's, which will be the focus of Chapter 2.

Static SPT

Let us first define symmetry-protected topological order and illustrate its properties with a prototypical example for an equilibrium $d = 1$ system.

A system described by a static Hamiltonian H with a symmetry group G is in a gapped SPT phase if the ground-state of H obeys the following requirements: i) the symmetry is not spontaneously broken and ii) the ground-state cannot be adiabatically connected to a trivial product state without *either* undergoing a phase transition and closing the gap *or* explicitly breaking the symmetry [207]. Intuitively, this emphasizes the *protecting* role of the symmetry. To understand the role of topology, we note that an SPT phase is “trivial” in the bulk, but exhibits non-trivial edge modes on the boundary.

To make things precise, consider the following Hamiltonian on a chain with N sites and open boundary conditions:

$$H = \lambda \sum_{i=2}^{N-1} \sigma^z_{i-1}\sigma^x_i\sigma^z_{i+1} = \lambda \sum_{i=2}^{N-1} \mathcal{O}_i, \tag{1.95}$$

which is known as a stabilizer code in the quantum information community. We can easily see that the $N-2$ stabilizers $\mathcal{O}_i$ are Hermitian operators with the following properties

$$\begin{aligned} [H, \mathcal{O}_i] &= 0 \\ [\mathcal{O}_i, \mathcal{O}_j] &= 0 \quad \forall\, i,j = 2,\ldots,N-1 \\ \mathcal{O}_i^2 &= \mathbb{1}. \end{aligned} \tag{1.96}$$

In other words, the stabilizers correspond to $N-2$ conserved quantities of the Hamiltonian H and each conserved quantity has eigenvalues ±1. Consequently, there are 2^{N-2} different collections of quantum numbers for the stabilizers. The missing factor of 4 is due to the edge modes of the system. In particular, note that we can define two edges modes, located around sites 1 and N, as follows:

$$\begin{aligned} \Sigma^x_1 &= \sigma^x_1\sigma^z_2 \\ \Sigma^y_1 &= \sigma^y_1\sigma^z_2 \\ \Sigma^z_1 &= \sigma^z_1, \end{aligned} \tag{1.97}$$

and similar expressions hold for the Σ_N operators. Then we see that these modes obey the standard Pauli algebra, namely $[\Sigma_1^\alpha, \Sigma_1^\beta] = 2i\epsilon^{\alpha\beta\gamma}\Sigma_1^\gamma$, where $\epsilon^{\alpha\beta\gamma}$ is the Levi-Civita tensor. Finally, both edge modes commute with the Hamiltonian H and behave like free $S = \frac{1}{2}$ spins located on the boundaries of the system, leading to a four-fold degeneracy for a system with open boundary conditions. Thus, we can label all eigenstates of H by specifying the quantum numbers for the $N-2$ stabilizers and specifying the states of each edge mode. Conversely, in a system with periodic boundary conditions, the ground-state is unique—intuitively, there are no "edges" and, thus, no edge modes. This observation explains the role of topology in symmetry-protected *topological* order.

The symmetry of H is $\mathbb{Z}_2 \times \mathbb{Z}_2$ and it is generated by $\Theta_\text{e} = \prod_i \sigma_{2i}^x$ and $\Theta_\text{o} = \prod_i \sigma_{2i+1}^x$. We immediately see that the edge operators, Σ_1 and Σ_N, are both *odd* under this symmetry. This means that the symmetry protects the gapless edge modes: to gap them out, we would have to add an operator Σ^α to the Hamiltonian, but this would break the $\mathbb{Z}_2 \times \mathbb{Z}_2$ symmetry of H! Moreover, this SPT and its edge modes are robust to generic and local perturbations that do *not* break the protecting symmetry.

Protecting symmetries and projective representations

An immediate question is whether it is possible to obtain an SPT state with a simpler symmetry group—for instance, a single $\mathbb{Z}_2$. We will briefly introduce the idea of projective representations of symmetry groups to explain why this is not possible. This will allow us to further appreciate the subtlety of intrinsically-Floquet SPT's.

The main observation stemming from the $\mathbb{Z}_2\times\mathbb{Z}_2$ SPT we discussed above is that the edges transform projectively under the symmetry group. In fact, there is a one-to-one mapping between $d = 1$ bosonic SPT's with a symmetry group G and equivalence classes of projective representations of G [183, 234, 58].

Consider a unitary symmetry described by the group G, whose elements are g_i. Then we know that a set of matrices $U(g_i)$ form a *linear* representation of G if

$$U(g_i)U(g_j) = U(g_ig_j). \tag{1.98}$$

More generally, a *projective* representation of G is a linear representation modulo a $U(1)$ phase factor:

$$U(g_i)U(g_j) = \omega(g_i, g_j)U(g_ig_j), \tag{1.99}$$

where $\omega(g_i, g_j) \in U(1)$ are known as the factor set. From group associativity $(g_ig_j)g_k = g_i(g_jg_k)$, we immediately see that the following must hold:

$$\omega(g_i, g_j)\omega(g_ig_j, g_k) = \omega(g_j, g_k)\omega(g_i, g_jg_k). \tag{1.100}$$

If we just re-define the matrices $\overline{U}(g_i) = \alpha(g_i)U(g_i)$ by a phase factor $\alpha(g_i) \in U(1)$ then this will generate a new factor set:

$$\overline{\omega}(g_i, g_j) = \frac{\alpha(g_ig_j)}{\alpha(g_i)\alpha(g_j)}\omega(g_i, g_j). \tag{1.101}$$

Thus, two factor sets related by such a transformation lead to *equivalent* projective representations U and $\overline{U}$. Since the edges of an SPT transform projectively under the symmetry group G, then we are interested in non-trivial projective representation classes under this equivalence relation. It was proved by Schur that this is captured by the second cohomology group $H^2(G, U(1))$.

We are now ready to explain why there is no SPT protected solely by a $\mathbb{Z}_N$ symmetry. The elements of the cyclic group are $\{1, g, g^2, \ldots, g^{N-1}\}$ and we immediately see that any projective representation for $U(g)$ is equivalent to the linear representation after re-scaling by a phase factor $e^{i\phi/N}$. Consequently, there is no static $\mathbb{Z}_2$ SPT. Finally, the dihedral group $\mathbb{Z}_2 \times \mathbb{Z}_2$ has two projective representation classes, and the SPT we have previously discussed realizes the non-trivial one.

Floquet SPT

In this section we briefly discuss how a Floquet system can realize an SPT phase with a single $\mathbb{Z}_2$ internal symmetry. The crucial point is that this Floquet-SPT is protected by both the $\mathbb{Z}_2$ symmetry and the discrete time-translation symmetry $\mathbb{Z}$, which is why we use the terminology *intrinsically-Floquet.* We will illustrate these points using a non-interacting and exactly solvable model. In Chapter 2, we will explore these ideas in more detail in the context of a Floquet-SPT phase that is stabilized by many-body localization in an interacting system.

Consider the following binary drive of a transverse-field Ising model:

$$H(t) = \begin{cases} H_1 = \sum_i J\sigma_i^z\sigma_{i+1}^z & \text{if} \quad 0 \le t < T/2 \\ H_2 = \sum_{i=1}^{N} h_i\sigma_i^x & \text{if} \quad T/2 \le t < T. \end{cases} \tag{1.102}$$

This model has only nearest-neighbor interactions and it can be mapped to free Majorana fermions, but it helps illustrate the main properties of the FSPT [133, 131, 132]. We will study its interacting and disordered counterpart in Chapter 2.

The Floquet operator over a period T can be written as

$$U(T) = \exp(-iH_2T/2)\exp(-iH_1T/2). \tag{1.103}$$

Taking $\frac{JT}{2} = \frac{\pi}{2}$ and using open boundary conditions, we find that

$$\exp\left(-iH_1T/2\right) = \sigma_1^z\sigma_N^z.$$

Note that under periodic boundary conditions this would be proportional to the identity $\mathbb{1}$. We can also re-write the second piece of the Floquet unitary as

$$\exp\left(-iH_2T/2\right) = \left[-i\sin(\theta_1)\sigma_1^x + \cos(\theta_1)\right]\left[-i\sin(\theta_N)\sigma_N^x + \cos(\theta_N)\right]\exp\left(-iH_{\text{bulk}}T/2\right),$$

where $\theta_i = \frac{h_i T}{2}$ and $H_{\text{bulk}} = \sum_{1<i<N} h_i \sigma_i^x$ (see Appendix 2.6 for a detailed derivation). Putting both pieces together, we find that

$$U(T) \quad \propto \quad \tilde{\sigma}_1^z \tilde{\sigma}_N^z \exp\left(-iH_{\text{bulk}}T/2\right),$$

where $\tilde{\sigma}_{1,N}^z = \left[-\sin(\theta_{1,N})\sigma_{1,N}^y + \cos(\theta_{1,N})\sigma_{1,N}^z\right]$ and note that $\left(\tilde{\sigma}_{1,N}^z\right)^2 = 1$. Thus, the Floquet operator $U(T) = \tilde{\sigma}_1^z \tilde{\sigma}_N^z \exp\left(-iH_{\text{bulk}}T/2\right)$ has two pieces: a "charge pump" term $\tilde{\sigma}_1^z \tilde{\sigma}_N^z$ corresponding to the product of two operators localized around the edges; and a unitary time evolution over $T/2$ with a local *bulk* Hamiltonian $H_{\text{bulk}} = \sum_{1<i<N} h_i \sigma_i^x$.

A few observations are in order. First, the operators $\tilde{\sigma}_{1,N}^z$ localized around the edges commute with each other, with the bulk operator H_{bulk}, and, thus, with the Floquet unitary $U(T)$. Second, these edge operators are odd under the global $\mathbb{Z}_2$ symmetry generated by $\Theta = \prod \sigma_i^x$:

$$\begin{aligned} \Theta \tilde{\sigma}_{1,N}^z \Theta^\dagger &= \sigma_{1,N}^x \left[-\sin(\theta_{1,N})\sigma_{1,N}^y + \cos(\theta_{1,N})\sigma_{1,N}^z\right] \sigma_{1,N}^x \\ &= -\tilde{\sigma}_{1,N}^z. \end{aligned}$$

Therefore, these are the protected edge modes of the FSPT.

Finally, note that $U(2T) = U^2 = \mathbb{1}_{\text{edges}} \otimes \exp\left(-iH_{\text{bulk}}T\right)$ and the edge operators that are even under the $\mathbb{Z}_2$ Ising symmetry, for instance $\tilde{\sigma}_{1,N}^x$, obey the following equation of motion:

$$U(nT)\tilde{\sigma}_{1,N}^x U^\dagger(nT) = (-1)^n \tilde{\sigma}_{1,N}^x. \tag{1.104}$$

This means that, given any generic initial state of the system, the edge operators $\tilde{\sigma}_{1,N}^x$ will oscillate with a period $2T$, as opposed to the period T of the drive! We emphasize that this does *not* hold for bulk operators, whose correlations are trivial in the FSPT phase. Therefore, the Floquet system exhibits a form of *discrete time-translation symmetry breaking* (TTSB) on the boundary of the system. In Chapter 2, we will further explore this observation for interacting and Floquet-MBL systems, and explain how the FSPT is dual to a discrete-time crystal phase that exhibits TTSB in the bulk.

1.6 Organization

The rest of this dissertation is organized as follows.

Chapter 2 is based on [186]. We study how strong disorder, leading to many-body localization, can arrest the heating of an interacting Floquet system and stabilize symmetry-protected topological order. We analyze two conceptually different routes. By driving a simple model, one can engineer complex interactions that enable the *emulation* of an equilibrium phase. In a different approach, driving can *simulate* an intrinsically-Floquet phase that does not have an equilibrium analogue. We discuss how these two phases can be distinguished via a special entanglement spectrum signature of the latter and emphasize its duality to a discrete time crystal [250, 61]: although not included here, we present this phase in detail in Ref. [244]. We then propose a unifying implementation in a one-dimensional chain of cold atoms and show that protected edge modes are observable on realistic experimental time scales.

Chapter 3 is based on [187]. Recent work by De Roeck *et al.* [70] has argued that many-body localization is unstable in two and higher dimensions due to a thermalization avalanche triggered by rare regions of weak disorder. To examine these arguments, we construct several models of a finite ergodic bubble coupled to an Anderson insulator. In one case, our results are in excellent agreement with a refined theory of the thermalization avalanche. In the second model, where we can access much larger system sizes, we find a non-trivial back-action effect due to the insulator onto the ergodic bubble. The main consequence of this back-action is to renormalize the critical bubble size needed to sustain the avalanche. This allows us highlight the unrealistically large time scales involved in this process.

Chapter 4 is based on [33]. We propose an experimentally accessible non-local spin system as a paradigmatic platform to study integrability, chaos, and thermalization in closed many-body quantum systems. It has a rich, highly tunable dynamical phase diagram, including regions of Richardson-Gaudin quantum integrability, classical chaos, and of a novel form of integrability that is distinct from (and possibly intermediate between) Bethe Ansatz and Many-Body Localization. These phases are accessible in state-of-the-art cavity QED setups by tuning the local atomic density and the direction of an applied magnetic field.

Lastly, Chapter 5 is based on [188]. We introduce a statistical ensemble that interpolates between the classical k-Satisfiability (k-SAT) and the quantum k-Satisfiability (k-QSAT). For $k \geq 3$, these two problems are complete for the complexity classes NP and QMA, respectively, and are believed to be intractable for both classical and quantum computers. Moreover, as discussed in Section 1.2, they have interesting connections to classical and quantum spin glass problems, respectively. For the simplest 2-SAT–2-QSAT ensemble, we find the exact boundary that separates SAT and UNSAT instances.

Chapter 2

Floquet symmetry-protected topological phases

The discovery of topological insulators—materials which are insulating in their interior but can conduct on their surface—has led to a multitude of advances at the interface of condensed matter physics and materials engineering [34, 59, 110, 191, 35]. At their core, such insulators are characterized by the existence of non-trivial topology in their underlying single-particle electronic band structure [128, 171]. Generalizing our understanding of topological phases to the presence of strong many-body interactions represents one of the central questions in modern physics. Some of the simplest generalizations that have emerged along this direction are symmetry protected topological (SPT) phases [207, 233, 58], which represent the minimal extension of topological band insulators to include many-body correlations. Featuring short-range entanglement, SPT phases do not exhibit anyonic excitations in their bulk, but nevertheless possess protected edge modes on their surface; as a result, they represent a particularly fertile ground for studying the interplay between symmetry, topology, and interactions.

While indirect signatures of certain ground state SPT's have been observed in the solid state [51, 172, 242], directly probing the quantum coherence of their underlying edge modes represents an outstanding experimental challenge. In principle, cold atomic quantum simulations could offer a powerful additional tool set—including locally-resolved measurements and interferometric protocols—for probing the robustness of edge modes and systematically exploring their stability to specific perturbations [23, 21, 60, 108, 181]. Moreover, such platforms could also enable the controlled storage and transmission of quantum information [57, 22, 247]. Despite these advantages, and owing to the complexity of typical model SPT Hamiltonians, it remains difficult to engineer and stabilize SPT phases in cold atomic systems.

One approach to this challenge is to emulate the complex interactions giving rise to static, equilibrium SPT (ESPT) phases by periodically driving a simpler Hamiltonian at frequencies much larger than its intrinsic energy scales [119]. In addition to this approach, seminal results on classifying driven (Floquet) phases [133, 131, 132, 189, 77, 197] have also

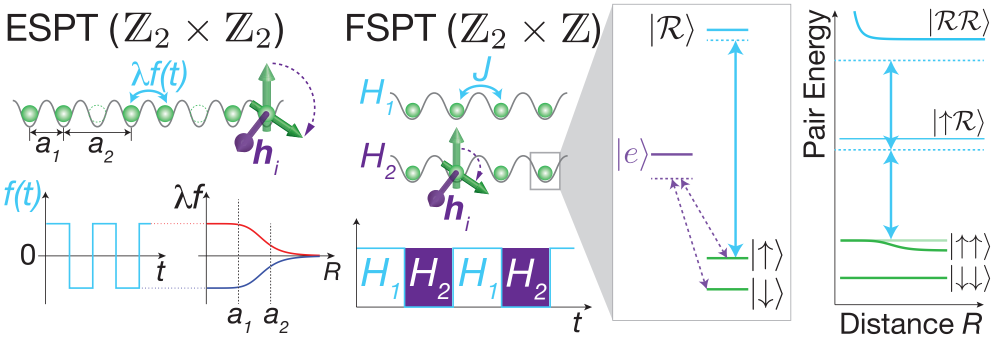

Figure 2.1: A 1D array of atoms is trapped in an optical lattice or tweezer array. Ising interactions for pseudo-spin states $|\downarrow\rangle$, $|\uparrow\rangle$ are generated by optically coupling $|\uparrow\rangle$ to Rydberg state $|\mathcal{R}\rangle$ (solid blue arrows). Random fields h_i are generated by a spatially varying Raman coupling (dotted purple arrows) between $|\downarrow\rangle$ and $|\uparrow\rangle$. While emulating the ESPT phase requires a dimerized chain with Ising couplings $\lambda f(t)$ of dynamically switchable sign, the FSPT phase is simulated simply by alternating between two Hamiltonians consisting of Ising interactions (H_1) and a disordered transverse field (H_2).

shown that there exist Floquet-SPT's (FSPT) which are inherently dynamical and have no static analogue. Interestingly, such an FSPT can be realized at driving frequencies that are *comparable* to the energy scales of the bare Hamiltonian.

The power of periodic driving for engineering topological phases has been extensively explored in cold-atom [8, 127, 129], solid-state [177, 155, 239], and photonic [193, 232] systems. For cold atoms, where Floquet control has so far been applied only to single-particle band structures [65, 8, 111, 127, 129, 88], recent advances in optically controlling interactions [63, 94, 122, 249, 101, 143, 248, 36] offer new opportunities for accessing strongly correlated phases [246, 39, 97, 81]. Notably, coherent spin-spin interactions with a range of several microns [122, 249, 248, 36] can be introduced via Rydberg dressing [125, 112, 190, 96, 122, 249, 101, 248, 36]. However, prospects for modulating such dressing light in order to Floquet engineer many-body Hamiltonians has remained largely unexplored.

This owes, in part, to the difficulty of generating quantum coherent order in an interacting Floquet system which will typically absorb energy from the driving field, eventually heating to a featureless infinite temperature state [67, 148]. This difficulty is further exacerbated for isolated atomic systems, where the lack of coupling to an external bath renders the system incapable of releasing excess energy and entropy [224]. A fruitful strategy for combating such heating is to harness many-body localization (MBL) [118, 175, 12, 185, 133], which has been predicted to stabilize quantum coherent behavior without the need for stringent cooling or adiabatic preparation of low temperature many-body states [22, 57, 247, 26].

We propose to exploit periodically driven interactions to realize two distinct nonequilibrium MBL SPT phases in a one-dimensional array of cold atoms (Fig. 2.1). Driving the interaction term of a transverse-field Ising model (TFIM) enables the emulation of an ESPT whose edge modes are protected by an emergent $\mathbb{Z}_2 \times \mathbb{Z}_2$ symmetry [119]. This phase remains stable only within a parametric time scale controlled by the driving frequency, beyond which its topological features break down. Alternatively, toggling between Hamiltonians with solely Ising interactions or purely transverse fields yields an intrinsically dynamical FSPT which has no equilibrium analogue. We explore the stability of both phases to long-range interactions and provide a detailed experimental blueprint using Rydberg-dressed atoms.

2.1 Emulating a static, equilibrium SPT phase

Inspired by pioneering work on emulating static phases in driven systems [177, 138, 155, 124, 119, 199, 198, 150], we first consider the realization of a many-body localized version of the Haldane phase [107]. This SPT phase can be protected by a discrete dihedral symmetry, $\mathbb{Z}_2 \times \mathbb{Z}_2$, and exhibits boundary modes that are odd under the symmetry; these edge modes behave as decoupled spin-1/2 degrees of freedom that are robust to any perturbation which preserves the symmetry.

We begin by examining the robustness of the edge modes in a periodically driven and dimerized spin chain (Fig. 2.1):

$$H_0(t) = \sum_{i=1}^{N} h_i \sigma_i^x + \sum_{i=1}^{N-1} f(t)\lambda_i \sigma_i^z \sigma_{i+1}^z + V_x \sigma_i^x \sigma_{i+1}^x, \tag{2.1}$$

where N represents an even number of spins, σ_i^α are the Pauli operators on site i, $\lambda_{2k+1} = \lambda_1$, $\lambda_{2k} = \lambda_2$ (with $\lambda_1, \lambda_2 > 0$) and $f(t) = \omega\cos(\omega t)$ is the driving function [1]. For $V_x = 0$, the model is non-interacting and exhibits edge dynamics which never decohere [119]. Here, we first verify that the SPT phase remains stable under the addition of short-range interactions $V_x \neq 0$ that preserve the dihedral symmetry (generated by products of σ_i^x on the even and odd sites). We then assess the effects of more generic, longer range, interactions.

In the limit of large driving frequencies ω, the dynamics are described by an effective time-independent Floquet Hamiltonian, H_F, which can be constructed perturbatively in orders of $1/\omega$ using a Magnus expansion [1, 142, 3]. At leading order, we obtain the time-averaged Floquet Hamiltonian (see Appendix 2.5 for details)

$$\begin{aligned} H_\mathrm{F}^{(0)} &= \sum_{i=1}^{N} h_i a(\lambda_1,\lambda_2)\sigma_i^x - \sum_{i=2}^{N-1} h_i b(\lambda_1,\lambda_2)\sigma_{i-1}^z \sigma_i^x \sigma_{i+1}^z \qquad (2.2) \\ &+ V_x J_0(2\lambda_2)(\sigma_1^x\sigma_2^x + \sigma_{N-1}^x\sigma_N^x) + V_x \sum_{i=2}^{N-2}\left[c(\lambda_{i+1})\sigma_i^x\sigma_{i+1}^x + d(\lambda_{i+1})\sigma_{i-1}^z\sigma_i^y\sigma_{i+1}^y\sigma_{i+2}^z\right], \end{aligned}$$

---

[1] Any driving function that changes sign every half-period will suffice. For instance, tweaking the binary drive from [133] to have this property would also yield an ESPT.

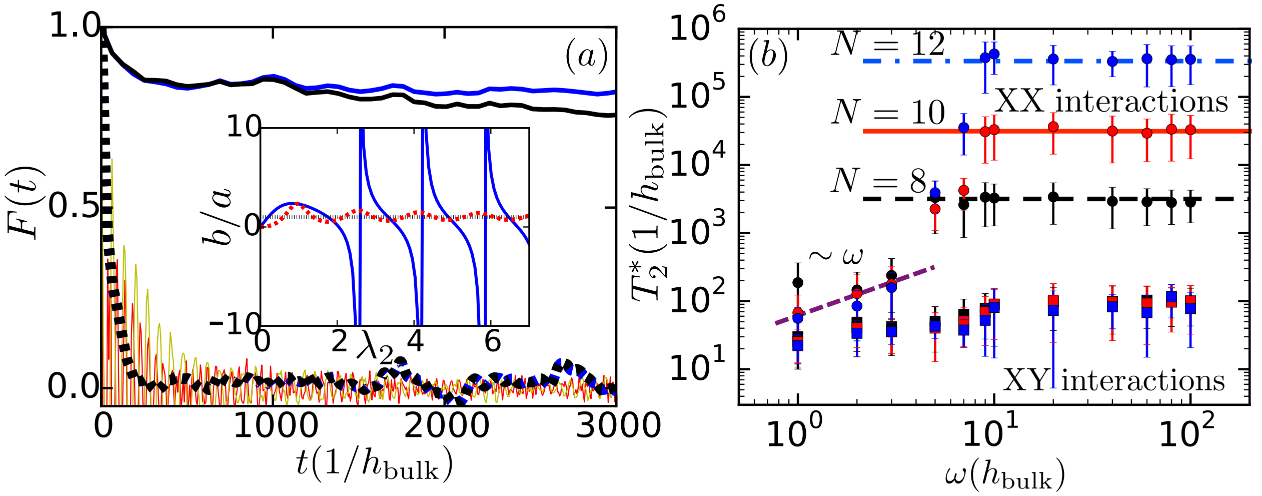

Figure 2.2: ESPT phase—(a) $F^{\alpha}(t)$ for $N = 10$ spins with $\omega = 100$, $V_x = 0.05$, $V_y = 0$, $\lambda_1 = 1.54$ and $\lambda_2 = 0.69$, yielding $b(\lambda_1, \lambda_2)/a(\lambda_1, \lambda_2) \sim 10$. Almost overlapping dotted lines represent the clean undisordered case (black and blue for F^z and F^x, respectively). Solid lines correspond to strong on-site disorder, with thick black and blue lines for F^z and F^x in the dimerized case and thin solid yellow and red lines for F^z and F^x in the un-dimerized case. (inset) Ratio $b(1, \lambda_2)/a(1, \lambda_2)$ in the dimerized (solid blue) and the un-dimerized (dotted red) models. The SPT phase corresponds to $b/a > 1$ (delimited by the dotted black line). (b) T_2^* as a function of frequency and system size. As ω is increased for $V_x = 0.05$ (circles), T_2^* saturates consistent with being bounded by $T_2^* \sim \min(\mathcal{O}(\omega), e^{\mathcal{O}(N)})$. Adding generic interactions, $V_y \sum_i \sigma_i^y \sigma_{i+1}^y$ with $V_y = 0.2$ (squares), leads to a breakdown of the edge coherence for all parameters.

where $J_0(x)$ is the Bessel function of the first kind,

$$\begin{aligned} a(\lambda_1, \lambda_2) &= \frac{1}{2}\left[J_0\left(2(\lambda_1 - \lambda_2)\right) + J_0(2(\lambda_1 + \lambda_2))\right], \\ b(\lambda_1, \lambda_2) &= J_0(2(\lambda_1 - \lambda_2)) - a(\lambda_1, \lambda_2), \\ c(\lambda) &= \frac{1}{2}\left[1 + J_0(4\lambda)\right], \\ d(\lambda) &= 1 - c(\lambda). \end{aligned} \tag{2.3}$$

We have absorbed a factor of $\frac{J_0(2\lambda_1)}{a(\lambda_1,\lambda_2)}$ in the definitions of h_1 and h_N [2].

A few remarks are in order. First, the periodic driving, $f(t)$, effectively generates multi-spin interactions [Eqn. (2.2)] [119]. Secondly, while $H_{\mathrm{F}}^{(0)}$ exhibits a $\mathbb{Z}_2 \times \mathbb{Z}_2$ symmetry, the parent Hamiltonian [Eqn. (2.1)] possesses only a smaller $\mathbb{Z}_2$ symmetry group, indicating that the "emergent" dihedral symmetry of $H_{\mathrm{F}}^{(0)}$ must be broken at higher orders in the

---

[2] Note that for finite frequency drives, the n^{th} order perturbative correction to $H_{\mathrm{F}}^{(0)}$ is of order $1/\omega^n$.

Magnus expansion (see Appendix 2.5). Finally, the $V_x = 0$ limit of Eqn. (2.2) describes a pair of decoupled 1D p-wave superconductors [135] and harbors two simple limits: for $a(\lambda_1, \lambda_2) > b(\lambda_1, \lambda_2)$, the ground state is a trivial insulator, while for $a(\lambda_1, \lambda_2) < b(\lambda_1, \lambda_2)$, the ground state is a bosonic SPT insulator. The key signature of this latter ESPT phase is the existence of protected modes localized around the boundary of the system. Crucially, the λ_1, λ_2-dimerization of the Ising interaction enables us to arbitrarily tune the correlation length of the edge mode (inset of Fig. 2.2a), leading to coherent dynamics with significantly higher fidelity than those of the un-dimerized TFIM [119].

To characterize the edge coherence, we introduce the trace fidelity

$$F^{\alpha}(t) = \frac{1}{Z}\mathrm{Tr}\left[e^{-\beta H(t)}\Sigma^{\alpha}(t)\Sigma^{\alpha}(0)\right] \tag{2.4}$$

as a function of time, where Z is the partition function, $\beta = 1/k_{\mathrm{B}}T$, and Σ^{α} are the zero correlation length edge operators $\Sigma^x = \sigma_1^x\sigma_2^z$, $\Sigma^y = \sigma_1^y\sigma_2^z$, and $\Sigma^z = \sigma_1^z$. This auto-correlation function at infinite temperature will serve as a proxy for the coherence time. Furthermore, since we are interested in coherent MBL-protected dynamics at finite energy densities, from hereon we add strong disorder to the system via random on-site fields h_i [3].

As alluded to above, there are two mechanisms of edge spin decoherence introduced by interactions: 1) scattering with thermal excitations and 2) breaking of the $\mathbb{Z}_2 \times \mathbb{Z}_2$ symmetry. While the first is ameliorated via MBL (Fig. 2.2a), the second is intrinsic to the stroboscopic approach—the ESPT is stable only up to a finite parametric time scale, $T^*_{2,\mathrm{symm}} \sim (h^2/\omega)^{-1}$, beyond which the protecting symmetry is broken.

The first effect is reminiscent of similar discussions in the static context [22, 57, 247], where disorder can localize thermal bulk excitations and suppress scattering. Since the edge operators are odd under the $\mathbb{Z}_2 \times \mathbb{Z}_2$ symmetry, their dressed MBL-counterparts will not appear in the effective "l-bit" Hamiltonian [175, 12] and dephasing occurs solely via coupling to the other edge mode [247] on a time scale that is exponential in system size, $T^*_{2,\mathrm{MBL}} \sim e^{\mathcal{O}(N)}$, as depicted in Fig. 2.2b. Thus, so long as the effective dynamics are described by $H_{\mathrm{F}}^{(0)}$, one finds that even in the interacting, periodically driven system, disorder [4] can lead to a revival of the coherence time (Fig. 2.2a).

This MBL enhancement of edge coherence is cut off by the fact that the first order Magnus correction, $H_{\mathrm{F}}^{(1)}$, breaks the $\mathbb{Z}_2 \times \mathbb{Z}_2$ symmetry. For time scales $t > T^*_{2,\mathrm{symm}}$, even though bulk excitations remain many-body localized, there is no symmetry protecting the edge operators, which can then scatter locally. Thus, for a finite size system, decoherence in the presence of interactions that preserve the dihedral symmetry occurs on a time scale:

$$T_2^* \sim \min(T^*_{2,\mathrm{MBL}}, T^*_{2,\mathrm{symm}}) \sim \min(e^{\mathcal{O}(N)}, \mathcal{O}(\omega/h^2)), \tag{2.5}$$

---

[3] The fields for the ESPT are sampled from uniform distributions with $\langle h_{\mathrm{bulk}}\rangle = 1.0$ and width $\delta h_{\mathrm{bulk}} = 2.0$ in the bulk $(1 < i < N)$; $\langle h_{\mathrm{edge}}\rangle = a(\lambda_1, \lambda_2)/J_0(2\lambda_1) \approx -0.11$ and width $\delta h_{\mathrm{edge}} = 2\langle h_{\mathrm{edge}}\rangle$ on the edges.

[4] For each disorder realization, we numerically obtain $F^{\alpha}(t)$, fit an exponential e^{-t/T_2^*} through the peaks, extract T_2^*, and average over 30-1000 realizations.

as illustrated in Fig. 2.2b.

The addition of a more generic symmetry-breaking interaction term, such as $V_y \sum_i \sigma_i^y \sigma_{i+1}^y$ or a long-range power-law tail, breaks the $\mathbb{Z}_2 \times \mathbb{Z}_2$ symmetry at lowest order in the Magnus expansion. In this case, there is no parametric time scale where we expect ESPT dynamics (i.e. $T^*_{2,\mathrm{symm}} \sim \mathcal{O}(1)$), and the edge modes rapidly decohere via local scattering (Fig. 2.2b).

2.2 Engineering an intrinsically-Floquet SPT phase

To obtain edge modes with coherence that persists to arbitrary times and is robust to long-range interactions, we now turn to the realization of an intrinsically Floquet SPT phase. We engineer an FSPT protected by both $\mathbb{Z}_2$ symmetry and periodic driving which cannot exist in equilibrium [131, 132, 189, 77, 197]. Consider the stroboscopic Hamiltonian

$$H(t) = \begin{cases} H_1 = \displaystyle\sum_{i \neq j} \frac{J}{|R_i - R_j|^p} \sigma_i^z \sigma_j^z & \text{if} \quad 0 \leq t < T/2 \\ H_2 = \displaystyle\sum_{i=1}^{N} h_i \sigma_i^x & \text{if} \quad T/2 \leq t < T, \end{cases} \tag{2.6}$$

where $R_i = i$ is the position of the i^{th} spin and $h_i \in [0, W]$. The protecting symmetries are the product of σ_x on all sites ($\mathbb{Z}_2$) and discrete translations in time ($\mathbb{Z}$). The unitary evolution under $H(t)$ is given by $U(t) = \mathcal{T} \exp\left(-i \int_0^T H(t)dt\right)$ and the Floquet operator by $U = U(T)$. Building upon previous studies [133, 124, 30, 231], we expect to observe the FSPT phase at $\frac{JT}{2} \approx \frac{\pi}{2}$ (see Appendix 2.6).

Since the disorder strength is limited to $W \lesssim 1/T$ by the periodic structure of the binary drive, the system cannot be localized for arbitrarily strong interactions. By computing the level-statistics ratio $\langle r \rangle$ [5] as a function of the power-law exponent p (Fig. 2.3a), we observe a clear MBL-delocalization phase transition at $p_c \approx 3.5$ [245]. For the remainder of the text, we set $p = 4$ as a computationally tractable model within the MBL phase.

To probe the nature of edge coherence in the FSPT phase, we again compute the trace fidelity $F^\alpha = \frac{1}{2^N} \mathrm{Tr}\left[\sigma_i^\alpha(t) \sigma_i^\alpha(0)\right]$. As depicted in the inset of Fig. 2.3a, and similar to the ESPT phase, the edge spin exhibits a significantly longer coherence time than bulk spins. However, a crucial difference emerges in the scaling with N. For long-range interactions, the coherence time of the ESPT phase scales independently of the system size, $T_2^* \sim \mathcal{O}(1)$, whereas the FSPT exhibits a quartic scaling $T_2^* \sim \mathcal{O}(N^4)$ (owing to the $1/R^4$ power-law interactions between the two edge modes), as shown in the inset of Fig. 2.3a).

To further distinguish between the topological features of the ESPT and FPST phases, we introduce a novel micro-motion-based entanglement spectrum signature of the latter [189].

---

[5] For each disorder realization, we diagonalize the Floquet Hamiltonian H_{F} defined via $U = e^{-iH_{\mathrm{F}}T}$ and obtain a set of quasi-energies ϵ_n modulo 2π. We define the energy gaps as $\delta_n = \epsilon_{n+1} - \epsilon_n$ and the ratio $r = \min(\delta_n, \delta_{n+1}) / \max(\delta_n, \delta_{n+1})$. Finally, we average over all the quasi-energies and over 2500-100000 disorder realizations.

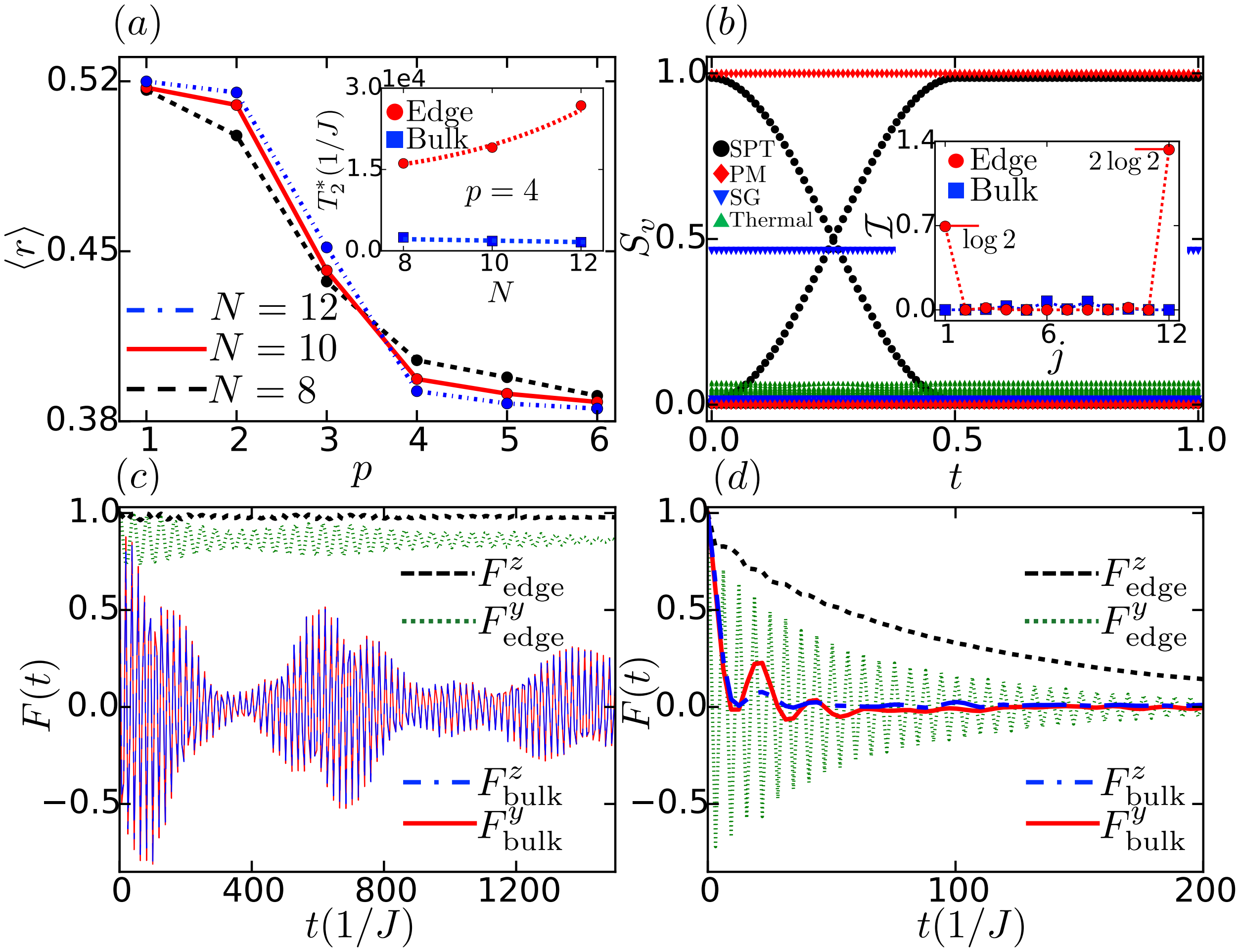

Figure 2.3: FSPT phase—(a) The $\langle r \rangle$ ratio as a function of the power law exponent p for a chain with periodic boundary conditions. The h_i's are sampled from the uniform distribution $[0.1, 0.9]$ and $T = \pi$ (in units of $J = 1$). There is an MBL-delocalization phase transition around $p_c \approx 3.5$. (inset) T_2^* as a function of N, where the edge coherence is fit to $\sim N^4$. (b) The entanglement spectrum micro-motion for $N = 12$. The parameters (p, T, J, W) are: $(4, \pi, 1, 1)$ for the SPT; $(1, \pi, 1, 1)$ for the thermal behavior; $(4, \pi, 0.05, 0.8)$ for the paramagnet; $p = 4$, $T = \pi$, $J = 0.5$, $h \in [0.5, 1]$ for the spin glass. (inset) Mutual information $\mathcal{I}(i, j) = S_i + S_j - S_{ij}$ (where S is the von Neumann entropy) within the SPT phase: $\mathcal{I}(1, j)$ (red circles) and $\mathcal{I}(6, j)$ (blue squares) (see Appendix 2.6). (c) $F^y(t)$ and $F^z(t)$ for the edge and the bulk in a system of $N = 10$ spins for the model in Eqn. 2.6. The bulk curves are almost overlapping. (d) Same as in (c), but with an additional term, $V_x \sum_i \sigma_i^x \sigma_{i+1}^x$ ($V_x = 0.3$) added to H_1.

In particular, for an eigenstate $|\psi\rangle$ of the Floquet operator U, we compute the entanglement spectrum, $\{\eta_i(t)\}$, associated with the half-chain cut of $|\psi(t)\rangle = U(t)|\psi\rangle$ for $0 \leq t \leq T$. By Schmidt decomposing

$$|\psi(t)\rangle = \sum_{i=1}^{2^{N/2}} \eta_i(t) \, |\text{Left}_i(t)\rangle \otimes |\text{Right}_i(t)\rangle \,, \tag{2.7}$$

we obtain $\{\eta_i(t)\}$ across the two sets, $\{|\text{Left}_i(t)\rangle\}$ and $\{|\text{Right}_i(t)\rangle\}$, which span the Hilbert spaces of the left and right halves of the chain. Unlike in equilibrium, where a single snapshot of the entanglement spectrum shows the existence of topological edge modes, we find that, at any given time t, the spectrum is trivial and there is no signature of FSPT order (Fig. 2.3b). However, by following the micro-motion evolution of the spectrum over a single Floquet period, we can robustly identify the topological signature of the FSPT phase [189].

To see this, we note that the entanglement spectrum is gapped at $t = 0$ and $t = T$ which allows us to associate an SPT invariant to each non-trivial band—namely, the $\mathbb{Z}_2$ symmetry charge of the corresponding Schmidt states, $\langle\text{Left}_i(t)| \prod_j \sigma_j^x |\text{Left}_i(t)\rangle = \pm 1$. There exists a band crossing during the micro-motion (Fig. 2.3b), pointing to the fact that the charges of each band are flipping during a Floquet period. This difference between the initial and final $\mathbb{Z}_2$ charges cannot be altered without closing the entanglement gap, suggesting that the band-crossing is, in fact, a robust feature of FSPT order. Indeed, this non-trivial behavior is absent in the paramagnetic and spin glass phases (Fig. 2.3b).

Finally, an additional entanglement-based feature of the FSPT's non-trivial protected edge modes is captured by the spatial dependence of two-spin mutual information. We observe a $\log 2$ entropy in each edge spin, $2\log 2$ mutual information shared between the two edges, and approximately zero mutual information shared between bulk spins (inset of Fig. 2.3b). In combination, this points to the fact that the two edge modes are well localized to a single site and behave like an EPR pair.

2.3 Experimental realization

Both the ESPT and FPST Hamiltonians can be implemented in a chain of Rydberg-dressed alkali atoms [39, 97, 101, 249, 248] trapped in a 1D optical lattice or tweezer array [153, 79] (Fig. 2.1). The spin degree of freedom is formed by two ground hyperfine states, with a resonant Raman coupling of spatially varying Rabi frequency h_i simulating the on-site transverse fields. Random fields can be formed by optical speckle disorder or with a spatial light modulator.

Strong spin-spin interactions are introduced by coupling state $|\uparrow\rangle$ to a Rydberg state $|\mathcal{R}\rangle$ with an off-resonant laser field of Rabi frequency Ω and detuning $\Delta > \Omega$. The result is an effective (dressed) Ising interaction [96, 249]

$$H_I = -\frac{\Omega^4}{8\Delta^3} \frac{1}{1 + |R_i - R_j|^6 / R_c^6} \sigma_i^z \sigma_j^z, \tag{2.8}$$

where the interaction range $R_c = (-C_6/\Delta)^{1/6}$ depends on the van der Waals coefficient C_6 of the Rydberg-Rydberg interaction and is typically on the few-micron scale. At fixed lattice spacing a_1, the ratio of nearest to next-nearest-neighbor couplings is set by R_c (Fig. 2.1).

While the Rydberg dressing is subject to dissipation from the finite lifetime Γ^{-1} of the Rydberg state [101, 249], the interaction-to-decay ratio can be large [97, 39] in a 1D system. At fixed Rabi frequency Ω, the ratio of the Ising coupling J to the lifetime $\gamma = (\Omega^2/4\Delta^2)\Gamma$ of the Rydberg-dressed state is limited to $J/\gamma = \frac{\Omega^2}{2\Delta\Gamma} < \frac{\Omega}{\Gamma}$. This limit is set by the condition $\Omega^2/\Delta^2 \ll 1$ that the Rydberg-state population within the radius $R_c \sim a_1$ be small, so that the perturbative result of Eq. 2.8 holds. At realistic laser power on the $6S_{1/2} \rightarrow nP_{3/2}$ transitions (with $n \gtrsim 40$) in cesium [149], parameters $(\Omega, \Gamma) \approx 2\pi \times (4, 0.002)$ MHz allow for large coupling-to-decay ratios $J/\gamma \lesssim 10^3$.

To observe the FSPT phase, we envision initializing the system in a product state with high energy density and letting it undergo unitary time evolution. After each Floquet period T, one measures the spin-spin autocorrelation function $\langle \sigma^\alpha(nT)\sigma^\alpha(0)\rangle$ for both an edge and bulk spin. Numerics (Fig. 2.3c) for $N = 10$ atoms indicate that a time $t \sim 10^2/J$ suffices to observe a significant difference between the bulk- and edge-spin fidelities. The difference can be observed over an even shorter time scale $t \sim 30/J$ (Fig. 2.3d) by adding a decohering interaction term $V_x \sum_i \sigma_i^x \sigma_{i+1}^x$ to H_1 in Eqn. 2.6. Experimentally, V_x can be introduced by simultaneously dressing both states $|\downarrow\rangle$ and $|\uparrow\rangle$ [97] to generate flip-flop processes $\propto \sigma_i^+ \sigma_{i+1}^-$.

To experimentally verify the distinct advantages of the intrinsically Floquet SPT phase, our scheme can be modified to emulate the ESPT for comparison. Realizing the ESPT Hamiltonian requires alternating stroboscopically between ferromagnetic and antiferromagnetic Ising interactions by simultaneously changing the signs of the detuning Δ and of the van der Waals coefficient C_6. While a conceptually simple approach is to switch between two different laser fields detuned by $\Delta_2 \approx -\Delta_1$ from two different Rydberg states $|\mathcal{R}_2\rangle, |\mathcal{R}_1\rangle$, a more practical approach may be to dynamically control the sign of C_6 with an electric field [237].

2.4 Conclusion

Our proposal raises the tantalizing possibility of observing coherent quantum dynamics at high temperatures in strongly interacting disordered systems [22, 57, 247]. We have studied two different routes towards SPT phases in driven, disordered spin chains: by engineering effective three-spin interactions (ESPT) or by intrinsically dynamical quantized pumping of spin (FSPT). In both cases, decoherence can be caused by breaking the protecting symmetry group. However, as the ESPT relies on a symmetry that is only approximately realized in the high frequency limit, it survives only up to a finite time scale for short-range interactions, and is fragile to generic interactions. By contrast, the FSPT survives at arbitrary times and is robust to long-range interactions.

2.5 Appendix A: Details on the ESPT phase

Deriving the Floquet Hamiltonian

We begin by providing details about the Magnus expansion and deriving Eq. 2.2 from the main text. First, we define a unitary transformation to a "rotating frame", $U_{\mathrm{R}}(t) = \exp\left(i\sin(\omega t)\sum_{i=1}^{N-1}\lambda_i\sigma_i^z\sigma_{i+1}^z\right)$, which maps an arbitrary state $|\psi(t)\rangle$ to $|\psi_{\mathrm{R}}(t)\rangle = U_{\mathrm{R}}(t)\,|\psi(t)\rangle$. At stroboscopic times $t_n = n\frac{2\pi}{\omega} = nT$ ($n \in \mathbb{Z}$), one finds that $|\psi_{\mathrm{R}}(t_n)\rangle = e^{-iH_{\mathrm{F}}t_n}\,|\psi_{\mathrm{R}}(0)\rangle$, where H_{F} is the so-called Floquet Hamiltonian which we construct perturbatively in orders of $1/\omega$; the Schrodinger equation becomes $i\partial_t\,|\psi_{\mathrm{R}}(t)\rangle = H_{\mathrm{R}}(t)\,|\psi_{\mathrm{R}}(t)\rangle$, where the "rotated" Hamiltonian is $H_{\mathrm{R}}(t) = U_{\mathrm{R}}(t)H(t)U_{\mathrm{R}}^\dagger(t) - iU_{\mathrm{R}}(t)\partial_t U_{\mathrm{R}}^\dagger(t)$. Using the driven TFIM Hamiltonian from Eq. 2.1 in the main text, we obtain

$$H_{\mathrm{R}}(t) = \sum_{i=1}^{N} h_i U_{\mathrm{R}}\sigma_i^x U_{\mathrm{R}}^\dagger + V_x\sum_{i=1}^{N-1} U_{\mathrm{R}}\sigma_i^x U_{\mathrm{R}}^\dagger U_{\mathrm{R}}\sigma_{i+1}^x U_{\mathrm{R}}^\dagger.$$

From the explicit form for $U_{\mathrm{R}}(t)$ we immediately find

$$\begin{aligned}
U_{\mathrm{R}}(t)\sigma_i^x U_{\mathrm{R}}^\dagger(t) &= \sigma_i^x\left[\cos(2\tilde{\lambda}_{i-1}(t)) - i\sin(2\tilde{\lambda}_{i-1}(t))\sigma_{i-1}^z\sigma_i^z\right]\times \\
&\times \left[\cos(2\tilde{\lambda}_i(t)) - i\sin(2\tilde{\lambda}_i(t))\sigma_i^z\sigma_{i+1}^z\right] \\
U_{\mathrm{R}}(t)\sigma_i^x\sigma_{i+1}^x U_{\mathrm{R}}^\dagger(t) &= \sigma_i^x\sigma_{i+1}^x\left[\cos(2\tilde{\lambda}_{i-1}(t)) - i\sin(2\tilde{\lambda}_{i-1}(t))\sigma_{i-1}^z\sigma_i^z\right]\times \\
&\times \left[\cos(2\tilde{\lambda}_{i+1}(t)) - i\sin(2\tilde{\lambda}_{i+1}(t))\sigma_{i+1}^z\sigma_{i+2}^z\right],
\end{aligned} \tag{2.9}$$

where $\tilde{\lambda}(t) = \lambda\sin(\omega t)$. For the operators acting at the boundary, we define $\lambda_0 = \lambda_N = 0$.

Lowest order term

The lowest order term in the Magnus expansion for the Floquet Hamiltonian is just the time-averaged rotated Hamiltonian: $H_{\mathrm{F}}^{(0)} = \frac{1}{T}\int_0^T H_{\mathrm{R}}(t')dt'$, where $T = \frac{2\pi}{\omega}$ is the period of driving. To avoid cluttering our formulae, we use $\frac{1}{T}\int_0^T dt(...) \equiv \langle ...\rangle$.

Then we immediately obtain these identities: $\left\langle\cos(2\tilde{\lambda}(t))\right\rangle = J_0(2\lambda)$ and $\left\langle\sin(2\tilde{\lambda}(t))\right\rangle = 0$. With these in hand, we also find

$$\begin{aligned}
\left\langle\cos(2\tilde{\lambda}_1(t))\sin(2\tilde{\lambda}_2(t))\right\rangle &= 0 \\
\left\langle\cos(2\tilde{\lambda}_1(t))\cos(2\tilde{\lambda}_2(t))\right\rangle &= a(\lambda_1,\lambda_2) \\
\left\langle\sin(2\tilde{\lambda}_1(t))\sin(2\tilde{\lambda}_2(t))\right\rangle &= b(\lambda_1,\lambda_2),
\end{aligned} \tag{2.10}$$

where $a(\lambda_1, \lambda_2) = \frac{1}{2}\left[J_0(2(\lambda_1 - \lambda_2)) + J_0(2(\lambda_1 + \lambda_2))\right]$ and $b(\lambda_1, \lambda_2) = J_0(2(\lambda_1 - \lambda_2)) - a(\lambda_1, \lambda_2)$. The ratio $b(\lambda_1, \lambda_2)/a(\lambda_1, \lambda_2)$ controls the correlation length of the edge mode and the λ_1, λ_2 -dimerization enables us to arbitrarily tune it (Fig. 2.4b).

Expanding the terms from Eqn. 2.9 and applying these identities, we get

$$\begin{aligned} \left\langle \sum_{i=1}^{N} h_i U_{\mathrm{R}} \sigma_i^x U_{\mathrm{R}}^\dagger \right\rangle &= J_0(2\lambda_1)\left(h_1\sigma_1^x + h_N\sigma_N^x\right) + \\ &+ \sum_{i=2}^{N-1} h_i\left[a(\lambda_1, \lambda_2)\sigma_i^x - b(\lambda_1, \lambda_2)\sigma_{i-1}^z\sigma_i^x\sigma_{i+1}^z\right] \\ \left\langle \sum_{i=1}^{N-1} V_x U_{\mathrm{R}} \sigma_i^x \sigma_{i+1}^x U_{\mathrm{R}}^\dagger \right\rangle &= V_x J_0(2\lambda_2)\left(\sigma_1^x\sigma_2^x + \sigma_{N-1}^x\sigma_N^x\right) + \\ &+ \sum_{i=2}^{N-2} V_x\left[c(\lambda_{i+1})\sigma_i^x\sigma_{i+1}^x + d(\lambda_{i+1})\sigma_{i-1}^z\sigma_i^y\sigma_{i+1}^y\sigma_{i+2}^z\right], \end{aligned} \tag{2.11}$$

which corresponds to the expression for $H_{\mathrm{F}}^{(0)}$ in the main text. Note that all terms commute with $\Theta_{\text{even}} = \prod_i \sigma_{2i}^x$ and $\Theta_{\text{odd}} = \prod_i \sigma_{2i+1}^x$ which generate the $\mathbb{Z}_2 \times \mathbb{Z}_2$ symmetry.

If we add another term, $V_y \sum_{i=1}^{N-1} \sigma_i^y \sigma_{i+1}^y$, to the driven TFIM Hamiltonian, then its contribution to $H_{\mathrm{F}}^{(0)}$ would be identical to the one on the second line of Eqn. 2.11 with $[x \to y]$. In that case, we note that the Floquet Hamiltonian would have only a smaller, $\mathbb{Z}_2$, symmetry group.

First order correction

The first order correction in the Magnus expansion is

$$H_{\mathrm{F}}^{(1)} = -\frac{i}{2T}\int_0^T dt_1 \int_0^{t_1} dt_2 \left[H_{\mathrm{R}}(t_1), H_{\mathrm{R}}(t_2)\right]. \tag{2.12}$$

We want to show that $H_{\mathrm{F}}^{(1)}$ contains a term that breaks the $\mathbb{Z}_2 \times \mathbb{Z}_2$ symmetry of $H_{\mathrm{F}}^{(0)}$. More specifically, there exists a contribution of the form $\sum_i f_i \sigma_i^y \sigma_{i+1}^y$, where $f_i \sim \mathcal{O}(\frac{h^2}{\omega})$. For simplicity, we will show that this holds even in the non-interacting case, $V_x = V_y = 0$.

Neglecting terms acting at the boundary, from Eqn. 2.9, we get

$$\begin{aligned} H_{\mathrm{R}}(t) &= \sum_i h_i\Big[\cos(2\tilde{\lambda}_1(t))\cos(2\tilde{\lambda}_2(t))\sigma_i^x - \cos(2\tilde{\lambda}_{i-1}(t))\sin(2\tilde{\lambda}_i(t))\sigma_i^y\sigma_{i+1}^z - \\ &- \cos(2\tilde{\lambda}_i(t))\sin(2\tilde{\lambda}_{i-1}(t))\sigma_{i-1}^z\sigma_i^y\Big] - \\ &- \sum_i h_i \sin(2\tilde{\lambda}_1(t))\sin(2\tilde{\lambda}_2(t))\sigma_{i-1}^z\sigma_i^x\sigma_{i+1}^z. \end{aligned}$$

When calculating the commutator $[H_\mathrm{R}(t_1), H_\mathrm{R}(t_2)]$, the only terms that give a $\sigma_i^y \sigma_{i+1}^y$ (or YY) contribution are

$$\begin{aligned}
& i \sum_i 2h_{i-1}h_i \left[\cos(2\tilde{\lambda}_1(t_1))\cos(2\tilde{\lambda}_2(t_1))\cos(2\tilde{\lambda}_i(t_2))\sin(2\tilde{\lambda}_{i-1}(t_2))\right] \sigma_{i-1}^y \sigma_i^y \\
- & i \sum_i 2h_{i-1}h_i \left[\cos(2\tilde{\lambda}_1(t_2))\cos(2\tilde{\lambda}_2(t_2))\cos(2\tilde{\lambda}_i(t_1))\sin(2\tilde{\lambda}_{i-1}(t_1))\right] \sigma_{i-1}^y \sigma_i^y \\
& i \sum_i 2h_i h_{i+1} \left[\cos(2\tilde{\lambda}_1(t_1))\cos(2\tilde{\lambda}_2(t_1))\cos(2\tilde{\lambda}_{i-1}(t_2))\sin(2\tilde{\lambda}_i(t_2))\right] \sigma_i^y \sigma_{i+1}^y \\
- & i \sum_i 2h_i h_{i+1} \left[\cos(2\tilde{\lambda}_1(t_2))\cos(2\tilde{\lambda}_2(t_2))\cos(2\tilde{\lambda}_{i-1}(t_1))\sin(2\tilde{\lambda}_i(t_1))\right] \sigma_i^y \sigma_{i+1}^y.
\end{aligned}$$

Combining all of these terms together, we obtain

$$i \sum_i 4h_{i-1}h_i \left[\cos(2\tilde{\lambda}_1(t_1))\cos(2\tilde{\lambda}_2(t_1))\cos(2\tilde{\lambda}_i(t_2))\sin(2\tilde{\lambda}_{i-1}(t_2)) - (t_1 \leftrightarrow t_2)\right] \sigma_{i-1}^y \sigma_i^y. \tag{2.13}$$

Plugging this expression into Eqn. 2.12, we finally see that $H_\mathrm{F}^{(1)}$ contains a term of the form $\sum_i \frac{h_{i-1}h_i}{\omega} f_i \sigma_{i-1}^y \sigma_i^y$, where

$$f_i = \frac{1}{\pi} \int_0^{2\pi} du_1 \int_0^{u_1} du_2 \cos(2\lambda_i \sin u_1)\cos(2\lambda_i \sin u_2)\sin[2\lambda_{i-1}(\sin u_2 - \sin u_1)]. \tag{2.14}$$

For the dimerized couplings used in the main text, $\lambda_1 = 1.54$ and $\lambda_2 = 0.69$, we obtain $f_1 \approx -0.08$ and $f_2 \approx 0.08$. Thus, the ESPT can only exist for a finite time scale $T^*_{2,\mathrm{symm}} \sim (h^2/\omega)^{-1}$ in the thermodynamic limit. At later times, the symmetry of the Floquet Hamiltonian is $\mathbb{Z}_2$ which cannot support SPT order.

Decoherence in the ESPT

Interactions	Symmetry	In Majorana operators	T_2^*
XX ($V_y = 0$)	$\mathbb{Z}_2 \times \mathbb{Z}_2$	Quartic	$\min(\mathcal{O}(\omega), e^{\mathcal{O}(N)})$
YY ($V_x = 0$)	$\mathbb{Z}_2$	Quadratic	∞
XY ($V_y = 4V_x$)	$\mathbb{Z}_2$	Quartic	$\mathcal{O}(1)$

We now consider a detailed analysis of the interplay between symmetry and decoherence in the ESPT phase. We start from the *non-interacting* driven TFIM [Eqn.(2.1) from the main text with $V_x = 0$]. Coherent oscillations (whose contrast never decays) are observed with a period $\tau = \frac{\pi}{a(\lambda_1,\lambda_2)} \left(\frac{b(\lambda_1,\lambda_2)}{a(\lambda_1,\lambda_2)}\right)^{N/2-1}$ [inset of Fig. 2.4a] which can easily be understood by recasting the Hamiltonian using a Jordan-Wigner transformation. Since the original

Hamiltonian is quadratic in Majorana operators, and hence non-interacting [135, 247], the resulting Floquet Hamiltonian must also describe free fermions (at all orders in the Magnus expansion). Thus, even though the first order correction, $H_{\mathrm{F}}^{(1)}$, explicitly breaks the protecting $\mathbb{Z}_2 \times \mathbb{Z}_2$ symmetry as seen in the previous section, it does *not* lead to decoherence owing to the lack of scattering between the free fermions. The observed coherent oscillations are simply due to finite-size interactions between the edge spins mediated by their bulk tails.

We now switch to the *interacting* case and consider interactions of the form $H_{\mathrm{int}} = \sum_{i=1}^{N-1} V_x \sigma_i^x \sigma_{i+1}^x + V_y \sigma_i^y \sigma_{i+1}^y$. Interestingly, the role of the XX and YY interactions are quite different, as summarized in Table 2.1. In the limit $V_x = 0$, $V_y \neq 0$ (YY interactions), $H_{\mathrm{F}}^{(0)}$ breaks the $\mathbb{Z}_2 \times \mathbb{Z}_2$ symmetry. Despite this fact, since the YY interaction preserves the non-interacting nature of the Hamiltonian, we still observe coherent oscillations. Conversely, if $V_y = 0$, $V_x \neq 0$ (XX interactions), then the stroboscopic Hamiltonian will include quartic terms. In the clean case, this would lead to the immediate decoherence of the edge modes (Fig. 2.4a). However, in the presence of strong disorder, since $H_{\mathrm{F}}^{(0)}$ preserves the $\mathbb{Z}_2 \times \mathbb{Z}_2$ symmetry of the ESPT (Table 2.1), we observe an exponential enhancement of the edge coherence time, T_2^*, compared to the clean case (Fig. 2.4c). We note in passing that in the undimerized case, $\lambda_1 = \lambda_2$, it is difficult to balance both the localized and topological nature of the phase. The strong disorder needed for MBL leads to large fluctuations of the effective couplings in $H_{\mathrm{F}}^{(0)}$ which introduces trivial puddles that fracture the original topological phase (Fig. 2.4a). Finally, if both $V_x \neq 0$ and $V_y \neq 0$ (XY interactions) the protecting $\mathbb{Z}_2 \times \mathbb{Z}_2$ symmetry is already broken at lowest order in the Magnus expansion, namely $H_{\mathrm{F}}^{(0)}$. In this case, there is no parametric scale where one expects SPT dynamics ($T_{2,\mathrm{symm}}^* \sim \mathcal{O}(1)$) and the Hamiltonian is also strongly interacting; thus, the edge modes decohere immediately via local scattering and disorder cannot revive the coherence time compared to the clean case (Fig 2.4c and Fig. 2.4d).

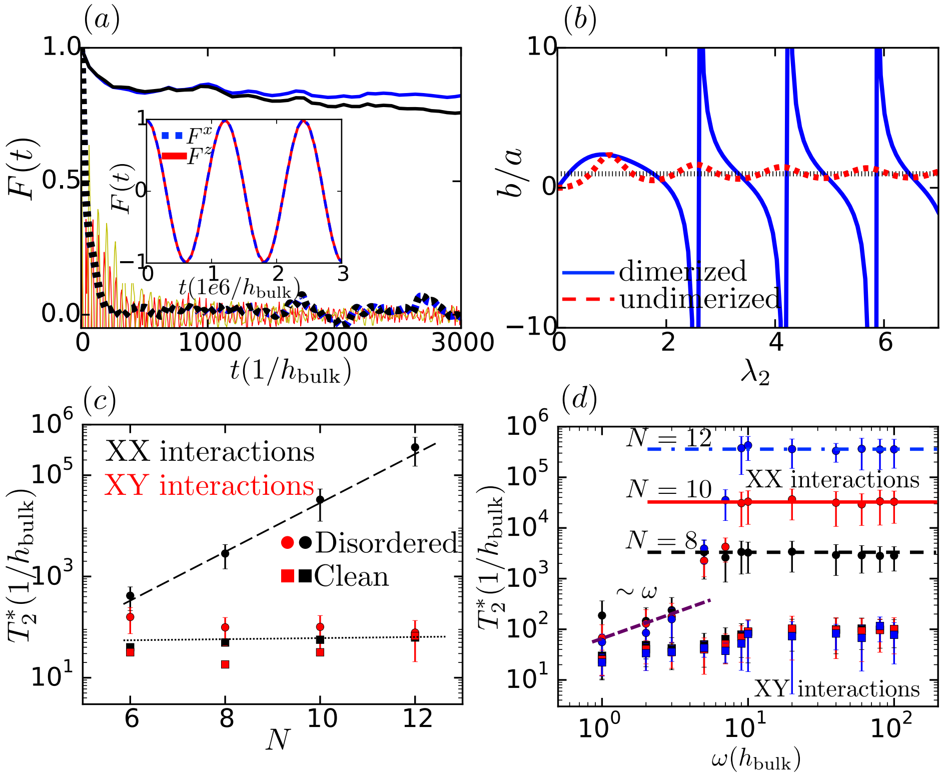

Figure 2.4: (a)-(d): The ESPT described by the Hamiltonian in Eq.(2.1) from the main text. (a) The overlapping dashed lines (black and blue for F^z and F^x, respectively) correspond to the interacting and clean (uniform fields h_i) ESPT. We see that interactions ($V_x \neq 0$) lead to decoherence. The solid black and blue lines (for F^z and F^x, respectively) correspond to the interacting ESPT in the presence of strongly disordered on-site fields h_i. We see that disorder leading to MBL restores the coherence in the *dimerized* case ($\lambda_1 = 1.54$ and $\lambda_2 = 0.69$). The thin solid yellow and red lines (for F^z and F^x, respectively) correspond to the interacting and strongly-disordered ESPT in the *un-dimerized* case ($\lambda_1 = \lambda_2$). In this model, it is difficult to balance both the localized and topological nature of the phase. The strong disorder needed for MBL leads to large fluctuations of the effective couplings in $H_{\mathrm{F}}^{(0)}$ which introduces trivial puddles that fracture the original topological phase. (inset) The dashed blue and solid red curves corresponding to F^x and F^z in the non-interacting ($V_x = V_y = 0$) and clean ESPT. We observe coherent oscillations whose contrast never decays (due to the lack of interactions) with a period $\sim 10^6$. (b) Ratio $b(1,\lambda_2)/a(1,\lambda_2)$ in the dimerized (solid blue) and the un-dimerized (dashed red) models. The SPT phase corresponds to $b/a > 1$ (dotted black). The dimerized model allows us to arbitrarily tune the correlation length of the edge mode. (c) T_2^* as a function of N in both clean (squares) and disordered (circles) systems for the ESPT. The interaction parameters are $V_x = 0.05$, $V_y = 0$ for XX interactions (black) and $V_y = 4V_x = 0.2$ for XY interactions (red). The exponential enhancement of the coherence time is seen only in the disordered XX case in which the $\mathbb{Z}_2 \times \mathbb{Z}_2$ symmetry is unbroken in $H_{\mathrm{F}}^{(0)}$. (d) T_2^* as a function of frequency and system size. As ω is increased for XX interactions (circles), T_2^* saturates consistent with being bounded by $T_2^* \sim \min(\mathcal{O}(\omega), e^{\mathcal{O}(N)})$. Turning on XY interactions (squares), breaks the $\mathbb{Z}_2 \times \mathbb{Z}_2$ symmetry at the level of $H_{\mathrm{F}}^{(0)}$ and leads to a breakdown of the edge coherence for all parameters.

2.6 Appendix B: Details on the FSPT phase

The location and properties of the phase

In the main text we have mentioned that we expect to observe the FSPT phase at $\frac{JT}{2} \approx \frac{\pi}{2}$. To see why this is the case, let us consider a simplified version of the Hamiltonian defined in Eq. 2.6 in the main text:

$$H(t) = \begin{cases} H_1 = \sum\limits_i J\sigma_i^z\sigma_{i+1}^z & \text{if} \quad 0 \leq t < T/2 \\ H_2 = \sum\limits_{i=1}^{N} h_i\sigma_i^x & \text{if} \quad T/2 \leq t < T. \end{cases} \tag{2.15}$$

This model has only nearest-neighbor interactions, but it is exactly solvable and illustrative of the main properties of the FSPT [133, 131, 132].

The Floquet operator over a period T can be written as $U = \exp(-iH_2T/2)\exp(-iH_1T/2)$. Taking $\frac{JT}{2} = \frac{\pi}{2}$ and using open boundary conditions, we find that

$$\begin{aligned} \exp\left(-iH_1T/2\right) &= \prod_{i=1}^{N-1} \exp\left(-i\frac{\pi}{2}\sigma_i^z\sigma_{i+1}^z\right) \\ &= \prod_{i=1}^{N-1} \left[-i\sin\left(\frac{\pi}{2}\right)\sigma_i^z\sigma_{i+1}^z + \cos\left(\frac{\pi}{2}\right)\mathbb{1}\right] \\ &\propto \prod_{i=1}^{N-1} \sigma_i^z\sigma_{i+1}^z \\ &= \sigma_1^z\sigma_N^z. \end{aligned}$$

Note that under periodic boundary conditions this would be proportional to the identity $\mathbb{1}$.

Secondly, we can also re-write the other piece of the Floquet operator as

$$\begin{aligned} \exp\left(-iH_2T/2\right) &= \exp\left(-i\frac{h_1T}{2}\sigma_1^x\right)\exp\left(-i\frac{h_NT}{2}\sigma_N^x\right)\exp\left(-i\sum_{1<i<N}\frac{h_iT}{2}\sigma_i^x\right) \\ &= \left[-i\sin\left(\frac{h_1T}{2}\right)\sigma_1^x + \cos\left(\frac{h_1T}{2}\right)\mathbb{1}\right]\left[-i\sin\left(\frac{h_NT}{2}\right)\sigma_N^x + \cos\left(\frac{h_NT}{2}\right)\mathbb{1}\right] \\ &\times \exp\left(-i\sum_{1<i<N}\frac{h_iT}{2}\sigma_i^x\right) \\ &= \left[-i\sin(\theta_1)\sigma_1^x + \cos(\theta_1)\right]\left[-i\sin(\theta_N)\sigma_N^x + \cos(\theta_N)\right]\exp\left(-iH_{\text{bulk}}T/2\right), \end{aligned}$$

where $\theta_i = \frac{h_iT}{2}$ and $H_{\text{bulk}} = \sum_{1<i<N} h_i\sigma_i^x$.

Putting both pieces together, we find

$$\begin{aligned} U &\propto \left[-i\sin(\theta_1)\sigma_1^x + \cos(\theta_1)\right]\sigma_1^z\left[-i\sin(\theta_N)\sigma_N^x + \cos(\theta_N)\right]\sigma_N^z \exp\left(-iH_{\text{bulk}}T/2\right) \\ &\propto \left[-\sin(\theta_1)\sigma_1^y + \cos(\theta_1)\sigma_1^z\right]\left[-\sin(\theta_N)\sigma_N^y + \cos(\theta_N)\sigma_N^z\right]\exp\left(-iH_{\text{bulk}}T/2\right) \\ &\propto \tilde{\sigma}_1^z\tilde{\sigma}_N^z \exp\left(-iH_{\text{bulk}}T/2\right), \end{aligned}$$

where $\tilde{\sigma}_{1,N}^z = \left[-\sin(\theta_{1,N})\sigma_{1,N}^y + \cos(\theta_{1,N})\sigma_{1,N}^z\right]$ and note that $\left(\tilde{\sigma}_{1,N}^z\right)^2 = 1$. Thus, the Floquet operator $U = \tilde{\sigma}_1^z\tilde{\sigma}_N^z\exp\left(-iH_{\text{bulk}}T/2\right)$ has two pieces: a "charge pump" term $\tilde{\sigma}_1^z\tilde{\sigma}_N^z$ corresponding to the product of two operators localized around the edges; and a unitary time evolution over $T/2$ with a local *bulk* Hamiltonian $H_{\text{bulk}} = \sum_{1<i<N} h_i\sigma_i^x$.

A few observations are in order. First, the operators $\tilde{\sigma}_{1,N}^z$ localized around the edges commute with each other, with the bulk operator H_{bulk}, and, thus, with the Floquet unitary $U(T)$. Second, these edge operators are odd under the global $\mathbb{Z}_2$ symmetry generated by $\Theta = \prod \sigma_i^x$:

$$\begin{aligned} \Theta\tilde{\sigma}_{1,N}^z\Theta^\dagger &= \sigma_{1,N}^x\left[-\sin(\theta_{1,N})\sigma_{1,N}^y + \cos(\theta_{1,N})\sigma_{1,N}^z\right]\sigma_{1,N}^x \\ &= \left[\sin(\theta_{1,N})\sigma_{1,N}^y - \cos(\theta_{1,N})\sigma_{1,N}^z\right]\left(\sigma_{1,N}^x\right)^2 \\ &= -\tilde{\sigma}_{1,N}^z. \end{aligned}$$

Third, we see that $U(2T) = U^2 = \mathbb{1}_{\text{edges}} \otimes \exp\left(-iH_{\text{bulk}}T\right)$ and the edge operators that are even under the $\mathbb{Z}_2$ Ising symmetry, for instance $\tilde{\sigma}_{1,N}^x$, obey the following equation of motion:

$$U(nT)\tilde{\sigma}_{1,N}^x U^\dagger(nT) = (-1)^n\tilde{\sigma}_{1,N}^x. \tag{2.16}$$

This means that, given any generic initial state of the system, the edge operators $\tilde{\sigma}_{1,N}^x$ will oscillate with a period $2T$, as opposed to the period T of the drive! We emphasize that this does *not* hold for bulk operators, whose correlations are trivial in the FSPT phase. Therefore, the Floquet system exhibits a form of *discrete time-translation symmetry breaking* (TTSB) on the boundary of the system.

To summarize, for $\frac{JT}{2} = \frac{\pi}{2}$ the exactly solvable model (2.15) with nearest-neighbor interactions has two coherent modes localized around the edges, which are odd under the protecting symmetry corresponding to a global spin flip $\prod \sigma_i^x$. And, moreover, the edge observables which are even under this $\mathbb{Z}_2$ symmetry exhibit TTSB, whereas bulk observables do not.

Finally, as argued in Refs. [131, 132, 189, 77, 197] and as sketched in the section 'The role of disorder' below, this phenomenology is not an artifact of the solvable model and it also holds for the model with generic interactions, such as power laws [Eqn. 2.6 in the main text], provided that there exists strong disorder leading to MBL.

Duality to a discrete time crystal

Before discussing the details of the many-body localized problem, we emphasize one last property of the FSPT phase, namely its duality to a discrete (Floquet) time crystal

(DTC) [133, 76, 244, 250, 61] (for a review see [78] and the references therein). We saw above that the FSPT exhibits time-translation symmetry breaking on the boundary of the system, but not in the bulk. Secondly, this phenomenon is robust only to perturbations that *do not* break the protecting $\mathbb{Z}_2$ symmetry and the discrete time translation symmetry $\mathbb{Z}$.

Let us show how the boundary TTSB occurring in the FSPT phase is related to the bulk dynamics and order in the DTC phase. Again, for brevity, we focus on the exactly solvable model (2.15). Under the well-known Ising duality $\sigma_i^x \leftrightarrow \sigma_i^z \sigma_{i+1}^z$, we see that the model H from Eq. 2.15 is mapped onto $\hat{H}$, where

$$\hat{H}(t) = \begin{cases} \hat{H}_1 = \sum_i J\sigma_i^x & \text{if} \quad 0 \leq t < T/2 \\ \hat{H}_2 = \sum_{i=1}^{N} h_i \sigma_i^z \sigma_{i+1}^z & \text{if} \quad T/2 \leq t < T, \end{cases} \tag{2.17}$$

and the FSPT phase $\frac{JT}{2} = \frac{\pi}{2}$ of H is mapped onto the DTC phase of $\hat{H}$. To understand why, note that in this limit, the Floquet unitary can be immediately written as

$$\hat{U}(T) = \exp\left(-i\frac{T}{2}\sum_i h_i \sigma_i^z \sigma_{i+1}^z\right) \prod \sigma_i^x = \exp\left(-i\frac{T}{2}\sum_i h_i \sigma_i^z \sigma_{i+1}^z\right) \Theta, \tag{2.18}$$

where $\Theta = \prod \sigma_i^x$ is the $\mathbb{Z}_2$ symmetry generator. Since the domain wall variables $\sigma_i^z \sigma_{i+1}^z$ commute with each other and with Θ, then they also commute with the unitary $\hat{U}(T)$. In turn, this entails that the Floquet eigenstates are cat states $|n, \pm\rangle$ of the form

$$|n, \pm\rangle = \frac{|\uparrow\uparrow\downarrow\uparrow\downarrow\downarrow \ldots\rangle \pm |\downarrow\downarrow\uparrow\downarrow\uparrow\uparrow \ldots\rangle}{\sqrt{2}}, \tag{2.19}$$

where $\pm$ corresponds to the parity under Θ and n corresponds to a pattern of domain walls. Therefore, we see that the bulk σ_i^z operators exhibit long-range order (i.e. non-vanishing connected correlation function $\langle \sigma_i^z \sigma_j^z \rangle$ for $|i - j| \to \infty$) and their equation of motion is

$$\hat{U}(nT)\sigma_i^z \hat{U}^\dagger(nT) = (-1)^n \sigma_i^z. \tag{2.20}$$

For a generic initial state that is experimentally accessible [6] we have $\langle \sigma_i^z \rangle \neq 0$ and, by the above equation of motion, we find that a *local bulk observable* will exhibit oscillations with a period $2T$: $\langle \sigma_i^z(nT) \rangle = (-1)^n \langle \sigma_i^z \rangle$.

The presence of spatial long-range order and the breaking of the discrete time-translation invariance for local bulk observables are the hallmark signatures of a discrete time crystal. Thus, it is in this sense that the Ising-duality maps the TTSB on the boundary in the FSPT phase to the TTSB in the bulk for the DTC phase. The key difference is that, while the

---

[6] For instance, any product state of the form $|\uparrow\downarrow\uparrow\downarrow\uparrow\uparrow \ldots\rangle$.

FSPT edge dynamics is robust to perturbations that respect both the $\mathbb{Z}_2$ *and* $\mathbb{Z}$ symmetries, the order in the DTC phase is robust to all perturbations that respect the $\mathbb{Z}$ symmetry. In the parlance of Ref. [130], the time crystallinity in the DTC phase is *absolutely stable* to local deformations of the Floquet drive, including Ising-symmetry-breaking perturbations, whereas the time crystallinity of the edge modes in the FSPT phase is *not*.

The role of disorder

We now turn to the Floquet-MBL problem.

In the FSPT, similar to ESPT phase, disordered on-site fields $h_i \in [0, W]$ play an equally crucial role in restoring the coherence of the edge modes (Fig. 2.5a and 2.5c), stabilizing the quantum order in the presence of interactions, and suppressing heating via the emergence of local integrals of motion. Yet the role of disorder is even more nuanced.

First, the classification and stability of *interacting* Floquet-SPT phases of matter [131, 132, 189, 77, 197] hinge on the system exhibiting MBL because this ensures that the eigenstates of the Floquet operator U and Hamiltonian H_{F} are short-range entangled.

Second, based on the classification of Floquet-MBL-SPT phases via the Künneth formula for group cohomology [131, 132, 189, 77, 197], each application of the Floquet unitary U pumps a lower dimensional SPT through the boundary: the analysis for the exactly solvable model in the previous sections generalizes to $U = \tilde{\sigma}_1 \tilde{\sigma}_N \exp(-if)$, where $\tilde{\sigma}_{1,N}$ are unitary operators localized around the edges which commute with each other and with the bulk localized bits ("l-bits"); and f is a local Hamiltonian acting on the bulk l-bits [131, 132]. As before, the $\tilde{\sigma}_1 \tilde{\sigma}_N$ piece of U entails that a $\mathbb{Z}_2$ charge (spin flip) is pumped across our system (see Fig. 2.5b), which is the entanglement spectrum signature described in the main text [189].

Third, from a more practical point of view, there is an upper bound on the disorder bandwith, $W_{\max}$. Instead of driving the Ising interaction term as in the ESPT case, we are toggling between two non-commuting parts, H_1 and H_2, of the Hamiltonian (Eqn. 2.6 in the main text). Since the Floquet operator is given by $U = \exp(-iH_2T/2)\exp(-iH_1T/2)$, then $h_iT/2$ should be viewed modulo $\pi/2$ [133] and, therefore, $W_{\max} = 1$. Since the amount of disorder present in the system is bounded by $W_{\max}$, there is an MBL-delocalization phase transition as a function of the interaction strength quantified by the power law exponent p (Fig. 2.6c). Conversely, the MBL-delocalization transition can also be observed by tuning the bandwidth W for a fixed power law exponent p, as shown in Fig. 2.6a and Fig. 2.6b.

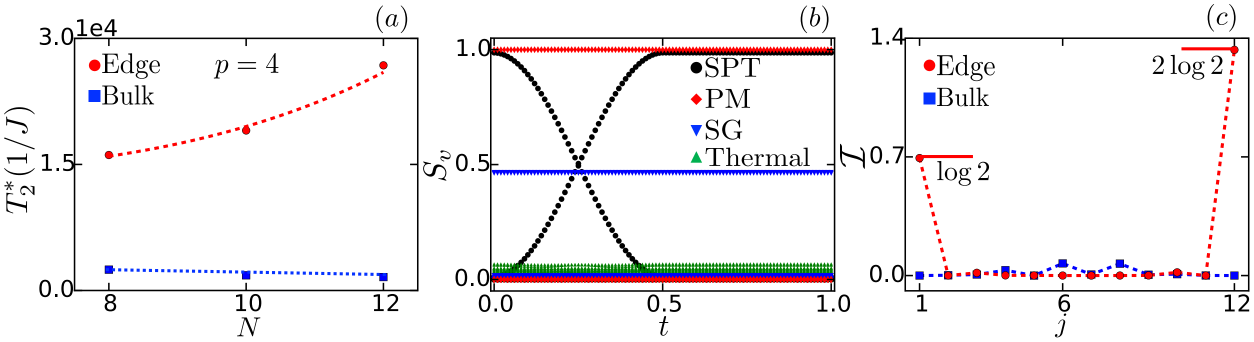

Figure 2.5: (a)-(c): The FSPT described by the Hamiltonian in Eq. 2.6 from the main text. The on-site fields h_i are sampled from the uniform distribution on $[0, W]$. (a) T_2^* as a function of N for both the edge and bulk fidelities. The edge coherence is fit to $\sim N^4$ due to the $1/N^4$ power-law interactions between the two edge modes. The bulk coherence does not show signs of enhancement. (b) The entanglement spectrum micro-motion. We see that the FSPT exhibits a non-trivial entanglement band-crossing due to the pumping of a $\mathbb{Z}_2$ symmetry charge, whereas the other phases have a trivial set of bands. (c) The two-spin mutual information $\mathcal{I}(i, j) = S_i + S_j - S_{ij}$ (where S is the von Neumann entropy) within the FSPT phase: $\mathcal{I}(1, j)$ (red circles) and $\mathcal{I}(6, j)$ (blue squares). We observe $\log 2$ entropy in each edge spin, $2\log 2$ mutual information shared between the two edges, and approximately zero (up to finite size effects) mutual information shared between bulk spins. This points to the fact that the two edge modes are well localized to a single site and behave like an EPR pair.

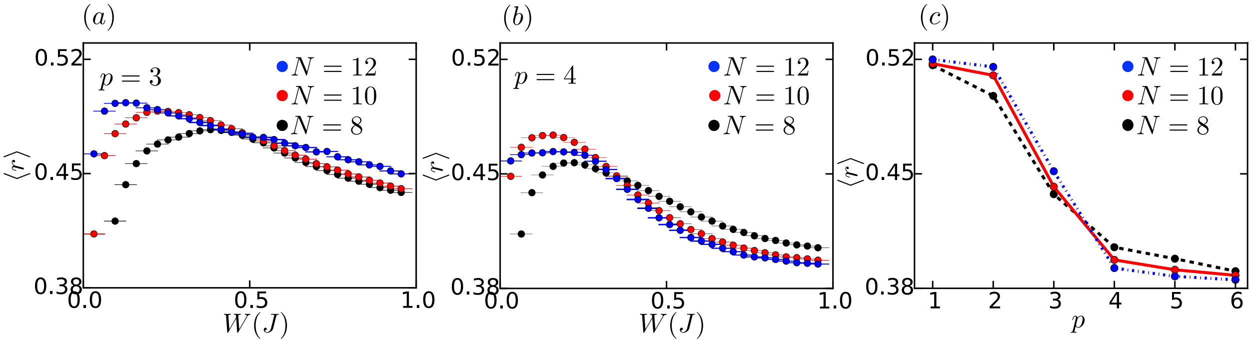

Figure 2.6: (a) The level statistics ratio $\langle r \rangle$ as a function of the disorder width W with the interactions power law exponent $p = 3$. Maximal disorder width $W = W_{\max} = 1$ is not strong enough to localize the system even though $\langle r \rangle$ is below the GOE value of 0.527. (b) $\langle r \rangle$ as a function of W for $p = 4$. At strong disorder strengths, $\langle r \rangle$ is close to the Poisson value of 0.386 signaling localization. At low disorder strengths, there is an anomalous scaling with N, but this provides a bound on the location of the critical point. (c) The $\langle r \rangle$ ratio as a function of the power law exponent p for the maximal disorder width. There is an MBL-delocalization phase transition with a critical point $p_c \approx 3.5$. For the remaining plots, we set $p = 4$.

Chapter 3

Exploration of the stability of many-body localization in $d > 1$

Recent works on many-body localization [120, 71, 70] have started to re-examine the case for the existence and stability of the MBL state, going beyond the perturbative arguments of Basko *et al* [29] (see also Ref. [103]). For instance, Imbrie has given a mathematical proof for the existence of MBL in spin chains with short range interactions [120]. On the other hand, other analyses have pointed to non-perturbative effects that can *destabilize* MBL under certain conditions [71, 70]. In particular, De Roeck and Huveneers [70] have argued that the MBL state is unstable in two or higher dimensions or in systems with interactions that decay sub-exponentially with distance. Their instability mechanism hinges upon finite ergodic "bubbles" of weak disorder that occur naturally inside an insulator (see Fig. 3.1). According to this narrative, such rare regions may trigger a "thermalization avalanche"—the avalanche commences by thermalizing the immediate surroundings of the bubble, thus creating a larger and more potent bubble which reinforces the process. Because this argument has far reaching implications such as the absence of MBL in two dimensional systems, it is important to test the crucial assumptions underlying this conclusion.

In this chapter, we scrutinize these assumptions using both an exact diagonalization study (ED) of small systems and a tractable toy model. In the first part we describe the thermal bubble using a GOE random matrix in the Hilbert space of 8 spins. To this core we gradually couple up to 6 more spins that, in the absence of coupling to the ergodic region, correspond to the local integrals of motion (LIOMs) of an Anderson insulator. The combined system, consisting of up to 14 spins, is diagonalized exactly.

We study models with three different spatial structures of the coupling to represent (Fig. 3.2): (i) a one dimensional Anderson insulator with an exponential decay of the localized single particle wave-functions; (ii) a one dimensional insulator with a stretched exponential decay of the localized wave-functions [1]; (iii) a two dimensional Anderson insulator.

---

[1] Even though this toy model is unphysical, we study it as an additional proxy for higher dimensional insulators since it allows us to analyze LIOMs farther away from the ergodic bubble than would be numerically

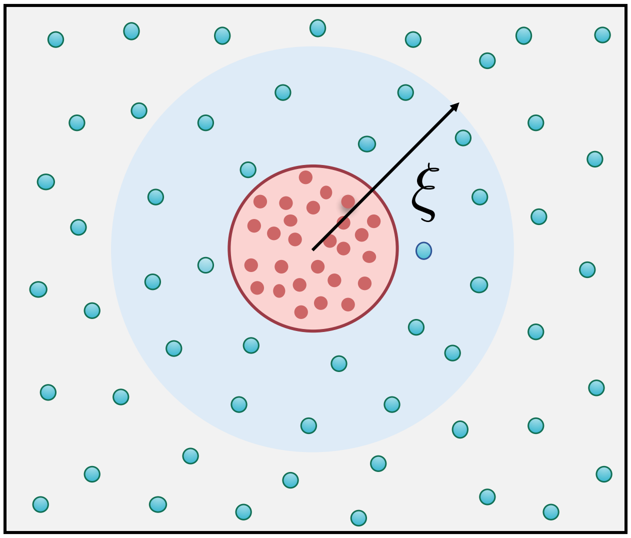

Figure 3.1: Schematic illustration of an ergodic bubble inside an Anderson insulator. The red dots represent sites in the bubble, while the blue dots are the positions of the localized states of the insulator. The blue shaded region within a distance of a localization length ξ from the bubble is strongly coupled to it.

In these systems we compute the eigenstate spectral function of a local operator acting on the farthest LIOM coupled to the thermal core which allows us to directly check if the LIOM is hybridized with the ergodic region [2]. We then use direct probes of localization to test whether the fully coupled system is thermalizing and if the avalanche persists. For all three models, we find a quantitative agreement between the ED results and a refined theory of the thermalization avalanche [70] that includes transient finite size effects. Thus, the exact diagonalization study provides further support to the avalanche scenario. We note that these results go beyond previous numerical analyses in two main ways. First, we additionally investigate models in higher dimensions and in one dimension with longer range coupling—models (ii) and (iii) above—in order to test for the existence of an inherent instability at any disorder strength. Second, we compare the numerical results with the predictions of a refined theory of the avalanche, which includes finite size effects, to explore the physics of critical bubble sizes.

Though the numerical results for small systems are consistent with the avalanche scenario, we cannot rule out a failure of the instability in a much larger system. In the second part of the chapter we discuss such a possible mode of failure caused by the collective back-action

---

possible in the case of a 2D insulator. We note, in passing, that it can also serve as a crude toy model for the eigenstate transition that separates the Ising-ordered and paramagnetic-MBL phases. Since the critical point is an infinite randomness point, the typical (though not average) correlations decay as a stretched exponential at the transition.

[2] LIOMs successfully hybridize with bath spins if and only if the Fermi Golden Rule decay rate of a local operator acting on the LIOM is non-zero.

of the insulator onto the bubble. We describe the ergodic region using a Hubbard model of N fermion sites with random, all-to-all hopping and on-site interactions. As before, to this core we couple non-interacting fermions that would otherwise realize a two dimensional Anderson insulator (germane to the third model above). For large N, after averaging over the disorder in the bubble and in the bubble-insulator coupling, we show that the problem can be mapped to an Anderson impurity problem akin to the dynamical mean field theory (DMFT) approximation [95]. We compute the spectral function of a local operator acting on the thermal core using an approximate impurity solver and track the evolution of the spectral function upon adding a growing number of Anderson sites localized at an increasing distance from the bubble (Fig. 3.1). This allows us to assess the back-action of the localized region on the bath spectral function and, thus, test a key assumption of Ref. [70]. While the instability arguments hinge on having a weak back-action, we find a dramatic back-action effect even for reasonably weak bubble-insulator coupling. This cumulative—emergent—effect is caused by the many-body interactions between a very large number of weakly-coupled LIOMs and the ergodic bubble.

While the analyses of these solvable models point to a possible failure of the instability, there are two important caveats in this approach. First, the strong back-action is the result of quantum fluctuations induced by virtual hops of fermions from the Anderson insulator onto the interacting bubble. Thus, the effect is greatly suppressed when the surrounding insulator is strongly localized. Naively, this implies that the *instability* of the insulator is more pronounced if the insulator is strongly, rather than weakly, localized. One possible resolution to this apparent paradox is that, although the solvable models allow us to compute the thermal spectral function, the quantity suitable for tracking and sustaining the instability is the spectral function in a *typical* eigenstate [209]. Second, we emphasize that the thermal spectral function of an interacting system at non-zero temperatures cannot detect localization [174]. Thus, an open and interesting direction for future work would be the development of a different approach for assessing the avalanche effect in the case of a strong insulator.

The remainder of the chapter is organized as follows. In Sec. 3.1, we briefly review the avalanche arguments of Ref. [70]. In Sec. 3.2, we present the exact diagonalization study of a generic model for a random matrix bubble coupled to the Anderson insulator and we discuss various thermalization diagnostics of the instability argument. In Sec. 3.3, we analyze a tractable model wherein we describe the ergodic region using a Hubbard model—this allows us to calculate thermal spectral functions for large system sizes that are inaccessible in ED studies. Finally, we summarize the results and outline possible extensions in Sec. 3.4.

3.1 Review of the rare region instability argument

Before describing our numerical results and toy models, we briefly summarize the main steps of the argument for the instability of MBL in the presence of a thermal bubble. The full system is described by the following Hamiltonian

$$\mathcal{H} = \mathcal{H}_b + \mathcal{H}_l + \mathcal{H}_{bl}, \tag{3.1}$$

where $\mathcal{H}_b$, describing the bubble, is a $2^N \times 2^N$ GOE random Hermitian matrix. For instance, $\mathcal{H}_b$ could correspond to a system of spinless fermions ($c_i^\dagger$) on $i = 1, \ldots, N$ sites. The bubble has a typical many-body level spacing $\delta_b \sim \mathcal{W}/2^N$, where $\mathcal{W}$ is the many-body bandwidth, taken to scale linearly with the system size N [3]. According to the Eigenstate Thermalization Hypothesis (ETH) [222, 223], the thermal region is characterized by a smooth function $\rho(\omega)$ of the energy difference $\omega = E_n - E_m$ between energy eigenstates, $|\Psi_n\rangle$, of $\mathcal{H}_b$ such that the matrix element is given by $\langle \Psi_n | c_i^\dagger | \Psi_m \rangle \simeq \sqrt{\delta_b \rho(\omega)}\eta_{nm}$. Here $\mathcal{H}_b|\Psi_n\rangle = E_n|\Psi_n\rangle$ and η_{nm} is a random number with zero mean and unit variance. The function $\rho(\omega)$ is called the bubble spectral function (see Section 3.2 for more details).

The insulating region is described in terms of a set of local integrals of motion (LIOM) $\{n_\alpha\}$, $\alpha = 1, \ldots, M$, via the Hamiltonian

$$\mathcal{H}_l = \sum_\alpha \epsilon_\alpha n_\alpha, \tag{3.2}$$

corresponding to an Anderson insulator of non-interacting fermions. We define $n_\alpha = \psi_\alpha^\dagger \psi_\alpha$, where $\psi_\alpha^\dagger$ is the operator creating a fermion in the localized eigenfunction

$$\phi_\alpha(\mathbf{r}) = e^{-|\mathbf{r}-\mathbf{r}_\alpha|/2\xi}/\xi^{d/2} \tag{3.3}$$

centered at $\mathbf{r}_\alpha$ in d spatial dimensions. The LIOM energies obey $|\epsilon_\alpha| \leq W$ and W is the single-particle bandwidth of the insulator. Envisaging the bubble as a "quantum dot" located at the origin, the bubble-insulator coupling is given by

$$\mathcal{H}_{bl} = \sum_{i\alpha} (V_{i\alpha} c_i^\dagger \psi_\alpha + \text{h.c.}), \tag{3.4}$$

with $V_{i\alpha} \sim V e^{-r_\alpha/\xi}$ decaying exponentially with the distance from the bubble. While a true MBL system contains interactions of the form $n_\alpha n_\beta$ between LIOMs, following Ref. [70], we neglect them for the following two reasons. First, since the avalanche arguments focus on a potential instability of MBL, one normally considers "the best-case scenario" for localization, namely a single finite ergodic region in an otherwise non-interacting Anderson insulator. This follows from the expectation that interactions among LIOMs can only enhance the instability. Second, since we couple each LIOM to the random matrix bubble which renders the full system interacting, the sole effect of LIOM-LIOM coupling would be a higher order, multi-spin, coupling between the LIOMs and the bubble.

The first step in the instability argument [70] is to consider whether the LIOM closest to the quantum dot, namely the localized site with the strongest coupling $V_{i\alpha}$, gets hybridized

---

[3] In our numerics we take $\mathcal{W} = wN$, where $w \approx 2.6$.

with the bubble. The criterion for this is given by the following condition for the matrix element:

$$\mathcal{T} \propto V|\langle\Psi_n|c_i^\dagger|\Psi_m\rangle| \approx V\sqrt{\delta_b\rho(W)} \gg \delta_b, \tag{3.5}$$

where $|E_n - E_m| \approx W$. Crucially, this entails a non-zero Fermi Golden Rule (FGR) decay rate $\sim \mathcal{T}^2/\delta_b$ for the LIOM. If this is the case then the site can be considered as part of the bubble and, once again, we assume the ETH ansatz for the matrix elements. Since the LIOM is absorbed into the ergodic region then the Hilbert space dimension of the combined system increases by a factor of 2, i.e. the level spacing gets reduced to $\delta_E \simeq \delta_b/2$. However, in the process, the spectral function of the ergodic grain also gets modified from $\rho(\omega)$ to $\tilde{\rho}(\omega)$. Based on certain assumptions about the eigenfunctions $|\widetilde{\Psi}_n\rangle$ of the combined system as a linear superposition of product states $\{|\Psi_n\rangle \otimes |n_\alpha\rangle\}$ of the initial bubble and the LIOM, Ref. [70] argues that $\tilde{\rho}(\omega) \simeq \rho(\omega)$, i.e. that the spectral function remains essentially the same after the LIOM becomes a *bona fide* member of the bubble.

If we iterate this argument multiple times such that the bubble grows to a radius R (see Fig.3.1), then the level spacing becomes $\delta_E(R) \sim \delta_b e^{-A_d R^d}$, where $A_d \sim \mathcal{O}(1)$. The matrix element to absorb an additional LIOM at distance R is $\mathcal{T}_R \sim V\sqrt{\delta_E(R)\rho(W)}e^{-R/\xi}$, leading to the following condition for the hybridization of the site into the bubble:

$$\frac{\mathcal{T}_R}{\delta_E(R)} \sim V\sqrt{\frac{\rho(W)}{\delta_b}}e^{A_d R^d/2 - R/\xi} \gg 1. \tag{3.6}$$

Evidently, the above condition can always be satisfied for $R \to \infty$ in $d > 1$, rendering the localized state unstable in any dimension higher than one. However, note that the exponential has a minimum at

$$R^* = [2/(dA_d\xi)]^{1/(d-1)} \tag{3.7}$$

when $d > 1$. For the avalanche to continue indefinitely, it must survive around R^*. Thus, a necessary and sufficient condition for the LIOM at an arbitrary distance $R > R^*$ to be hybridized with the ergodic region is that $\mathcal{T}_{R^*}/\delta_E(R^*) \gg 1$. This immediately holds if the initial bubble size $N > N^*$, where

$$N^* \sim (1/\xi)^{d/(d-1)}. \tag{3.8}$$

For $d = 1$, the function in Eq. 3.6 is monotonically increasing or decreasing if $\xi > \xi_c$ or $\xi < \xi_c$, respectively, where $\xi_c = \frac{2}{A_d}$.

Lastly, we want to emphasize the two key assumptions embedded in the instability argument. First, the thermalization avalanche continues indefinitely if and only if the FGR decay rate for all LIOMs is non-zero. Second, whenever a LIOM is hybridized with the bubble, the ETH holds and the spectral function of a local operator acting on the ergodic region stays qualitatively the same.

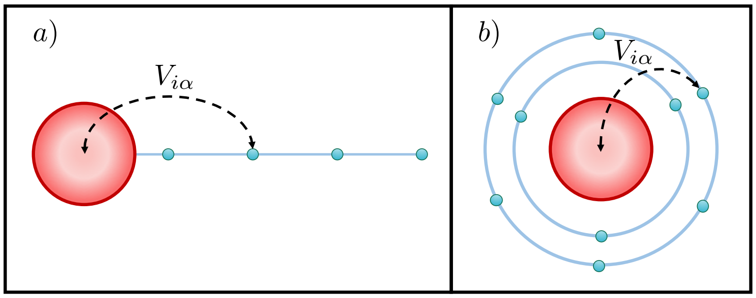

Figure 3.2: The two geometries under consideration. In both cases, the coupling between the first LIOM and the bubble is set to be $V_1 = 1.0$, independent of the localization length ξ. (a) One dimensional geometry: the other LIOMs, indexed by $\alpha \geq 2$, are located at distances $r_\alpha = (\alpha - 1)a$ in units of $a = 1$ from the ergodic bubble. The coupling strengths are $V_\alpha = V_1 e^{-r_\alpha/\xi}$ and $V_\alpha = V_1 e^{-\sqrt{r_\alpha/\xi}}$ for the 1D insulator and 1D insulator with sub-exponentially decaying wavefunctions, respectively. (b) Two dimensional geometry: LIOMs are arranged in concentric layers around the ergodic bubble such that the n^{th} layer (for $n \geq 2$) is at a distance $r_n = (n-1)a$ from the bubble; this layer contains n LIOMs indexed by $\alpha = \frac{n(n-1)}{2} + 1, \ldots, \frac{n(n+1)}{2}$ and their coupling strength is taken to be $V_\alpha = V_1 e^{-r_n/\xi}$.

3.2 Exact diagonalization of a generic model

We now test these two assumptions in an exact diagonalization study of a model akin to the one considered in Ref. [70] and defined in Eq. 3.1. For computational simplicity, we take $\mathcal{H}_b$, describing the ergodic bubble centered at the origin, to be a $2^N \times 2^N$ GOE random matrix on spin degrees of freedom $\sigma_i^{\{x,y,z\}}$ (where $i = 1, \ldots, N$) such that the many-body bandwidth scales linearly with N. We then fix the size of the ergodic region to $N = 8$ spins. We characterize the LIOMs also using Pauli spin variables $\tau_\alpha^{\{x,y,z\}}$, where $\alpha = 1, \ldots, M$, such that $\mathcal{H}_l = \sum_\alpha \epsilon_\alpha \tau_\alpha^z$. The random fields ϵ_α are sampled from the uniform distribution on $[0.5, 1.5]$.

The geometries we consider are shown in Fig. 3.2. The bubble-insulator coupling is taken to be $\mathcal{H}_{bl} = \sum_\alpha V_\alpha \sigma_1^x \tau_\alpha^x$, where V_α depends on the geometry under consideration (see Fig. 3.2) and we set the coupling of the first LIOM to be $V_1 = 1.0$, independent of ξ. Since the bubble is decribed by a random matrix without any notion of locality, coupling all LIOMs to the same bubble operator σ_1^x does not affect the subsequent discussion.

LIOM spectral functions

We obtain the full spectrum and many-body eigenstates $\mathcal{H}\left|\Psi_n\right\rangle = E_n \left|\Psi_n\right\rangle$ through the exact diagonalization (ED) of the spin Hamiltonian described in the preceding paragraphs. To check whether the LIOMs are successfully hybridized with the bubble spins, we define the spectral function of a local operator τ_M^x acting on the LIOM farthest from the ergodic

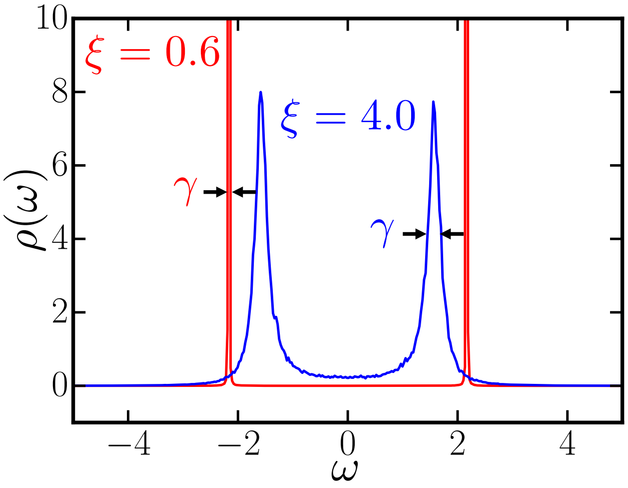

Figure 3.3: The spectral function $\rho(\omega)$ of a local operator acting on the M^{th} LIOM in a fixed disorder realization $\{\epsilon_\alpha\}$ and averaged over N_A eigenstates in the middle of the band. $\rho(\omega)$ is plotted as histogram with a bin width equal to twice the many-body level spacing, $2\delta_E$. The spectral function exhibits two peaks located at $\pm 2\epsilon_M$. For a large localization length ξ, the width γ of these peaks is much larger than the level spacing, indicating that the LIOM is hybridized with the ergodic bubble. For a small localization length, the LIOM is not hybridized and the width of the peaks is limited by the level spacing.

region for a given eigenstate $|\Psi_n\rangle$ as

$$\rho_n(\omega) = 2\pi \sum_{m \neq n} |\langle \Psi_n | \tau_M^x | \Psi_m \rangle|^2 \, \delta(\omega - \omega_{mn}), \tag{3.9}$$

where $\omega_{mn} = E_m - E_n$. We can also think of $\rho_n(\omega)$ as the dynamical structure factor:

$$\rho_n(\omega) = \operatorname{Im} \int_0^\infty e^{i\tilde{\omega} t} \langle \Psi_n | \tau_M^x(t) \tau_M^x(0) | \Psi_n \rangle \, dt, \tag{3.10}$$

where $\tilde{\omega} = \omega + i0^+$. Note that it obeys the following sum rule:

$$\int_{-\infty}^{+\infty} \rho_n(\omega) d\omega = 2\pi (1 - \langle \Psi_n | \tau_M^x | \Psi_n \rangle^2) \approx 2\pi. \tag{3.11}$$

In a fixed disorder realization for the LIOM fields $\{\epsilon_\alpha\}$, the eigenstate spectral function $\rho_n(\omega)$ exhibits two peaks located at $\pm 2\epsilon_M$, where $1 \leq 2|\epsilon_M| \leq 3$, as shown in Fig. 3.3. This is due to the fact that flipping the LIOM farthest from the bubble requires an energy of approximately $2\epsilon_M$. We average over $N_A = 2^{N+M}/(N+M)$ eigenstates in the middle of the band where the putative ergodicity is the most robust: $\rho(\omega) = N_A^{-1} \sum_n \rho_n(\omega)$. Because the LIOMs do not interact directly with each other, the position of the peak is not expected to depend on the eigenstate, but only on the value of the field ϵ_M on this LIOM.

We can diagnose the extent to which the farthest LIOM is hybridized with the bath by looking at the width γ of the spectral peaks of $\rho(\omega)$ compared to the many-body level spacing—for each disorder realization we compute the ratio γ/δ_E between the spectral width γ and the numerically computed many-body level spacing δ_E. We then study the evolution of the disorder averaged $\overline{\gamma/\delta_E}$ [4] as a function of M, the number of LIOMs coupled to the ergodic bubble, as shown in Fig. 3.4 for the three geometries under consideration.

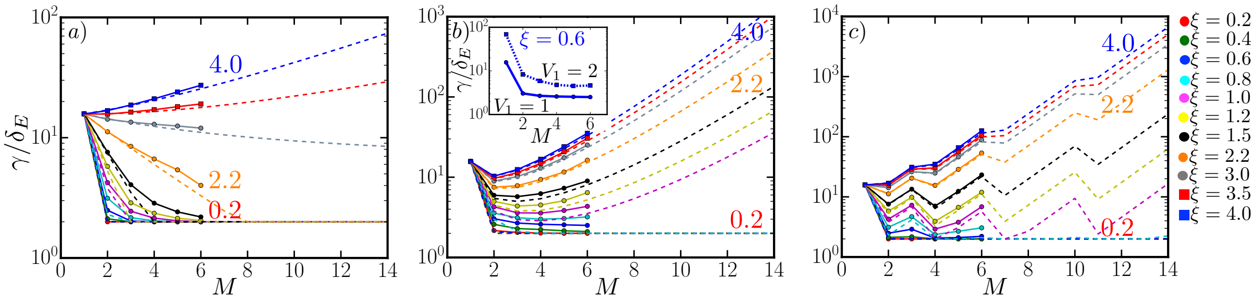

Figure 3.4: Exact diagonalization (ED) results for the spin model defined in Section 3.2 using an ergodic bubble of $N = 8$ spins coupled to $M = 1, \ldots, 6$ LIOMs. We plot the ratio γ/δ_E between the width γ of the spectral function peaks of a local operator acting on the M^{th} LIOM (see Fig. 3.3) and the many-body level spacing δ_E as a function of the number of LIOMs added. Different curves and colors (online) correspond to different localization lengths in the bulk—the solid curves represent numerical ED results, whereas the dashed lines represent the theoretical expectations from Eqs. 3.12 and 3.13 based on ETH assumptions. (a) One dimensional geometry with exponentially decaying couplings between the bubble and LIOMs. (b) One dimensional geometry with a stretched exponential decay of couplings. (c) Two dimensional geometry with an exponential decay of couplings. In (b) and (c) the failure of the avalanche is due to the sub-critical bubble size. In these cases, the avalanche can be restored by increasing the bubble size N or by increasing the bare bath-LIOM coupling V_1, as verified in the inset of panel (b) for the one dimensional model with stretched exponentials.

First, we notice that for very small localization lengths ξ the ratio $\overline{\gamma/\delta_E} \approx 2$ which means that $\gamma \sim e^{-\mathcal{O}(M)}$. In particular, this entails that the FGR decay rate for the M^{th} LIOM is approximately zero and the many-body eigenstates of the fully coupled system are product states of the form $|\Psi_n\rangle \otimes |\uparrow_M\rangle$ and $|\Psi_n\rangle \otimes |\downarrow_M\rangle$ with energies $E_n + \epsilon_M$ and $E_n - \epsilon_M$, respectively. Thus, $\rho(\omega)$ consists of two delta functions located at $\pm 2\epsilon_M$. Since we compute spectral functions as energy histograms wherein the bin size is taken to be $2\delta_E$, this means that a "delta function" peak has a width $\gamma/\delta_E = 2$. We have confirmed that the farthest LIOM does not get hybridized with the ergodic bubble by checking that the entanglement entropy of this LIOM is zero (see the Appendix A for details).

---

[4] We take $N = 8$ and average over 5000, 4000, 3000, 2000, 1000, 1000, and 200 disorder realizations for $M = 0, 1, 2, 3, 4, 5$, and 6 LIOMs, respectively.

Second, for a large localization length ξ we find that the peaks centered around $\pm 2\epsilon_M$ get broadened such that $\overline{\gamma/\delta_E} \gg 1$ (see Fig. 3.4). This is due to the fact that now there are many accessible multi-spin processes such as flipping the LIOM by flipping bubble spins and absorbing energy from the ergodic bubble. In other words, the LIOMs are successfully hybridized with the bubble, the full many-body eigenstates are superpositions of many product states of the form $|\Psi_n\rangle \otimes |\tau^z_M\rangle$, and the FGR decay rate is non-zero.

We now compare these numerical results with the avalanche scenario [70]. First, by the above arguments, we note that if the FGR is violated then $\gamma/\delta_E = 2$. Second, if the FGR decay rate for the M^{th} LIOM is non-zero, then the width $\gamma = \gamma_M \sim \frac{V_M^2}{w}$, where $w = \mathcal{W}/(N + M - 1)$ and V_M is the coupling strength between the farthest LIOM and the bubble: (i) for the $d = 2$ geometry $V_M = V_1 e^{-r_M/\xi}$, where $r_M = (n - 1)$ if the M^{th} LIOM is located on the n^{th} layer; (ii) for the $d = 1$ geometry with exponentially decaying LIOM wave-functions $V_M = V_1 e^{-r_M/\xi}$, where $r_M = (M - 1)$; (iii) for the $d = 1$ geometry with sub-exponentially decaying wave-functions $V_M = V_1 e^{-\sqrt{r_M/\xi}}$, where $r_M = (M - 1)$. Lastly, the many-body level spacing is $\delta_E = w(N + M - 1)/2^{N+M-1}$.

With these expressions in hand, we expect that

$$\frac{\gamma}{\delta_E} = \max\left[2,\ \frac{\gamma_1}{\delta_b}\frac{N}{N + M - 1}\exp\left((M - 1)\log 2 - 2\frac{r_M}{\xi}\right)\right] \tag{3.12}$$

for the two models with exponentially decaying wave-functions: see the dashed curves in Fig. 3.4(a) and Fig. 3.4(c) for $d = 1$ and $d = 2$, respectively. The maximum in Eq. 3.12 ensures that the ratio does not drop below 2 in the case where the FGR is violated. Note that when the FGR holds, we have written the ratio $\gamma_M/\delta_E(M)$ as a function of γ_1/δ_b to ensure that both the numerical and theoretical curves have the same starting point, namely the same ratio for the first LIOM that is coupled. The first term in the exponential in Eq. 3.12 comes from the many-body level spacing, whereas the second one comes from the exponential decay of the coupling strength V_M. The logarithmic correction (in M) comes from the linear scaling of the many-body bandwith.

Note that for the 1D model with a stretched exponential decay of the localized wave-functions [Fig. 3.4(b)] the expression becomes

$$\frac{\gamma}{\delta_E} = \max\left[2,\ \frac{\gamma_1}{\delta_b}\frac{N}{N + M - 1}\exp\left((M - 1)\log 2 - 2\sqrt{\frac{r_M}{\xi}}\right)\right]. \tag{3.13}$$

The comparison between the above expectations for γ/δ_E and the numerically obtained $\overline{\gamma/\delta_E}$ yields an excellent agreement for all three models, as shown in Fig. 3.4. We emphasize the monotonic behavior of the curves in the case of the 1D model with an exponential decay of the LIOM wave-functions: both the numerical results and the avalanche scenario predict that γ/δ_E is monotonically increasing when $\xi > \xi_c = \frac{2}{\log 2}$ and decreasing when $\xi < \xi_c$— this suggests that there is a localization-delocalization phase transition as a function of ξ independent of the initial bubble size [70]. In contrast to this behavior, the curves for the 2D model and the 1D model with stretched exponentials behave *non-monotonically* with a minimum at M^*. This suggests that for any given ξ, a sufficiently large initial bubble will thermalize the whole system.

We now test this latter point, to wit, that the apparent "localizing behavior" at small ξ's in Fig. 3.4(b) and Fig. 3.4(c) is due to an insufficiently potent initial thermal bubble. While it is numerically prohibitive to increase the bubble size N, we can increase V_1, the coupling strength to the bubble. We set $V_1 = 2 < w = 2.6$ and keep $N = 8$ fixed for the 1D model with a stretched exponential decay of the couplings. As shown in the inset of Fig. 3.4(c), the results are still in excellent quantitative agreement with the avalanche scenario and the predictions from Eq. 3.13: for a fixed localization length $\xi = 0.6$, the ergodic region is more effective at thermalizing the LIOMs than in the case of $V_1 = 1$ since the $\gamma/\delta_E(M)$ curve is shifted upwards.

Thus, after accounting for transient finite-size effects and the bare coupling strengths, the avalanche scenario is found to be in remarkably good quantitative agreement with our numerics. As long as LIOMs are hybridized with the ergodic region, the fully coupled system is thermal and the avalanche persists indefinitely. It only stops when the hybridization fails, but a larger or more potent ergodic region can overcome this issue.

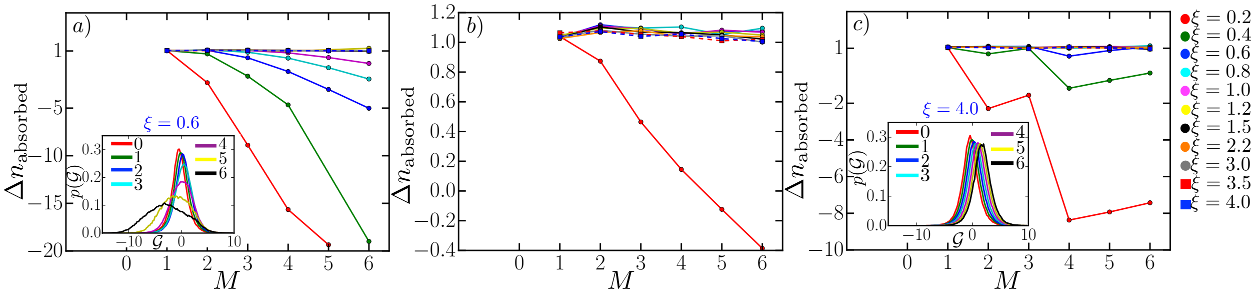

Figure 3.5: Increase of the effective bath size due to adding the M^{th} LIOM as measured by the change of the Thouless parameter (see Eq. 3.15). (a) One dimensional geometry with exponentially decaying couplings. The different curves and colors (online) correspond to different localization lengths: as described in the main text, a transition occurs at $\xi_c = 2/\log 2 \approx 2.9$. The inset shows how the distribution $p(\mathcal{G})$ for $\xi = 0.6$ evolves with the number of added spins M. The distribution eventually collapses to the left and broadens, signaling localization. (b) One dimensional geometry with stretched exponential decay of interactions. (c) Two dimensional geometry with exponentially decaying couplings. Inset: evolution of the distribution $p(\mathcal{G})$ for $\xi = 4.0$ in the one dimensional geometry with exponentially decaying interactions. The distribution moves to the right at a constant rate, signaling thermalization.

Bath spectral functions

Above, we have explored the conditions under which LIOMs added incrementally to a finite bath successfully hybridize with it in the usual sense of Fermi's Golden Rule: to wit, the local spectral function of a LIOM is broader than the many-body level spacing. An important assumption in the arguments of Ref. [70] is that once a LIOM is hybridized with the bath in this way, it is fully absorbed into it. In other words, the low frequency characteristics of the bath after absorbing the LIOM should be the same as those of a random matrix with one additional degree of freedom.

We test this assumption by analyzing the spectral function of an original bath spin. Specifically, we consider the many-body "Thouless conductance" defined in Ref. [208] (it will also be defined below for completeness). The typical value of this parameter in a thermalizing system is expected to grow linearly with the size of the bath, with a slope equal to the entropy density.

The computational scheme is as follows. After obtaining the full spectrum and eigenstates, we apply a local perturbation $\mathcal{O} = \sigma_N^z$ on a bubble spin different than the one to which we have coupled the LIOMs (i.e. σ_1) to mitigate the severity of finite size effects [5]. We rearrange the eigenstates based on the perturbed energies $E'_n = E_n + \langle\Psi_n|\,\mathcal{O}\,|\Psi_n\rangle$ and compute the matrix element between nearby eigenstates $\mathcal{T}_{n,n+1} = \langle\Psi_n|\,\mathcal{O}\,|\Psi_{n+1}\rangle$. Then we define the Thouless parameter as in Ref. [208]

$$\mathcal{G} = \log\frac{|\mathcal{T}_{n,n+1}|}{E'_{n+1} - E'_n}. \tag{3.14}$$

We compute this parameter for $N_A = 2^{N+M}/(N+M)$ eigenstates in the middle of the band and for many disorder realizations [6] to produce a distribution $p(\mathcal{G})$.

The results for different values of the localization length ξ are shown in Fig. 3.5. For a thermalizing quantum system whose eigenstates obey the ETH, we expect $\mathcal{G} \sim (N+M)$ since the matrix element $\mathcal{T}_{n,n+1}$ is essentially an overlap between two random states in a 2^{N+M}-dimensional Hilbert space and the level spacing is $\delta_E \sim 2^{-(N+M)}$. Conversely, if the system is localized then two nearby eigenstates can be connected only via extensively many rearrangements of $(N+M)$ local integrals of motion and $\mathcal{G} \sim -(N+M)$, as shown in Ref. [208].

Our numerical results support the assumption that when a LIOM is hybridized according to the local golden rule criterion, then that LIOM is truly an extra bath degree of freedom. To check this, we numerically compute

$$\Delta n_{\text{absorbed}} = \frac{2}{\log 2}\left[\langle\mathcal{G}(M+1)\rangle - \langle\mathcal{G}(M)\rangle\right], \tag{3.15}$$

where $\langle\mathcal{G}(M)\rangle$ is the average value of the Thouless parameter when we have coupled M LIOMs. If $\Delta n_{\text{absorbed}} = 1$ then the Thouless parameter increases as it would in the case of adding exactly one more strongly coupled degree of freedom to the bath. This is illustrated in Fig. 3.5.

---

[5] We have checked that our results are consistent for a different local perturbation $\mathcal{O}_2 = \sigma_N^z \tau_1^z$.

[6] We average over 5000, 4000, 3000, 2000, 1000, 1000, and 200 disorder realizations for $M = 0, 1, 2, 3, 4, 5,$ and 6 LIOMs, respectively.

On the other hand, in situations where ETH arguments predict the failure of the avalanche (either due to a sub-critical bubble size or a sub-critical localization length), adding LIOMs leads to a sublinear increase or even decrease of $\mathcal{G}$. In this case, each additionally coupled LIOM contributes as less than a full degree of freedom to the bath. In this situation, the distribution $p(\mathcal{G})$ of the Thouless parameter also becomes broader with each additional LIOM (inset of Fig. 3.5).

We reiterate that even this eventual termination of the avalanche is predicted by the avalanche scenario—it is due to the violation of the FGR and the failure of the added LIOMs to hybridize with the bath. In the 1D model with exponentially localized LIOM wave-functions, this signals a true localization transition [70] tuned by the localization length ξ. However, in the 2D model and the 1D model with stretched exponential interactions the termination of the avalanche is *not* a phase transition and it can be avoided by starting with a larger or more potent initial thermal bubble. Finally, as discussed in the Appendix A, the non-monotonic behavior of $\langle\mathcal{G}\rangle$ at small localization lengths stems from a non-trivial variation of the bath spectral function as M increases due to the breakdown of typicality.

3.3 A model for the back-action on the bubble

The exact diagonalization study described above provides evidence in support of the avalanche scenario. But there is a key assumption in Ref. [70] that we have not yet explicitly checked, namely that the spectral function $\rho(\omega)$ of a local operator acting on the ergodic bubble does not change qualitatively as an ever-increasing number of LIOMs are hybridized with the bubble degrees of freedom. This can be particularly problematic if the number of added LIOMs is very large. In particular, we ask if there is a collective effect due to the coupling of many LIOMs which we cannot capture by adding a few LIOMs one by one. Such an effect is inaccessible in the exact diagonalization approach taken in the previous sections.

To explore this regime, we introduce a model of an ergodic bubble coupled to an Anderson insulator which admits a controlled treatment of the interaction effects in the bubble. Once again, we consider a Hamiltonian that can be written as a sum of three parts: $\mathcal{H}_b$, $\mathcal{H}_l$, and $\mathcal{H}_{bl}$ as in Eq. 3.1. The ergodic bubble is described by a Hubbard model Hamiltonian of interacting fermions hopping on N sites

$$\mathcal{H}_b = \frac{1}{\sqrt{N}} \sum_{ij\sigma} t_{ij,\sigma} c^\dagger_{i\sigma} c_{j\sigma} + U \sum_i n_{i\uparrow} n_{i\downarrow}, \tag{3.16}$$

where the single-particle hopping matrix elements $t_{ij,\sigma} = t^*_{ji,\sigma}$ are sampled from a GOE random matrix with $\overline{|t_{ij,\sigma}|^2} = t^2$. The normalization $1/\sqrt{N}$ ensures the proper thermodynamic limit at large-N.

The LIOMs sitting outside the bubble are described by Eq. 3.2 and their energies $\epsilon_\alpha \in [-W, W]$ are sampled from a uniform random distribution. We consider a 2D geometry of concentric circles, as shown in the inset in Fig. 3.6(a), such that the number of insulating sites residing on a layer of radius r is proportional to r. This ensures that the total number of insulating sites M grows as r^2. In particular, we take $r_\alpha = r_0(n-1)$ for the LIOMs on the n-th circle and $r_0 = 1/(\sqrt{2\pi n_L})$ is a length scale related to the areal density n_L of the LIOMs.

Finally, the coupling of the LIOMs to the bubble degrees of freedom is given by

$$\mathcal{H}_{bl} = \sum_{i\alpha\sigma} (V_{i\alpha,\sigma} c^\dagger_{i\sigma} \psi_\alpha + \text{h.c.}). \tag{3.17}$$

Note that this is different from the coupling considered earlier in Eq. 3.4 since every LIOM couples to every degree of freedom in the bubble, not just to a single bath degree of freedom. Also, unlike in Eq. 3.4, $V_{i\alpha}$ are random complex numbers chosen from a Gaussian distribution with zero mean and $\overline{|V_{i\alpha}|^2} = V_\alpha^2/2\sqrt{N}$, where $V_\alpha^2 = (V/\xi)^2 e^{-r_\alpha/\xi}$. The factor of $1/\xi$ in V_α arises due to the scaling $\phi_\alpha(\mathbf{r}) \propto 1/\xi$ of the single-particle LIOM eigenfunctions in 2D. Secondly, since the underlying microscopic coupling is *local*, the contribution of $\mathcal{H}_{bl}$ to the free energy must scale as the surface area of the bubble, namely as $N^{(d-1)/d}$. The particular scaling of $\overline{|V_{i\alpha}|^2}$ with N ensures that the contribution of the coupling term (3.17) in the action (see the last term in Eq. 3.19 below) scales as $\sqrt{N}$ in $d = 2$.

In what follows we average over the random hopping t_{ij} and the bubble-LIOM coupling $V_{i\alpha,\sigma}$ using replicas in a fixed realization of the LIOM on-site energies $\{\epsilon_\alpha\}$. This averaging procedure over the couplings associated with the bubble degrees of freedom assumes that the self-averaging property holds for an ergodic bubble with a large number of sites N. The replicated partition function after disorder averaging is:

$$\overline{Z^n} = \int \mathcal{D}(\bar{c}_a, c_a, \bar{\psi}_a, \psi_a) e^{-S[\bar{c}_a, c_a, \bar{\psi}_a, \psi_a]}, \tag{3.18}$$

where the imaginary-time action is

$$\begin{aligned} S = \int_0^\beta d\tau \left[\sum_{ia} \left(\sum_\sigma \bar{c}_{i\sigma a}(\tau) \partial_\tau c_{i\sigma a}(\tau) - U n_{i\uparrow a}(\tau) n_{i\downarrow a}(\tau) \right) + \sum_{\alpha a} \bar{\psi}_{\alpha a}(\tau)(\partial_\tau + \epsilon_\alpha)\psi_{\alpha a}(\tau) \right] + \\ + \frac{N}{2} \int d\tau d\tau' \sum_{ab\sigma} G_{ab\sigma}(\tau, \tau') \left(t^2 G_{ba\sigma}(\tau', \tau) + \frac{1}{\sqrt{N}} \sum_\alpha V_\alpha^2 \bar{\psi}_{\alpha a}(\tau) \psi_{\alpha b}(\tau') \right). \end{aligned} \tag{3.19}$$

The $\{\bar{c}, c\}$ are Grassmann variables and $a, b = 1, \ldots, n$ denote replica indices; we have also introduced a large-N field:

$$G_{ab\sigma}(\tau, \tau') = (1/N) \sum_i \bar{c}_{ib}(\tau') c_{ia}(\tau). \tag{3.20}$$

We promote G to a fluctuating field by introducing a Lagrange multiplier field $\Sigma_{ab\sigma}(\tau, \tau')$ and, after integrating out the fermionic fields, obtain $\overline{Z^n} = \int \mathcal{D}(G, \Sigma) e^{-NS_{\text{eff}}[G, \Sigma]}$.

Assuming a paramagnetic and replica-diagonal symmetric ansatz (i.e. $G_{aa\sigma} = G$ and $G_{ab\sigma} = 0$ for $a \neq b$), we get

$$S_{\text{eff}} = \int d\tau d\tau' \left[t^2 G(\tau,\tau')G(\tau',\tau) - \Sigma(\tau,\tau')G(\tau',\tau)\right] - \frac{1}{N}\sum_{\alpha} \operatorname{Tr}\ln(-\mathcal{G}_\alpha^{-1}) - \ln \mathcal{Z}_{\text{imp}}, \tag{3.21}$$

where

$$\mathcal{G}_\alpha^{-1}(\tau,\tau') = -(\partial_\tau + \epsilon_\alpha)\delta(\tau-\tau') - V_\alpha^2\sqrt{N}G(\tau,\tau'). \tag{3.22}$$

We can see that $\mathcal{Z}_{\text{imp}} = \int \mathcal{D}(\bar{c}_\sigma, c_\sigma)e^{-S_{\text{imp}}}$ is the partition function of an effective Anderson impurity model described by

$$S_{\text{imp}} = \int d\tau d\tau' \sum_\sigma \bar{c}_\sigma(\tau)\tilde{\mathcal{G}}^{-1}(\tau,\tau')c_\sigma(\tau') - \int d\tau U n_\uparrow(\tau)n_\downarrow(\tau). \tag{3.23}$$

Here $\tilde{\mathcal{G}}^{-1}(\tau,\tau') = -\partial_\tau\delta(\tau-\tau') - \Sigma(\tau,\tau')$.

We use a saddle point approximation to obtain the bubble fermions Green's function self-consistently. To this end, the self-consistency conditions are obtained by setting

$$\delta S_{\text{eff}}/\delta G(\tau,\tau') = \delta S_{\text{eff}}/\delta\Sigma(\tau,\tau') = 0. \tag{3.24}$$

If we assume time-translation invariance, i.e. $G(\tau,\tau') = G(\tau-\tau')$, then we find:

$$G(\tau) = \langle \bar{c}_\sigma(0)c_\sigma(\tau)\rangle_{\text{imp}} \tag{3.25a}$$

$$\Sigma(\tau) = \Sigma_t(\tau) + \Sigma_V(\tau) = t^2G(\tau) + (1/\sqrt{N})\sum_\alpha V_\alpha^2\mathcal{G}_\alpha(\tau). \tag{3.25b}$$

The averaging $\langle \dots \rangle_{\text{imp}}$ is carried out using the effective Anderson impurity action from Eq. 3.23 where, due to the time translation invariance at the saddle point, the Green's function $\mathcal{G}\tilde{(\omega)}$ satisfies

$$\tilde{\mathcal{G}}^{-1}(\omega) = \omega - t^2G(\omega) - \frac{1}{\sqrt{N}}\sum_\alpha V_\alpha^2\mathcal{G}_\alpha(\omega) \tag{3.26}$$

for the real-frequency argument $\omega + i0^+$. This closes the self-consistency loop as we obtain $\mathcal{G}_\alpha(\tau)$ from Eq. 3.22, provided that the impurity Green's function $\langle \bar{c}_\sigma(0)c_\sigma(\tau)\rangle_{\text{imp}}$ can be calculated from the impurity action 3.23. $G(\omega)$ and

$$\mathcal{G}_\alpha(\omega) \;=\; \left[\omega + \epsilon_\alpha - V_\alpha^2\sqrt{N}G(\omega)\right]^{-1} \tag{3.27}$$

are the retarded Green's functions for the bubble fermions and the LIOMs, respectively.

The action in Eq. 3.23 is the usual one for the Anderson-Kondo impurity problem and it is routinely encountered in the implementation of single-site DMFT. The impurity problem can be exactly solved either via a Bethe ansatz [18] or by a numerical renormalization group approach [241, 50]. In our case, for the self-consistent solution of Eq. 3.25, we use the iterated perturbation theory (IPT) method which is expected to work very well at half-filling in both the weak and strong coupling regimes [95].

Using the IPT approximation, we obtain the impurity Green's function from the Dyson equation:

$$G^{-1}(\tau,\tau') = \widetilde{\mathcal{G}}_{\mathrm{H}}^{-1}(\tau,\tau') - \Sigma_U(\tau,\tau'), \tag{3.28}$$

where $\widetilde{\mathcal{G}}_{\mathrm{H}}^{-1}(\omega) = \widetilde{\mathcal{G}}^{-1}(\omega) - U/2$ is the Hartree-corrected Green's function at half-filling. The impurity self-energy is approximated by [95]

$$\Sigma_U(\omega) \approx U/2 + \tilde{\Sigma}^{(2)}(\omega). \tag{3.29}$$

The first term on the right is the Hartree shift and the second term corresponds to the second order self-energy

$$\tilde{\Sigma}^{(2)}(\tau,\tau') = -U^2 \widetilde{\mathcal{G}}_{\mathrm{H}}^2(\tau,\tau')\widetilde{\mathcal{G}}_{\mathrm{H}}(\tau',\tau). \tag{3.30}$$

Using the IPT Green's function we solve the saddle-point equations 3.25 iteratively.

In particular, we solve them numerically and track the evolution of the bubble and LIOM spectral functions, $\rho(\omega) = -(1/\pi)\mathrm{Im}G(\omega)$ and $\rho_\alpha(\omega) = -(1/\pi)\mathrm{Im}\mathcal{G}_\alpha(\omega)$, respectively, as we increase M. The results for $\rho(\omega)$ are shown in Fig. 3.6 for $N = 30$ and for a wide range of values $M \sim 3 - 10^4$, until the spectrum has converged at large M. We take $U = 2t$, to wit, equal to the bandwidth of the non-interacting GOE random matrix. The LIOM energies $|\epsilon_\alpha| \leq W = 2t$ with $t = 1$ have been sampled from a uniform random distribution. We emphasize that, unless otherwise mentioned, the following results correspond to a single realization of the ϵ_αs, without disorder averaging.

In Fig. 3.6(a) and (b) we show the evolution of $\rho(\omega)$ for a localization length $\xi = 10$ at a temperature $T = 2$ and in the presence of a bubble-LIOM coupling strength $V = 0.5$ with the LIOM density $n_L = 1$. For a small number of added LIOMs, the DOS has a semicircular form as expected from the non-interacting part of the Hamiltonian. However, at higher energies near the band edge there is an extended tail, due to the effect of the interaction U. As we couple more LIOMs, the DOS eventually becomes rugged, inheriting the sharp spectral peaks characterizing the insulator for a fixed disorder realization $\{\epsilon_\alpha\}$ of the LIOM energies. We find that, even for a very large number of added LIOMs [Fig. 3.6(b)], the DOS retains its qualitative features reminiscent of the original interacting bubble. For comparison, we also show the corresponding non-interacting result for large M when the interaction strength in the bubble is set to zero ($U = 0$). We see that the interacting and non-interacting DOSs are very different. Hence, our results for the particular coupling strength $V = 0.5$ ostensibly agree with the assumption behind the instability argument, namely that the spectral function

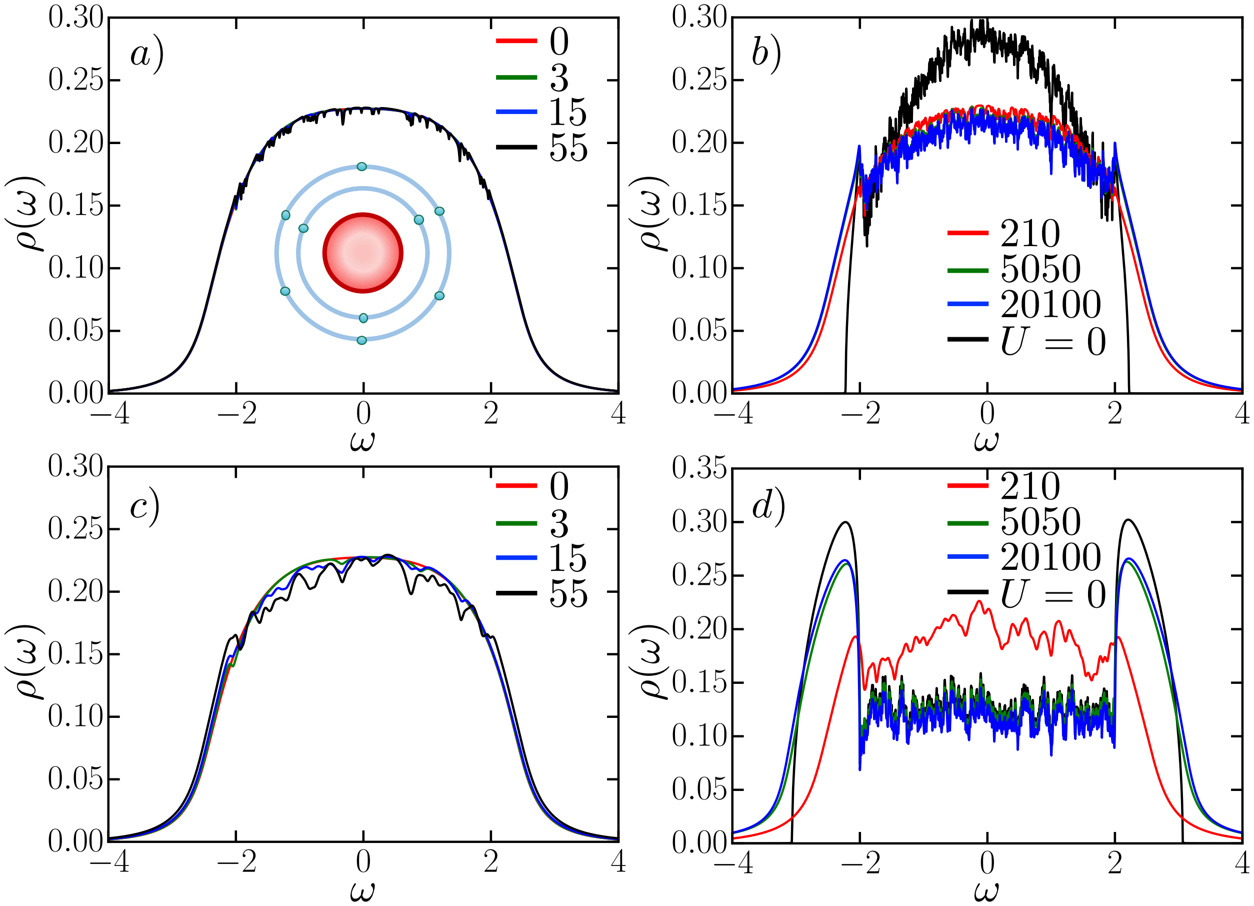

Figure 3.6: The evolution of the bubble spectral function $\rho(\omega)$ for (a)–(b) $V = 0.5$ and (c)–(d) $V = 1.5$ as a function of M, the number of LIOMs coupled to a Hubbard bubble of $N = 30$ sites. Each curve (color) corresponds to a different M. The inset in (a) shows the 2D geometry in which concentric layers of LIOMs are coupled to the bubble. Here $t = 1$, $U = 2$, $W = 2$, $\xi = 10$, $n_L = 1$, and $T = 2$. In (b), for the weak coupling $V = 0.5$, $\rho(\omega)$ does not change much even at large M. For comparison, we also show $\rho(\omega)$ for the non-interacting case ($U = 0$). For the stronger coupling $V = 1.5$, $\rho(\omega)$ changes drastically in (c) and (d) when large numbers of LIOMs are coupled to the bubble. In (d), $\rho(\omega)$ for the interacting case becomes identical to the non-interacting one over an interval $-W < \omega < W$ for large M.

of the interacting ergodic region remains qualitatively unchanged even when a large number of LIOMs are hybridized with it.

Conversely, the results for the DOS at a larger coupling strength $V = 1.5$ are shown in Fig. 3.6(c) and (d). Note that the *effective* coupling of the bubble with the closest LIOM in this case is still weak, $V/\xi = 0.15 \ll t, U$, and the coupling to LIOMs farther away decays exponentially with distance. Hence, this regime is well within the purview of the instability argument [70], which treats the coupling perturbatively through the FGR. We find that the DOS of the bubble undergoes a striking change, albeit when a substantially large number M of LIOMs are coupled, entirely destroying the spectrum of the original Hubbard model. The DOS becomes almost entirely dominated by the discrete poles of the localized sites. In fact, as shown in Fig. 3.6(d), for large M and over an energy interval $-W < \omega < W$ the DOS is identical to that of the system where $U = 0$ in the bubble. This implies that the interaction effects become irrelevant due to the feedback of the insulator onto the bubble. On the contrary, the smooth tails at $|\omega| > 2$ are not caused by the LIOMs, but by the interaction effects in the Hubbard bubble: note that the tails at $2 < |\omega| < 4$ are unaffected by coupling to the insulator, i.e. the tails of the $M = 0$ spectral function in Fig. 3.6(a) are the same as the tails of the large M spectral function in Fig. 3.6(d).

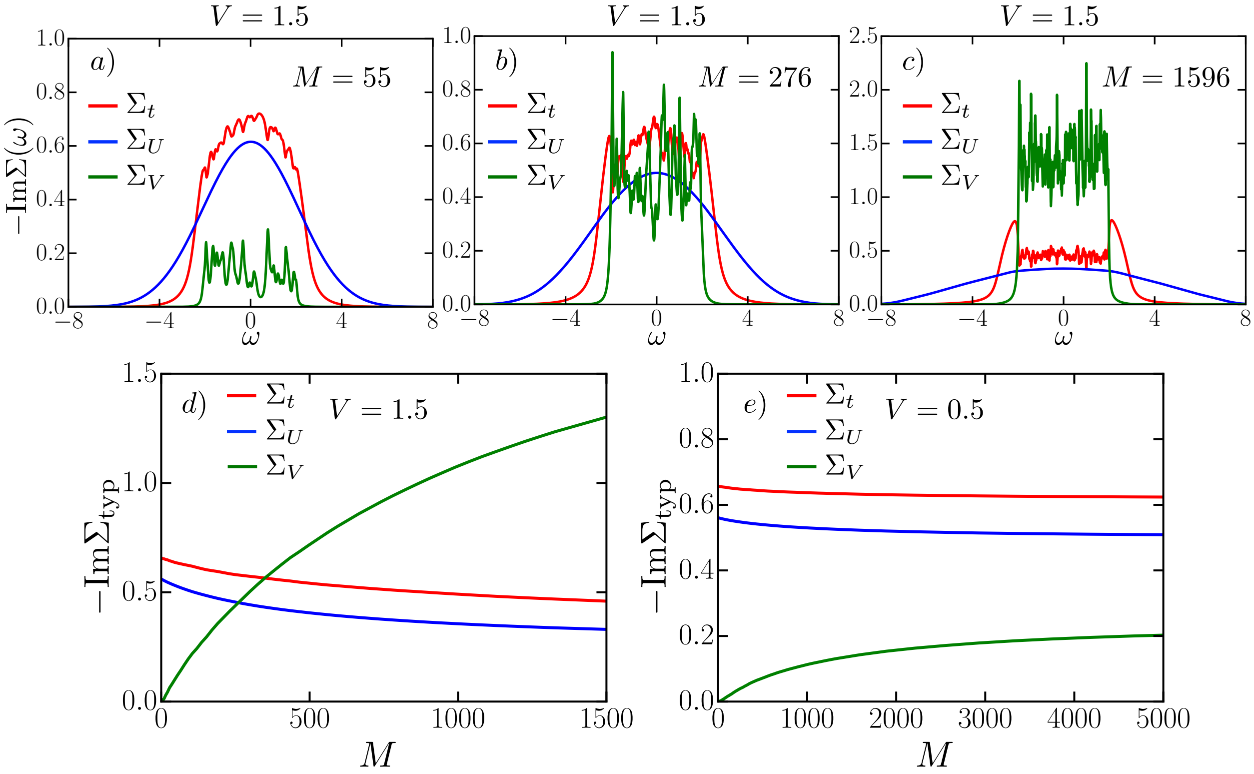

Figure 3.7: (a)–(c) The imaginary part of the three different contributions, Σ_t (due to the hopping), Σ_U (due to the interactions in the bubble), and Σ_V (due to the bubble-LIOM coupling), in the self-energy of the bubble for $V = 1.5$ at three different values of M. We find that Σ_V dominates the other two self-energies at large $M \gtrsim 300$. (d) and (e) compare the typical values (see the main text for the definition) of the three contributions for $V = 1.5$ and $V = 0.5$, respectively. For $V = 1.5$ in (d), Σ_V crosses Σ_t and Σ_U as a function of M, signaling the onset of the strong back-action in the spectral function, as shown in Fig. 3.6(d).

The above "strong" back-action of the insulator onto the bubble can be understood as a consequence of the cumulative, emergent, self-energy effect of a large number of LIOMs, as captured by Σ_V (the last term of Eq. 3.25b). The contribution of an individual LIOM to the self-energy is

$$\Sigma_V \sim (V_\alpha/\xi)^2/(W\sqrt{N}) \tag{3.31}$$

for $W \gtrsim t, U$. For $M \gg \pi\xi^2$, namely when the LIOMs over a radius much larger than ξ are added, the typical Σ_V is expected to saturate to $\sim V^2/(W\sqrt{N})$, becoming independent of ξ and varying as $\sim 1/\sqrt{N}$. As shown in Fig. 3.7, the strong back-action appears for sufficiently strong V, when a large number of LIOMs is coupled to the bubble and $\Sigma_V \gtrsim \Sigma_t,\ \Sigma_U$; the latter two are the self-energies in the DMFT formalism due to the hopping and the interactions in the bubble, respectively.

Figures 3.7(a)–(c) show how the imaginary part of Σ_V dominates those of the other two contributions to the self-energy as we increase M for $V = 1.5$. We emphasize that the mechanisms giving rise to the competition between self-energies are fundamentally dynamical, as shown by the strong energy (ω) dependence of $\Sigma_t(\omega)$, $\Sigma_V(\omega)$, and $\Sigma_U(\omega)$. Moreover, one self-energy leads to a strong feedback onto the other self-energies via the DMFT self-consistency.

To better understand the effect of the coupling strength V, we compare the typical self-energies, defined as the geometric mean over the interval $-W < \omega < W$ and over several disorder realizations. Figs. 3.7(d) and (e) correspond to $V = 1.5$ and $V = 0.5$, respectively. In the former case, Σ_V becomes comparable to Σ_t and Σ_U for $M \approx 300$, consistent with the onset of the strong back-action in the spectral function shown in Fig. 3.6(d). Conversely, for $V = 0.5$ shown in Fig. 3.7(e), $\Sigma_V \ll \Sigma_t, \Sigma_U$ and the effect of the LIOMs on the bubble is very weak [Figs. 3.6(a)–(b)].

This brings us to our main observation. Even though the coupling $V = 1.5$ is "strong" because it induces a strong back-action, it is *"weak"* in the sense of the ETH theory [70] since the effective coupling of the closest LIOM is $(V/\xi) = 0.15 \ll t = 1$. In this regime, the avalanche theory based on ETH would assess the back-action by considering the change of the spectral function upon adding LIOMs one at a time. Within this sequential approach, if the change of spectral function after coupling the closest LIOM is small, then it is expected to remain so after adding farther LIOMs (whose couplings decay exponentially with the distance).

Indeed, in the strong back-action regime shown in Fig. 3.6(c), we find that there is no substantial change after coupling a significant number of LIOMs. However, after coupling an even larger number, as shown in Fig. 3.6(d), the strong back-action on the bubble spectral function becomes apparent. We stress that this emergent effect *cannot* be captured within the ETH framework [70]. Ref. [70] alludes to certain cumulative strong back-action effects such as an MBL proximity effect à la Ref. [173]. However, the effect we described is different from an MBL proximity one since it is caused by quantum fluctuations induced by virtual hops of fermions from the Anderson insulator onto the interacting bubble.

Nonetheless, our study of $\rho(\omega)$ in this model cannot indicate whether the system is localized or not—generically, the thermal spectral function of an interacting system at a finite temperature does not contain direct information about localization [174]. Moreover, capturing localization effects in this model might require the inclusion of non-perturbative effects in $1/N$, whereas we have only kept the leading term up to $\mathcal{O}(1/\sqrt{N})$. Nevertheless, the saddle-point results in the effective Anderson impurity model capture the thermal spectral function of the bubble quite accurately for large system sizes. The drastic change of the thermal spectral function $\rho(\omega)$, which we can compute, implies that the spectral functions of typical eigenstates $\rho_{typ}(\omega)$ must also change substantially as a function of M, even in the regime of weak bubble-LIOM coupling. This might have important consequences for the critical bubble size, estimated naively from the ETH arguments presented in Section II, as we discuss in the concluding section below.

3.4 Conclusion

We have assessed the stability of the MBL phase in two and higher dimensions and in the presence of long range interactions, in light of recent arguments that have called this stability into question [70]. Specifically, it was argued that an instability to rare regions of weak disorder occurring naturally in an insulator can trigger an avalanche that would eventually thermalize the entire system.

As a first test of the assumptions underlying the arguments from Ref. [70], we have used an exact diagonalization study of small systems. The numerical calculations modeled an ergodic bubble coupled to a localized system in both one and two dimensional geometries. We found that the numerical results are in excellent agreement with a refined theory of the avalanche based on ETH that also includes corrections due to small system sizes. Thus, our numerical calculations provide further evidence for the validity of the avalanche scenario. The only failure of thermalization in the two dimensional geometry, as well as in the one dimensional geometry with stretched exponential interactions, occurred when the ergodic bubble was below a critical size also predicted by the ETH arguments.

As a second test of the avalanche scenario, we have analyzed an effective model of an ergodic bubble coupled to an Anderson insulator. The goal in this analysis has been to check the assumption, central to the avalanche scenario, that the bubble spectral function does not suffer a significant back-action from coupling to the LIOMs. From the numerical solution of the effective model, we found that even for reasonably weak bubble-LIOM coupling there could be substantial back-action of the insulator onto the bubble, leading to a strong modification of the bubble spectral function.

The back-action of the surrounding insulator on the bubble presents a possible mode of failure of the avalanche for a given bubble size. However, we have seen that the effective coupling that generates the back-action is suppressed by $1/\sqrt{N}$ as we increase the bubble size N. Thus, the avalanche can always recover from the back-action effect if the bubble is sufficiently large. We conclude that the main effect of the back-action is to renormalize the critical bubble size needed to sustain the avalanche. Hence, the system may well be delocalized as predicted by the avalanche arguments [70], but seeing that it is so will require much larger system sizes than predicted by naive arguments based on ETH.

While our analysis generally lends support to the avalanche scenario, it also highlights the unrealistically large thermalization time scales required to observe the instability, even without the back-action effect. Consider a strongly disordered system, deep in the putative insulating phase, such that its localization length is almost vanishing (i.e. much smaller than a lattice constant). The analysis in section 3.2 implies that the minimal bubble size required to sustain an avalanche is $\sim 1/\xi \gg 1$. Bubbles of this size represent extremely rare fluctuations occurring with a frequency that decays at least as $\exp(-2A/\xi^2)$ with decreasing ξ. In other words, the distance between such bubbles is at least $l_b \sim \exp(A/\xi^2)$. This quickly becomes much larger than any reasonable system size; even if the system is large enough, the time for the thermalization avalanche to reach LIOMs that are not close to any of the bubbles is

$$\tau \sim e^{l_b/\xi} = \exp\left[\xi^{-1} e^{A/\xi^2}\right]. \tag{3.32}$$

In other words, the local thermalization time quickly becomes very large (note, however, that ξ is related to the logarithm of the disorder strength: $\xi \sim 1/\log W$). Thus, on practical time scales, systems deep in the MBL state remain localized and do not suffer from this instability. On the other hand, the avalanche instability can have a significant effect in the vicinity of the many-body localization transition, eliminating the sharp phase transition. In future work, it would be interesting to explore how the instability, if it indeed occurs, interrupts the critical scaling and broadens the transition into a crossover.

3.5 Appendix A: Details on the exact diagonalization study

The model we are studying is defined as

$$\mathcal{H} = \mathcal{H}_b + \mathcal{H}_l + \mathcal{H}_{bl}. \tag{3.33}$$

As mentioned in the main text, $\mathcal{H}_b$ is a $2^N \times 2^N$ Hermitian matrix sampled from the Gaussian Orthogonal Ensemble such that the many-body bandwidth $\mathcal{W} = E_{\max} - E_{\min}$ (where $E_{\max}$ and $E_{\min}$ are the largest and smallest eigenvalues, respectively) scales linearly with the system size, i.e. $\mathcal{W} = wN$ and $w \approx 2.6$. For the remainder of the chapter, we place the ergodic quantum dot at the origin and we fix its size to $N = 8$ bath spins defined by the Pauli operators $\sigma^{\{x,y,z\}}$. The insulating region consists of M LIOMs defined by the Pauli operators $\tau^{\{x,y,z\}}$ and the Hamiltonian is given by $\mathcal{H}_l = \sum_{\alpha=1}^{M} \epsilon_\alpha \tau_\alpha^z$, where the local fields ϵ_α are sampled from the uniform distribution on $[0.5, 1.5]$. Lastly, $\mathcal{H}_{bl} = \sum_\alpha V_\alpha \sigma_1^x \tau_\alpha^x$ describes the bubble-insulator coupling and the V_α's depend on the geometry under consideration, as described below.

First, in a $d = 2$ geometry with exponentially decaying couplings, we arrange the LIOMs in concentric layers around the ergodic bubble: the n^{th} layer has a radius $r_n = (n-1)a$ (in units of the inter-layer distance $a = 1$) and it contains n LIOMs such that the insulator-bubble coupling strength is $V_\alpha = V_1 e^{-r_n/\xi}$ for

$$\alpha = \frac{n(n-1)}{2} + 1, ..., \frac{n(n+1)}{2}. \tag{3.34}$$

We set $V_1 = 1$ for the first LIOM and ξ is the localization length. The total number of LIOMs, M, is related to the total number of layers n via $M = \frac{n(n+1)}{2}$. Second, in a $d = 1$ geometry with exponentially decaying couplings we also take $V_\alpha = V_1 e^{-r_\alpha/\xi}$, but $r_\alpha = (\alpha - 1)$ for $\alpha = 1, ..., M$. Third, in a $d = 1$ geometry with stretched exponentials we take $V_\alpha = V_1 e^{-\sqrt{r_\alpha/\xi}}$, where $r_\alpha = (\alpha - 1)$ and $\alpha = 1, ..., M$.

In all three scenarios, we couple up to $M = 6$ LIOMs to the $N = 8$ bubble spins and obtain the many-body eigenstates $|\Psi_n\rangle$ and eigenvalues E_n of the full Hamiltonian: $\mathcal{H}|\Psi_n\rangle = E_n|\Psi_n\rangle$.

Spectral functions

In the main text we have defined the spectral function of a local operator $\mathcal{O}$ in an eigenstate $|\Psi_n\rangle$ via

$$\rho_n(\omega) = 2\pi \sum_{m\neq n} |\langle\Psi_n| \mathcal{O} |\Psi_m\rangle|^2 \delta(\omega - \omega_{mn}), \tag{3.35}$$

where $\omega_{mn} = E_m - E_n$. Note that $\rho_n(\omega)$ obeys a sum rule whereby $\int_{-\infty}^{+\infty} \rho_n(\omega) d\omega = 2\pi\left(1 - \langle\Psi_n| \mathcal{O} |\Psi_n\rangle^2\right) \approx 2\pi$.

For a local operator $\mathcal{O} = \sigma_1^x$ acting in the ergodic region, one expects $\rho_n(\omega)$ to be a smooth function for a thermal eigenstate and a set of narrow peaks for an MBL eigenstate [126]. Moreover, in the MBL case, the narrow peaks occur at different frequencies for different eigenstates even within a given disorder realization. Thus, another diagnostic of localization can be obtained from the "breakdown of typicality" of the eigenstate spectral function. To this end, we define the *typical* spectral function via the geometric mean:

$$\rho_{\text{typ}}(\omega) = \exp\left(\frac{1}{N_A} \sum_n \overline{\log \rho_n(\omega)}\right), \tag{3.36}$$

where, as before, the overline corresponds to disorder averaging and we also average over $N_A = 2^{N+M}/(N+M)$ eigenstates in the middle of the band. For the above equation to be well-defined, we have to consider the limiting cases in which the eigenstate spectral function in a given disorder realization is either zero or a delta function at a frequency $\widetilde{\omega}$. First, if we have $\rho_n(\widetilde{\omega}) = 0$ then we implicitly take $\rho_{\text{typ}}(\widetilde{\omega})$ to be defined as the limit of the right hand side, namely $\rho_{\text{typ}}(\widetilde{\omega}) = 0$. Second, since we are interested in a finite-size system that has a discrete spectrum, we always work with a finite energy binning and we take the bin size to be $2\delta_E$: thus, a delta function peak in a thermodynamic system becomes a narrow peak of width $2\delta_E$ and height $(2\delta_E)^{-1}$ in a finite-size system. Note that a similar prescription is to introduce an even wider "energy smearing" by replacing delta functions with finite-width Lorentzians whose tails give non-zero contributions everywhere. While the two approaches are equally valid, we choose the former since it is computationally faster: see the "Numerical implementation" section below for details.

Thus, if the system is thermal then $\rho_{\text{typ}}(\omega)$ should be non-zero and a smooth function. However, in contrast to the eigenstate spectral function, $\rho_{\text{typ}}(\omega)$ does not have an exact sum rule for $\mathcal{I} = \int_{-\infty}^{\infty} \rho_{\text{typ}}(\omega) d\omega$, but rather an upper bound for $\mathcal{I}$, as detailed in the section below. On the other hand, for an MBL system $\rho_{\text{typ}}(\omega)$ vanishes since $\rho_n(\omega)$ consists of discrete peaks and the peaks occur at different frequencies for different eigenstates even for a single disorder realization.

Bounds on the typical spectral function

Since $\rho_n(\omega) \geq 0$ for all frequencies and n's, we can apply the inequality of arithmetic and geometric means to find that

$$0 \leq \rho_{\text{typ}}(\omega) \leq \frac{1}{N_A} \sum_n \overline{\rho_n(\omega)} = \rho_{\text{th}}(\omega), \tag{3.37}$$

where $\rho_{\text{th}}(\omega)$ is the thermal spectral function at infinite temperature:

$$\rho_{\text{th}}(\omega) = \frac{1}{N_A} \sum_n \overline{\rho_n(\omega)}. \tag{3.38}$$

Defining $\mathcal{I} = \int_{-\infty}^{+\infty} \rho_{\text{typ}}(\omega) d\omega$ we see that

$$0 \leq \mathcal{I} \leq \int_{-\infty}^{+\infty} \rho_{\text{th}}(\omega) d\omega = \frac{1}{N_A} \sum_n \overline{\int_{-\infty}^{+\infty} \rho_n(\omega)} \approx 2\pi. \tag{3.39}$$

Thus, the upper bound for the typical spectral function's sum rule is 2π. Since the geometric and arithmetic means are equal solely when all numbers being averaged are equal, then $\mathcal{I}$ saturates the 2π bound if and only if $\rho_n^{(i)}(\omega) = \rho_m^{(j)}(\omega)$ for any n, m, i, j, where $\rho_n^{(i)}(\omega)$ is the spectral function in an eigenstate $|\Psi_n\rangle$ in the i^{th} disorder realization. Conversely, $\mathcal{I}$ saturates the 2π upper bound when the typical and thermal spectral functions coincide, $\rho_{\text{typ}}(\omega) = \rho_{\text{th}}(\omega)$.

Thus, we expect that in the MBL phase $\mathcal{I} \approx 0$ due to the breakdown of typicality and in the thermal phase $\mathcal{I} \approx 2\pi$.

Numerical implementation

The definition in Eq. 3.36 is reasonable for a thermodynamic system. However, for a finite system and for a finite number of disorder realizations, $\rho_{\text{typ}}(\omega)$ will be dominated by

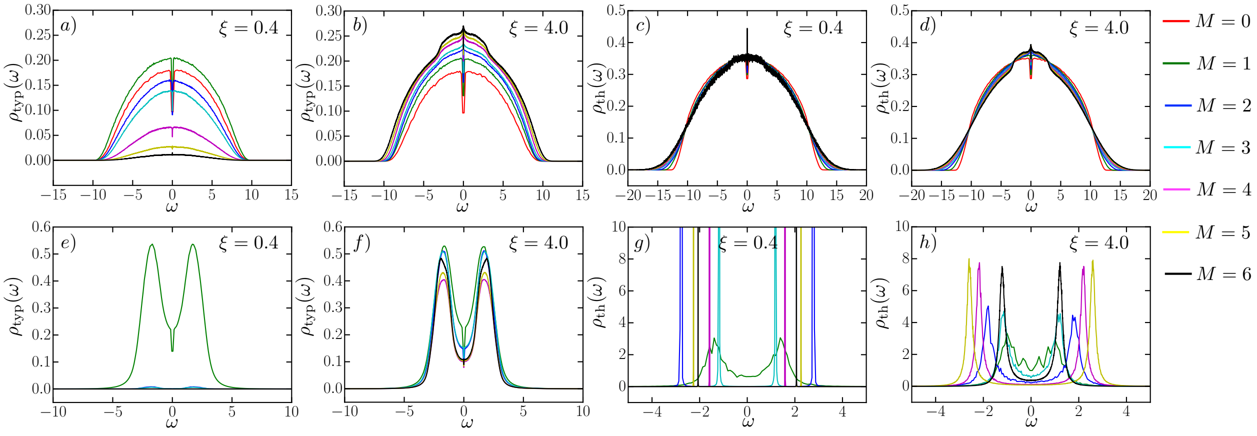

Figure 3.8: (a)-(d) correspond to the spectral functions of a bath spin, whereas (e)-(h) correspond to the spectral functions of a LIOM in a 2D geometry with exponentially decaying couplings. The curves in (a)-(f) have been averaged over N_A eigenstates in the middle of the spectrum and over many disorder realizations. The curves in (g)-(h) correspond to a given disorder realization.

the rare instances in which $\rho_n^{(i)}(\omega) = 0$. To be more precise, suppose we are interested in the value of $\rho_{\mathrm{typ}}(\omega)$ at a given frequency $\omega = \omega_0$ and we are taking the geometric average over $\mathcal{N}$ eigenstate spectral functions ($\mathcal{N}$ is the product of N_A and the number of disorder realizations). Under the definition in Eq. 3.36, if a single number out of these $\mathcal{N}$ values is zero and the remaining $\mathcal{N} - 1 \gg 1$ are non-zero then $\rho_{\mathrm{typ}}(\omega_0) = 0$ which runs counter to our intuition behind "typicality".

As mentioned before, a solution would be to replace delta functions by finite-width Lorentzians whose tails contribute non-zero values everywhere. Since we found this to be computationally slow, we chose the following alternative: we shift all values by 10^{-20}, namely $\rho'_n(\omega) = \rho_n(\omega) + 10^{-20}$. If $p\mathcal{N}$ of these values are zero, $(1-p)\mathcal{N}$ are non-zero, and the geometric average of the non-zero ones is ρ_0, then shifting everything by 10^{-20} gives, to leading order, $\rho'_{\mathrm{typ}}(\omega_0) \approx 10^{-20p}\rho_0^{1-p}$. If $p = 0.01$ then $\rho'_{\mathrm{typ}}(\omega_0) \approx 0.6\rho_0$, i.e. if 1% of the values are zero then our numerically obtained typical spectral function is of the same order of magnitude as ρ_0; if $p = 0.1$ then $\rho'_{\mathrm{typ}}(\omega_0) \approx 0.01\rho_0^{0.9}$, i.e. if 10% of the values are zero then our numerically obtained typical spectral function is two orders of magnitudes smaller than ρ_0. Thus, roughly speaking, "typical" means that $\sim 99\%$ of the eigenstate spectral functions share a given feature of interest.

Bath spectral functions

For illustrative purposes, in Fig. 3.8(a)-(d) we plot examples of both $\rho_{\mathrm{typ}}(\omega)$ and $\rho_{\mathrm{th}}(\omega)$ for local bath operator $\mathcal{O} = \sigma_1^x$ in a $d = 2$ geometry with exponentially decaying coupling

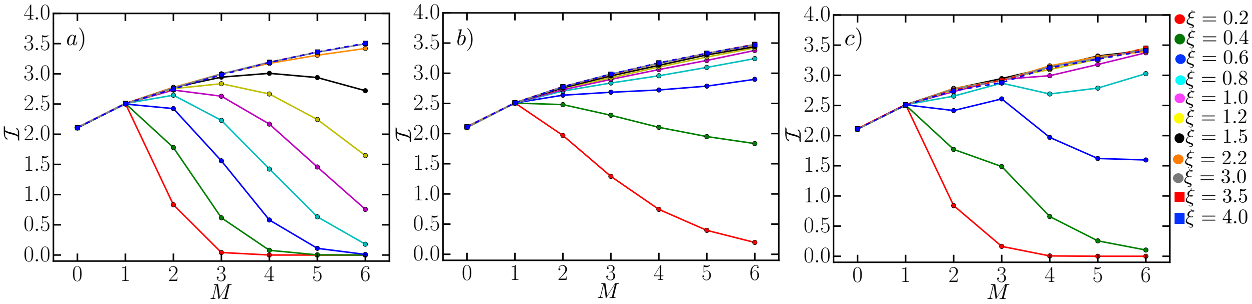

Figure 3.9: The integral over all frequencies for the typical (geometrically averaged over eigenstates and disorder realizations) spectral function of a local operator acting on a bath spin: $\mathcal{I} = \int_{-\infty}^{\infty} \rho_{\text{typ}}(\omega) d\omega$. We plot $\mathcal{I}$ as a function of the LIOMs added and each curve (color) corresponds to a different localization length. (a) Corresponds to a $d = 1$ geometry with exponentially decaying couplings. (b) Corresponds to a $d = 1$ geometry with stretched exponentials. (c) Corresponds to a $d = 2$ geometry with exponentially decaying couplings.

strengths for both small and large localization lengths ξ—we note that qualitatively similar behaviors occur for the $d = 1$ models with exponentials and stretched exponentials.

In Fig. 3.8(a) we can see the collapse of the typical spectral function for a small localization length, $\xi = 0.4$. In Fig. 3.8(c) we plot the *thermal* spectral function for the same parameters and we observe that $\rho_{\text{th}}(\omega)$ is insensitive to the breakdown of typicality. This is due to the fact that $\rho_{\text{th}}(\omega)$ "washes out" the differences between the collections of peaks characterizing different eigenstates, leading to a smooth function that remains more or less unchanged with the addition of LIOMs. As emphasized in the main text, this behavior is consistent with the fact that the thermal spectral function *cannot detect localization*.

We also plot $\rho_{\text{typ}}(\omega)$ and $\rho_{\text{th}}(\omega)$ for a large localization length, $\xi = 4.0$ (Fig. 3.8(b) and (d), respectively). First, in both panels we observe the emergence of a plateau at small frequencies for the largest system sizes. This can be understood as an emergent Thouless energy scale [209]—even though the original ergodic bubble was a zero dimensional quantum dot, adding spatial structure via the LIOMs gives rise to signatures of locality in the bath. Second, we see that the area under the *typical* spectral function increases monotonically with the addition of LIOMs.

As argued in Sec. 3.5, for a thermalizing system, this process will continue until $\rho_{\text{typ}}(\omega) = \rho_{\text{th}}(\omega)$ and $\mathcal{I} \approx 2\pi$. In Fig. 3.9 we further analyze this phenomenon by studying the evolution of $\mathcal{I}$ as a function of the number M of coupled LIOMs for different localization lengths ξ. For a large localization length the integral $\mathcal{I}$ increases monotonically with the successive addition of LIOMs, approaching the upper bound allowed by the spectral sum rule. However, in the regime of small localization lengths, the addition of the first few LIOMs strengthens the bubble by increasing $\mathcal{I}$, but coupling more insulating sites eventually collapses the typical

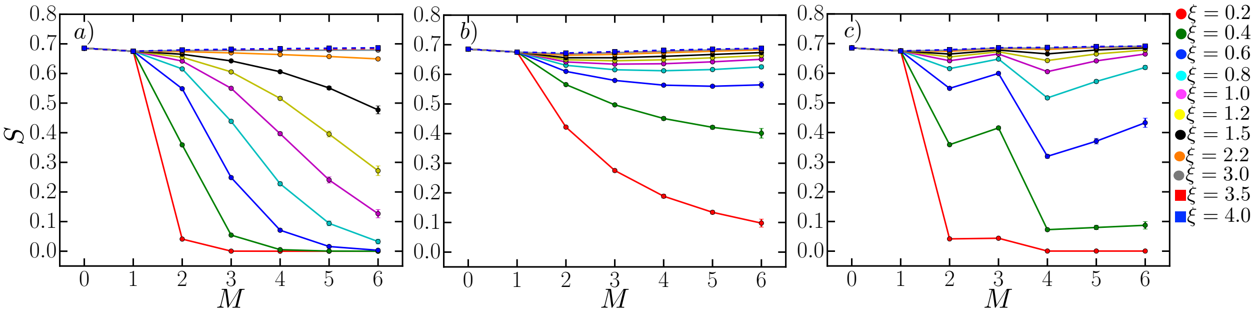

Figure 3.10: The entanglement entropy S of the farthest LIOM coupled to the ergodic bubble as a function of M. Each curve (color) corresponds to a different localization length and we have averaged over N_A eigenstates in the middle of the spectrum and over many disorder realizations. (a) Corresponds to a $d = 1$ geometry with exponentially decaying couplings. (b) Corresponds to a $d = 1$ geometry with stretched exponentials. (c) Corresponds to a $d = 2$ geometry with exponentially decaying couplings.

spectral function, i.e. $\mathcal{I} \to 0$. As mentioned in the main text, this breakdown of typicality is a consequence of the fact that the Fermi Golden Rule (FGR) decay rate for the farthest LIOMs is approximately zero.

LIOM spectral functions

In the main text we have discussed the width γ of the spectral function peaks for a local operator acting on a LIOM, $\mathcal{O} = \tau_M^x$. We now plot in Fig. 3.8(e)-(f) a few examples of these LIOM spectral functions. In particular, in Fig. 3.8(e) and (f) we plot the typical spectral function $\rho_{\text{typ}}(\omega)$ corresponding the farthest LIOM that was coupled to the ergodic region for $\xi = 0.4$ and $\xi = 4.0$, respectively. For a small localization length, we also observe the collapse of the *typical* spectral function [Fig. 3.8(e)], whereas for a large localization length we observe two broad peaks [Fig. 3.8(f)] of equal width.

The structure becomes more transparent when we look at the thermal spectral function of the LIOM farthest from the ergodic region in a *fixed disorder realization* for the local fields $\{\epsilon_\alpha\}$. As shown in Fig. 3.8(g) and (h), the thermal spectral function corresponds to two sharp peaks located at $\pm 2\epsilon_M$, where $1 \leq 2|\epsilon_M| \leq 3$. From these we extract the widths γ and compute the numerical ratio γ/δ_E, as described in the main text, which allows us to check whether the FGR decay rate is non-zero.

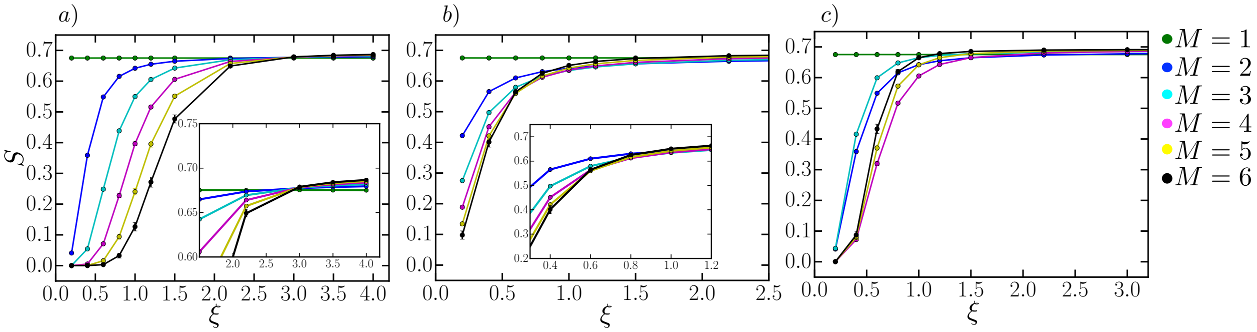

Figure 3.11: The entanglement entropy S of the farthest LIOM coupled to the ergodic region as a function of the localization length ξ. Each curve (color) corresponds to a different total number M of LIOMs (i.e. a different system size). (a) Corresponds to a $d = 1$ geometry with exponentially decaying couplings. (Inset) is a zoom-in around the crossing point $\xi_c \sim 2.9$ between the different curves and this value of ξ_c is in very good agreement with the one obtained in Refs. [158, 70]. (b) Corresponds to a $d = 1$ geometry with stretched exponentials. (Inset) is a zoom-in around $\xi \sim 0.7$ between the curves, showing that there is no crossing (i.e. it is not a transition). (c) Corresponds to a $d = 2$ geometry with exponentially decaying couplings.

Entanglement entropy of the LIOM farthest from the ergodic region

As a final diagnostic, we track the entanglement entropy S of the farthest LIOM coupled to the ergodic bubble. For a many-body eigenstate $|\Psi\rangle$ of the full system we compute the reduced density matrix of the farthest, M^{th}, LIOM: $\rho = \text{Tr}' |\Psi\rangle \langle\Psi|$, where Tr' corresponds to tracing out the other $(N + M - 1)$ degrees of freedom. Then, the entanglement entropy is defined as $S = -\,\text{Tr}\,(\rho \log \rho)$ and takes a value between 0 (no entanglement) and $\log 2$ (fully entangled). In passing, we have explicitly checked that the entanglement entropy of a bath spin is always the maximal $\log 2$ for all ξ's and M's—this suggests that $|\Psi_{\text{bath}}\rangle$ is a fully thermal state for the $N = 8$ spins in the ergodic region regardless of how many LIOMs we couple to it.

As shown in Fig. 3.10, for small enough localization lengths ξ the entanglement entropy eventually collapses, $S \to 0$ as M increases, indicating that LIOMs far away from the bubble will be disentangled. In the case of a 1D insulator, this is due to the fact that an ergodic bubble, regardless of its initial size, cannot sustain the thermalization avalanche indefinitely for localization lengths ξ below the critical value, $\xi < \xi_c = 2/\log 2$. In the case of a 2D insulator or a 1D insulator with sub-exponentially decaying wavefunctions, this is due to the fact that the initial bubble size is not large enough to sustain the avalanche: recall that, in the former case, there exists a critical bubble size $N^* \sim \xi^{-2}$ below which the avalanche is eventually arrested. Since we fix $N = 8$, for small localization lengths, $\xi \lesssim \frac{1}{\sqrt{N}}$, we expect that $S \to 0$ for large enough M. Conversely, for large localization lengths, $\xi \gtrsim \frac{1}{\sqrt{N}}$, we see that $S \to \log 2$ for large enough M (see Fig. 3.10).

Secondly, we note that the behavior of S exhibits signatures of the 2D geometry, as shown in Fig. 3.10(a): the entropy slightly increases for LIOMs within a given layer, but it sharply drops as we move on to the next layer.

Similarly, in Fig. 3.11 we plot $S(\xi)$ for different Ms (system sizes). For the 2D geometry or the 1D geometry with stretched exponentials, we observe a crossover between no entanglement ($S = 0$) and maximally entangled ($S = \log 2$) as a function of the localization length, as shown in Fig. 3.11. For the $d = 1$ model with exponentially decaying couplings [Fig. 3.11(b)] we find that there is a crossing between the $S(\xi)$ curves corresponding to different system sizes (Ms) that occurs at $\xi_c \sim 2.9$. Ref. [158], which has shown extensive numerical data for this geometry, found that there exists a *transition* at $\xi_c = \frac{2}{\log 2} \approx 2.88$ which is in very good agreement with our results.

Lastly, we have also analyzed the average ratio

$$\overline{r}(\xi) = \frac{\min\{\Delta E_k, \Delta E_{k+1}\}}{\max\{\Delta E_k, \Delta E_{k+1}\}}, \tag{3.40}$$

where $\Delta E_k = E_{k+1} - E_k$, and found a behavior very similar to that of $S(\xi)$. Naturally, we find that there is no such crossing and transition for the $d = 1$ model with stretched exponentials or the $d = 2$ model.

Chapter 4

Integrable and chaotic dynamics of spins coupled to an optical cavity

As mentioned in Chapter 1, significant progress has been made in describing the scrambling of information through quantum chaos, which allows effectively irreversible dynamics to emerge from unitary quantum time evolution. Notably, Maldacena *et al.*, inspired by the chaotic properties of black holes, established that quantum mechanics places an upper bound on the Lyapunov exponent that characterizes the growth of chaos [162]. In a related development, Kitaev constructed a class of quantum many-body models whose dynamics saturates this bound on chaos [137, 163] and can be related to black holes through the AdS/CFT correspondence [200, 123, 225]. The fact that these models admit controlled solutions, despite being chaotic, has further conferred on them a paradigmatic status within the field of quantum dynamics.

Finding accessible systems which realize such models is therefore highly desirable, but also, *a priori*, very challenging: a common feature shared by all of these maximally chaotic, holographic models is that they lack spatial locality, since they couple together an extensive number of degrees of freedom. For instance, the Sachdev-Ye (SY) model [201] was originally proposed as a quantum spin model with random all-to-all couplings:

$$H = \frac{1}{\sqrt{NM}} \sum_{i,j=1}^{N} U_{ij} \mathbf{S}_i \cdot \mathbf{S}_j, \tag{4.1}$$

where $\mathbf{S}_i$ are SU(M) spin operators. A fermionic variant, the Sachdev-Ye-Kitaev (SYK) model, was subsequently introduced by Kitaev.

While infinite-range spin interactions do not occur in magnetic materials, they can be realized rather naturally in cold atomic ensembles coupled to an optical cavity mode [40, 161, 152, 156, 27, 113, 140, 151, 176, 141, 144, 139, 105, 69, 47]. In this setup, the delocalized cavity mode mediates infinite-range interactions between the internal states of atoms through the local coupling at each site, regardless of the distance between atoms [17, 221, 203, 102, 116, 165, 170, 64, 169]. However, there is a crucial difference, already pointed out in

Ref. [164], between the interactions in the SY model and the ones mediated by the cavity. The second-order process that couples the atomic degrees of freedom via the cavity mode gives a separable (rank-1) matrix $U_{ij} = J_i J_j$, rather than the full-rank matrix assumed in the different variants of the SY model. Although non-separable interactions are, in principle, accessible in multi-mode cavities [102, 227, 230, 140, 151, 164, 105], separable all-to-all couplings are realized in numerous existing experiments [152, 113, 141, 144, 176, 69, 47, 139] and arise generically for interactions mediated by a single bosonic mode.

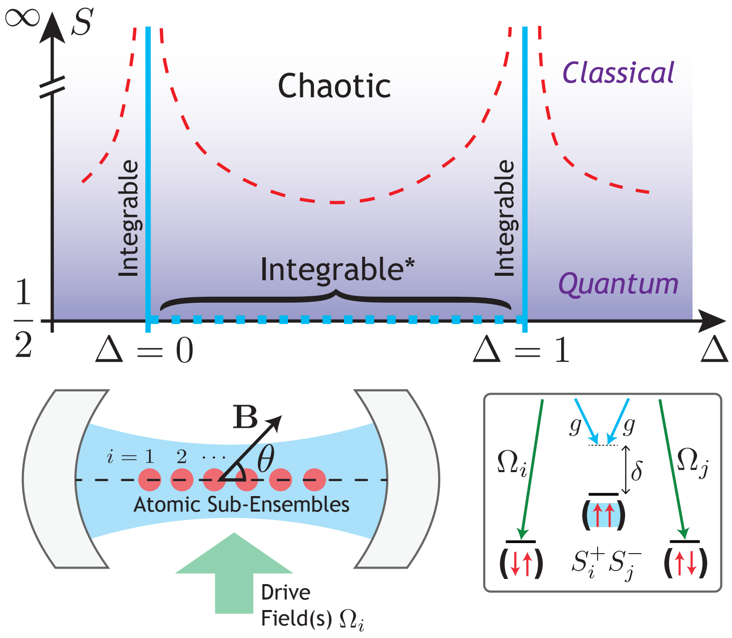

Figure 4.1: (top) The dynamical phase diagram of the model (4.2) in the plane of the spin size S and anisotropy Δ. The main features are: the integrable lines at $\Delta = 0$ and $\Delta = 1$ (solid blue); the novel integrable line at $S = 1/2$ (dotted blue and marked by an asterisk); and the onset of chaos at large S, indicated schematically by the dashed red curves. (bottom) Schematic of the atomic sub-ensembles (red) trapped inside a single-mode optical cavity (blue). A drive field (green) at a detuning δ from the cavity resonance generates effective spin-spin interactions between the atoms (bottom right). The tunable angle θ between the spin quantization axis (along the applied magnetic field $\mathbf{B}$) and the cavity's longitudinal axis leads to an anisotropy $\Delta = 2\cot^2\theta$. By changing the local atomic density in a region of constant coupling to the cavity mode, the effective spin size S can also be varied, allowing for the systematic exploration of the full phase diagram.

Moreover, this ostensible limitation of the cavity-QED scheme turns out to be a boon: the separability of the interaction is responsible for an even richer dynamical phase diagram (see Fig. 4.1), which includes regions of chaos, Gaudin-type integrability characterized by spin-bilinear conserved quantities, and of a novel form of integrability—labeled Integrable* in Fig. 4.1—with *quasi*-bilinear integrals of motion.

The class of models we consider in this chapter is described by the following quantum spin Hamiltonian:

$$H = \frac{1}{S\sqrt{N}} \sum_{i,j=1}^{N} J_i J_j \left(S_i^x S_j^x + S_i^y S_j^y + \Delta S_i^z S_j^z \right), \tag{4.2}$$

where $\mathbf{S}_i$ are SU(2) spin-S operators encoded in the magnetic sub-levels of individual atoms or atomic sub-ensembles located at sites $i = 1, \ldots, N$. The site-dependent coefficients J_i are determined by the local coupling of the atoms at site i to the spatially-varying cavity mode, or by the local Rabi frequency Ω_i of an inhomogeneous drive field. The non-uniformity of the couplings J_i is a crucial element of the models under consideration. For perfectly uniform couplings ($J_i = \overline{J}$), the model is integrable and exactly solvable in terms of the macroscopic spin $\boldsymbol{\mathcal{F}} = \sum_i J_i \mathbf{S}_i$. The $S^x S^x$ and $S^y S^y$ terms in (4.2) describe spin-exchange interactions between pairs of atoms, mediated by virtual cavity photons, while the $S^z S^z$ terms describe state-dependent ac Stark shifts. The normalization of H, which is not important for the dynamical properties, ensures that the high-temperature specific heat and free energy have a proper thermodynamic limit (see Appendix Section 4.10).

The dynamical phases generated by this non-local spin model, shown in Fig. 4.1, are accessible via two experimentally tunable parameters. The spin-anisotropy parameter Δ, controlling the relative strength of the spin-exchange and $S^z S^z$ interactions, can be tuned by changing the angle of an applied magnetic field $\mathbf{B}$ (see Fig. 4.1). In addition, it is possible to control the strength of quantum effects by changing the spin size S on each site. While the choice of internal atomic states provides some flexibility in varying S, a larger range of spin sizes can be achieved by varying the number of atoms trapped at each site and letting S_i^α represent the collective spin of the sub-ensemble at site i. This enables the tuning of quantum effects from semi-classical dynamics at large S all the way down to a spin-1/2 system that is dominated by quantum fluctuations. In combination with the possibility of varying the anisotropy Δ, this tunability allows for a thorough exploration of the dynamical phase diagram.

The chapter and the presentation of the various regimes shown in Fig. 4.1 are organized as follows. We provide a brief overview of these dynamical phases in Section 4.1 and we emphasize the novel features, which constitute our main results. In Section 4.2 we describe in detail the proposed experimental scheme to realize and control the couplings of the Hamiltonian (4.2). We also describe ways of inducing perturbations that go beyond separable interactions. In Section 4.3 we begin the derivation of the main results. We analytically construct the integrals of motion that demonstrate the integrability of the dynamics at the special points $\Delta = 0$ and $\Delta = 1$. In Section 4.4 we present a computational method for finding integrals of motion using numerical or experimental data. In Section 4.5 we deploy this technique and provide numerical evidence for the existence of a novel quantum integrable regime away from the special points $\Delta = 0, 1$. Specifically, we present an exact diagonalization study of the spin-1/2 model, showing that the integrable structure persists for anisotropy values $\Delta \neq 0, 1$ away from the integrable points, with quasi-bilinear integrals of motion. In Section 4.6 we simulate the classical model ($S \to \infty$) and show that it becomes chaotic, albeit in the presence of slowly decaying modes, away from the special points. In Section 4.7 we discuss experimental limitations and assess the extent to which the various features of the model are accessible in the presence of dissipation. Finally, in Section 4.8 we comment on the implications of these results before concluding.

4.1 Overview of the phase diagram

The best understood part of the dynamical phase diagram in Fig. 4.1 is the line at $\Delta = 1$, for all spin sizes S, on which the Hamiltonian from Eq. 4.2 is equivalent to a rational Gaudin model [93]. This model is quantum integrable in the mathematical sense of possessing an underlying quantum group structure [216]. In the context of Gaudin-type models, quantum integrability is characterized by the existence of an extensive family of commuting, *bilinear* conserved quantities and there exist analytical expressions for each one. Even though there is no notion of spatial locality, the conserved quantities are “2-local” in the complexity theory sense [136, 7]. By interchanging commutators with Poisson brackets, it follows that the integrable structure persists in the classical limit.

We find that the model is integrable at $\Delta = 0$ as well. We obtain analytical expressions for an extensive family of conserved quantities that are also bilinear in spin. As in the case of $\Delta = 1$, this integrability holds for any value of S, including the classical limit $S \to \infty$. The integrability of the model at $\Delta = 0$ is connected to the existence of a non-standard class of Gaudin models [24, 217, 205, 220, 218, 219, 160, 62].

However, the most surprising part of the phase diagram occurs away from these integrable points, i.e. in the regions $\{\Delta < 0\}$, $\{0 < \Delta < 1\}$, and $\{\Delta > 1\}$. There, we find a novel integrable structure that is markedly different from the type of integrability found at the two integrable points, $\Delta = 0$ and $\Delta = 1$. First, unlike the latter, integrability for $\Delta \neq 0, 1$ appears to depend crucially on the spin size S. We show strong evidence that the model is integrable for a spin-1/2 system, while it is chaotic with a finite Lyapunov exponent λ_L in the classical limit ($S \to \infty$). Nevertheless, in this latter limit, we also find that there exist modes that relax only on time scales much larger than λ_L^{-1}. We conjecture that this is a consequence of the “quasi-integrable” nature [99] of the classical model. The putative transition from quantum integrable to (semiclassical) chaotic dynamics, schematically shown in Fig. 4.1, can be probed experimentally.

Second, the integrals of motion (IOM) of the $S = 1/2$ model at $\Delta \neq 0, 1$ are not bilinear (or 2-local), but may instead be termed *quasi*-bilinear. We present compelling numerical evidence that each IOM has appreciable support in the space of bilinear spin operators that does *not* depend on the system size N. The fact that the integrals of motion persist while developing tails of multi-spin terms on top of the dominant two-spin contribution is reminiscent of the quasi-local integrals of motion that characterize Many-Body Localized phases [238, 211, 117, 56, 196].

4.2 Proposed experimental scheme

As advertised, the full phase diagram of Fig. 4.1a can be accessed in experiments with atomic ensembles in single-mode optical cavities. In such experiments, each spin is encoded in internal states of an individual atom. The cavity generically couples to a weighted collective spin

$$\boldsymbol{\mathcal{F}} \equiv \sum_i \xi_i \mathbf{S}_i, \tag{4.3}$$

where each weight ξ_i is set by the amplitudes of the cavity mode and drive field at the position of the i^{th} atom. Experiments to date have realized either Ising interactions [152, 113, 47, 144, 141] $H \propto \mathcal{F}_z^2$ or spin-exchange interactions [176, 69] $H \propto \mathcal{F}_+\mathcal{F}_-$, in the latter case directly imaging the spatial dependence of the weights ξ_i and the resulting spin dynamics [69]. We now show how to extend the approach of Ref. [69] to realize generic XXZ models of the form

$$H \propto \mathcal{F}_x\mathcal{F}_x + \mathcal{F}_y\mathcal{F}_y + \Delta\mathcal{F}_z\mathcal{F}_z, \tag{4.4}$$

where the anisotropy Δ is tuned by the angle of a magnetic field. An alternative approach to engineering Heisenberg models has been proposed in Ref. [169].

The experimental setup proposed here is shown in Fig. 4.1b. We consider spins encoded in Zeeman states of atoms whose positions in the cavity are fixed by a deep optical lattice. A magnetic field $\mathbf{B} = B\hat{z}$, which defines the quantization axis for the spins, is oriented at an angle θ to the longitudinal axis $\hat{c}$ of the optical cavity. Driving the atoms with a control field, incident either through the cavity or from the side, allows pairs of atoms to interact by scattering photons via the cavity. The interaction strengths are governed by the spatially dependent Rabi frequency Ω_i of the control field and vacuum Rabi frequency $2g_i$ of the cavity, where i denotes the value for the i^{th} atom.

For large detuning between the atomic and cavity resonances, the atom-cavity interaction takes the form of a Faraday effect in which each atom couples to the Stokes vector $\mathbf{I}_i$, representing the local polarization and intensity of light. This effect is described by a Hamiltonian

$$H_I = 2\chi \sum_i (\mathbf{I}_i \cdot \hat{c})(\mathbf{S}_i \cdot \hat{c}), \tag{4.5}$$

where χ is the vector ac Stark shift of a maximally coupled atom and the component of the Stokes vector along the cavity is $\mathbf{I}_i \cdot \hat{c} = (A^\dagger_{+,i}A_{+,i} - A^\dagger_{-,i}A_{-,i})/2$. The field operators

$$A_{\pm,i} = \left(\frac{\Omega_i e^{-i\delta t}}{2\sqrt{2}} + g_i a_\pm\right)/g \tag{4.6}$$

include the quantum field $a_\pm$ of the cavity for $\sigma_\pm$-polarized modes, weighted by the local amplitude g_i of the cavity mode, and displaced by a classical drive field with local Rabi frequency Ω_i. The normalization is set by the vacuum Rabi frequency $2g$ of a maximally-coupled atom. We assume that the drive field has horizontal polarization $\hat{x} = \hat{z} \times \hat{c}$ and is detuned by δ from the cavity resonance.

In the limit where the drive field is weak and far detuned, we can obtain an effective Hamiltonian for the spin dynamics by adiabatically eliminating the photon modes. To this end, we first expand H_I to lowest order in the operators $a_\pm$ to obtain

$$H_I \approx \frac{i}{2}\chi\left(\xi_i^* v e^{i\delta t} - \xi_i v^\dagger e^{-i\delta t}\right)(\mathbf{S}_i \cdot \hat{c}), \tag{4.7}$$

where $v = (a_+ - a_-)/\sqrt{2}$ represents the vertically polarized cavity mode, and we have introduced the weights

$$\xi_i = \frac{\Omega_i g_i^*}{g^2}. \tag{4.8}$$

These weights determine the collective spin $\mathcal{F}$ defined in Eq. 4.3, which couples to the cavity mode. Then, for $\langle v^\dagger v\rangle \ll 1$ and for large detuning $\delta \gg \kappa, \omega_Z$ compared to the cavity linewidth κ and Zeeman splitting ω_Z, we find that the effective spin Hamiltonian is

$$H = \frac{\chi^2}{4\delta}\left[\cos^2\theta \mathcal{F}^z\mathcal{F}^z + \frac{1}{2}\sin^2\theta\left(\mathcal{F}^x\mathcal{F}^x + \mathcal{F}^y\mathcal{F}^y\right)\right], \tag{4.9}$$

as detailed in the Appendix 4.9. We see that Eq. 4.9 matches the Hamiltonian (4.2) with couplings $J_i = \chi\xi_i S^{1/2}N^{1/4}\sin\theta/2\sqrt{2\delta}$ and anisotropy $\Delta = 2\cot^2\theta$. Note that arbitrary control over the set of weights ξ_i can be obtained by designing the spatial dependence of the control field.

In addition to the coherent dynamics generated by H from Eq. 4.9, the cavity-mediated interactions are subject to dissipation due to photon loss from the cavity mirrors and atomic free-space scattering. Formally, these processes can be described by a family of Lindblad operators acting within a quantum master equation (see Appendix 4.9). The key parameter governing the interaction-to-decay ratio is the single-atom cooperativity $\eta = 4g^2/\kappa\Gamma$, where Γ is the atomic excited-state linewidth. Moreover, we find that the interaction-to-decay ratio is collectively enhanced, scaling as $S\sqrt{N\eta}$ for a system of N sub-ensembles consisting of S atoms each.

After we discuss the various properties and measurable signatures of chaotic and integrable dynamics in (4.2), we shall return to quantifying the effects of dissipation in Section 4.7. In particular, we will estimate the atom number and cooperativity η requisite for observing these signatures in the experimental setup.

4.3 Integrability at $\Delta = 0$ and $\Delta = 1$

In this section, we demonstrate the quantum integrability of the Hamiltonian (4.2) along the two lines at $\Delta = 0$ and $\Delta = 1$ in the dynamical phase diagram (Fig. 4.1). To place our discussion in context for the non-specialist reader, we begin by recalling some key features of integrable many-body systems. Broadly speaking [1], such systems are characterized by an

---

[1] For a comprehensive discussion of the subtleties involved in achieving a generally valid definition of quantum integrability, see Ref. [55].

extensive number of local conservation laws that give rise to exotic transport and thermalization properties. Important examples of quantum integrable systems include the Lieb-Liniger Bose gas and the spin-1/2 Heisenberg chain.

To illustrate the main ideas, consider a one-dimensional, local, quantum Hamiltonian $H = \sum_{n=1}^{N} h_n$, on N lattice sites. For this type of model, integrability means the existence of $N-1$ independent, local charges,

$$Q^{(n)} = \sum_{i=1}^{N} q_i^{(n)}, \quad n = 2, \dots, N, \tag{4.10}$$

that commute with each other and with the Hamiltonian, namely

$$[Q^{(m)}, Q^{(n)}] = 0, \quad [Q^{(m)}, H] = 0. \tag{4.11}$$

The existence of extensively many local conservation laws can be regarded as a strong constraint on the dynamics of such systems, and leads to unusual physical effects such as non-dissipative heat transport[251] and equilibration to non-thermal steady-states[195, 28].

In contrast with more standard integrable systems, the Gaudin-type models that arise in the present chapter are somewhat unusual, since they exhibit non-local couplings and are therefore essentially zero-dimensional. To construct these models, one starts from a set of N operators,

$$G^{(i)} = \sum_{j=1}^{N} \sum_{\alpha=1}^{3} w_{ij}^{\alpha} S_i^{\alpha} S_j^{\alpha}, \quad i = 1, 2, \dots, N, \tag{4.12}$$

that are linear combinations of spin bilinears, with real coefficients $w_{ij}^{\alpha} \in \mathbb{R}$, and satisfy the defining commutation relations:

$$[G^{(i)}, G^{(j)}] = 0. \tag{4.13}$$

The physical Hamiltonian and the independent conserved charges are then given by linear combinations of the $G^{(i)}$, of the form

$$H = \sum_{i=1}^{N} a_i^{(0)} G^{(i)}, \quad Q^{(n)} = \sum_{i=1}^{N} a_i^{(n)} G^{(i)}, \quad n = 2, \dots, N, \tag{4.14}$$

where the coefficients $a_i^{(n)} \in \mathbb{R}$ are elements of a non-singular N-by-N matrix. Note that by the commutation relations (4.13), the Hamiltonian H and its associated charges $Q^{(n)}$ automatically satisfy the commutation relations (4.11) required for integrability. Although these operators are not local, they are sums of spin bilinears and can therefore be regarded as "2-local" in the complexity theory sense.

We now show that the Hamiltonian Eq. (4.2) defines a Gaudin-type integrable model for $\Delta = 0$ and $\Delta = 1$ and all values of spin S. Specifically, we will demonstrate that along these lines in the dynamical phase diagram Fig. 4.1, there exist $N-1$ independent, conserved and mutually commuting spin bilinears. The Hamiltonian at $\Delta = 1$ is related to the rational Gaudin model [93], which is well-known to be quantum integrable in the mathematically rigorous sense of possessing an underlying quantum group structure [216]. Meanwhile, the Hamiltonian at $\Delta = 0$ lies in a less well-known class of "non-skew" Gaudin models, which arise from Gaudin's equations upon relaxing the constraint of antisymmetry under interchange of site indices [24, 217, 205, 220, 218, 219, 160, 62].

It will be helpful to review the problem first studied by Gaudin [93]: under what circumstances do a set of spin bilinears, as in Eq. (4.12), define a mutually commuting set, with $[G^{(i)}, G^{(j)}] = 0$? If the couplings $w_{ij}^{\alpha} \in \mathbb{R}$ are taken to be antisymmetric under interchange of indices, with $w_{ij}^{\alpha} + w_{ji}^{\alpha} = 0$, then the $G^{(i)}$ mutually commute if and only if the *Gaudin equations*

$$w_{ij}^{\alpha} w_{jk}^{\gamma} + w_{ji}^{\beta} w_{ik}^{\gamma} - w_{ik}^{\alpha} w_{jk}^{\beta} = 0, \tag{4.15}$$

hold for all pairwise distinct $\{i, j, k\}$ and $\{\alpha, \beta, \gamma\}$. The isotropic solution $w_{ij}^{\alpha} = J_i J_j/(J_i - J_j)$ defines the *rational Gaudin Hamiltonians*

$$G^{(i)}(\vec{J}\,) = \sum_{j \neq i} \frac{J_i J_j}{J_i - J_j} \mathbf{S}_i \cdot \mathbf{S}_j. \tag{4.16}$$

The all-to-all spin model from Eq. 4.2 at $\Delta = 1$ is simply a linear combination of rational Gaudin Hamiltonians and Casimirs, to wit

$$H = \sum_{i,j=1}^{N} J_i J_j \mathbf{S}_i \cdot \mathbf{S}_j = \sum_{i=1}^{N} 2 J_i G^{(i)}(\vec{J}) + J_i^2 \mathbf{S}_i \cdot \mathbf{S}_i. \tag{4.17}$$

By rotational symmetry, H conserves the total spin $\mathbf{S}_{\text{tot}} = \sum_i \mathbf{S}_i$, and the linear span of the $G^{(i)}(\vec{J}\,)$ includes the squared spin $\mathbf{S}_{\text{tot}} \cdot \mathbf{S}_{\text{tot}} = \sum_{i,j} \mathbf{S}_i \cdot \mathbf{S}_j$. The mathematical structure of traditional Gaudin models has been studied in depth [216, 82].

Let us now consider relaxing the constraint of antisymmetric couplings. Then Gaudin's equations (4.15) must be augmented by two equations constraining "on-site" couplings, which read

$$\begin{aligned} (w_{ij}^{\beta} w_{ji}^{\gamma} - w_{ji}^{\beta} w_{ij}^{\gamma}) + 2 w_{ji}^{\alpha}(w_{ii}^{\gamma} - w_{ii}^{\beta}) = 0, \\ (w_{ij}^{\alpha} w_{ji}^{\gamma} - w_{ji}^{\alpha} w_{ij}^{\gamma}) + 2 w_{ji}^{\beta}(w_{ii}^{\gamma} - w_{ii}^{\alpha}) = 0. \end{aligned} \tag{4.18}$$

The model from Eq. 4.2 at $\Delta = 0$ arises from an "non-skew XXZ" solution $w_{ij}^1 = w_{ij}^2 = J_i J_j/(J_i^2 - J_j^2)$, $w_{ij}^3 = J_j^2/(J_i^2 - J_j^2)$ to the usual Gaudin equation (4.15), augmented by onsite terms $w_{ii}^1 = w_{ii}^2 = 1/2$, $w_{ii}^3 = 0$, which solve Eq. 4.18. The corresponding Gaudin Hamiltonians read

$$\widetilde{G}^{(i)}(\vec{J}\,) = \sum_{j \neq i} \frac{J_i J_j}{J_i^2 - J_j^2} \left(S_i^x S_j^x + S_i^y S_j^y\right) + \frac{J_j^2}{J_i^2 - J_j^2} S_i^z S_j^z + \frac{1}{2}\left(S_i^x S_i^x + S_i^y S_i^y\right). \tag{4.19}$$

By the Gaudin equations Eq. 4.15 and Eq. 4.18, these mutually commute and the Hamiltonian (4.2) at $\Delta = 0$ can be expressed as

$$H = \sum_{i,j=1}^{N} J_i J_j (S_i^x S_j^x + S_i^y S_j^y) = \sum_{i=1}^{N} 2J_i^2 \widetilde{G}^{(i)}(\vec{J}\ ). \tag{4.20}$$

At spin-1/2, this coincides with the Hamiltonian obtained in Ref. [160] or the "Wishart-SYK" model [121], and can consequently be derived as a special case of the integrable spin-1/2 Hamiltonians considered in the recent work Ref. [62]. The integrability of (4.20) for arbitrary spin S was first discussed in Refs. [220, 218, 219] (see also the references therein). We conclude that there is an integrable line in the phase diagram of the model (4.2) at $\Delta = 0$. By rotational symmetry about the z-axis, this Hamiltonian conserves $S^z_{\text{tot}} = \sum_i S_i^z$ and $(S^z_{\text{tot}})^2$ lies in the linear span of the $\widetilde{G}^{(i)}(\vec{J}\ )$. Finally, we note that upon replacing commutators with Poisson brackets in the derivation of the Gaudin equations, the integrable structure identified for $\Delta = 0$ and $\Delta = 1$ remains unaltered in the classical limit ($S \to \infty$) of the Hamiltonian.

4.4 Extracting integrals of motion from numerical or experimental data

Having characterized the integrable structure for $\Delta = 0$ and $\Delta = 1$, it is natural to ask whether the integrability of (4.2) extends to other, more generic, values of the anisotropy: can we find similar extensive sets of commuting bilinear conserved charges for $\Delta \neq 0, 1$? To tackle this question in the absence of analytical tools, such as those used in the previous section, we develop a numerical method that enables the systematic search for bilinear (2-local) integrals of motion (IOM). We emphasize that this novel technique can be applied to either numerical or experimental data.

Let us first define a set of 2-local operators $\{\hat{O}_a\}$:

$$\hat{O}_a \equiv \frac{3}{S(S+1)} \hat{S}_i^\alpha \hat{S}_j^\alpha, \tag{4.21}$$

where $i > j$ and the index a is a shorthand notation for (i, j, α). We note that this family of $3N(N-1)/2$ operators defines an orthonormal set with respect to the infinite-temperature inner product:

$$\frac{1}{\mathcal{D}} \text{Tr}[\hat{O}_a^\dagger \hat{O}_b] = \delta_{ab}, \tag{4.22}$$

where $\mathcal{D} \equiv \text{Tr}[\mathbf{1}] = (2S+1)^N$ is the dimension of the Hilbert space.

Now suppose that we can measure, experimentally or numerically, the time evolution of the expectation value $\langle \hat{O}_a(t) \rangle \equiv \langle \Phi | \hat{O}_a(t) | \Phi \rangle$, where $|\Phi\rangle$ is a random initial state (i.e. far from any energy eigenstate). A bilinear integral of motion $\hat{I}$ is a special linear combination of the $\hat{O}_a$ that remains constant in time, to wit

$$\langle \hat{I} \rangle = \langle \hat{I}(t) \rangle \equiv \sum_a u_a \langle \hat{O}_a(t) \rangle = \sum_a u_a \overline{\langle \hat{O}_a \rangle}. \tag{4.23}$$

Here and below, the overline denotes a time average, such as $\overline{\langle \hat{O}_a \rangle} \equiv \int_0^T \frac{dt}{T} \langle \hat{O}_a(t) \rangle$ over a time interval $[0, T]$. It is useful to recast the above equation in terms of the following time series matrix:

$$M_{a,t} \equiv \sqrt{\frac{1}{T}} \left(\langle \hat{O}_a(t) \rangle - \overline{\langle \hat{O}_a \rangle} \right) . \tag{4.24}$$

Note that $M_{a,t}$ is a rectangular matrix with $3N(N-1)/2$ rows and a continuum of columns indexed by $t \in [0, T]$, where $TJ^2 \gg 1$. In practice, the time axis is discretized such that the number of columns in M is much larger than the number of rows. We immediately see that, by Eq. 4.23, a 2-local IOM corresponds to a left zero mode of M, i.e. $\sum_a u_a M_{a,t} = 0$ for any t.

Thus, to find bilinear IOMs, we want to search for zero modes of M. More generally, we can consider the singular value decomposition (SVD) of M, or equivalently, the spectrum of the real Hermitian matrix

$$L_{a,b} \equiv M M^\dagger = \int_0^T \frac{dt}{T} M_{a,t} M_{b,t} = \sum_{l=1}^{3N(N-1)/2} \sigma_l^2 u_{a,l} u_{b,l} \, . \tag{4.25}$$

In the second line, $\sigma_l \geq 0$ are the corresponding singular values of M and σ_l^2 are the eigenvalues of L; $\vec{u}_l$ are the left singular vectors of M and eigenvectors of L. Equivalently, $(u_{a,l})_{a,l=1}^{3N(N-1)/2}$ is a real orthogonal matrix, defining a family of operators

$$\hat{Q}_l \equiv \sum_{a=1}^{3N(N-1)/2} u_{a,l} \hat{O}_a \, , \; l = 1, \ldots, 3N(N-1)/2 \, , \tag{4.26}$$

which are also orthonormal:

$$\frac{1}{\mathcal{D}} \mathrm{Tr}[\hat{Q}_l^\dagger \hat{Q}_k] = \delta_{lk} \, . \tag{4.27}$$

As mentioned above, Q_l is an integral of motion if and only if $\sigma_l = 0$. Furthermore, for small $\sigma_l > 0$, we consider Q_l to be approximately conserved and call it a “slow mode.” The rationale for this terminology comes from the identity

$$\overline{\langle Q_l(t) \rangle^2} - \overline{\langle Q_l(t) \rangle}^2 = \sigma_l^2, \tag{4.28}$$

which means that the singular value σ_l is the standard deviation of the expectation value of Q_l over the time interval $[0, T]$. A small σ_l entails that $\langle Q_l(t) \rangle$ exhibits small fluctuations around its time-average value.

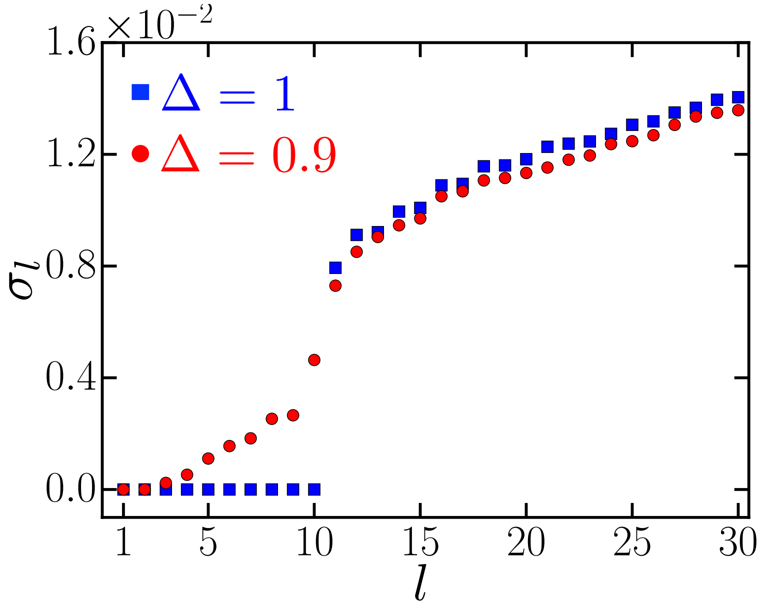

Figure 4.2: Scatter plot of the smallest 30 of the $3N(N-1)/2$ singular values σ_l at $N=9$ for $\Delta = 1$ (blue squares) and $\Delta = 0.9$ (red circles) in a fixed disorder realization of $\{J_i\}$. At $\Delta = 1$, we see $N+1$ zeros corresponding to the $N+1$ conserved charges that can be written as a sum over bilinear operators; these zeros are separated from the rest of the singular values by a "spectral" gap. At $\Delta = 0.9$, we see two zeros corresponding to the conservation of H and $(S^z_{\mathrm{tot}})^2$. We also see the lift-off of $N-2$ singular values corresponding to the previously conserved bilinear charges at $\Delta = 1$. Note that they, too, are separated from the rest by a "spectral" gap.

To summarize, we propose the following procedure: compute the time series matrix M, perform an SVD decomposition on M, analyze its singular values, and identify the possible IOMs and slow modes. In the next two sections, we use this method to characterize the behavior of the model along the $S = 1/2$ and $S \to \infty$ lines in the phase diagram of Fig. 4.1, for anisotropies $\Delta \neq 0, 1$. In Section 4.5, we numerically simulate the time evolution for the quantum spin-$1/2$ model and we further characterize the resulting slow modes by measuring their temporal auto-correlation functions. In Section 4.6, we simulate the dynamics of the model (4.2) describing classical spin degrees of freedom and, upon slightly modifying the above method, we extract the behavior of the auto-correlation functions directly from the singular values.

4.5 Integrability* for $S = \frac{1}{2}$

Identifying integrals of motion

We now focus on the spin-1/2 system with up to $N = 14$ sites and implement the technique proposed above. We initialize the system in a random product state [2] $|\Phi\rangle$ and numerically compute the time evolution of the wavefunction with the Hamiltonian (4.2) via exact diagonalization. The random fields J_i are sampled from the normal distribution $\mathcal{N}(0, J^2)$ and we set $J^2 = 1$. We have checked that we obtain similar results for other distributions with zero mean and unit variance. We then record the expectation values of all the operators $\hat{O}_a$ defined in Eq. 4.21 and construct the time series matrix $M_{a,n}$ (defined in Eq. 4.24) at each discrete time $t_n = n\delta t$ with $\delta t = 1\ J^{-2}$, integer n, and up to a maximal time $T = 10^3 J^{-2}$.

Fig. 4.2 presents results for the singular values of M obtained for two values of Δ in a fixed disorder realization. As expected, at $\Delta = 1$ we find $N + 1$ vanishing singular values, in agreement with the analysis of Section 4.3. All other singular values lie above a gap of about 0.01, indicating that there are no other 2-local integrals of motion beyond those identified in Section 4.3.

The results at $\Delta = 0.9$, slightly away from the integrable point, are markedly different. We find only two exactly vanishing singular values corresponding to the space spanned by the two obvious integrals of motion, H and $(S^z_{\text{tot}})^2$. This behavior persists on the entire open segment $\Delta \in (0, 1)$, showing unambiguously that there are no other purely bilinear integrals of motion in this range. Nonetheless, we see that the remaining set of $N - 2$ nontrivial IOMs at $\Delta = 1$ are transformed, upon moving to the point $\Delta = 0.9$, into left singular vectors with non-zero yet small singular values. It stands to reason that these small singular values correspond to operators that exhibit a slow decay because the system is close to the $\Delta = 1$ integrable point. We now test this hypothesis by directly examining the decay of these putative "slow modes."

Characterizing the slow operators

We have seen that the nontrivial IOMs at the points $\Delta = 0$ and $\Delta = 1$ transform into a set of $N - 2$ "slow operators," indicated by small singular values, away from those two points. Let us examine the dynamics of these presumed slow modes. Their decay can be studied by numerically computing the auto-correlation functions

$$G_l(t) = \frac{1}{\mathcal{D}} \operatorname{Tr}\left[\hat{Q}_l(t)\hat{Q}_l(0)\right], \tag{4.29}$$

---

[2] We initialize each spin i in a randomly chosen (with equal probability $p = 1/6$) eigenstate of either $\hat{S}^x_i$, $\hat{S}^y_i$ or $\hat{S}^z_i$.

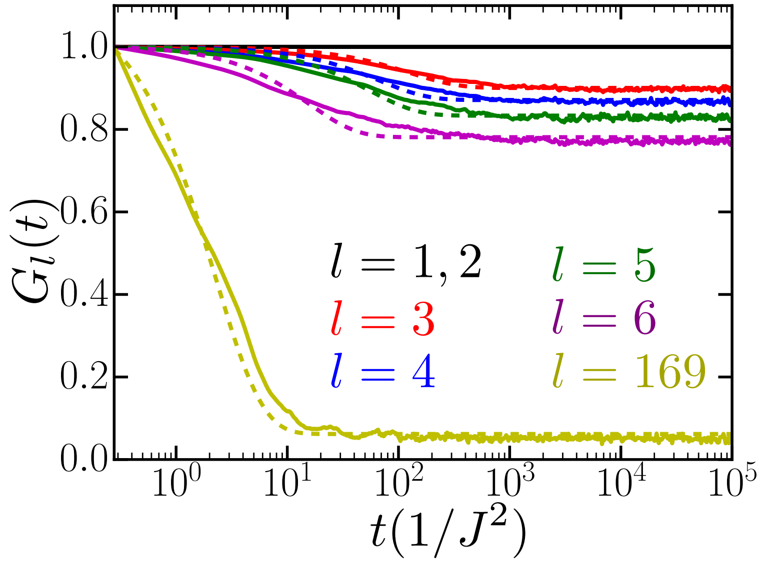

Figure 4.3: Plot of the auto-correlation function $G_l(t)$ in a given disorder realization for $N = 13$ spins at $\Delta = 0.75$. The solid curves represent the numerically computed $G_l(t)$: the black curve corresponds to either of the two exactly conserved bilinear quantities; the red, blue, green, and magenta curves correspond to the next four modes (arranged by increasing singular value); the yellow curve corresponds to a mode in the middle of the singular value "spectrum." The dashed curves represent fits of the form $\widetilde{G}_l(t) = \zeta_l \exp(-t/\tau_l) + g_l$ through the data.

where the normalization $\mathcal{D} = (2S+1)^N$ ensures that $G_l(0) = 1$. For conserved modes, we expect the auto-correlation function to remain fixed at $G_l(t) = 1$ for all time. For generic non-conserved operators, we expect $G_l(t)$ to decay to values near zero as these modes thermalize.

An example of the results for a system with $N = 13$ sites and $\Delta = 0.75$ is shown in Fig. 4.3. We see that the correlation functions related to the two zero singular values, $G_1(t)$ and $G_2(t)$, are perfectly non-decaying, as they must be. Also as expected, the correlation functions $G_l(t)$ associated with the small non-vanishing singular values $(3 \leq l \leq N)$ show a slow initial decay. However, the surprise is that, at very long times, these correlation functions saturate to a non-vanishing and rather appreciable value g_l. Fig. 4.4 shows that this phenomenon persists when varying Δ on the segment $[-0.5, 1.5]$. Moreover, we find no significant size dependence of the saturation value g_l, as shown in Fig. 4.5a. We have also checked that the large plateau values are not due to the overlap between the slow modes $\hat{Q}_l$ with higher powers of the known conservation laws $\hat{H}$ and $\hat{S}^z_{\text{tot}}$, such as $\hat{H}^2, \hat{H}^3, \ldots$, nor with projectors to energy eigenstates (for details, see Appendix 4.10). In contradistinction, the operators corresponding to higher singular values $(l \gg N)$ decay to a vanishing, or very small, saturation value (see Appendix 4.10).

Altogether, in addition to the obvious bilinear IOMs, H and $(S^z_{\text{tot}})^2$, we find $N-2$ operators whose correlation functions saturate to an appreciable non-vanishing value. This

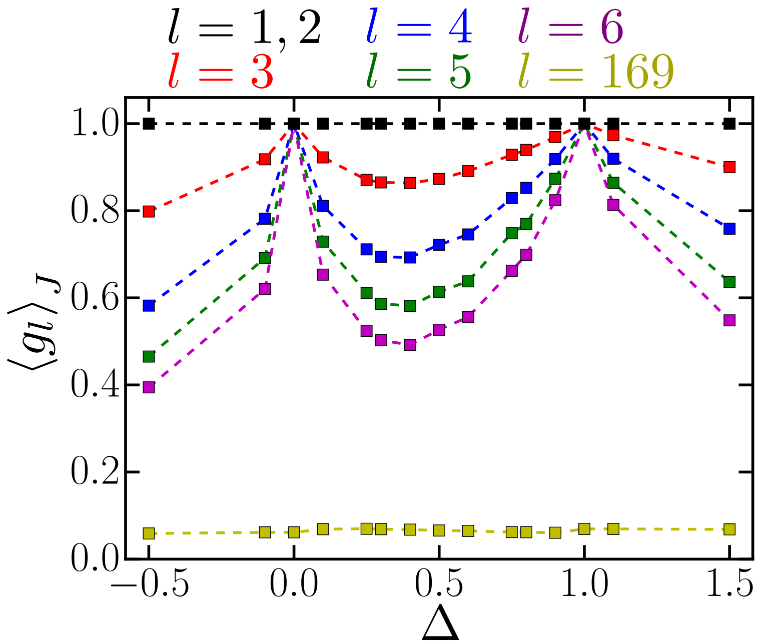

Figure 4.4: Plot of the plateau values $\langle g_l \rangle_J = \langle G_l\,(t \to \infty) \rangle_J$ as a function of the anisotropy Δ for $N = 11$ spins ($S = 1/2$). The brackets $\langle \dots \rangle_J$ denote an average over 2000 disorder realizations for the $\{J_i\}$. Different colors correspond to different modes: black corresponds to the two lowest and exactly conserved modes; red, blue, green, and magenta correspond to the next four modes; yellow corresponds to a mode in the middle of the singular value "spectrum". We find no strong dependence on the system size N: see Fig. 4.5 for a plot of the plateau value $\langle g_l \rangle_J$ as a function of the system size N for the $l = 3$ (red) mode at $\Delta = 0.5$.

result suggests that the model remains integrable even away from the Gaudin-like points $\Delta = 0$ and $\Delta = 1$: the bilinear integrals of motion are transformed into quasi-bilinear ones, which retain appreciable support in the space of 2-local operators. Based on the results shown in Fig. 4.4, we argue that this holds everywhere away from the integrable points, namely in the regions $\{\Delta < 0\}$, $\{0 < \Delta < 1\}$, and $\{\Delta > 1\}$. In general, we can write the new integrals of motion as bilinear operators dressed by a sum over higher, $2n$-local terms:

$$\hat{I}_l = Z_l \hat{Q}_l + \sum_{n>1} \sum_{i_1,\dots,i_{2n}} \sum_{\alpha_1,\dots,\alpha_{2n}} K^{\alpha_1 \dots \alpha_{2n}}_{i_1 \dots i_{2n}} \hat{S}^{\alpha_1}_{i_1} \hat{S}^{\alpha_2}_{i_2} \dots \hat{S}^{\alpha_{2n}}_{i_{2n}}, \tag{4.30}$$

where Z_l is the weight of the integral of motion I_l on 2-local operators. The saturation value of the auto-correlation function of $\hat{Q}_l$ that we plot in Fig. 4.4 is, essentially, $g_l \sim |Z_l|^2$. It would be interesting to further characterize how the coefficients $K^{\alpha_1 \dots \alpha_{2n}}_{i_1 \dots i_{2n}}$, which encode the overlap of the IOMs with the different $2n$-body spin operators, decay with increasing n. We leave this for future work.

The structure of the integrals of motion (4.30) is, in some ways, reminiscent of the Local Integrals of Motion (LIOM) in the Many-Body Localized (MBL) state [238, 211, 173]. The latter is characterized by quasi-local integrals of motion τ_i^z that are adiabatically connected to the microscopic degrees of freedom σ_i^z. As in our case, the LIOMs are dressed versions of the microscopic bits with weight on higher n-body operators decaying exponentially with n. There are, however, crucial differences from MBL. The integrals of motion in our case are not local, but rather extensive sums of bi-local operators. Hence, the IOMs of the all-to-all spin model do not facilitate a direct-product partition of the Hilbert space into single qubit spaces. Additionally, the integrability we observe does not depend on strong disorder—in fact, we found that its signatures are more pronounced as the couplings becomes more uniform, namely as $\mathrm{std}(J_i) \lesssim \overline{J_i}$.

Lastly, we also find signatures of integrability in the spectrum of H: the level statistics are almost perfectly Poissonian at $\Delta = 0, 1$ and close to Poisson (although not exactly) at intermediate Δ (see Appendix 4.10). Nonetheless, for $0 < \Delta < 1$ we find many level crossings and the violation of the Wigner-von Neumann non-crossing rule represents further evidence of integrability despite the fact that there seems to be some degree of correlation between the energy levels [204, 178, 202].

Perturbing away from integrability*

After establishing the existence of a novel integrable structure for the spin-1/2 model, characterized by quasi-2-local IOMs, it is natural to investigate its robustness to perturbations away from the class of models (4.2) with separable disorder. This question is relevant from a theoretical point of view, but also from a practical, experimental perspective.

A natural perturbation to test in this context is one that adds a non-separable, SY-like, contribution to the interaction. Specifically, we add the term

$$H_\epsilon^{(1)} = \frac{\epsilon}{2S\sqrt{N}} \sum_{i,j=1}^{N} V_{ij} \left[S_i^x S_j^x + S_i^y S_j^y + \Delta S_i^z S_j^z \right], \tag{4.31}$$

where the elements V_{ij} are also sampled from a normal distribution $\mathcal{N}(0,1)$.

We explicitly check that at $\epsilon > 0$ and $\Delta = 1$ for $H + H_\epsilon^{(1)}$ there are only 4 zero singular values corresponding to exactly conserved and linearly-independent 2-local quantities: the Hamiltonian, S_{tot}^2, $(S_{\mathrm{tot}}^x)^2$, and $(S_{\mathrm{tot}}^y)^2$. At intermediate $0 < \Delta < 1$, there are only two vanishing singular values corresponding to $H + H_\epsilon^{(1)}$ and $(S_{\mathrm{tot}}^z)^2$. Second, we verify that the lowest bilinear modes that are not exactly conserved (i.e. either the $l = 3$ one at $0 < \Delta < 1$ or the $l = 5$ one at $\Delta = 1$) decay to smaller plateau values which *decrease* as we increase the system size N, as shown in Fig. 4.5a. This suggests that a perturbation $H_\epsilon^{(1)}$, even at $\epsilon \ll 1$, can spoil the integrability for a large system $N \gg 1$.

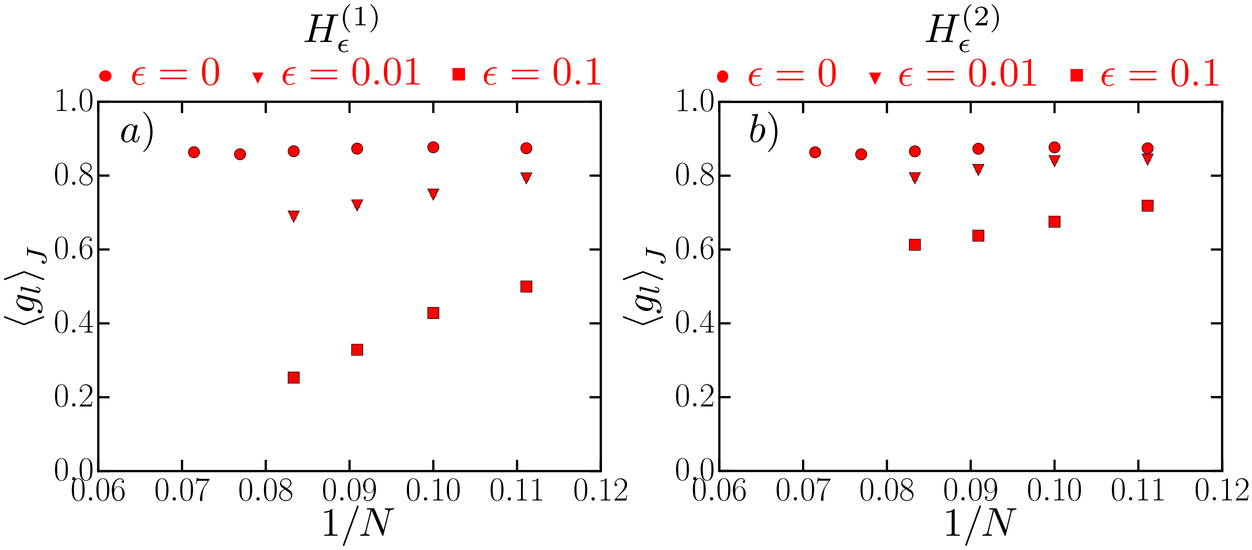

Figure 4.5: Plot of the disorder-averaged plateau values $\langle g_l \rangle_J = \langle G_l\,(t \to \infty) \rangle_J$ as a function of the system size N for $l = 3$ mode, i.e. the lowest mode that is not exactly conserved (corresponding to the red markers in Fig. 4.4) at $\Delta = 0.5$. The different markers correspond to various strengths ϵ of the perturbations $H_\epsilon^{(1)}$ (left panel) and $H_\epsilon^{(2)}$ (right panel) from Eq. 4.31 and Eq. 4.32, respectively: the round markers correspond to the unperturbed Hamiltonian H (4.2); the triangular and square markers correspond to $\epsilon = 0.01$ and $\epsilon = 0.1$, respectively. The error bars related to disorder averaging $\langle \dots \rangle_J$ are included, but they are smaller than the size of the markers. We see that the plateau value for the unperturbed H is independent of the system size. Converserly, upon adding even a small perturbation $\epsilon \ll 1$, the plateau value decreases with N, suggesting that the autocorrelation function $G_l\,(t \to \infty)$ vanishes for a thermodynamic system ($N \to \infty$).

Another type of perturbation that arises naturally in the experimental set-up, due to the driving field, is represented by random stray magnetic fields along the z-axis:

$$H_\epsilon^{(2)} = \epsilon \sum_{i=1}^{N} h_i S_i^z, \tag{4.32}$$

where the fields h_i are also sampled from $\mathcal{N}(0, 1)$. Note that $H + H_\epsilon^{(2)}$ has a single zero singular value corresponding to $(S_{\text{tot}}^z)^2$ for all Δ; this is due to the fact that the full Hamiltonian is no longer *purely* bilinear and that $H_\epsilon^{(2)}$ breaks the SU(2) symmetry at $\Delta = 1$. Aside from this effect, the behavior upon perturbing with $H_\epsilon^{(2)}$ is similar to that obtained by perturbing with $H_\epsilon^{(1)}$, as shown in Fig. 4.5b.

Last, we consider the effect of adding the perturbation

$$H^{(3)} = \frac{1}{S\sqrt{N}} \sum_i J_i^2 S_i^z. \tag{4.33}$$

This term appears in the model

$$\widetilde{H} = \frac{1}{S\sqrt{N}} \sum_{ij} J_i J_j \left(S_i^+ S_j^- + \Delta S_i^z S_j^z \right), \tag{4.34}$$

which is similar to Eq. 4.2, but differs from it by the term $H^{(3)}$, arising due to the commutator $\left[S_i^+, S_i^-\right]$. As noted in Ref. [164], the model Eq. (4.34) is also experimentally accessible in a system of cold atoms interacting with cavity photons. It is clear that the perturbation $H^{(3)}$, having a $1/\sqrt{N}$ normalization, is sub-extensive and will not matter in the thermodynamic limit. Moreover, we find that it does *not* qualitatively affect the integrability of our quantum model even for the small systems considered in ED (see Appendix 4.10 for the numerical results).

In sum, our numerical analysis of the response to perturbations indicates that the novel integrability of the spin-1/2 model (4.2) is not particularly robust to non-separable interactions or stray magnetic fields. Nevertheless, in a finite-size system and at finite times (see Section 4.7 for more details), there are signatures of proximate integrability, as shown by the finite saturation values in Fig. 4.5.

To recapitulate our study of the dynamical phase diagram Fig. 4.1 thus far, we have found that the system is integrable along three lines: at $\Delta = 0, 1$ for any value of the spin size S (characterized by bilinear IOMs), and at $S = 1/2$ for any $\Delta \neq 0, 1$ (characterized by quasi-bilinear IOMs). The remaining line in the phase boundary of Fig. 4.1 corresponds to the classical, $S \to \infty$, limit of the model (4.2), which we now discuss.

4.6 Chaos for $S \to \infty$

Since Gaudin-type integrability at $\Delta = 0$, 1 persists for all values of the spin size S, it is natural to ask whether the integrability* structure at $S = \frac{1}{2}$, presented in the previous section, also survives for larger values of S. Although it is numerically challenging to extend the exact diagonalization study of the previous section to intermediate S, the limit $S \to \infty$ leads to classical equations of motion that are amenable to numerical simulation.

These simulations allow us to analyze another boundary in the phase diagram, namely the $S \to \infty$ line, where we find chaotic dynamics with a finite Lyapunov exponent, as explained in Section 4.6. The presence of chaos in the infinite-S limit clearly implies that the $S = \frac{1}{2}$ integrability* does not extend to all S, unlike the Gaudin-type integrability at $\Delta = 0$ and 1. Remnants of an integrability* structure can nevertheless be revealed by applying the SVD analysis of Section 4.4 to the classical dynamics, which we do in Section 4.6. This technique reveals the presence of a large number of slow modes, which are known to occur classically in "quasi-integrable" systems, i.e. chaotic systems in the vicinity of integrable points. We characterize these slow modes in Section 4.6.

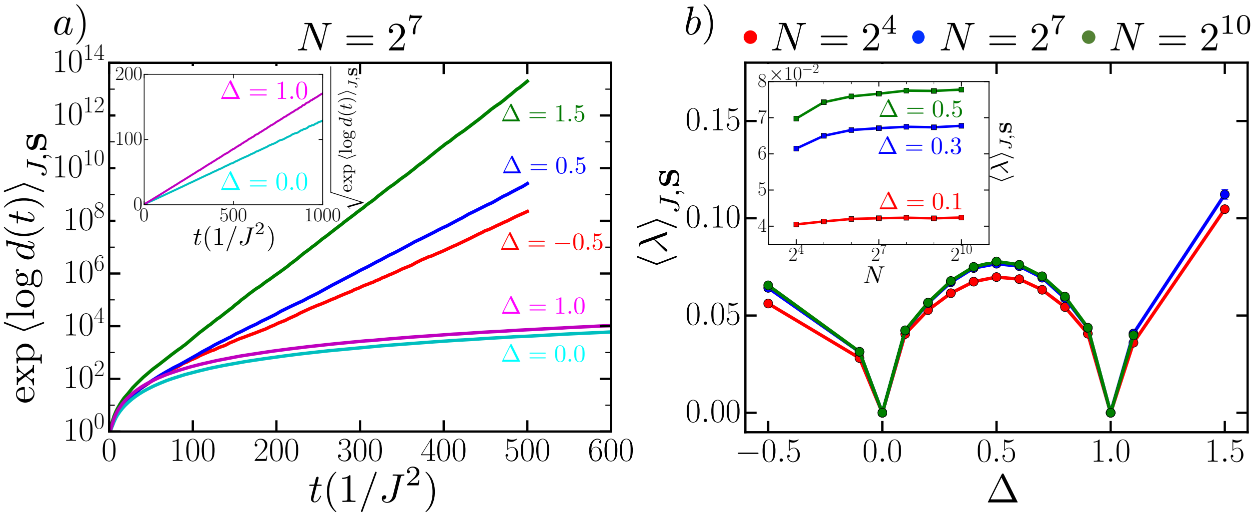

Figure 4.6: a) The sensitivity $d(t)$ from Eq. 4.40 geometrically averaged over 10^4 disorder realizations $\{J_i\}$ and initial states $\{\mathbf{S}(0)\}$ as a function of time for a system of $N = 128$ classical spins. After non-universal dynamics at early times, we find an exponential growth at later times for $\Delta = -0.5$ (red curve), $\Delta = 0.5$ (blue curve), and $\Delta = 1.5$ (green curve). (inset) The square root of the same quantity, namely $\sqrt{\exp\left(\langle \log d(t)\rangle_{J,\mathbf{S}}\right)}$, at the two integrable points, $\Delta = 0.0$ (cyan curve) and $\Delta = 1.0$ (magenta curve): we obtain an almost perfect straight line, which indicates that $d(t) \sim t^2$, as expected for an integrable system. b) Lyapunov exponent $\langle\lambda\rangle_{J,\mathbf{S}}$ averaged over 10^5 disorder realizations and initial states as a function of the anisotropy Δ for different systems consisting of $N = 16$ (red circles), $N = 128$ (blue circles), and $N = 1024$ (green circles) classical spins. (inset) Disorder-averaged Lyapunov exponent $\langle\lambda\rangle_{J,\mathbf{S}}$ as a function of the system size N for $\Delta = 0.1$ (red squares), $\Delta = 0.3$ (blue squares), and $\Delta = 0.5$ (green squares).

Classical chaos

In the infinite-S limit, the model (4.2) behaves as a classical system of coupled spin degrees of freedom S_i^α on the unit sphere, whose Hamiltonian dynamics can be written in terms of Poisson brackets:

$$\frac{dS_i^\alpha}{dt} = \{S_i^\alpha, H\}, \tag{4.35}$$

where

$$H = \frac{S}{2\sqrt{N}} \sum_{ij} J_i J_j \left(S_i^x S_j^x + S_i^y S_j^y + \Delta S_i^z S_j^z\right). \tag{4.36}$$

For our numerical investigation, we sample the random fields J_i from the uniform distribution $[-J, J]$ and set $J = 1$ (we choose a bounded distribution to avoid large J_i's that could cause numerical instabilities). The classical spin variables S_i^α obey

$$\{S_i^\alpha, S_j^\beta\} = \frac{1}{S}\delta_{ij}\varepsilon^{\alpha\beta\gamma}S_i^\gamma. \tag{4.37}$$

We shall probe the infinite-temperature dynamics of this classical system by direct numerical simulation.

In order to study chaos, we use the standard tangent space method [32] to study the divergence of classical trajectories and measure the leading Lyapunov exponent. Let $\mathbf{S}(t) = (\mathbf{S}_1(t), \ldots, \mathbf{S}_N(t))$ denote the $3N$-dimensional vector describing the directions of all the spins at time t. We initialize the system in a random infinite-temperature state $\mathbf{S}(0)$, within which each spin points in a random direction, uniformly distributed on the unit sphere S_2. We also keep track of the trajectory of the deviation vector $\delta\mathbf{S}(t)$, which lives in the tangent space of $S_2 \times \cdots \times S_2$ at the point $\mathbf{S}(t)$; we further set $\delta\mathbf{S}(0)$ such that $\delta\mathbf{S}_i(0) \perp \mathbf{S}_i(0)$ for all spins and $\|\delta\mathbf{S}(0)\|^2 = \sum_{i,\alpha}(\delta S_i^\alpha)^2 = 1$.

If we define the local effective field $\mathbf{F}_i = (F_i^x, F_i^y, F_i^z) = \frac{1}{S}\left(-\frac{\partial H}{\partial S_i^x}, -\frac{\partial H}{\partial S_i^y}, -\frac{\partial H}{\partial S_i^z}\right)$, we see that the Hamilton equations of motion (4.35) can be written as

$$\frac{d\mathbf{S}_i}{dt} = \mathbf{S}_i \times \mathbf{F}_i. \tag{4.38}$$

For our model (4.36) we have $F_i^{x,y} = \frac{J_i}{\sqrt{N}}\sum_j J_j S_j^{x,y}$ and $F_i^z = \Delta\frac{J_i}{\sqrt{N}}\sum_j J_j S_j^z$.

We immediately see that the variational equations of motion for the deviation vector $\delta\mathbf{S}$ can be written as

$$\frac{d(\delta\mathbf{S}_i)}{dt} = \delta\mathbf{S}_i \times \mathbf{F}_i + \mathbf{S}_i \times \delta\mathbf{F}_i, \tag{4.39}$$

where $\delta F_i^{x,y} = \frac{J_i}{\sqrt{N}}\sum_j J_j \delta S_j^{x,y}$ and $\delta F_i^z = \Delta\frac{J_i}{\sqrt{N}}\sum_j J_j \delta S_j^z$.

We numerically integrate the coupled differential equations (4.38) and (4.39) to find the trajectory $(\mathbf{S}(t), \delta\mathbf{S}(t))$ in the tangent bundle up until a time $T = 500J^{-2}$ in increments $\delta t = 1\ J^{-2}$. We then compute the sensitivity, defined as $d(t) = \|\delta\mathbf{S}(t)\|^2$, or in full,

$$d(t) = \sum_{i=1}^N \sum_\alpha \left[\delta S_i^\alpha(t)\right]^2. \tag{4.40}$$

Note that $d(0) = 1$, since we have normalized the initial deviation vector. For an integrable system we expect $d(t)$ to exhibit a power-law dependence on time; the flow on invariant tori specified by the N conservation laws is linear in time and, since we have defined the sensitivity as $\|\delta\mathbf{S}(t)\|^2$, we expect $d(t) \sim t^2$. In a chaotic system $d(t)$ should increase exponentially with t. In Fig. 4.6a, we average over disorder realizations $\{J_i\}$ and initial states $\{\mathbf{S}(0)\}$ to find $\exp\left(\langle \log d(t)\rangle_{J,\mathbf{S}}\right)$. We find that the classical system exhibits chaotic dynamics and an exponential divergence of trajectories in the regions $\{\Delta < 0\}$, $\{0 < \Delta < 1\}$, and $\{\Delta > 1\}$. We also find integrable dynamics and a power law divergence of trajectories at the special points $\Delta = 0, 1$.

Moreover, using the multiplicative ergodic theorem, we can define the maximal Lyapunov exponent [32] as

$$\lambda = \lim_{t\to\infty} \frac{2}{t} \log \frac{\|\delta \mathbf{S}(t)\|}{\|\delta \mathbf{S}(0)\|}. \tag{4.41}$$

Using the normalization $\|\delta \mathbf{S}(0)\| = 1$ and our definition of the sensitivity from Eq. 4.40, we see that

$$\lambda = \lim_{t\to\infty} \frac{1}{t} \log d(t). \tag{4.42}$$

In practice, we compute the Lyapunov exponent by fitting a line $\lambda t + b$ through the late time behavior of $\log d(t)$, as discussed in Ref. [100]. In Fig. 4.6b we plot the Lyapunov exponent $\langle\lambda\rangle_{J,\mathbf{S}}$, averaged over disorder realizations $\{J_i\}$ and initial states $\{\mathbf{S}(0)\}$, as a function of the anisotropy Δ and find that the system exhibits the most chaotic behavior (largest Lyapunov exponent) at $\Delta = 1.5$. Second, we find that $\langle\lambda\rangle_{J,\mathbf{S}}$ tends to a finite value for large system sizes N, as shown in the inset of Fig. 4.6b.

SVD analysis

Although the presence of chaos in the classical dynamics excludes proper integrability in the infinite-S limit, it does not rule out the possibility of "quasi-integrability," whereby some operators have very slow decay. We investigate this possibility by applying the SVD analysis of Section 4.4 to the classical dynamics. This allows us to determine the number of exactly conserved quantities, corresponding to zero singular values, but also to look for slow modes, corresponding to small but finite singular values.

As expected, we find an extensive number of conserved quantities at $\Delta = 0, 1$ and only 2 exactly conserved quantities, corresponding to the Hamiltonian H and $(S^z_{\text{tot}})^2$, for all other values of the anisotropy Δ. This intermediate regime, however, exhibits a large number of slow modes, which will be discussed in the next section.

Since we are now working with a classical system, a few important distinctions ought to be made from our earlier, quantum analysis. First, we consider a slightly enlarged collection of bilinear operators:

$$O_a = \begin{cases} 3S_i^\alpha S_j^\alpha & a = (i,j,\alpha)\,,\; i<j \\ c_1\left(S_i^x S_i^x - S_i^y S_i^y\right) & a = (i,i,1)\,, \\ c_2\left(3S_i^z S_i^z - 1\right), & a = (i,i,2)\,, \end{cases} \tag{4.43}$$

where $c_1 = \sqrt{15}/2$ and $c_2 = \sqrt{5}/2$. As before, $a = (i,j,\alpha)$ is a composite index. In the classical case, we also include bilinears with $i = j$ (which would be trivial in the spin-1/2 case). Note that there are only two independent such bilinears for each i, and the spherical harmonics (with spin 1) provide an orthonormal basis. Indeed, it can be checked that the bilinears O_a defined in Eq. 4.43 satisfy the orthonormality relation

$$\langle O_a O_b\rangle_{\mathbf{S}} \equiv \int \prod_i \frac{D\mathbf{S}_i}{4\pi} O_a O_b = \delta_{ab}, \tag{4.44}$$

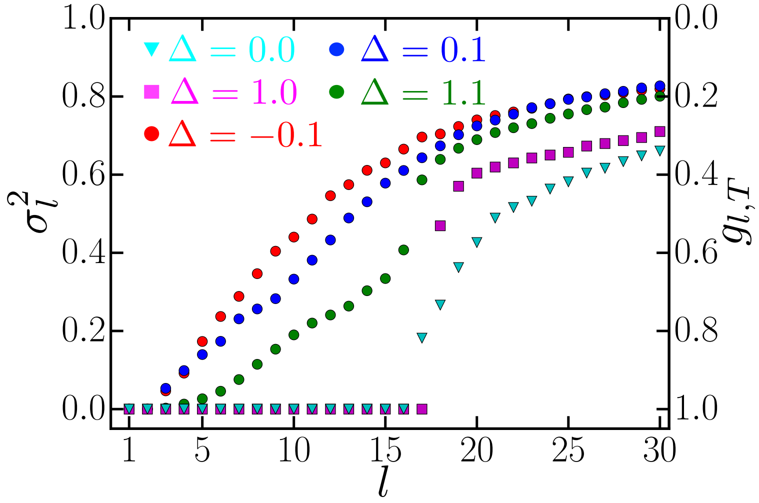

Figure 4.7: Scatter plot of the smallest 30 squared singular values σ_l^2 and the plateau value $g_{l,T}$ from Eq. 4.50 for a classical model (4.36) of $N = 16$ spins at different values of the anisotropy Δ. We average σ_l^2 over $\mathcal{N} = 10^3$ random initial conditions $\{S_0\}$ and 10 disorder realizations for the fields $\{J_i\}$ and we set $T = 8192 J^{-2}$. At the integrable points $\Delta = 0$ (cyan triangles) and $\Delta = 1$ (magenta squares) we see N and $N+1$ zero singular values, respectively, corresponding to the conserved quantities that can be written as a sum over bilinear operators (4.43). These are separated from the rest of the singular values by a "spectral" gap. At $\Delta = -0.1$ (red circles), $\Delta = 0.1$ (blue circles), and $\Delta = 1.1$ (green circles) we see two precisely zero singular values corresponding to the conservation of H and $(S^z_{\text{tot}})^2$, along with the lift-off of the other $N-2$ singular values. For $\Delta = 1.1$, the first N singular values are also separated by a spectral gap from the rest. And, although for $\Delta = -0.1$ and $\Delta = 0.1$ the spectral gap is not visible, one can still see a rounded "cusp" occurring around $l = N$—this suggests that there still exist slow modes Q_l for $l = 3, \ldots, N$.

where $\langle [\ldots] \rangle_{\mathbf{S}}$ denotes an average over the infinite temperature ensemble, while the integral $\int D\mathbf{S}_i$ is over the unit sphere.

Second, while a single initial state is sufficient in the quantum SVD analysis, we have to consider an ensemble of initial states in the classical setting. This is because a single classical trajectory cannot visit the whole phase space due to energy conservation (a linear superposition of configurations does not exist classically). Here, we take the infinite-temperature ensemble, namely we sample $S_0 = \{\mathbf{S}_1(0), \ldots, \mathbf{S}_N(0)\}$ as independent random points on the unit sphere. We then time evolve with (4.35) for a total time T, and measure the expectation value of the bilinears $O_a(t_n, S_0)$ at discrete intervals $t_n = n\delta t \in [0, T]$. Repeating this for a large number $\mathcal{N}$ of initial conditions $\{S_0\}$ in the infinite-temperature ensemble, we construct the following matrix, analogous to the one in Eq. 4.24:

$$M_{a,(t,S_0)} = \left(O_a(t, S_0) - \overline{O_a}(S_0) \right), \tag{4.45}$$

where $\overline{O_a}(S_0) = \int_0^T \frac{dt}{T} O_a(t, S_0)$ represents the time average over one trajectory. The number of rows indexed by a is, according to Eq. 4.43, $3N(N-1)/2 + 2N$. The columns are indexed by time $t \in [0, T]$ and initial condition S_0—in practice, we discretize the time axis (with the time-step $\delta t = 1J^{-2}$) and draw a large number (10^3) of samples for S_0.

Then the singular value decomposition of M is equivalent to diagonalizing the real Hermitian matrix $L \equiv MM^\dagger$, which can be obtained by averaging over the initial conditions S_0:

$$L_{a,b} = \left\langle \int_0^T \frac{dt}{T} M_{a,(t_n,S_0)} M_{b,(t_n,S_0)} \right\rangle_{\mathbf{S}} . \tag{4.46}$$

Note that the average $\langle \dots \rangle_{\mathbf{S}}$ is with respect to S_0 in the infinite-temperature thermal ensemble and should not be confused with the quantum expectation values $\langle \dots \rangle$ (i.e. without a subscript) used in Sections 4.4 and 4.5. Diagonalizing L allows us to obtain the slow mode operators Q_l, together with their corresponding eigenvalues σ_l^2. Similarly to (4.28), we have

$$\sigma_l^2 = \left\langle \overline{Q_l(t, S_0)^2} - \overline{Q_l(t, S_0)}^2 \right\rangle_{\mathbf{S}} . \tag{4.47}$$

In other words, σ_l^2 is equal to the variance, averaged over initial conditions S_0, of the fluctuations of Q_l along a given trajectory.

The behavior of the singular values σ_l (shown in Fig. 4.7) is similar, in several ways, to that obtained in Section 4.5 for the quantum spin-1/2 model [3]. At the first integrable point $\Delta = 0$, we obtain N zero singular values corresponding to the family of N spin-bilinear conserved quantities $\widetilde{G}^{(i)}$ from Eq. 4.19. At the second integrable point $\Delta = 1$, we find $N + 1$ zero singular values corresponding to the conserved quantities lying in the linear span of the $G^{(i)}$s from Eq. 4.17. Lastly, as shown in Fig. 4.7, away from these integrable points, i.e. for $\{\Delta < 0\}, \{0 < \Delta < 1\}$, and $\{\Delta > 1\}$, we find two precisely zero singular values, corresponding to the two exactly conserved spin-bilinear quantities, H and $(S^z_{\text{tot}})^2$. The small magnitude of the following singular values, for $l = 3, 4, \dots$, signals the presence of slow modes, which will be studied in the next section.

Decay of slow operators

The SVD analysis of the previous section revealed a large number of operators with small singular values. In principle, we could characterize the thermalization (or lack thereof) of these operators Q_l using, in analogy to the quantum case, a two-point correlation function

$$G_l(t) = \langle Q_l(t) Q_l(0) \rangle_{\mathbf{S}} , \tag{4.48}$$

where $\langle \dots \rangle_{\mathbf{S}}$, as before, designates an average over the $\mathcal{N}$ initial conditions S_0. As in the quantum case, the operators Q_l are orthonormal such that $G_l(0) = 1$ (as $\mathcal{N} \to \infty$). Yet, the

---

[3] The main difference between the classical and quantum SVD results is that the classical singular values are considerably larger than the quantum ones (compare Fig. 4.2 and Fig. 4.7). This is because the expectation value of O_a is evaluated on a single classical configuration in the former case, while the quantum expectation value is a result of a coherent average.

accurate computation of $G_l(t)$ at long times is typically very demanding because it requires averaging an increasingly complex function in phase space.

Fortunately, in classical systems, the singular value σ_l already informs us about the long time plateau value of $G_l(t)$. This can be seen from Eq. 4.47, which implies that

$$\begin{aligned}
\sigma_l^2 =& \left\langle \int_0^T \frac{dt}{T} Q_l(t)^2 \right\rangle_{\mathbf{S}} - \left\langle \int_0^T \int_0^T \frac{ds}{T}\frac{dt}{T} Q_l(t) Q_l(s) \right\rangle_{\mathbf{S}} \\
=& 1 - \left\langle \int_0^T \int_0^T \frac{ds}{T}\frac{dt}{T} Q_l(t) Q_l(s) \right\rangle_{\mathbf{S}} \\
\sigma_l^2 =& 1 - g_{l,T} \ , \ g_{l,T} \equiv \int_0^T G_l(u) \frac{2(T-u)du}{T^2} \, .
\end{aligned} \tag{4.49}$$

In the second line, we used the normalization $\langle Q_l(t)^2 \rangle_{\mathbf{S}} = 1$; in the third line, we performed a change of variables $u = |t-s|$ (recall that $G_l(u) = \langle Q_l(t) Q_l(t \pm u) \rangle_{\mathbf{S}}$ by the invariance of the infinite-temperature ensemble under time evolution). Now, it is not hard to show that $g_{l,T}$ and G_l have the same infinite-time limit if that exists for G_l:

$$\lim_{u \to \infty} G_l(u) = g_l \ \Rightarrow \ \lim_{T \to \infty} g_{l,T} = g_l \, .$$

Thus, $g_{l,T}$ is a finite-time proxy for g_l. In the infinite-time limit, the relation (4.49) becomes

$$g_l = 1 - \sigma_l^2|_{T \to \infty} . \tag{4.50}$$

Using Eq. 4.49 or 4.50, this allows us to infer the plateau values of slow modes from the data of Fig. 4.7. Unsurprisingly, the exactly conserved quantities have $g_l = 1$. Away from the integrable points at $\Delta = 0, 1$, we find that the slowest non-conserved modes, corresponding to $l = 3, 4, \dots,$ (the distinction between the slow modes and the rest is less sharp here than in the quantum case, and it is suggested by the rounded cusp around $l = N$ in Fig. 4.7), have a remarkably slow decay: the plateau values $g_{l,T}$ at a finite but large time $T = 10^4 J^{-2}$ are close unity [4], comparable to their spin-1/2 counterparts.

In a future companion paper, we will demonstrate that any conserved operator in the $S = 1/2$ quantum case is approximately conserved in the $S \to \infty$ classical model as well, up to $1/N$ corrections in large systems. Therefore, the classical model is expected to display some signatures of integrability. In this section, we saw that such signatures cannot be found from the Lyapunov exponent, but only from the relaxation of slow modes. This is intriguing, but a similar phenomenon has previously been observed. Ref. [99] showed that for certain systems near integrability (called "quasi-integrable" by the authors), the relaxation time of certain operators can be significantly longer than the finite Lyapunov time $1/\lambda_L$. Given that our classical system is surrounded by integrable lines $\Delta = 0, 1$ and (arguably) $S = 1/2$ in the

---

[4] We have checked that this persists up to $T = 10^6 J^{-2}$. Nonetheless, we find that these plateaus eventually decay for a finite-size system, albeit after a very long time. We leave the quantitative analysis for future work.

(Δ, S) parameter plane (see Fig. 4.1), we conjecture that it is also quasi-integrable. From this perspective, the existence of slow modes is compatible with the finite classical Lyapunov exponent found in Section 4.6.

4.7 Experimental realities

We have provided analytical and numerical evidence for the rich dynamical phase diagram depicted in Fig. 4.1, including clear signatures of chaotic dynamics at large S and $\Delta \neq 0, 1$, along with signatures of integrability at the special points $\Delta = 0, 1$ for any S. Further, we demonstrated signatures of a novel integrability* phase at $S = 1/2$ for $\Delta \neq 0, 1$. We now discuss prospects for observing these signatures in the laboratory. First, what should one measure to identify the chaotic and integrable regimes of the phase diagram? Second, given the inevitable presence of dissipation in realistic experiments, what are the requirements on cavity cooperativity to access the relevant time-scales experimentally?

To identify integrals of motion, the SVD method of Section 4.4 can equivalently be implemented with experimental data. Using state-sensitive imaging of the atomic ensemble [69], one may immediately extract the bilinear spin correlation functions $\langle O_a(t)\rangle \propto \langle S_i^\alpha(t) S_j^\alpha(t)\rangle$ defined in Eq. 4.21. As each image is obtained from a destructive measurement, one must repeat the experiment many times to obtain statistics of the spin bilinears at a fixed time t, and then repeat this procedure for many time-points t to obtain the full matrix $M_{a,t}$. With this matrix in hand, one can then directly apply the singular-value decomposition performed above in Section 4.4.

A caveat is that measurements of the spin bilinears can be affected by dissipation due to photon loss and atomic free-space scattering. Photon loss from the cavity mode causes a random walk in the orientation of the weighted collective spin $\boldsymbol{\mathcal{F}}$ defined in Eq. 4.3. This effect is described by Lindblad operators

$$L_\pm = \sqrt{\gamma/2}\, \mathcal{F}_\pm, \tag{4.51a}$$

$$L_z = \sqrt{\Delta\gamma}\, \mathcal{F}_z, \tag{4.51b}$$

where the decay rate (derived in Sec. 4.9) is given by

$$\gamma = \frac{J^2}{S\sqrt{N}} \frac{\kappa}{\delta}. \tag{4.52}$$

The collective dissipation can be suppressed by increasing the detuning δ and compensating with increased drive strength, until limited by free-space scattering.

The effect of free-space scattering is to project or flip individual spins, as described by a set of Lindblad operators

$$L_{n,(m,m')} = \sqrt{C_{m,m'}\Gamma_{\rm sc}}\, |m\rangle \langle m'|_n \,, \tag{4.53}$$

where m or m' indicates the spin state of an individual atom indexed by n, and $C_{m,m'}$ is an order-unity branching ratio. At large detuning, the scattering rate scales as

$$\Gamma_{\mathrm{sc}} \sim \frac{J^2}{\eta S \sqrt{N}} \frac{\delta}{\kappa}. \tag{4.54}$$

Comparing Eqs. 4.52 and 4.54 shows that the cooperativity η will dictate an optimal detuning for minimizing the net effect of the two forms of dissipation, with higher cooperativity enabling increasingly coherent dynamics.

To determine the cooperativity required to observe the signatures of integrability, we first write down explicit equations of motion for the spin bilinears $\langle S_i^\alpha(t) S_j^\alpha(t)\rangle$ evolving under the influence of pure collective dissipation or pure single-atom decay, respectively (see Appendix 4.9). We find that the spin bilinears decay exponentially at a rate Γ_{sc} due to free-space scattering and at a rate γ due to photon loss from the cavity. Notably, the rate of spin relaxation due to photon loss is *not* superradiantly enhanced, thanks to the counterbalanced effects of the $L_\pm$ Lindblad operators. Thus, at weak to moderate cooperativity $\eta \lesssim 1$ and large detuning $\delta > \kappa$, free-space scattering dominates and the bilinears decay on a time-scale $\tau J^2 \sim \sqrt{N}\eta S \kappa/\delta$. For strong coupling $\eta \gg 1$, where free-space scattering is suppressed relative to cavity decay, the total dissipation can be minimized at a detuning $\delta \sim \sqrt{\eta}\kappa$, leading the spin bilinears to decay on a time-scale $\tau J^2 \sim \sqrt{N\eta} S$.

To compare the decay time τ with the characteristic time-scales for observing the signatures of integrability, we refer to the time dependence of the autocorrelation functions $G_l(t)$ shown in Fig. 4.3. To observe the slow modes, a minimum requirement is to evolve the system for a time $t \gtrsim t^* \approx 10\ J^{-2}$, which governs the rapid decay of all non-integrable autocorrelation functions. This time can be reached even at $S = 1/2$ in a strong-coupling cavity $\eta \sim 10$ with a system of $N = 10^3$ sites, or with weaker single-atom cooperativity at larger S. To observe the plateaus themselves, we must evolve the system for a significantly longer time, at least $t \approx 10^3\ J^{-2}$ according to Fig. 4.3, which places a more stringent requirement $\sqrt{N}\eta S \gtrsim 10^3 \delta/\kappa$. This regime is challenging to access for $S = 1/2$ but readily accessible with large-S subensembles, e.g., at $\eta \gtrsim 1$ with $N = 10^2$ sites each consisting of $S = 10^3$ spin-1 atoms.

Thus, current experiments are well positioned to explore the regime of mesoscopic spin S, in between the quantum ($S = 1/2$) and classical ($S \to \infty$) limits. This will allow for testing the prediction that the plateaus in $G_l(t)$ calculated for spin $S = 1/2$, indicating integrability across the full range $\{\Delta < 0\}$,$\{0 < \Delta < 1\}$, and $\{\Delta > 1\}$, persist for larger spin S up to $1/N$ corrections (see Sec. 4.6). Experiments with scalable spin size S may furthermore shed light on the transition from quantum integrability to chaos in the classical limit, as signified by the positive Lyapunov exponent in Fig. 4.6.

The chaotic dynamics observed in the classical limit $S \to \infty$ can be studied experimentally via the hallmark of sensitivity to perturbations. Recent theoretical and experimental work has shown that such sensitivity is accessible in quantum systems by measuring out-of-time-order correlators (OTOCs) [145, 213, 162, 114, 230, 92, 235, 154], which quantify the spread of operators in time via the commutator $C(t) = \langle [V(t), W(0)]^2 \rangle$. The connection to classical chaos is made clear in the semi-classical limit: for operators $V = S_i^z$, $W = S_j^z$, one can show that, to lowest order in a $1/S$ expansion, $C(t) \propto (\partial S_i^z(t)/\partial \phi_j)^2$ for a small rotation ϕ_j at site j about the z-axis [66]. Thus, semi-classically the OTOC $C(t)$ measures the sensitivity of the coordinate $S_i^z(t)$ to changes in initial conditions $S_j^z(0)$, and may therefore be regarded as a quantum generalization of the classical sensitivity $d(t)$ defined in Section 4.6.

One way to access out-of-time-order correlators experimentally is to "reverse the flow of time" by dynamically changing the sign of the Hamiltonian [230, 92]. In the cavity-QED system considered here [69], this sign reversal is achieved by switching the sign of the laser detuning δ in Eq. 4.9. The resilience of such time-reversal protocols to experimental imperfections, including dissipation, has been analyzed theoretically in Ref. [229].

To allow for probing chaos in the cavity-QED system proposed here, the rates of collective dephasing and of decoherence via single-atom decay must be small compared with the Lyapunov exponent. We thus require $\lambda\tau \gg 1$, where τ is the characteristic decay time defined above. More specifically, given the Lyapunov exponents $\lambda \leq 0.08J^2$ shown in Fig. 4.6, and the requirement of observing the system for several Lyapunov "decades" to clearly identify exponential growth (Fig. 4.6a), we would like to evolve the system for times $t \gtrsim 100\ J^{-2}$, which are readily accessible in the large-S regime that is of interest for approaching the classical limit.

Even in this regime, the light leaking from the cavity produces a continuous weak measurement of the collective spin $\boldsymbol{\mathcal{F}}$ whose quantum back-action may have consequences for the dynamics. The interplay of measurement back-action with chaos in open quantum systems, while beyond the scope of the present chapter, is a subject of active inquiry [75, 243] and of fundamental importance for elucidating the quantum-to-classical transition [106]. The proposed experimental scheme, including the possibility of tuning the strength and form of coupling to the environment, opens new prospects for exploring this interplay.

4.8 Conclusion

We have studied a class of spin models with separable, all-to-all, random interactions and found a complex dynamical phase structure that depends on the spin size S and the anisotropy Δ along the z-axis. We showed that our model at $\Delta = 1$ is equivalent to the well-studied rational Gaudin model, and exhibits special integrable dynamics for all values of S. We also proved and confirmed numerically that there exists another special point at $\Delta = 0$ where the model is also integrable (in the same sense), regardless of the spin size. Surprisingly, we found compelling numerical evidence that the system at $S = 1/2$ is integrable for any anisotropy $\Delta \notin \{0, 1\}$. In contrast to the special points $\Delta = 0, 1$, the integrals of motion at other values of Δ are *not* purely spin bilinears and develop tails on $2n$-body terms. We leave the detailed characterization of these dressing tails to future work. Lastly, we found that integrability away from $\Delta = 0, 1$ is a purely quantum phenomenon: by numerically solving the Hamilton equations of motion for the classical model ($S \to \infty$), we showed that its dynamics is chaotic with a non-zero Lyapunov exponent and that there exist only two exactly conserved quantities, as opposed to the extensive family of conservation laws characterizing a classically integrable system. However, even in the classical regime we find an extensive number of quasi-conserved charges, whose decay time appears to diverge in the large-N limit. A more thorough study of this regime will be given in future work.

Our analysis opens up several further lines of inquiry. First, since the Hamiltonian (4.2) at the special point $\Delta = 1$ (and, presumably, at $\Delta = 0$ as well [24, 217, 220, 218, 219]) possesses a quantum group structure, does the integrable* phase exhibit any algebraic structure? Is it possible to construct explicitly the dressed conserved quantities in terms of the model couplings?

Second, we have seen that even though the level statistics of the spin-1/2 system deviates from Wigner-Dyson statistics, exhibiting many level crossings (this holds also for spin-1, as shown in Appendix 4.10), its classical counterpart is chaotic with a finite Lyapunov exponent. We note that this does not contradict the Berry-Tabor conjecture [37, 43], which applies to the semiclassical, large-S, regime. In fact, the same phenomenon is known to occur in integrable quantum spin chains, such as the anisotropic Heisenberg model (or XXZ chain): its Hamiltonian $\sum_j \left[S_j^x S_{j+1}^x + S_j^y S_{j+1}^y + \Delta S_j^z S_{j+1}^z\right]$ is quantum integrable only for spin-1/2, and it is classically chaotic; its *integrable* higher-spin extensions have different Hamiltonians and are nontrivial to obtain [52]. We wonder whether our integrable* phase admits any such extensions, which might shed light on the quasi-integrability of our classical model.

Third, we have only characterized the *boundaries* of the phase diagram in Fig. 4.1. A straightforward and interesting next step would be to study the quantum-to-classical crossover by better understanding how classical chaos (and perhaps quasi-integrability) at $S \to \infty$ emerges from the integrable* regime at $S = 1/2$.

In fact, this putative transition between (quantum) integrability and (semiclassical) chaos may also be probed experimentally. The model (4.2) can be implemented in a near-term experiment using atomic ensembles confined in a single-mode optical cavity. This would allow for a systematic exploration of the rich physics contained in the dynamical phase diagram (Fig. 4.1). By changing the local atom density to increase the number of atoms in a given region of constant coupling to the cavity mode, the spin size S can be varied from $S = 1/2$ all the way to a semiclassical regime $S \gg 1$: this would enable the experiment to tune between quantum and classical dynamics. Meanwhile, changing the angle between the magnetic field defining the spins' z-axis and the axis of the optical cavity allows for tuning of the anisotropy Δ, so that both the special points $\Delta = 0, 1$ and the regions $\{\Delta < 0\}$, $\{0 < \Delta < 1\}$, and $\{\Delta > 1\}$ can be investigated.

Last, we emphasize that the SVD technique described in Section 4.4 can be applied directly to the experimental data, revealing the conserved quantities and slow modes. More broadly, we envision using this approach in studying a wider class of physical systems wherein the integrals of motion or their number are not *a priori* known.

In summary, the model (4.2) and its associated experimental setup represent a novel paradigmatic platform for studying integrability, chaos, and thermalization under closed many-body quantum dynamics.

4.9 Appendix A: Details on the experimental realization

Derivation of the effective Hamiltonian

Here we elaborate on the derivation of the effective spin Hamiltonian (4.8) from the atom-light interaction Hamiltonian (4.7), which we now repeat for completeness:

$$H_I \approx \frac{i}{2}\chi\left(\xi_i^* v e^{i\delta t} - \xi_i v^\dagger e^{-i\delta t}\right)(\mathbf{S}_i \cdot \hat{c}). \tag{4.55}$$

To simplify the following derivation, we will assume that the weights ξ_i are real numbers (although it is interesting to speculate whether one can access an even richer set of dynamics if the weights are allowed to have both non-uniform phases and amplitudes). In this case, we may write the full Hamiltonian as:

$$H = \frac{i}{2}\chi\left[v e^{i\delta t} - v^\dagger e^{-i\delta t}\right]\left[\mathcal{F}_z \cos\theta + \frac{1}{2}\sin\theta\left(\mathcal{F}_+ e^{i\omega_Z t} + \mathcal{F}_- e^{-i\omega_Z t}\right)\right], \tag{4.56}$$

where we have passed into a rotating frame with respect to the atomic Zeeman splitting ω_Z.

Provided the occupation of the v mode remains small, we can adiabatically eliminate it from the dynamics following the approach of Reiter and Sørenson [194]. This procedure is essentially a perturbation theory calculation that considers 2-photon scattering processes in which a virtual photon is scattered into the v mode and reabsorbed by the atomic ensemble. Inspecting the Hamiltonian (4.56), we find three distinct processes that add one photon to the v mode:

$$-\frac{i}{2}\chi\cos\theta\; v^\dagger \mathcal{F}_z e^{-i\delta t},$$
$$-\frac{i}{4}\chi\sin\theta\; v^\dagger \mathcal{F}_+ e^{-i\delta t + i\omega_Z t},$$
$$-\frac{i}{4}\chi\sin\theta\; v^\dagger \mathcal{F}_- e^{-i\delta t - i\omega_Z t}.$$

In addition, the Hermitian conjugates of these terms remove a photon from the mode v. We must consider all pairs of processes that add a photon to the mode and subsequently reabsorb it. However, only the two-photon processes that are resonant will dominate the slow, effective, ground-state dynamics. For instance, the two-photon process proportional to $vv^\dagger\mathcal{F}_-\mathcal{F}_-$ is an off-resonant process and is, therefore, accompanied by a rapidly rotating phase factor $e^{-2i\omega_Z t}$. As a result, this term quickly averages to zero on timescales $t \gg 1/\omega_Z$, and we are justified in ignoring it. In fact, the only resonant 2-photon processes that survive are the terms proportional to $\mathcal{F}_z\mathcal{F}_z, \mathcal{F}_-\mathcal{F}_+$, and $\mathcal{F}_+\mathcal{F}_-$, since all other terms have rapidly oscillating phase factors. The result of this elimination scheme is an effective Hamiltonian for the spins:

$$H_{\text{eff}} = \frac{\chi^2}{4}\left[\mathcal{F}_z\mathcal{F}_z\;\zeta(\delta)\cos^2\theta + \frac{1}{4}\mathcal{F}_+\mathcal{F}_-\;\zeta(\delta_-)\sin^2\theta + \frac{1}{4}\mathcal{F}_-\mathcal{F}_+\;\zeta(\delta_+)\sin^2\theta\right], \tag{4.57}$$

where $\delta_\pm = \delta \mp \omega_Z$ are the detunings from the two-photon resonance, κ is the cavity linewidth, and $\zeta(\delta) = \delta/[\delta^2 + (\kappa/2)^2]$. At large detuning $\delta \gg \kappa, \omega_Z$, Eq. 4.57 simplifies to Eq. 4.9, and we obtain the desired model with an anisotropy parameter Δ controlled by the angle θ of the magnetic field.

The effective Hamiltonian (4.9), however, is obtained only if the $\mathcal{F}_+\mathcal{F}_-$ and $\mathcal{F}_-\mathcal{F}_+$ terms in Eq. 4.57 are balanced, which occurs perfectly only in the limit $\delta \to \infty$. More generally, at finite δ, the cross-terms $\mathcal{F}_x\mathcal{F}_y$ do not cancel and we obtain an effective Hamiltonian

$$\begin{aligned} H_{\text{eff}} &= \frac{\chi^2}{4}\left[\mathcal{F}_z\mathcal{F}_z\ \zeta(\delta)\cos^2\theta + \frac{1}{4}\left(\mathcal{F}_x\mathcal{F}_x + \mathcal{F}_y\mathcal{F}_y\right)\ \left(\zeta(\delta_-) + \zeta(\delta_+)\right)\sin^2\theta\right] + \\ &+ \frac{\chi^2}{4}\sum_i \xi_i^2 S_i^z\left(\zeta(\delta_-) - \zeta(\delta_+)\right), \end{aligned} \tag{4.58}$$

which is of the same form as Eq. 4.9, but with additional non-uniform longitudinal magnetic field terms. Such on-site terms, however, are sub-extensive relative to the spin-spin interaction terms. Moreover, we show numerically in Section 4.10 that these additional terms do not affect the integrability of the model at $S = 1/2$ and finite N.

Effects of dissipation

In addition to the coherent dynamics, the driven cavity system suffers from dissipation due to photon loss from the v mode and atomic free-space scattering from the excited states. These processes can be described formally in a quantum master equation by the relaxation operators

$$L_v = \sqrt{\kappa}\ v \tag{4.59}$$

and

$$L_{n,(m,m')} = \sqrt{C_{m,m'}\Gamma_{\text{sc},n}}\left(|m\rangle\langle m'|\right)_n, \tag{4.60}$$

respectively. Here, (m, m') label internal states of the individual atoms indexed by $n = 1, \ldots, 2SN$. $C_{m,m'}$ are branching ratios that sum to unity. $\Gamma_{\text{sc},n} = (\Omega_n/\mathcal{D})^2\Gamma$ is the free-space scattering rate for the nth atom, where $\mathcal{D}$ is the detuning from atomic resonance and Γ is the natural excited-state linewidth. In comparison to the scheme presented in Section 4.2, note that the Rabi frequency Ω_n and detuning $\mathcal{D}$ enter likewise into the interaction strength in the Hamiltonian (4.9), where $(\chi\xi_n)^2 \sim (\Omega_n/\mathcal{D})^2 g_n^2$. Thus, the scattering rate scales as $\Gamma_{\text{sc},n} \sim (\chi\xi_n)^2/(\eta\kappa)$.

The cavity dissipation described by L_v generates collective dephasing of the atomic ensemble. Upon adiabatically eliminating the cavity mode using the Reiter-Sørenson procedure, we find that cavity dissipation leads to an effective relaxation operator

$$L_{v,\text{eff}} = \sqrt{\kappa}\ \frac{\chi}{2}\left[\mathcal{F}_z\frac{\cos\theta}{\delta + i\kappa/2} + \mathcal{F}_+\frac{\sin\theta}{2\delta_+ + i\kappa}e^{i\omega_Z t} + \mathcal{F}_-\frac{\sin\theta}{2\delta_- + i\kappa}e^{-i\omega_Z t}\right]. \tag{4.61}$$

Due to the rapidly oscillating phase factors $e^{\pm i\omega_z t}$, this relaxation operator may be split into three effective relaxation operators

$$L_\pm = \sqrt{\gamma/2}\;\mathcal{F}_\pm, \tag{4.62a}$$

$$L_z = \sqrt{\Delta\gamma}\;\mathcal{F}_z, \tag{4.62b}$$

where we have introduced the collective decay rate

$$\gamma = \frac{\kappa\chi^2\sin^2\theta}{8[\delta^2 + (\kappa/2)^2]}. \tag{4.63}$$

By contrast, the free-space scattering operators $L_{n,(m,m')}$ act directly on the spins so there is no need to apply the adiabatic elimination procedure.

To what extent do these dissipative processes spoil the signatures of the integrability studied in Section 4.5? In the strongly quantum regime at small S, for instance, one might be interested in being able to evolve the system long enough to see the plateaus in the autocorrelation function $G_l(t)$, as observed in Fig. 4.5. To do so, we must ensure that the dissipation timescale is short compared to the timescale τ_l required for the plateaus to appear. While the full dynamics including both coherent and dissipative processes is difficult to access numerically, we can estimate the dissipative timescales by solving for the dynamics in the presence of dissipation alone. In the absence of coherent dynamics (i.e. $H = 0$), one can compute the equations of motion for the expectation values of operators using the Lindblad equation:

$$\frac{d}{dt}\langle\mathcal{O}\rangle = \sum_r \left\langle L_r^\dagger \mathcal{O} L_r - \frac{1}{2}L_r^\dagger L_r\mathcal{O} - \frac{1}{2}\mathcal{O}L_r^\dagger L_r\right\rangle, \tag{4.64}$$

where r runs over the set of relaxation operators. Plugging in the free-space scattering operators $L_r = L_{n,(m,m')}$, and assuming an approximately uniform scattering rate $\Gamma_{\mathrm{sc},n} = \Gamma_{\mathrm{sc}}$, one can show that bilinears of spin-S operators S_j^α obey the following equations of motion for $j \neq k$:

$$\frac{d}{dt}X_{jk} = -2(1+C)\Gamma_{\mathrm{sc}}X_{jk}, \tag{4.65a}$$

$$\frac{d}{dt}Z_{jk} = -4\Gamma_{\mathrm{sc}}Z_{jk}, \tag{4.65b}$$

where we have introduced the notation

$$X_{jk} = \left\langle S_j^x S_k^x + S_j^y S_k^y\right\rangle,$$
$$Z_{jk} = \left\langle S_j^z S_k^z\right\rangle.$$

Thus, the bilinear operators decay on a timescale $\tau \sim 1/\Gamma_{\mathrm{sc}}$ due to free-space scattering.

We can perform a similar calculation for the collective relaxation operators (4.62) generated by photon loss from the cavity mode. For large detuning $\delta_\pm \approx \delta \gg \kappa, \omega_z$, one can show that the spin bilinears obey the following equations of motion for $j \neq k$:

$$\frac{d}{dt}X_{jk} = -\gamma\left[\frac{1}{2}\cos^2\theta\left(\xi_j - \xi_k\right)^2 + \frac{1}{4}\sin^2\theta\left(\xi_j^2 + \xi_k^2\right)\right]X_{jk} + 2\gamma\sin^2\theta\xi_j\xi_k Z_{jk}, \tag{4.66a}$$

$$\frac{d}{dt}Z_{jk} = -\frac{\gamma}{4}\sin^2\theta\left[2\left(\xi_j^2 + \xi_k^2\right)Z_{jk} - \xi_j\xi_k X_{jk}\right]. \tag{4.66b}$$

Assuming that the weights ξ_i are numbers of order one, the bilinear operators therefore decay on a timescale $\tau \sim 1/\gamma$. A key result of this analysis is that the collective dissipation rate is, somewhat surprisingly, independent of the atom number $\sim NS$, exhibiting no superradiant enhancement. The reason for this is that the average effects of the $L_\pm$ Lindblad operators cancel in the large-detuning limit, where $\delta_+ \approx \delta_-$. In practice, at finite detuning, any imbalance in these terms can be corrected by adding a weak auxiliary drive field, with no other significant effect on the dynamics.

The relative strengths of decay via the cavity (γ) and via spontaneous emission (Γ_{sc}) are controlled by the detuning δ. The total decay rate $\gamma + \Gamma_{\text{sc}}$, at fixed interaction strength J^2, is minimized by choosing a detuning $\delta = \sqrt{1+\eta}\kappa$. For weak to moderate cooperativity $\eta \lesssim 1$, we may instead choose a larger detuning satisfying the conditions $\delta \gg \kappa, \omega_Z$ assumed above.

4.10 Appendix B: Details on the integrability* phase

Many-body bandwidth

We now present analytical and numerical evidence that the choice of normalization for the Hamiltonian in Eq. 4.2 leads to a sensible thermodynamic limit. On the one hand, we show that the many-body bandwidth W scales *superlinearly*, to wit: $W \sim \mathcal{O}(N^{3/2})$. An important caveat is that W *per se* does not mean much unless it is weighed by the many-body density of states $\rho(E)$. On the other hand, the energy fluctuations ΔE (at least at high temperatures) scale as $\Delta E \sim \mathcal{O}(\sqrt{N})$ which leads to an extensive specific heat, as one would normally expect.

Let us start by rewriting the Hamiltonian as

$$H = \frac{1}{S\sqrt{N}}\left[\mathcal{F}_x^2 + \mathcal{F}_y^2 + \Delta\mathcal{F}_z^2\right], \tag{4.67}$$

where $\boldsymbol{\mathcal{F}} \equiv \sum_i J_i \mathbf{S}_i$. Each operator $\mathcal{F}_\alpha^2$ has non-negative eigenvalues and we denote the largest one by f_0^2. Note that it is the same for all $\alpha \in \{x, y, z\}$ by isotropy. Thus, the largest eigenenergy E_M of H is bounded by

$$E_M \leq \frac{f_0^2}{S\sqrt{N}}(2 + \Delta). \tag{4.68}$$

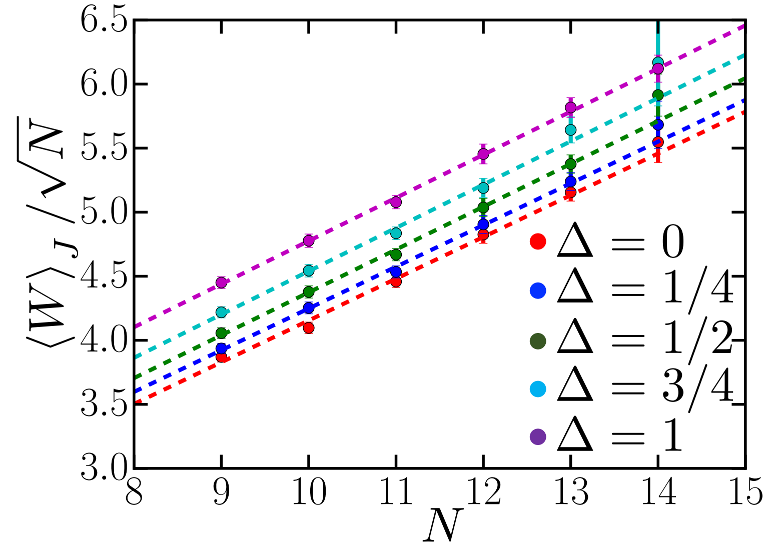

Figure 4.8: Numerically obtained and disorder-averaged many-body bandwidth $\langle W \rangle_J N^{-1/2}$ as a function of the system size N for different values of the anisotropy Δ (different colors). The dashed lines correspond to a linear fit. This is consistent with the prediction that $\langle W \rangle_J \sim \mathcal{O}(N^{3/2})$, as detailed below.

We can also bound E_M below by using any properly normalized variational state $|\psi\rangle$ since $E_\psi = \langle\psi| H |\psi\rangle = \sum_n E_n |\langle\psi|n\rangle|^2 \leq E_M \sum_n |\langle\psi|n\rangle|^2 = E_M$. Let us choose

$$|\psi\rangle = \bigotimes_{i=1}^{N} |S_i^z = \mathrm{sgn}\,(J_i)\, S\rangle \tag{4.69}$$

as a variational state. Then $\langle\psi| H |\psi\rangle = \frac{\Delta}{S\sqrt{N}} \langle\psi| \mathcal{F}_z^2 |\psi\rangle$ and

$$\langle\psi| \mathcal{F}_z^2 |\psi\rangle = S^2 \left(\sum_{i=1}^{N} |J_i| \right)^2 . \tag{4.70}$$

Moreover, this variational state is an eigenstate of $\mathcal{F}_z$ and has the largest eigenvalue $f_0 = S \sum_i |J_i|$. Thus, we find that

$$\frac{\Delta S}{\sqrt{N}} \left(\sum_{i=1}^{N} |J_i| \right)^2 \leq E_M \leq \frac{(2+\Delta) S}{\sqrt{N}} \left(\sum_{i=1}^{N} |J_i| \right)^2 . \tag{4.71}$$

Since the fields J_i are sampled from $\mathcal{N}(0,1)$, the random variable $|J_i|$ has a half-normal distribution with mean $\mu = \sqrt{2/\pi}$ and variance $\sigma^2 = \left(1 - \frac{2}{\pi}\right)$. Then $Z \equiv \sum_i |J_i|$ has mean $N\mu$ and variance $N\sigma^2$ so $\langle Z^2 \rangle_J = N^2\mu^2 + N\sigma^2$. Thus, at large N, $\left\langle (\sum_i |J_i|)^2 \right\rangle_J \approx 2N^2/\pi$.

After disorder averaging Eq. 4.71 we get

$$\frac{2\Delta S}{\pi}N^{3/2} \lesssim \langle E_M\rangle_J \lesssim \frac{2(2+\Delta)S}{\pi}N^{3/2}, \tag{4.72}$$

which shows that the disorder averaged $\langle E_M\rangle_J \sim \mathcal{O}(N^{3/2})$.

We now put bounds on the ground state energy E_m. Clearly, $E_m \geq 0$. More importantly, we note that

$$|\phi\rangle = \bigotimes_i |S_i^z = S\rangle \tag{4.73}$$

is an exact eigenstate of H with energy $E_\phi = \frac{\Delta S}{\sqrt{N}}\left(\sum_i J_i\right)^2$. Since $\left\langle\left(\sum_i J_i\right)^2\right\rangle_J = N$, we find that

$$0 \leq \langle E_m\rangle_J \leq \langle E_\phi\rangle_J = \Delta S N^{1/2}, \tag{4.74}$$

which shows that $\langle E_m\rangle_J \sim \mathcal{O}(N^{1/2})$. Since $\langle E_M\rangle_J \sim \mathcal{O}(N^{3/2})$, this concludes our proof that the disorder-averaged bandwidth scales as $\langle W\rangle_J \sim N^{3/2}$. We have also computed $\langle W\rangle_J$ numerically and we find an excellent agreement with the above analysis, as shown in Fig. 4.8.

Finally, we note that although W scales superlinearly, it is quite possible that the bulk of the many-body states are located around a typical energy $E_{\text{typ}} \sim \mathcal{O}(N)$ and that the density of states has a long and thin tail extending all the way to $\mathcal{O}(N^{3/2})$.

Energy fluctuations

We now show that the disorder-averaged thermal energy fluctuations $(\Delta E)^2$ at high temperatures scale as $\langle(\Delta E)^2\rangle_J = cN$ for some constant c. Note that, by the fluctuation-dissipation theorem, this means that the specific heat *per particle* behaves as $\frac{C_v}{N} \approx \frac{c}{T^2}$ at high temperatures T.

The energy fluctuations are defined as

$$(\Delta E)^2 = \langle H^2\rangle_T - \langle H\rangle_T^2, \tag{4.75}$$

where $\langle\ldots\rangle_T \equiv \left(\operatorname{Tr} e^{-\beta H}\right)^{-1}\operatorname{Tr}\left[e^{-\beta H}\ldots\right]$ denotes thermal averaging. For simplicity, we will focus on the $S = 1/2$ and $\Delta = 1$ case. At lowest order in β we can approximate

$$\begin{aligned}\langle H\rangle_T &\approx \frac{1}{2^N}\frac{3}{S\sqrt{N}}\sum_{ij} J_i J_j \operatorname{Tr}\left[S_i^\alpha S_j^\alpha\right] \\ &= \frac{3}{2\sqrt{N}}\left(\sum_i J_i^2\right) \\ &= \frac{3}{2\sqrt{N}}Z,\end{aligned} \tag{4.76}$$

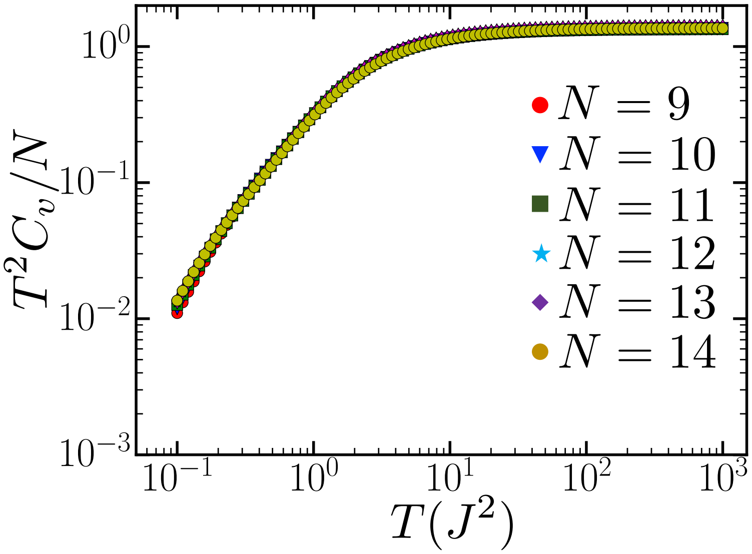

Figure 4.9: Numerically obtained scaling collapse of C_vT^2/N (where C_v is the specific heat) as a function of the temperature T. We see that at high temperatures the specific heat approaches $\frac{c}{T^2}N$ with $c \approx 1.4$. This is in very good agreement with the result from Eq. 4.78 wherein the constant is $3/2$.

where $Z \sim \chi^2(N)$. Similarly, the first term becomes

$$\begin{aligned}\langle H^2\rangle_T &\approx \frac{1}{2^N}\frac{1}{S^2N}\sum_{ijkl} J_iJ_jJ_kJ_l \sum_{\alpha\beta} \mathrm{Tr}\left[S_i^\alpha S_j^\alpha S_k^\beta S_l^\beta\right] \\ &= \frac{1}{N2^{N-2}}\sum_{ijkl} J_iJ_jJ_kJ_l \left\{\sum_\alpha \mathrm{Tr}\left[S_i^\alpha S_j^\alpha S_k^\alpha S_l^\alpha\right] + \sum_\alpha\sum_{\beta\neq\alpha} \mathrm{Tr}\left[S_i^\alpha S_j^\alpha\right]\mathrm{Tr}\left[S_k^\beta S_l^\beta\right]\right\} \\ &= \frac{1}{N}\sum_{ijkl} J_iJ_jJ_kJ_l\left\{9\left[\mathrm{Tr}\,(S_i^z)^2\right]^2\delta_{ij}\delta_{kl} + 6\left[\mathrm{Tr}\,(S_i^z)^2\right]^2\delta_{ij}\delta_{kl}\right\} \\ &= \frac{15}{4N}\left(\sum_i J_i^2\right)^2 \\ &= \frac{15}{4N}Z^2.\end{aligned} \tag{4.77}$$

Putting the two results together we find that $(\Delta E)^2 \approx \frac{3}{2N}Z^2$. Since Z is chi-squared distributed $\chi^2(N)$, we know that $\mathbb{E}\left[Z^2\right] = N^2 + 2N$. Thus, after averaging over disorder, we get

$$\left\langle(\Delta E)^2\right\rangle_J \approx \frac{3}{2}N. \tag{4.78}$$

This ensures that the specific heat $C_v = \frac{3}{2T^2}N$ is extensive. We can also compute this

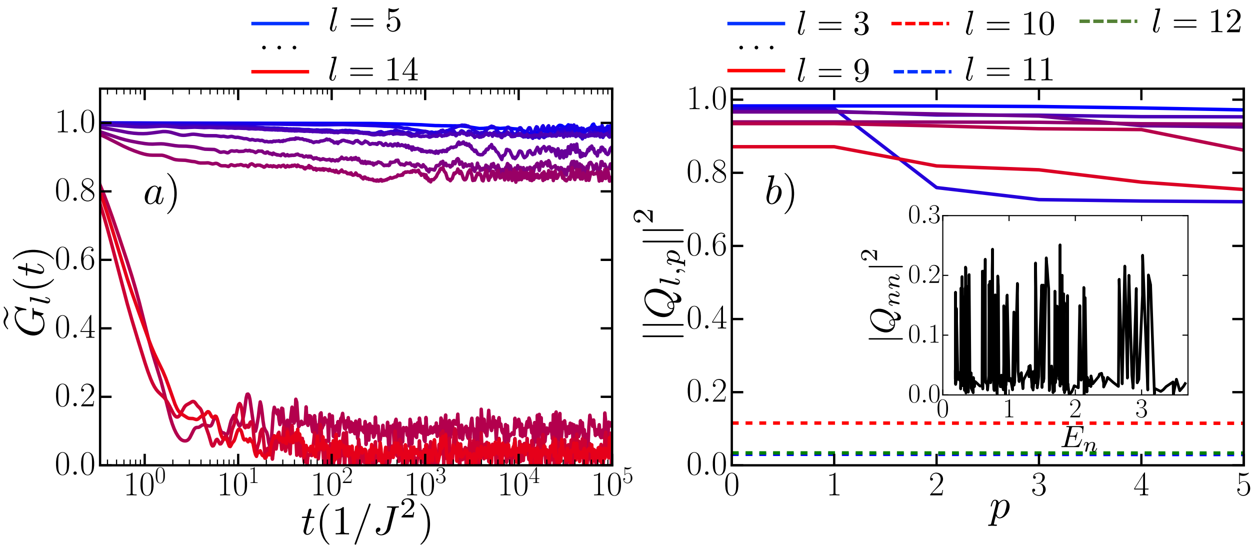

Figure 4.10: Effects due to the overlap between the slow modes $\hat{Q}_l$ and higher powers of the exactly conserved quantities, $\hat{H}$ and $\hat{S}^z_{\mathrm{tot}}$. These results correspond to a fixed disorder realization for the $\{J_i\}$ in a system of $N = 9$ spins ($S = 1/2$) with $\Delta = 0.9$. a) The correlation function $\widetilde{G}_l(t)$ for the slow modes $\widetilde{Q}_l$ with $l > 4$ in a space orthogonal to the one spanned by the operators defined in Eq. 4.79. We use a color gradient between $l = 5$ (blue curve) and $l = 14$ (red curve). b) The plateau values after we substract the contributions from $\hat{H}^p$ as a function of the power p (see the definition in Eq. 4.80). We use a color gradient for the solid curves in which $l = 3$ corresponds to the blue curve and $l = 9$ corresponds to the red curve; the red, blue, green dashed curves correspond to $l = 10, 11, 12$, respectively. (inset) The diagonal matrix elements $\left|\langle n| \hat{Q}_3 |n\rangle\right|^2$ for the mode $l = 3$ as a function of the energy eigenvalue E_n. This example provides further evidence that the slow modes $\hat{Q}_l$ are far away from being projectors on many-body energy eigenstates.

quantity numerically using the exact spectrum of H and we find an excellent agreement, as shown in Fig. 4.9.

Overlaps with higher powers of the conserved quantities $\hat{H}$ and $\hat{S}^z_{\mathrm{tot}}$

We now address the possibility that the large plateau values (Fig. 4.4) observed in the quantum model at intermediate $\Delta \in (0, 1)$ are caused by a significant overlap between the slow operators $\hat{Q}_l$ and higher powers of the conserved quantities, $\hat{H}$ and $\hat{S}^z_{\mathrm{tot}}$. We use a twofold approach, as detailed below.

Let us first summarize why this is a legitimate concern. Recall that at $\Delta \in (0, 1)$, the SVD analysis finds two exactly conserved spin bilinears, $\hat{H}$ and $(\hat{S}^z_{\mathrm{tot}})^2$, along with another $N - 2$ slow modes Q_l, where $l = 3, \ldots, N$. The auto-correlation function of the latter operators exhibits a large long-time plateau, which we interpreted as a consequence of the existence of further conservation laws (4.30) and of quantum integrability. However, it is possible the the $\hat{Q}_l$s overlap non-trivially with exactly conserved operators such as $\hat{H}^p(\hat{S}^z_{\text{tot}})^{p'}$: these higher powers of the exactly conserved quantities consist of k-body terms, including $k = 2$, so they have non-zero support in the space of spin bilinears and, thus, can conceivably overlap with $\hat{Q}_l$.

Furthermore, the support in the space of 2-local operators can be non-zero even in the thermodynamic limit $N \to \infty$ due to the all-to-all nature of the interaction. For instance, consider $\hat{\mathcal{O}}_1 = \frac{1}{\sqrt{N}}\hat{H}$. By the previous section, we know that $\frac{1}{\text{Tr}[\mathbf{1}]}\,\text{Tr}\left[\hat{\mathcal{O}}_1^2\right]$ is of order one even in the thermodynamic limit. Similarly, let $\hat{\mathcal{O}}_2 = \frac{1}{N}\left(\hat{S}^z_{\text{tot}}\right)^2$ such that $\frac{1}{\text{Tr}[\mathbf{1}]}\,\text{Tr}\left[\hat{\mathcal{O}}_2^2\right]$ is also of order one as $N \to \infty$. It is not hard to check that the only 2-body terms emerging from higher powers of the conserved quantities, namely operators of the form $\hat{\mathcal{O}}_1^p\hat{\mathcal{O}}_2^{p'}$, that do *not* vanish in the thermodynamic limit are:

$$\begin{aligned}
\hat{\mathcal{O}}_1 &= \frac{1}{\sqrt{N}}\hat{H}, \\
\hat{\mathcal{O}}_2 &= \frac{1}{N}\left(\hat{S}^z_{\text{tot}}\right)^2, \\
\hat{\mathcal{O}}_3 &= \frac{1}{N}\sum_{ij} J_iJ_j\hat{S}^z_i\hat{S}^z_j, \\
\hat{\mathcal{O}}_4 &= \frac{1}{N}\sum_{ij} J_i\hat{S}^z_i\hat{S}^z_j.
\end{aligned} \tag{4.79}$$

Above, $\hat{\mathcal{O}}_3$ can be generated by $\hat{\mathcal{O}}_1\hat{\mathcal{O}}_1$ as long as $\Delta \in (0, 1)$, and $\hat{\mathcal{O}}_4$ by $\hat{\mathcal{O}}_1\hat{\mathcal{O}}_2$ (in fact, one gets a prefactor $\frac{1}{N}\sum_k J_k$; it scales as $1/\sqrt{N}$ typically if J_k has zero mean and as $O(1)$ if $\overline{J_k} \neq 0$; by precaution, we still include it in the following analysis). We perform a Gram-Schmidt orthonormalization of these four operators to obtain a basis set $\left\{\widetilde{\mathcal{O}}_1, \widetilde{\mathcal{O}}_2, \widetilde{\mathcal{O}}_3, \widetilde{\mathcal{O}}_4\right\}$ wherein $\frac{1}{\text{Tr}[\mathbf{1}]}\,\text{Tr}\left[\widetilde{\mathcal{O}}_i\widetilde{\mathcal{O}}_j\right] = \delta_{ij}$. We then define a matrix R whose columns vectors are the $\widetilde{\mathcal{O}}_i$s. This allows us to perform the SVD analysis in the operator space orthogonal to the one spanned by the $\widetilde{\mathcal{O}}_i$s: using the time series matrix M from Eq. 4.24, we perform the SVD decomposition of $\left(\mathbf{1} - RR^\dagger\right)M$ instead. Trivially, we find that the first four singular values are exactly zero so we focus on the modes corresponding to $l > 4$. Following the prescription from Section 4.5, we define the slow operators $\widetilde{Q}_l$ for $l \geq 5$ and compute their auto-correlation function $\widetilde{G}_l(t) = \frac{1}{\text{Tr}[\mathbf{1}]}\,\text{Tr}\left[\widetilde{Q}_l(t)\widetilde{Q}_l(0)\right]$, as shown in Fig. 4.10a. Thus, we see that the overlap with higher powers of $\hat{H}$ and $\hat{S}^z_{\text{tot}}$ has a negligible effect on the plateau values of the slow modes $\hat{Q}_l$.

In the second approach, we numerically study the effect of $\hat{H}^p$ on the plateau values by analyzing the matrix elements $Q_{l,nn} \equiv \langle n|\,\hat{Q}_l\,|n\rangle$, where $|n\rangle$ is an energy eigenstate, $H\,|n\rangle =$

$E_n\,|n\rangle$. Let us define the vector $\vec{q}_l$ whose elements are $q_l^{(n)} = \frac{1}{\sqrt{\mathrm{Tr}[\mathbf{1}]}}\,|Q_{l,nn}|$. It is known that the norm of this vector is just the plateau value of the Q_l mode, whenever the latter is well-defined: $g_l = \|\vec{q}_l\|^2$. Another way of studying the effect of $\hat{H}^p$ on the plateau value is to analyze the overlap between $\vec{q}_l$ and the set of vectors $\left\{\vec{E}^{(p)} : E_n^{(p)} = (E_n)^p\,, 0 \le p \le P\right\}$, i.e. the powers of the energy eigenvalues.

Once again, we perform a Gram-Schmidt orthonormalization of the above vectors to obtain a set $\{\vec{\eta}_i : 0 \le i \le P\}$ wherein $\langle\vec{\eta}_i|\vec{\eta}_j\rangle \equiv \vec{\eta}_i^{\,T} \cdot \vec{\eta}_j = \delta_{ij}$. We then define

$$\|Q_{l,p}\|^2 = \|\vec{q}_l\|^2 - \sum_{i=1}^{p} \left|\vec{q}_l^{\,T} \cdot \vec{\eta}_i\right|^2\,, \tag{4.80}$$

which is a measure of the residual plateau value for the mode $\hat{Q}_l$ after removing the contributions of $\hat{H}^0, \hat{H}^1, \ldots, \hat{H}^p$. Naturally, for any fixed mode index l, $\|Q_{l,p}\|^2$ decreases from the plateau value $\|Q_{l,0}\|^2 = \|\vec{q}_l\|^2 = g_l$ as p increases. Numerically, in Fig. 4.10b (main plot), we observe that for the slow modes, $2 < l < N$, the decrease is small compared to g_l for powers up to $p \sim N/2$, at which point $\hat{H}^p$ becomes an N-body operator. In fact, $\|Q_{l,p}\|^2$ depends roughly linearly on p and decays approximately to zero only when $p \sim 2^N \gg N$. We have also checked that the result is not altered upon including low powers of $\hat{S}^z_{\mathrm{tot}}$ (i.e. removing contributions from $\hat{H}^p(\hat{S}^z_{\mathrm{tot}})^r$, for $p, r \le N$). Therefore, the plateaus of the slow modes are not caused by simple functions of the exactly conserved quantities, $\hat{H}$ and $\hat{S}^z_{\mathrm{tot}}$, at $\Delta \in (0, 1)$. Finally, the inset of Fig. 4.10b shows that slow modes $\hat{Q}_l$ are not a linear combination of a few projectors onto energy eigenstates.

To summarize, these analyses render highly unlikely the possibility that the slow mode plateaus at intermediate Δ are solely due to the overlap with the known conserved quantities. This reinforces the thesis of the existence of further *nontrivial* conserved quantities (4.30), as put forth in the main text.

The middle of the SVD spectrum

We now check that, at $\Delta = 1.0$, we do not find more than $N + 1$ bilinear conserved quantities, as suggested by the analytic results of Section 4.3. More precisely, we numerically compute the plateau values corresponding to the $l = N + 2$, $l = 3N$, and $l = N^2$ modes obtained from the quantum SVD analysis. As shown in Fig. 4.11, we see that the latter two plateau values decrease with the system size N. However, this is not entirely clear for the $N + 2$ mode as its flow with system size is inconclusive—we conjecture that this is a finite size effect rather than a sign of an additional conserved quantity.

Level statistics

We also analyze the level statistics of the quantum Hamiltonian (4.2) by studying the ratio of adjacent energy levels E_n defined by $r_n = \min\{\Delta E_n, \Delta E_{n+1}\}/\max\{\Delta E_n, \Delta E_{n+1}\}$,

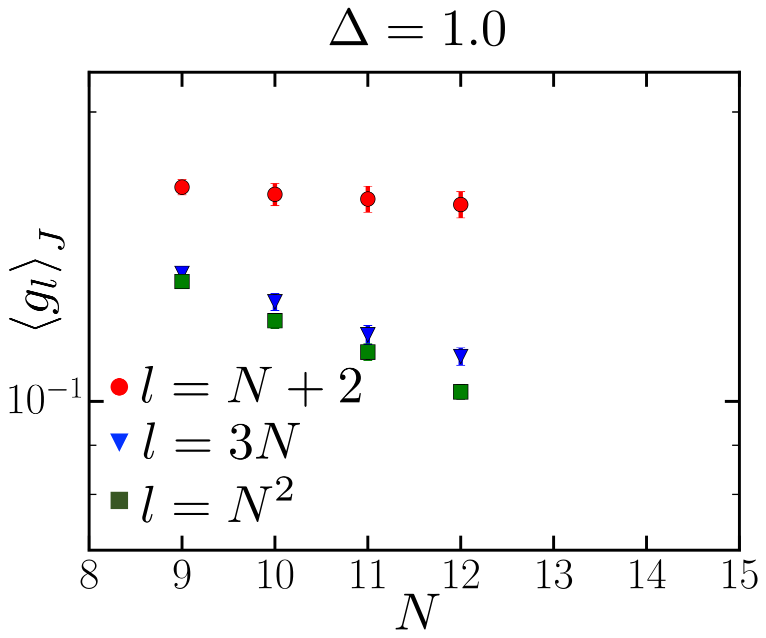

Figure 4.11: Semilog plot of of the disorder-averaged plateau values $\langle g_l \rangle_J = \langle G_l\,(t \to \infty)\rangle_J$ as a function of N for three modes in the middle of the SVD spectrum at $\Delta = 1.0$: the $N+2$ mode which is expected to be the first decaying mode, the $3N$ mode, and the $3N^2$ mode. We see that the latter two decay as N increases, but this is not completely clear for the $N+2$ mode.

where $\Delta E_n = E_{n+1} - E_n$. We now provide details vis-à-vis the various symmetries and subsequent degeneracies we have to take into account.

At $\Delta = 1$ the Hamiltonian has the full SU(2) symmetry and the eigenstates of H are grouped in blocks corresponding to irreducible representations (irreps). Each state is simultaneously an eigenstate of $\hat{S}^2_{\text{tot}}$ with an eigenvalue $S_{\text{tot}}(S_{\text{tot}}+1)$ and of $\hat{S}^z_{\text{tot}}$ with an eingenvalue $S^z_{\text{tot}} \in \{-S_{\text{tot}}, \ldots, S_{\text{tot}}\}$. Thus, each block contains $2S_{\text{tot}}+1$ eigenstates of H. We keep the states in a fixed sector of both $\hat{S}^2_{\text{tot}}$ and $\hat{S}^z_{\text{tot}}$ by selecting the block S_{tot} that has the largest multiplicity in the irreps. decomposition (i.e. the most frequent block to obtain the largest number of viable states).

At $\Delta \neq 1$ the symmetry is $\mathrm{U}(1) \rtimes \mathcal{T}$: U(1) is generated by $U_\phi = \exp\left(-i\phi S^z_{\text{tot}}\right)$ and it corresponds to the conservation of S^z_{tot}, whereas $\mathcal{T}$ represents the anti-unitary time reversal symmetry. Moreover, there is a mirror symmetry corresponding to $\hat{S}_z \to -\hat{S}_z$. For the cases wherein $\mathcal{T}^2 = -1$, we have Kramers doublets and we keep the states solely in the $S^z_{\text{tot}} = 1/2$ sector because it is the most populous. For the cases where $\mathcal{T}^2 = +1$, we keep states solely in the $S^z_{\text{tot}} = 1$ sector in order to account for the mirror symmetry as well (the states in the $S^z_{\text{tot}} = 0$ sector are degenerate under the mirror symmetry).

Having selected the eigenstates of H to account for the degeneracies due to symmetries, we compute the ratio r_n for the adjacent levels. We then average over all r_n and over disorder

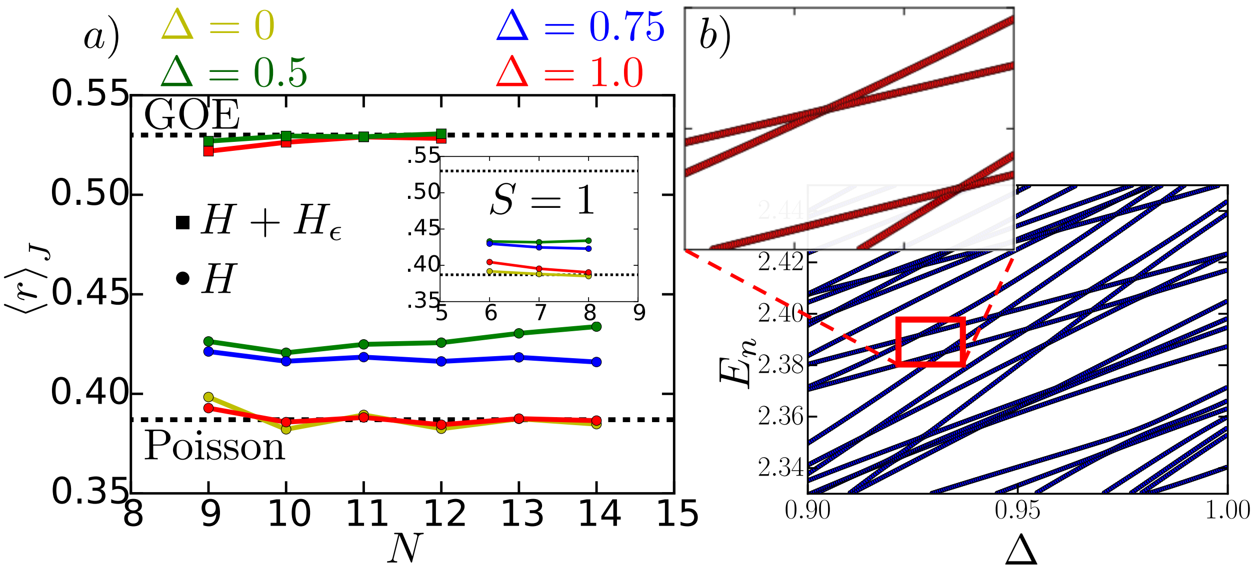

Figure 4.12: a) Plot of the disorder-averaged $\langle r \rangle_J$ as a function of the system size N for $S = 1/2$. Different colors correspond to different values of the anisotropy: red for $\Delta = 1$, blue for $\Delta = 0.75$, green for $\Delta = 0.5$, and yellow for $\Delta = 0$. We see that, for the Hamiltonian H from Eq. 4.2, the level statistics is close to Poisson (the round markers) as it would be for an integrable model. Adding the perturbation $H^{(1)}_{\epsilon=0.1}$ from Eq. 4.31 renders the level statistics of $H + H^{(1)}_{\epsilon}$ close to GOE (the square markers), signaling level repulsion and a chaotic behavior. (inset) We obtain qualitatively similar results for a Hamiltonian (4.2) consisting of $S = 1$ degrees of freedom. b) Energy levels of H within a fixed $S^z_{\rm tot} = 1/2$ sector as a function of Δ in a single disorder realization $\{J_i\}$ for a system of $N = 11$ spins ($S = 1/2$). We see many "real" (i.e. not avoided) level crossings, as shown in the inset which is a zoom on two such events. This violation of the Wigner-von Neumann non-crossing rule provides further evidence of quantum integrability at intermediate $0 < \Delta < 1$.

realizations to obtain $\langle r \rangle_J$. We know that a chaotic system exhibits level repulsion and has GOE level statistics characterized by a value $\langle r \rangle_{\rm GOE} \approx 0.53$. An integrable system does not have level repulsion (its energy levels are uncorrelated) and generically has Poissonian level statistics characterized by a value $\langle r \rangle_{\rm Poisson} \approx 0.387$.

In Fig. 4.12a we plot $\langle r \rangle_J (N)$ for different values of the anisotropy Δ. We find that both $\Delta = 0$ and $\Delta = 1$ exhibit almost perfectly Poissonian level statistics. However, for intermediate $0 < \Delta < 1$, the system of $S = 1/2$ spins (or $S = 1$ for the inset) is not as close to Poisson, although it is even farther away from GOE. Moreover, we cannot extract a meaningful flow with the system size N towards either GOE or Poisson. We note, in passing, that there are exceptions from the equivalence between integrability and Poissonian level statistics: as detailed in Ref. [55] (see also the references therein), there are well-known counterexamples [25, 37, 204, 202] of integrable systems whose level statistics are neither

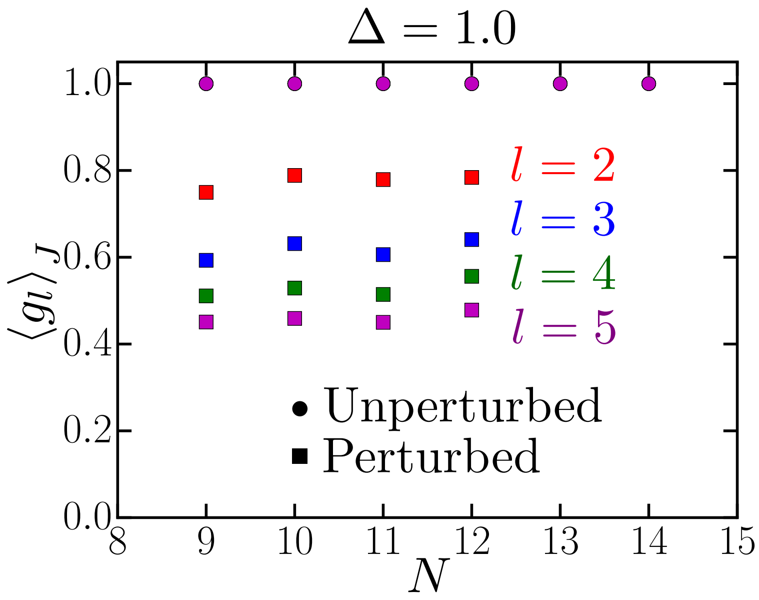

Figure 4.13: Plot of the disorder-averaged plateau values $\langle g_l \rangle_J = \langle G_l \left(t \to \infty\right) \rangle_J$ as a function of the system size N at $\Delta = 1.0$. The overlapping circular markers correspond to the lowest four modes of the unperturbed model (4.2), which has $N + 1$ bilinear conserved quantities. The square markers correspond to adding a perturbation $\frac{1}{S\sqrt{N}} \sum_i J_i^2 S_i^z$ and the different colors correspond to the lowest four modes (that are not exactly conserved) in increasing order of their singular values: red, blue, green, and magenta. While the perturbation decreases the plateau value, we note that there is no flow with system size: the perturbation is sub-extensive (suppressed by $1/\sqrt{N}$).

Poisson nor GOE.

Nonetheless, if we add the perturbation $H_\epsilon^{(1)}$ from Eq. 4.31 to H we immediately see that the system obeys almost perfectly GOE statistics even for rather small system sizes (see the curves with square markers in Fig. 4.12a).

In Fig. 4.12b we work in a fixed disorder realization for the fields $\{J_i\}$ and we adiabatically change the anisotropy Δ. Then we plot the exact energy levels within a fixed symmetry sector, as detailed above, and explicitly check whether there exist level crossings or if they are avoided (level repulsion). We find that there are numerous real crossings at intermediate Δ, which provides further qualitative evidence that H is integrable for $S = 1/2$.

Stability to the commutator perturbation

We conclude by studying the effect of the perturbation (4.33) that arises upon recasting the Hamiltonian into the "flip-flop" form of Eq. 4.34. The term $J_i J_j S_i^+ S_j^-$ from (4.34) in the main text can be written as

$$\begin{aligned} S_i^+ S_j^- &= \left(S_i^x + iS_i^y\right)\left(S_j^x - iS_j^y\right) \\ &= S_i^x S_j^x + S_i^y S_j^y + i\left[S_i^y, S_j^x\right] \\ &= S_i^x S_j^x + S_i^y S_j^y + S_i^z \delta_{ij}, \end{aligned} \tag{4.81}$$

which leads an overall term $\frac{1}{S\sqrt{N}}\sum_i J_i^2 S_i^z$ in addition to the Hamiltonian H defined in Eq. 4.2. We have argued that this is an irrelevant perturbation in a thermodynamic system with $N \gg 1$ degrees of freedom.

We now explicitly study its impact on the plateau values of the auto-correlation function $G_l(t)$. As shown in Fig. 4.13, we find that the effect of this perturbation is only quantitative: the modes reach plateau values that are lower than those occurring in the unperturbed model, but they do *not* decay as the system size N increases. We note that the quantitative shift is also due to the fact that the slow modes we compute are bilinear operators even though the perturbation $\frac{1}{S\sqrt{N}}\sum_i J_i^2 S_i^z$ is a linear combination of 1-body terms.

Chapter 5

Spin glasses and quantum Satisfiability

The potential power of quantum computers drives the immense effort to build and understand them. There are two primary theoretical approaches to characterizing the precise extent of this potential. Complexity theory [19] proceeds by identifying so-called ‘complete’ problems which are the hardest problems in a given class, such as NP. Classically, under the widely believed conjecture that P $\neq$ NP, *all* algorithmic approaches to NP-complete problems such as satisfiability (SAT) must fail on at least some subset of worst-case instances. Over the last decade, these venerable considerations have been extended to the quantum case, where QMA-complete problems are now believed to be intractable and to capture the intrinsic differences between quantum and classical computing [136]. The natural quantum generalization of SAT, so-called quantum satisfiability (QSAT) [48, 104], is conveniently such a QMA$_1$-complete problem [1].

In the second approach, the introduction of an appropriate measure on the instances of a problem generates a question in statistical Physics. Instead of worrying about worst case complexity, we attempt to understand the structure of problems which are typical with respect to the measure. For example, phase transitions which arise as functions of parameters controlling the measure often signal the regimes where the most complicated problems may be found [109]. This approach builds on the seminal insight of Fu and Anderson [91] that the intractability of NP-complete problems is a form, indeed an extreme one, of (spin) glassiness. Ensembles of both classical SAT [167, 134] and, more recently, QSAT [146, 147, 115] have been studied in this fashion.

In this chapter we build on the second approach and introduce new ensembles that interpolate between the SAT and QSAT ones. The mixture provides a convenient framework for characterizing the crossover from classical to quantum search complexity. For example, the classical PCP theorem [20] shows that it is computationally hard to approximately determine the ground state of the SAT problem, while it is still an open question whether an analogous hardness result applies in the quantum case. The interpolation allows the study of the crossover in entanglement properties of low energy states, which may bear

---

[1] While both NP and QMA complete problems are believed to be hard for both classical and quantum computers to solve, the latter are such that a classical computer cannot even verify the solution efficiently.

on this question. Similarly, in statistical physics, the mixed ensemble can shed light on entanglement phase transitions in spin-glass models with quenched disorder: the classical problem has no entangled solutions, whereas the mixed one exhibits entangled states in the UNSAT regime.

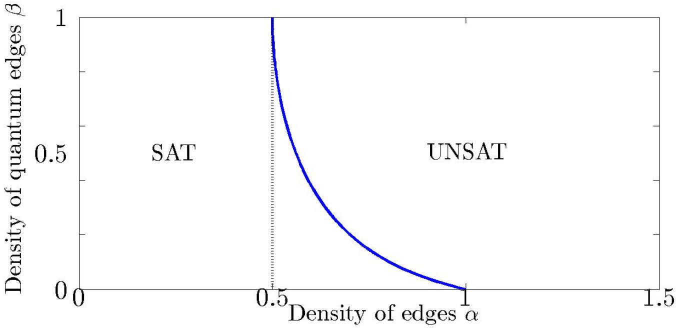

Figure 5.1: The phase boundary in the $\alpha - \beta$ plane that separates the SAT and the UNSAT regimes for the mixed classical-quantum problem. The dashed line indicates the emergence of a giant component in the ER graph (the percolation phase transition). $\beta = 0$ corresponds to the 2-SAT problem and $\beta = 1$ corresponds to the 2-QSAT problem.

Specifically for the 2-SAT/2-QSAT interpolation, we show that there is a sharp phase boundary (Fig. 5.1) which we determine rigorously by deriving coincident lower and upper bounds on the extent of the UNSAT and SAT regions, respectively. The interest in this interpolation flows considerably from a "geometrization" theorem that applies to the QSAT limit [146]. As this result is not widely known, we begin with a quick review of the relevant background which will also enable a proper definition of the problem studied herein. We then present our central technical results on the phase boundary and close with some remarks on the lessons learned and future directions.

5.1 Classical-Quantum mixing in the random 2-Satisfiability problem

An instance of k-QSAT is defined by a positive semi-definite Hamiltonian on N qubits given by the sum of M k-body interactions, $H = \sum_{m=1}^{M} \Pi_m$. Here, each interaction $\Pi_m = |\phi\rangle\langle\phi|_m$ projects onto a particular state in the local Hilbert space of the k qubits associated with interaction m. The computational problem is to decide whether H has a ground state of energy zero. If so, the problem is SAT and if not, it is UNSAT [2]. If the states $|\phi\rangle_m$ are computational basis states, we recover classical k-SAT as a special case. We can now summarize the statistical ensembles used in previous work. These involve the uniform Erdős-Rényi measure [206, 80, 44], parametrized by the 'clause density' $\alpha = M/N$, over the set

---

[2] The ground state energy is at least a promised gap Δ above zero if it is not precisely zero.

of k-hypergraphs representing the interactions in H. The interaction associated to each hyperedge is likewise uniformly chosen from the 2^k projectors in classical SAT or from the Haar measure over the rays in the 2^k dimensional Hilbert space for QSAT. We observe that the latter makes classical SAT instances highly non-generic within the QSAT ensemble and so these two can be expected to behave very differently, and indeed they do [167, 134].

The classical ensemble has been studied intensively. The broad picture that has emerged is that for all $k \geq 2$ there is a sharp SAT-UNSAT transition in the $N \to \infty$ limit as a function of α. For $k \geq 3$, there are additional transitions in the SAT regime wherein the structure of the solution space changes. For the quantum ensemble, it is known that there is a SAT-UNSAT transition for $k \geq 2$ [146, 147, 49, 31] and that there is at least one sharp transition involving the growth of entanglement in the satisfying states for $k \geq 12$ [147, 14]. A remarkable result to come out of the quantum generalization is a "geometrization theorem" [146] wherein uniformly chosen quantum projectors on *any* graph exhibit the same dimension of the satisfying manifold with probability 1. This reduces the generic QSAT decision problem to a purely graph theoretic question! The identification of this implicit graph theoretic property for $k \geq 3$ and understanding its computational difficulty is an outstanding problem.

As advertised above, we initiate a new approach by introducing ensembles that interpolate between the fully classical and quantum regimes. We do this by constraining each realization to include a fraction β of uniformly chosen quantum projectors and $1 - \beta$ uniformly chosen classical ones. As β varies between 0 and 1, we pass from the classical ensemble to the quantum one. As the classical ensemble does not exhibit geometrization and typically has larger satisfying manifolds, the interpolation has the potential to shed light on the emergence of geometrization in the quantum limit and thence on precisely where in the ensemble one might look for genuinely difficult quantum cases.

As a first step in this program, we study the case of 2-SAT/QSAT. We generate the underlying 2-graphs by drawing edges between any two sites with probability $\alpha N/\binom{N}{2}$. In the thermodynamic limit $N \to \infty$ this generates an Erdős-Rényi (ER) random graph with $M = \alpha N$ expected edges. For each edge $m = 1...M$ we label it 'quantum' with probability β and 'classical' with probability $1 - \beta$: we write $e_m \in \{Q, C\}$ if the edge between sites $(m, m+1)$ is quantum or classical. The purely classical and quantum limits are very well understood. At $\beta = 0$ [98, 90, 46] there is a sharp SAT-UNSAT transition at $\alpha_c = 1$ while for $\beta = 1$, there is a SAT-UNSAT transition at $\alpha_q = 1/2$ [146]. The quantum transition coincides with the emergence of a giant component in the underlying random graph [80].

5.2 The snip-core

The primary tool in our analysis is snipping qubits out of an interaction graph G. Classically, a node i such that $G = G' \cup \{i\}$ is *snippable* if all of the bonds connected to it agree about the bit arrangement they locally disfavor. All clauses attached to such a snippable node i can then be trivially satisfied by assigning the appropriate value to qubit i without reference to the state on G'. Thus, these bonds can be snipped from the graph G to produce a smaller graph G' which is SAT if and only if the original G is.

This definition extends naturally to the mixed classical-quantum problem ($\beta \neq 0$): a degree-one site i with a quantum projector attaching it to site j of G' is snippable. From Bravyi's construction [48], we know that the satisfying state for G' can be written as a product state $|\psi_j\rangle \otimes |\Psi_{G'\setminus\{j\}}\rangle$. If the quantum edge attaching site i disfavors the state $|\phi_{j,i}\rangle$, then we can use the transfer matrix $T_\phi = \epsilon\phi^\dagger_{j,i}$ (ϵ is the 2×2 Levi-Civita symbol) to find $|\xi_i\rangle = T_\phi |\psi_j\rangle$ such that $\langle\phi_{j,i}| |\psi_j\rangle \otimes |\xi_i\rangle = 0$. Therefore, $|\xi_i\rangle \otimes |\psi_j\rangle \otimes |\Psi_{G'\setminus\{j\}}\rangle$ is a satisfying state for $G = G' \cup \{i\}$ which shows that a degree-one site with a quantum projector attached is snippable.

However, if a generic quantum edge attaches to a site i of degree greater than 1, it cannot be locally satisfied by the state on i without reference to the rest of the graph (with probability 1). Thus, any site of degree at least 2 with a quantum edge attached is unsnippable.

For a random instance G of the mixed problem, we can iteratively remove snippable sites and the incident edges in a similar fashion to the "Leaf Removal" Algorithm [168]. When there are no snippable qubits left, this algorithm stops and we end up with a unique maximal *snip-core*. Clearly, G is SAT iff its snip-core is SAT. Moreover, if the snip-core is empty then G is SAT. Behind our considerations lies the result that when G is SAT we can always find a satisfying product state [48]. We will now analyze the structure and probability of non-empty snip-cores in order to determine the SAT-UNSAT boundary.

5.3 Upper bound on SAT region

The basic idea in this part is to identify an UNSAT motif that must be present on all snip-cores for $\alpha > \alpha_c(\beta)$ thus establishing an upper bound on the extent of the SAT region. To this end, we first note that the simplest motif that is unsnippable is the *unsnippable loop*. A loop with classical and quantum edges is said to be *unsnippable* if all of its sites are unsnippable (see Fig. 5.2a). We can find a simple example in the fully classical problem: a loop that dislikes 01 on each edge. While this loop is unsnippable, it is SAT: it has exactly two satisfying states comprised of all sites 0 or all sites 1. The same is true of the other 2^L such classical unsnippable loops of length L which are equivalent under "gauge" transformations. It can be shown that the fully quantum loop also has two SAT states [146, 48]. Moreover, based on the Geometrization Theorem we can conclude that the dimension of the kernel of the fully quantum problem is a lower bound for the mixed problem, whereas the fully classical one is an upper bound: we start from the classical unsnippable loop and slowly turn classical projectors into generic quantum ones; this can only decrease the degeneracy of satisfying states. But since both kernels have dimension two, we conclude that the mixed classical-quantum unsnippable loop always has exactly two linearly independent SAT states. Finally, an unsnippable but UNSAT motif can be constructed by decorating the unsnippable

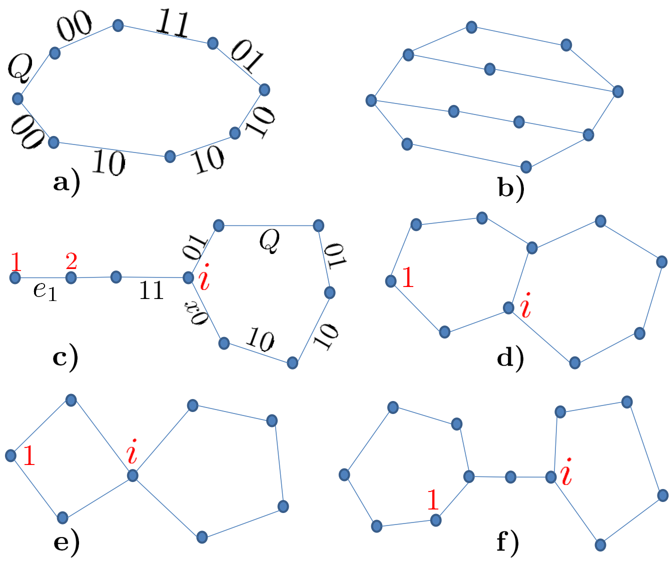

Figure 5.2: a) An unsnippable loop that contains both classical and quantum edges. b) A loop with two cross-links. If all the strings are unsnippable and the cross-links penalize the loop's two linearly independent satisfying states, this motif becomes UNSAT. c) The "lasso" motif. We start from a random site 1 and move along an unsnippable path until we pass through the same site i twice. The loop can either be unsnippable ($x = 1$) or snippable at site i ($x = 0$). d) The loop with a single cross-link. We encounter this motif if we traverse the dangling branch of the lasso and end up at a site located on the initial loop. e) The "figure eight". We encounter this motif if we traverse the dangling branch of the lasso and end up at the same starting point i. f) The "dumbbell". We encounter this motif if we traverse the dangling branch of the lasso and pass through the same point twice (located outside of the initial loop).

loop with two unsnippable cross-links—strings joining two different points on the loop whose interior sites are unsnippable (Fig. 5.2b) that penalize the two SAT states.

We now turn to the probability of finding UNSAT unsnippable loops with cross-links. Quite generally, the expected number of subgraphs A in the ER ensemble on N nodes is

$$\mathbb{E}(\#\text{ of } A) = \frac{N!}{(N-|A|)!\mathrm{Aut}(A)} p^{e(A)}, \tag{5.1}$$

where $|A|$ and $e(A)$ represent the number of vertices and edges of A, respectively; $\mathrm{Aut}(A)$ is the number of automorphisms of A and $p = \alpha N/\binom{N}{2}$. For a loop of length L we have $|L| = e(L) = L$ and $\mathrm{Aut}(L) = 2L$. Introducing the probability that a given loop is unsnippable, we find the expected number of unsnippable loops $\#_{\mathrm{uns}}(L)$ is

$$\#_{\mathrm{uns}}(L) = \binom{N}{L} \frac{L!}{2L} \left(\frac{2\alpha}{N-1}\right)^{L} p(L \text{ is unsnippable}). \tag{5.2}$$

For any fixed length L and as $N \to \infty$, $\#_{\text{uns}}(L)$ scales as $\mathcal{O}(N^0)$. More generally, the number of subgraphs with $m = e(A) - |A|$ cross-links vanishes in the thermodynamic limit as $\mathcal{O}(N^{-m})$. This result holds irrespective of the form of $p(A$ is unsnippable) since this probability has no explicit dependence on N. It follows that in order to get a non-vanishing number of UNSAT motifs we must consider *giant loops* whose size scales with N as $L = lN$ $(0 < l \leq 1)$.

To calculate the number of unsnippable giant loops we need the last factor in Eq. (5.2). For a collection $\{e_i\}$ of M edges, the probability that site i is unsnippable is $1 - \delta_{e_i,C}\delta_{e_{i+1},C}/2$. In words, if it is connected to a quantum edge then it is unsnippable with probability 1; otherwise it is unsnippable with probability 1/2. Also, from the definition of the random ensemble we have $p(e_i = Q) = \beta$ and $p(e_i = C) = 1 - \beta$. Hence, for a loop of length L

$$p(\text{L is unsnippable}) = \sum_{\{e_i\}} \prod_{i=1}^{L} p(e_i) \left(1 - \frac{\delta_{e_i,C}\delta_{e_{i+1},C}}{2}\right). \tag{5.3}$$

Using a standard transfer matrix technique and focusing solely on the dominant eigenvalue λ_+ which controls the result for large loops, we find that

$$p(\text{L is unsnippable}) \approx \left(\frac{1 + \beta + \sqrt{-7\beta^2 + 10\beta + 1}}{4}\right)^L. \tag{5.4}$$

With this in hand, we return to Eq. (5.2) and use Stirling's approximation to find the extensive part of the entropy,

$$S_{\text{uns}}(l) = N\left[l\left(\log(2\alpha\lambda_+) - 1\right) - (1 - l)\log(1 - l)\right]. \tag{5.5}$$

Giant unsnippable loops proliferate exponentially in N if the entropy function is positive for some $1 \geq l > 0$. Since $S_{\text{uns}}(0) = 0$ and $S'_{\text{uns}}(l) = N\left[\log(2\alpha\lambda_+) + \log(1 - l)\right] \leq N\log(2\alpha\lambda_+)$, we see that $S_{\text{uns}}(l)$ is a negative and decreasing function on $0 < l \leq 1$ for $2\alpha\lambda_+ < 1$. However, for $2\alpha\lambda_+ > 1$, the entropy goes positive for small l and large numbers of giant unsnippable loops emerge. As we find $e^{\mathcal{O}(N)}$ loops on just N sites, the loops must intersect and overlap repeatedly. It follows that any given giant loop is covered by a finite density of cross-links and therefore the probability of finding an UNSAT unsnippable loop with cross-links approaches 1 as $N \to \infty$ for α greater than

$$\alpha_c(\beta) = \frac{2}{1 + \beta + \sqrt{-7\beta^2 + 10\beta + 1}}. \tag{5.6}$$

Hence, we conclude that that $\alpha_c(\beta)$ is an upper bound on the extent of the SAT region at any fixed β.

5.4 Lower bound on UNSAT region

We will now show that for $\alpha < \alpha_c(\beta)$ the snip-core is always SAT so that $\alpha_c(\beta)$ is also a lower bound on the extent of the UNSAT region. We do this by showing that the snip-core must contain one of a finite list of motifs [3] and that all of these *except* SAT unsnippable loops are not present as $N \to \infty$ for $\alpha < \alpha_c(\beta)$.

To show that there is a finite list of necessary motifs, we start from an arbitrary site in the snip-core which we label 1 and walk along any edge which we label e_1 that connects it to a site 2 (see Fig. 5.2c). At step 2, we walk along an edge e_2 to site 3 such that 2 is unsnippable with respect to edges e_1 and e_2. Thus, e_2 can either be quantum or, if it is classical, it has to disagree with e_1 on site 2. From this point onward, we take further steps as follows:

- At step k: we move along an edge e_k that connects it to $k + 1$ such that site k is unsnippable.
- Iterate until we pass through a site i twice.

Since the size of the snip-core is finite at any given N, then each such path must be self-intersecting. Therefore, the algorithm stops in either of the following scenarios:

1. The path returns to the starting point ($i = 1$) and we end up with a loop. There are two subcases:
    a) If all sites on the loop have degree 2 then the loop must be unsnippable (Fig. 5.2a).
    b) If there exists a site on the loop that has a degree of at least 3 then we walk one step away from the loop starting at that site as before and get a “lasso motif” (Fig. 5.2c).
2. The path crosses itself at a site $i \neq 1$ and we encounter the same lasso motif.

At this point, we continue from the open end of the lasso and generate unsnippable sites as before. Again, our path necessarily returns and touches the lasso. When this happens, we end up with one of three motifs: an unsnippable loop with one cross-link (Fig. 5.2d), a “figure eight” (Fig. 5.2e) or a “dumbbell” (Fig. 5.2f). Together with the unsnippable loop (Fig. 5.2a), these constitute the set of structures of which at least one *must* be present on each non-empty disconnected component of a snip-core. Strictly speaking, we should classify somewhat more finely by specifying the unsnippability of each loop passing through the degree 3 and 4 sites in these motifs. But that only changes our estimates below by constant factors as $N \to \infty$ so we refrain from exhibiting these details here.

---

[3] We use motif to mean a fixed subgraph up to isomorphisms, irrespective of its frequency of occurrence. This is midway between the everyday meaning of the term and the more technical graph theoretic usage which makes reference to its frequency.

Now for the frequency of occurrence of these motifs. In the limit $N \to \infty$ for any fixed number of sites L, the expected number of loops is $O(N^0)$, while the expected numbers of the other three are $O(1/N)$ and hence vanish. As before, we are led to examine giant versions of these graphs. The most optimistic case assumes that all the individual legs of the motifs are large and diverge with N. In this case, the expected numbers take the form

$$\mathbb{E}(\#\text{ motifs}) = c\binom{N}{L-1}\frac{(L-1)!}{a}\left(\frac{2\alpha}{N-1}\right)^{L}\lambda_+^L, \tag{5.7}$$

where a is the number of automorphisms ($a = 4$ for the figure eight and the dumbbell and $a = 2$ for the loop with a single cross-link) and c is an $\mathcal{O}(1)$ number (dependent on β) associated with the precise unsnippability of vertices that have degree at least 3 alluded to above.

For $\alpha < \alpha_c(\beta)$ these expected numbers vanish also for large motifs of size $L = lN^\gamma$ as $N \to \infty$ for any l and $0 < \gamma \leq 1$. Using Stirling's approximation, the $\mathcal{O}(N^\gamma)$ part of the entropy $S(l) = \log(\mathbb{E}(\#\text{ motifs}))$ is approximately

$$S(l) = lN^\gamma \log(2\alpha\lambda_+) - lN^\gamma - N(1 - lN^{\gamma-1})\log(1 - lN^{\gamma-1}). \tag{5.8}$$

Once again, $S(0) = 0$ and the derivative

$$S'(l) = N^\gamma\left[\log(2\alpha\lambda_+) + \log(1 - lN^{\gamma-1})\right] \leq N^\gamma \log(2\alpha\lambda_+) \tag{5.9}$$

for any l. We see that for $\alpha < \alpha_c(\beta)$, $S(l)$ is a negative and decreasing function so the expected number of motifs vanishes in the thermodynamic limit as $e^{-\mathcal{O}(N^\gamma)}$.

Hence, the loop with cross-link, figure eight, and dumbbell are entirely absent for $\alpha < \alpha_c(\beta)$ and the snip-core is either empty or composed entirely of unsnippable loops. Such snip-cores are SAT so we can conclude that our starting graphs are SAT for $\alpha < \alpha_c(\beta)$ with probability 1 and thus $\alpha_c(\beta)$ is a lower bound on the extent of the UNSAT region at fixed β. Putting together the upper and the lower bounds, we conclude that $\alpha_c(\beta)$ from Eq. (5.6) represents the exact location of the phase boundary between SAT and UNSAT in the $\alpha - \beta$ plane as shown in Fig. 5.1.

5.5 Conclusion

In the preceding we have introduced a new family of mixed classical-quantum ensembles for the k-SAT/QSAT problems and established the exact phase diagram for the simplest member of this family with $k = 2$. We note that the shape of the phase boundary is consistent with what is known about the limits. The quantum limit is insensitive to the choice of projectors and we find that the restriction of a dilute concentration of projectors to classical values barely shifts the phase boundary. The classical limit is sensitive to the choice of projectors and the phase boundary near it is maximally sensitive to the inclusion of a dilute set of quantum projectors. A problem that we leave open is the nature of scaling near the phase boundary. One basic question concerns the scaling of the probability P_{SAT} that a random instance is SAT. Work on the classical problem by Bollobás *et al.* [46] showed that this has the scaling form $P_{\mathrm{SAT}}(N, \alpha) = f((\alpha - \alpha_c)/N^{1/3})$. Work on the ER ensemble by Bollobás [45] and Luczak [157] implies that the same scaling holds for the purely quantum problem. Qualitatively, our work makes sense of this apparent coincidence and implies that this scaling will hold everywhere along the phase boundary—that everywhere there exists a single transition involving the proliferation of unsnippable loops with the mix of projectors along such loops changing continuously with β. However, more work is required to show this rigorously and to try and extract more detailed information on the scaling functions near the transition. Finally, we intend to examine similar ensembles for $k = 3$. The current work suggests that perturbing about the classical limit by introducing a dilute set of quantum projectors into the Hamiltonian could be informative in quantum mechanical perturbation theory.

Bibliography

[1] Dmitry A. Abanin, Wojciech De Roeck, and F. Huveneers. "Exponentially Slow Heating in Periodically Driven Many-Body Systems". In: *Phys. Rev. Lett.* 115 (25 Dec. 2015), p. 256803. DOI: `10.1103/PhysRevLett.115.256803`. URL: `http://link.aps.org/doi/10.1103/PhysRevLett.115.256803`.

[2] Dmitry A. Abanin et al. "Colloquium: Many-body localization, thermalization, and entanglement". In: *Rev. Mod. Phys.* 91 (2 May 2019), p. 021001. DOI: `10.1103/RevModPhys.91.021001`. URL: `https://link.aps.org/doi/10.1103/RevModPhys.91.021001`.

[3] Dmitry Abanin et al. "A rigorous theory of many-body prethermalization for periodically driven and closed quantum systems". In: *arXiv preprint arXiv:1509.05386* (2016). URL: `https://arxiv.org/abs/1509.05386`.

[4] R Abou-Chacra, D J Thouless, and P W Anderson. In: *Journal of Physics C: Solid State Physics* 6.10 (May 1973), pp. 1734–1752. DOI: `10.1088/0022-3719/6/10/009`. URL: `https://doi.org/10.1088%2F0022-3719%2F6%2F10%2F009`.

[5] E. Abrahams et al. "Scaling Theory of Localization: Absence of Quantum Diffusion in Two Dimensions". In: *Phys. Rev. Lett.* 42 (10 Mar. 1979), pp. 673–676. DOI: `10.1103/PhysRevLett.42.673`. URL: `https://link.aps.org/doi/10.1103/PhysRevLett.42.673`.

[6] A. A. Abrikosov, L. P. Gorkov, and I. E. Dzyaloshinski. *Methods of Quantum Field Theory in Statistical Physics.* Trans. by Richard A. Silverman. Dover Publications, Inc, 1975.

[7] Dorit Aharonov and Tomer Naveh. "Quantum NP - A Survey". In: (Oct. 2002). arXiv: `quant-ph/0210077`. URL: `https://arxiv.org/abs/quant-ph/0210077`.

[8] M. Aidelsburger et al. "Experimental Realization of Strong Effective Magnetic Fields in an Optical Lattice". In: *Phys. Rev. Lett.* 107 (25 Dec. 2011), p. 255301. DOI: `10.1103/PhysRevLett.107.255301`. URL: `http://link.aps.org/doi/10.1103/PhysRevLett.107.255301`.

[9] Vincenzo Alba. "Eigenstate thermalization hypothesis and integrability in quantum spin chains". In: *Phys. Rev. B* 91 (15 Apr. 2015), p. 155123. DOI: `10.1103/PhysRevB.91.155123`. URL: `https://link.aps.org/doi/10.1103/PhysRevB.91.155123`.

[10] J R L de Almeida and D J Thouless. "Stability of the Sherrington-Kirkpatrick solution of a spin glass model". In: *Journal of Physics A: Mathematical and General* 11.5 (May 1978), pp. 983–990. DOI: `10.1088/0305-4470/11/5/028`. URL: `https://doi.org/10.1088%2F0305-4470%2F11%2F5%2F028`.

[11] Alexander Altland and Ben D. Simons. *Condensed Matter Field Theory*. 2nd ed. Cambridge University Press, 2010. DOI: `10.1017/CBO9780511789984`.

[12] E. Altman and R. Vosk. "Universal Dynamics and Renormalization in Many-Body-Localized Systems". In: *Annu. Rev. Condens. Matter Phys.* 6 (2015), p. 383. DOI: `10.1146/annurev-conmatphys-031214-014701`. URL: `http://www.annualreviews.org/doi/10.1146/annurev-conmatphys-031214-014701`.

[13] Boris L. Altshuler et al. "Quasiparticle Lifetime in a Finite System: A Nonperturbative Approach". In: *Phys. Rev. Lett.* 78 (14 Apr. 1997), pp. 2803–2806. DOI: `10.1103/PhysRevLett.78.2803`. URL: `https://link.aps.org/doi/10.1103/PhysRevLett.78.2803`.

[14] Andris Ambainis, Julia Kempe, and Or Sattath. "A Quantum Lovasz Local Lemma". In: *J. ACM* 59.5 (2012), 24:1–24:24. ISSN: 0004-5411. DOI: `10.1145/2371656.2371659`. URL: `http://doi.acm.org/10.1145/2371656.2371659`.

[15] P. W. Anderson. "Absence of Diffusion in Certain Random Lattices". In: *Physical Review* 109.5 (Mar. 1958), pp. 1492–1505. DOI: `10.1103/PhysRev.109.1492`. URL: `http://link.aps.org/doi/10.1103/PhysRev.109.1492` (visited on 11/02/2015).

[16] P. W. Anderson. "More Is Different". In: *Science* 177.4047 (1972), pp. 393–396. ISSN: 0036-8075. DOI: `10.1126/science.177.4047.393`. eprint: `https://science.sciencemag.org/content/177/4047/393.full.pdf`. URL: `https://science.sciencemag.org/content/177/4047/393`.

[17] A. André, L.-M. Duan, and M. D. Lukin. "Coherent Atom Interactions Mediated by Dark-State Polaritons". In: *Phys. Rev. Lett.* 88 (24 May 2002), p. 243602. DOI: `10.1103/PhysRevLett.88.243602`. URL: `https://link.aps.org/doi/10.1103/PhysRevLett.88.243602`.

[18] N. Andrei, K. Furuya, and J. H. Lowenstein. "Solution of the Kondo problem". In: *Rev. Mod. Phys.* 55 (2 Apr. 1983), pp. 331–402. DOI: `10.1103/RevModPhys.55.331`. URL: `https://link.aps.org/doi/10.1103/RevModPhys.55.331`.

[19] S. Arora and B. Barak. *Complexity Theory: A Modern Approach*. Cambridge: Cambridge University Press, 2009.

[20] Sanjeev Arora et al. "Proof Verification and the Hardness of Approximation Problems". In: *J. ACM* 45.3 (1998), pp. 501–555. ISSN: 0004-5411. DOI: `10.1145/278298.278306`. URL: `http://doi.acm.org/10.1145/278298.278306`.

[21] Marcos Atala et al. "Direct measurement of the Zak phase in topological Bloch bands". In: *Nature Physics* 9.12 (2013), pp. 795–800. URL: `https://www.nature.com/nphys/journal/v9/n12/full/nphys2790.html`.

[22] Yasaman Bahri et al. "Localization and topology protected quantum coherence at the edge of hot matter". en. In: *Nature Communications* 6 (July 2015), p. 7341. DOI: `10.1038/ncomms8341`. URL: `http://www.nature.com/ncomms/2015/150710/ncomms8341/abs/ncomms8341.html` (visited on 11/02/2015).

[23] Waseem S Bakr et al. "A quantum gas microscope for detecting single atoms in a Hubbard-regime optical lattice". In: *Nature* 462.7269 (2009), pp. 74–77. URL: `https://www.nature.com/nature/journal/v462/n7269/full/nature08482.html`.

[24] A B Balantekin, T Dereli, and Y Pehlivan. "Solutions of the Gaudin equation and Gaudin algebras". In: *Journal of Physics A: Mathematical and General* 38.25 (June 2005), pp. 5697–5707. DOI: `10.1088/0305-4470/38/25/007`. URL: `https://doi.org/10.1088%2F0305-4470%2F38%2F25%2F007`.

[25] J. C. Barba et al. "The Berry-Tabor conjecture for spin chains of Haldane-Shastry type". In: *EPL (Europhysics Letters)* 83.2 (June 2008), p. 27005. DOI: `10.1209/0295-5075/83/27005`. URL: `https://doi.org/10.1209%2F0295-5075%2F83%2F27005`.

[26] M. Barkeshli, N. Y. Yao, and C. R. Laumann. "Continuous Preparation of a Fractional Chern Insulator". In: *Phys. Rev. Lett.* 115 (2 July 2015), p. 026802. DOI: `10.1103/PhysRevLett.115.026802`. URL: `http://link.aps.org/doi/10.1103/PhysRevLett.115.026802`.

[27] Giovanni Barontini et al. "Deterministic generation of multiparticle entanglement by quantum Zeno dynamics". In: *Science* 349.6254 (2015), pp. 1317–1321. ISSN: 0036-8075. DOI: `10.1126/science.aaa0754`. URL: `https://science.sciencemag.org/content/349/6254/1317`.

[28] T. Barthel and U. Schollwöck. "Dephasing and the Steady State in Quantum Many-Particle Systems". In: *Phys. Rev. Lett.* 100 (10 Mar. 2008), p. 100601. DOI: `10.1103/PhysRevLett.100.100601`. URL: `https://link.aps.org/doi/10.1103/PhysRevLett.100.100601`.

[29] D.M. Basko, I.L. Aleiner, and B.L. Altshuler. "Metal-insulator transition in a weakly interacting many-electron system with localized single-particle states". In: *Annals of Physics* 321.5 (2006), pp. 1126–1205. ISSN: 0003-4916. DOI: `http://doi.org/10.1016/j.aop.2005.11.014`. URL: `http://www.sciencedirect.com/science/article/pii/S0003491605002630`.

[30] V. M. Bastidas et al. "Nonequilibrium quantum phase transitions in the Ising model". In: *Phys. Rev. A* 86 (6 Dec. 2012), p. 063627. DOI: `10.1103/PhysRevA.86.063627`. URL: `http://link.aps.org/doi/10.1103/PhysRevA.86.063627`.

[31] Niel de Beaudrap. "Difficult instances of the counting problem for 2-quantum-SAT are very atypical". In: *arXiv preprint arXiv:1403.1588* (2014). URL: `http://arxiv.org/abs/1403.1588` (visited on 02/24/2015).

[32] Giancarlo Benettin et al. “Lyapunov Characteristic Exponents for smooth dynamical systems and for hamiltonian systems; A method for computing all of them. Part 2: Numerical application”. In: *Meccanica* 15.1 (Mar. 1980), pp. 21–30. ISSN: 1572-9648. DOI: `10.1007/BF02128237`. URL: `https://doi.org/10.1007/BF02128237`.

[33] Gregory Bentsen et al. “Integrable and chaotic dynamics of spins coupled to an optical cavity”. In: *arXiv preprint arXiv:1904.10966* (2019). URL: `https://arxiv.org/abs/1904.10966`.

[34] B Andrei Bernevig, Taylor L Hughes, and Shou-Cheng Zhang. “Quantum spin Hall effect and topological phase transition in HgTe quantum wells”. In: *Science* 314.5806 (2006), pp. 1757–1761. URL: `http://science.sciencemag.org/content/314/5806/1757`.

[35] B.A. Bernevig and T.L. Hughes. *Topological Insulators And Topological Superconductors*. Princeton University Press, 2013.

[36] Hannes Bernien et al. “Probing many-body dynamics on a 51-atom quantum simulator”. In: *arXiv preprint arXiv:1707.04344* (2017). URL: `https://arxiv.org/abs/1707.04344`.

[37] Michael Victor Berry and Michael Tabor. “Level clustering in the regular spectrum”. In: *Proceedings of the Royal Society of London. A. Mathematical and Physical Sciences* 356.1686 (1977). DOI: `https://doi.org/10.1098/rspa.1977.0140`. URL: `https://royalsocietypublishing.org/doi/abs/10.1098/rspa.1977.0140`.

[38] Bruno Bertini et al. “Transport in Out-of-Equilibrium XXZ Chains: Exact Profiles of Charges and Currents”. In: *Phys. Rev. Lett.* 117 (20 Nov. 2016), p. 207201. DOI: `10.1103/PhysRevLett.117.207201`. URL: `https://link.aps.org/doi/10.1103/PhysRevLett.117.207201`.

[39] RMW van Bijnen and T Pohl. “Quantum Magnetism and Topological Ordering via Rydberg Dressing near Forster Resonances”. In: *Phys. Rev. Lett.* 114.24 (2015), p. 243002. URL: `http://journals.aps.org/prl/abstract/10.1103/PhysRevLett.114.243002`.

[40] Adam T. Black, Hilton W. Chan, and Vladan Vuleti ć. “Observation of Collective Friction Forces due to Spatial Self-Organization of Atoms: From Rayleigh to Bragg Scattering”. In: *Phys. Rev. Lett.* 91 (20 Nov. 2003), p. 203001. DOI: `10.1103/PhysRevLett.91.203001`. URL: `https://link.aps.org/doi/10.1103/PhysRevLett.91.203001`.

[41] R. Blatt and C. F. Roos. “Quantum simulations with trapped ions”. In: *Nature Physics* 8 (2012), pp. 277–284. DOI: `https://doi.org/10.1038/nphys2252`. URL: `https://doi.org/10.1038/nphys2252`.

[42] Immanuel Bloch, Jean Dalibard, and Wilhelm Zwerger. "Many-body physics with ultracold gases". In: *Rev. Mod. Phys.* 80 (3 July 2008), pp. 885–964. DOI: `10.1103/RevModPhys.80.885`. URL: `https://link.aps.org/doi/10.1103/RevModPhys.80.885`.

[43] O. Bohigas, M. J. Giannoni, and C. Schmit. "Characterization of Chaotic Quantum Spectra and Universality of Level Fluctuation Laws". In: *Phys. Rev. Lett.* 52 (1 Jan. 1984), pp. 1–4. DOI: `10.1103/PhysRevLett.52.1`. URL: `https://link.aps.org/doi/10.1103/PhysRevLett.52.1`.

[44] B. Bollobás. *Modern Graph Theory.* New York: Springer, 1998.

[45] B. Bollobás. "The evolution of random graphs". In: *Transactions of the American Mathematical Society* 286.1 (1984), p. 257. DOI: `10.1090/S0002-9947-1984-0756039-5`.

[46] B. Bollobás et al. "The scaling window of the 2-SAT transition". In: *Random Structures and Algorithms* 18.3 (2001), p. 201. DOI: `10.1002/rsa.1006`.

[47] Boris Braverman et al. "Near-Unitary Spin Squeezing in 171Yb". In: (2019). arXiv: `1901.10499`. URL: `https://arxiv.org/abs/1901.10499`.

[48] S. Bravyi. "Efficient algorithm for a quantum analogue of 2-SAT". In: *arXiv preprint quant-ph/0602108v1* (2006). URL: `http://arxiv.org/abs/quant-ph/0602108v1`.

[49] Sergey Bravyi, Cristopher Moore, and Alexander Russell. "Bounds on the quantum satisfiability threshold". In: *arXiv preprint arXiv:0907.1297* (2009). URL: `http://arxiv.org/abs/0907.1297` (visited on 02/02/2015).

[50] Ralf Bulla, Theo A. Costi, and Thomas Pruschke. "Numerical renormalization group method for quantum impurity systems". In: *Rev. Mod. Phys.* 80 (2 Apr. 2008), pp. 395–450. DOI: `10.1103/RevModPhys.80.395`. URL: `https://link.aps.org/doi/10.1103/RevModPhys.80.395`.

[51] W. J. L Buyers et al. "Experimental evidence for the Haldane gap in a spin-1 nearly isotropic, antiferromagnetic chain". In: *Phys. Rev. Lett.* 56 (4 Jan. 1986), pp. 371–374. DOI: `10.1103/PhysRevLett.56.371`. URL: `http://link.aps.org/doi/10.1103/PhysRevLett.56.371`.

[52] Andrei G. Bytsko. "On integrable Hamiltonians for higher spin XXZ chain". In: *Journal of Mathematical Physics* 44.9 (2003), pp. 3698–3717. DOI: `10.1063/1.1591054`. eprint: `https://aip.scitation.org/doi/pdf/10.1063/1.1591054`. URL: `https://aip.scitation.org/doi/abs/10.1063/1.1591054`.

[53] Léonie Canet et al. "Nonperturbative Renormalization Group for the Kardar-Parisi-Zhang Equation". In: *Phys. Rev. Lett.* 104 (15 Apr. 2010), p. 150601. DOI: `10.1103/PhysRevLett.104.150601`. URL: `https://link.aps.org/doi/10.1103/PhysRevLett.104.150601`.

[54] Tommaso Castellani and Andrea Cavagna. “Spin-glass theory for pedestrians”. In: *Journal of Statistical Mechanics: Theory and Experiment* 2005.05 (May 2005), P05012. DOI: `10.1088/1742-5468/2005/05/p05012`. URL: `https://doi.org/10.1088%2F1742-5468%2F2005%2F05%2Fp05012`.

[55] Jean-Sébastien Caux and Jorn Mossel. “Remarks on the notion of quantum integrability”. In: *Journal of Statistical Mechanics: Theory and Experiment* 2011.02 (2011), P02023. URL: `http://stacks.iop.org/1742-5468/2011/i=02/a=P02023`.

[56] Anushya Chandran et al. “Constructing local integrals of motion in the many-body localized phase”. In: *Phys. Rev. B* 91 (8 Feb. 2015), p. 085425. DOI: `10.1103/PhysRevB.91.085425`. URL: `https://link.aps.org/doi/10.1103/PhysRevB.91.085425`.

[57] Anushya Chandran et al. “Many-body localization and symmetry-protected topological order”. In: *Phys. Rev. B* 89 (14 Apr. 2014), p. 144201. DOI: `10.1103/PhysRevB.89.144201`. URL: `http://link.aps.org/doi/10.1103/PhysRevB.89.144201`.

[58] Xie Chen, Zheng-Cheng Gu, and Xiao-Gang Wen. “Classification of gapped symmetric phases in one-dimensional spin systems”. In: *Physical Review B* 83.3 (Jan. 2011), p. 035107. DOI: `10.1103/PhysRevB.83.035107`. URL: `http://link.aps.org/doi/10.1103/PhysRevB.83.035107` (visited on 11/03/2015).

[59] YL Chen et al. “Experimental realization of a three-dimensional topological insulator, Bi2Te3”. In: *Science* 325.5937 (2009), pp. 178–181. URL: `http://science.sciencemag.org/content/325/5937/178`.

[60] Lawrence W Cheuk et al. “Quantum-gas microscope for fermionic atoms”. In: *Physical review letters* 114.19 (2015), p. 193001. URL: `https://journals.aps.org/prl/abstract/10.1103/PhysRevLett.114.193001`.

[61] Soonwon Choi et al. “Observation of discrete time-crystalline order in a disordered dipolar many-body system”. In: *Nature* 543.21426 (2017), pp. 221–225. URL: `https://www.nature.com/articles/nature21426`.

[62] Pieter W Claeys et al. “Integrable spin-1/2 Richardson-Gaudin XYZ models in an arbitrary magnetic field”. In: *Journal of Physics A: Mathematical and Theoretical* 52.8 (Jan. 2019), 08LT01. DOI: `10.1088/1751-8121/aafe9b`. URL: `https://doi.org/10.1088%2F1751-8121%2Faafe9b`.

[63] Logan W. Clark et al. “Quantum Dynamics with Spatiotemporal Control of Interactions in a Stable Bose-Einstein Condensate”. In: *Phys. Rev. Lett.* 115 (15 Oct. 2015), p. 155301. DOI: `10.1103/PhysRevLett.115.155301`. URL: `http://link.aps.org/doi/10.1103/PhysRevLett.115.155301`.

[64] E. Colella et al. “Quantum phases of spinful Fermi gases in optical cavities”. In: *Phys. Rev. B* 97 (13 Apr. 2018), p. 134502. DOI: `10.1103/PhysRevB.97.134502`. URL: `https://link.aps.org/doi/10.1103/PhysRevB.97.134502`.

[65] N. R. Cooper. "Optical Flux Lattices for Ultracold Atomic Gases". In: *Phys. Rev. Lett.* 106 (17 Apr. 2011), p. 175301. DOI: `10.1103/PhysRevLett.106.175301`. URL: `http://link.aps.org/doi/10.1103/PhysRevLett.106.175301`.

[66] Jordan S. Cotler, Dawei Ding, and Geoffrey R. Penington. "Out-of-time-order operators and the butterfly effect". In: *Annals of Physics* 396 (2018), pp. 318–333. ISSN: 0003-4916. DOI: `https://doi.org/10.1016/j.aop.2018.07.020`. URL: `http://www.sciencedirect.com/science/article/pii/S000349161830191X`.

[67] Luca D'Alessio and Marcos Rigol. "Long-time Behavior of Isolated Periodically Driven Interacting Lattice Systems". In: *Phys. Rev. X* 4 (4 Dec. 2014), p. 041048. DOI: `10.1103/PhysRevX.4.041048`. URL: `http://link.aps.org/doi/10.1103/PhysRevX.4.041048`.

[68] Luca D'Alessio et al. "From quantum chaos and eigenstate thermalization to statistical mechanics and thermodynamics". In: *Advances in Physics* 65.3 (2016), pp. 239–362. DOI: `10.1080/00018732.2016.1198134`. eprint: `https://doi.org/10.1080/00018732.2016.1198134`. URL: `https://doi.org/10.1080/00018732.2016.1198134`.

[69] Emily J. Davis et al. "Photon-Mediated Spin-Exchange Dynamics of Spin-1 Atoms". In: *Phys. Rev. Lett.* 122 (1 Jan. 2019), p. 010405. DOI: `10.1103/PhysRevLett.122.010405`. URL: `https://link.aps.org/doi/10.1103/PhysRevLett.122.010405`.

[70] Wojciech De Roeck and Francois Huveneers. "Stability and instability towards delocalization in many-body localization systems". In: *Phys. Rev. B* 95 (15 Apr. 2017), p. 155129. DOI: `10.1103/PhysRevB.95.155129`. URL: `https://link.aps.org/doi/10.1103/PhysRevB.95.155129`.

[71] Wojciech De Roeck et al. "Absence of many-body mobility edges". In: *Phys. Rev. B* 93 (1 Jan. 2016), p. 014203. DOI: `10.1103/PhysRevB.93.014203`. URL: `https://link.aps.org/doi/10.1103/PhysRevB.93.014203`.

[72] Joshua M Deutsch. "Eigenstate thermalization hypothesis". In: *Reports on Progress in Physics* 81.8 (July 2018), p. 082001. DOI: `10.1088/1361-6633/aac9f1`. URL: `https://doi.org/10.1088%2F1361-6633%2Faac9f1`.

[73] Barbara Dietz and Fritz Haake. "Taylor and Padé analysis of the level spacing distributions of random-matrix ensembles". In: *Zeitschrift für Physik B Condensed Matter* 80.1 (Feb. 1990), pp. 153–158. ISSN: 1431-584X. DOI: `10.1007/BF01390663`. URL: `https://doi.org/10.1007/BF01390663`.

[74] Freeman J. Dyson. "Statistical Theory of the Energy Levels of Complex Systems". In: *Journal of Mathematical Physics* 3.1 (1962), pp. 140–156. DOI: `10.1063/1.1703773`. eprint: `https://doi.org/10.1063/1.1703773`. URL: `https://doi.org/10.1063/1.1703773`.

[75] Jessica K Eastman, Joseph J Hope, and André RR Carvalho. “Tuning quantum measurements to control chaos”. In: *Scientific reports* 7 (2017), p. 44684. URL: `https://www.nature.com/articles/srep44684`.

[76] Dominic V. Else, Bela Bauer, and Chetan Nayak. “Floquet Time Crystals”. In: *Phys. Rev. Lett.* 117 (9 Aug. 2016), p. 090402. DOI: `10.1103/PhysRevLett.117.090402`. URL: `https://link.aps.org/doi/10.1103/PhysRevLett.117.090402`.

[77] Dominic V. Else and Chetan Nayak. “Classification of topological phases in periodically driven interacting systems”. In: *Phys. Rev. B* 93 (20 May 2016), p. 201103. DOI: `10.1103/PhysRevB.93.201103`. URL: `http://link.aps.org/doi/10.1103/PhysRevB.93.201103`.

[78] Dominic V. Else et al. “Discrete Time Crystals”. In: *arXiv preprint arXiv:1905.13232* (2019). URL: `https://arxiv.org/abs/1905.13232`.

[79] Manuel Endres et al. “Cold Matter Assembled Atom-by-Atom”. In: *arXiv:1607.03044* (2016). URL: `https://arxiv.org/abs/1607.03044`.

[80] P. Erdős and A. Rényi. “On the evolution of random graphs”. In: *Magyar Tud. Akad. Mat. Kutató Int. Közl* 5 (1960), p. 17. URL: `http://www.renyi.hu/~p_erdos/1960-10.pdf`.

[81] S. Fazzini et al. “Hidden Magnetism in Periodically Modulated One Dimensional Dipolar Fermions”. In: *arXiv preprint arXiv:1607.05682* (2016). URL: `https://arxiv.org/abs/1607.05682`.

[82] Boris Feigin, Edward Frenkel, and Nikolai Reshetikhin. “Gaudin model, Bethe Ansatz and critical level”. In: *Communications in Mathematical Physics* 166.1 (Dec. 1994), pp. 27–62. ISSN: 1432-0916. DOI: `10.1007/BF02099300`. URL: `https://doi.org/10.1007/BF02099300`.

[83] R.P. Feynman. “Simulating physics with computers”. In: *International journal of theoretical physics* 21.6 (1982), pp. 467–488. (Visited on 04/26/2014).

[84] Daniel S. Fisher and David A. Huse. “Equilibrium behavior of the spin-glass ordered phase”. In: *Phys. Rev. B* 38 (1 July 1988), pp. 386–411. DOI: `10.1103/PhysRevB.38.386`. URL: `https://link.aps.org/doi/10.1103/PhysRevB.38.386`.

[85] Daniel S. Fisher and David A. Huse. “Nonequilibrium dynamics of spin glasses”. In: *Phys. Rev. B* 38 (1 July 1988), pp. 373–385. DOI: `10.1103/PhysRevB.38.373`. URL: `https://link.aps.org/doi/10.1103/PhysRevB.38.373`.

[86] Daniel S. Fisher and David A. Huse. “Ordered Phase of Short-Range Ising Spin-Glasses”. In: *Phys. Rev. Lett.* 56 (15 Apr. 1986), pp. 1601–1604. DOI: `10.1103/PhysRevLett.56.1601`. URL: `https://link.aps.org/doi/10.1103/PhysRevLett.56.1601`.

[87] K.H. Fisher and J.A. Hertz. *Spin glasses*. Cambridge University Press, 1991.

[88] N Flaschner et al. “Experimental reconstruction of the Berry curvature in a Floquet Bloch band”. In: *Science* 352.6289 (2016), pp. 1091–1094. URL: `http://science.sciencemag.org/content/352/6289/1091`.

[89] L. Fleishman and P. W. Anderson. “Interactions and the Anderson transition”. In: *Physical Review B* 21.6 (Mar. 1980), pp. 2366–2377. DOI: `10.1103/PhysRevB.21.2366`. URL: `http://link.aps.org/doi/10.1103/PhysRevB.21.2366` (visited on 11/03/2015).

[90] E. Friedgut and J. Bourgain. “Sharp thresholds of graph properties, and the k-SAT problem”. In: *Journal of the American Mathematical Society* 12.4 (1999), p. 1017. DOI: `10.1090/S0894-0347-99-00305-7`.

[91] Y.-T. Fu and P.W. Anderson. *Lectures in the Sciences of Complexity*. Reading, MA: Addison-Wesley, 1989.

[92] Martin Gärttner et al. “Measuring out-of-time-order correlations and multiple quantum spectra in a trapped-ion quantum magnet”. In: *Nature Physics* 13 (May 2017), p. 781. URL: `https://www.nature.com/articles/nphys4119`.

[93] Gaudin, M. “Diagonalisation d’une classe d’hamiltoniens de spin”. In: *J. Phys. France* 37.10 (1976), pp. 1087–1098. DOI: `10.1051/jphys:0197600370100108700`. URL: `https://doi.org/10.1051/jphys:0197600370100108700`.

[94] C. Gaul et al. “Resonant Rydberg Dressing of Alkaline-Earth Atoms via Electromagnetically Induced Transparency”. In: *Phys. Rev. Lett.* 116 (24 June 2016), p. 243001. DOI: `10.1103/PhysRevLett.116.243001`. URL: `http://link.aps.org/doi/10.1103/PhysRevLett.116.243001`.

[95] A. Georges et al. “Dynamical mean-field theory of strongly correlated fermion systems and the limit of infinite dimensions”. In: *Rev. Mod. Phys.* 68 (1 Jan. 1996), pp. 13–125. DOI: `10.1103/RevModPhys.68.13`. URL: `https://link.aps.org/doi/10.1103/RevModPhys.68.13`.

[96] L. I. R. Gil et al. “Spin Squeezing in a Rydberg Lattice Clock”. In: *Phys. Rev. Lett.* 112 (Mar. 2014), p. 103601. URL: `http://journals.aps.org/prl/abstract/10.1103/PhysRevLett.112.103601`.

[97] Alexander W Glaetzle et al. “Designing Frustrated Quantum Magnets with Laser-Dressed Rydberg Atoms”. In: *Phys. Rev. Lett.* 114.17 (2015), p. 173002. URL: `http://journals.aps.org/prl/abstract/10.1103/PhysRevLett.114.173002`.

[98] A. Goerdt. “A threshold for unsatisfiability”. In: *Journal of Computer and System Sciences* 53.3 (1996), p. 469. DOI: `doi:10.1006/jcss.1996.0081`.

[99] Tomer Goldfriend and Jorge Kurchan. “Equilibration of quasi-integrable systems”. In: *Phys. Rev. E* 99 (2 Feb. 2019), p. 022146. DOI: `10.1103/PhysRevE.99.022146`. URL: `https://link.aps.org/doi/10.1103/PhysRevE.99.022146`.

[100] Isaac Goldhirsch, Pierre-Louis Sulem, and Steven A. Orszag. “Stability and Lyapunov stability of dynamical systems: A differential approach and a numerical method”. In: *Physica D: Nonlinear Phenomena* 27.3 (1987), pp. 311–337. ISSN: 0167-2789. DOI: `https://doi.org/10.1016/0167-2789(87)90034-0`. URL: `http://www.sciencedirect.com/science/article/pii/0167278987900340`.

[101] E. A. Goldschmidt et al. “Anomalous Broadening in Driven Dissipative Rydberg Systems”. In: *Phys. Rev. Lett.* 116 (11 Mar. 2016), p. 113001. DOI: `10.1103/PhysRevLett.116.113001`. URL: `http://link.aps.org/doi/10.1103/PhysRevLett.116.113001`.

[102] Sarang Gopalakrishnan, Benjamin L. Lev, and Paul M. Goldbart. “Frustration and Glassiness in Spin Models with Cavity-Mediated Interactions”. In: *Phys. Rev. Lett.* 107 (27 Dec. 2011), p. 277201. DOI: `10.1103/PhysRevLett.107.277201`. URL: `https://link.aps.org/doi/10.1103/PhysRevLett.107.277201`.

[103] I. V. Gornyi, A. D. Mirlin, and D. G. Polyakov. “Interacting Electrons in Disordered Wires: Anderson Localization and Low-T Transport”. In: *Phys. Rev. Lett.* 95 (20 Nov. 2005), p. 206603. DOI: `10.1103/PhysRevLett.95.206603`. URL: `https://link.aps.org/doi/10.1103/PhysRevLett.95.206603`.

[104] D. Gosset and D. Nagaj. “Quantum 3-SAT Is QMA1-Complete”. In: *Foundations of Computer Science (FOCS), 2013 IEEE 54th Annual Symposium on.* Oct. 2013, pp. 756–765. DOI: `10.1109/FOCS.2013.86`.

[105] Yudan Guo et al. “Sign-changing photon-mediated atom interactions in multimode cavity QED”. In: (2018). arXiv: `1810.11086`. URL: `https://arxiv.org/abs/1810.11086`.

[106] Salman Habib, Kosuke Shizume, and Wojciech Hubert Zurek. “Decoherence, Chaos, and the Correspondence Principle”. In: *Phys. Rev. Lett.* 80 (20 May 1998), pp. 4361–4365. DOI: `10.1103/PhysRevLett.80.4361`. URL: `https://link.aps.org/doi/10.1103/PhysRevLett.80.4361`.

[107] F. D. M. Haldane. “Nonlinear Field Theory of Large-Spin Heisenberg Antiferromagnets: Semiclassically Quantized Solitons of the One-Dimensional Easy-Axis Neel State”. In: *Physical Review Letters* 50.15 (Apr. 1983), pp. 1153–1156. DOI: `10.1103/PhysRevLett.50.1153`. URL: `http://link.aps.org/doi/10.1103/PhysRevLett.50.1153` (visited on 11/02/2015).

[108] Elmar Haller et al. “Single-atom imaging of fermions in a quantum-gas microscope”. In: *Nature Physics* 11.9 (2015), pp. 738–742. URL: `https://www.nature.com/nphys/journal/v11/n9/full/nphys3403.html`.

[109] A.K. Hartmann and M. Weigt. *Phase Transitions in Combinatorial Optimization Problems.* Weinheim: Wiley-VCH Verlag GmbH and Co. KGaA, 2005.

[110] M Zahid Hasan and Charles L Kane. “Colloquium: topological insulators”. In: *Reviews of Modern Physics* 82.4 (2010), p. 3045. URL: `https://journals.aps.org/rmp/abstract/10.1103/RevModPhys.82.3045`.

[111] Philipp Hauke et al. “Non-Abelian Gauge Fields and Topological Insulators in Shaken Optical Lattices”. In: *Phys. Rev. Lett.* 109 (14 Oct. 2012), p. 145301. DOI: `10.1103/PhysRevLett.109.145301`. URL: `http://link.aps.org/doi/10.1103/PhysRevLett.109.145301`.

[112] N Henkel, R Nath, and T Pohl. “Three-dimensional roton excitations and supersolid formation in Rydberg-excited Bose-Einstein condensates”. In: *Phys. Rev. Lett.* 104.19 (2010), p. 195302. URL: `http://journals.aps.org/prl/abstract/10.1103/PhysRevLett.104.195302`.

[113] O. Hosten et al. “Quantum phase magnification”. In: *Science* 352.6293 (2016), pp. 1552–1555. ISSN: 0036-8075. DOI: `10.1126/science.aaf3397`. URL: `https://science.sciencemag.org/content/352/6293/1552`.

[114] Pavan Hosur et al. “Chaos in quantum channels”. In: *Journal of High Energy Physics* 2016.2 (2016), pp. 1–49. ISSN: 10298479. DOI: `10.1007/JHEP02(2016)004`. arXiv: `1511.04021`.

[115] B. Hsu et al. “Approximating random quantum optimization problems”. en. In: *Physical Review A* 87.6 (2013). ISSN: 1050-2947, 1094-1622. DOI: `10.1103/PhysRevA.87.062334`. (Visited on 02/16/2015).

[116] C.-L. Hung et al. “Quantum spin dynamics with pairwise-tunable, long-range interactions”. In: *Proceedings of the National Academy of Sciences* 113.34 (2016), E4946–E4955. ISSN: 0027-8424. DOI: `10.1073/pnas.1603777113`. URL: `https://www.pnas.org/content/113/34/E4946`.

[117] David A. Huse, Rahul Nandkishore, and Vadim Oganesyan. “Phenomenology of fully many-body-localized systems”. In: *Phys. Rev. B* 90 (17 Nov. 2014), p. 174202. DOI: `10.1103/PhysRevB.90.174202`. URL: `https://link.aps.org/doi/10.1103/PhysRevB.90.174202`.

[118] David A. Huse et al. “Localization-protected quantum order”. In: *Physical Review B* 88.1 (July 2013), p. 014206. DOI: `10.1103/PhysRevB.88.014206`. URL: `http://link.aps.org/doi/10.1103/PhysRevB.88.014206` (visited on 11/02/2015).

[119] Thomas Iadecola, Luiz H. Santos, and Claudio Chamon. “Stroboscopic symmetry-protected topological phases”. In: *Physical Review B* 92.12 (Sept. 2015). DOI: `10.1103/PhysRevB.92.125107`. URL: `http://link.aps.org/doi/10.1103/PhysRevB.92.125107` (visited on 11/02/2015).

[120] John Z. Imbrie. “On Many-Body Localization for Quantum Spin Chains”. In: *Journal of Statistical Physics* 163.5 (2016), pp. 998–1048. ISSN: 1572-9613. DOI: `10.1007/s10955-016-1508-x`. URL: `http://dx.doi.org/10.1007/s10955-016-1508-x`.

[121] Eiki Iyoda, Hosho Katsura, and Takahiro Sagawa. “Effective dimension, level statistics, and integrability of Sachdev-Ye-Kitaev-like models”. In: *Phys. Rev. D* 98 (8 Oct. 2018), p. 086020. DOI: `10.1103/PhysRevD.98.086020`. URL: `https://link.aps.org/doi/10.1103/PhysRevD.98.086020`.

[122] Y. -Y. Jau et al. "Entangling atomic spins with a Rydberg-dressed spin-flip blockade". In: *Nat Phys* 12 (2016), pp. 71–74. URL: `http://dx.doi.org/10.1038/nphys3487`.

[123] Kristan Jensen. "Chaos in AdS_2 Holography". In: *Phys. Rev. Lett.* 117 (11 Sept. 2016), p. 111601. DOI: `10.1103/PhysRevLett.117.111601`. URL: `https://link.aps.org/doi/10.1103/PhysRevLett.117.111601`.

[124] Liang Jiang et al. "Majorana Fermions in Equilibrium and in Driven Cold-Atom Quantum Wires". In: *Physical Review Letters* 106.22 (June 2011), p. 220402. DOI: `10.1103/PhysRevLett.106.220402`. URL: `http://link.aps.org/doi/10.1103/PhysRevLett.106.220402` (visited on 11/03/2015).

[125] J. E. Johnson and S. L. Rolston. "Interactions between Rydberg-dressed atoms". In: *Phys. Rev. A* 82 (2010), p. 033412. URL: `https://journals.aps.org/pra/abstract/10.1103/PhysRevA.82.033412`.

[126] Sonika Johri, Rahul Nandkishore, and R. N. Bhatt. "Many-Body Localization in Imperfectly Isolated Quantum Systems". In: *Phys. Rev. Lett.* 114 (11 Mar. 2015), p. 117401. DOI: `10.1103/PhysRevLett.114.117401`. URL: `https://link.aps.org/doi/10.1103/PhysRevLett.114.117401`.

[127] Gregor Jotzu et al. "Experimental realization of the topological Haldane model with ultracold fermions". In: *Nature* 515.7526 (2014), pp. 237–240. URL: `http://www.nature.com/nature/journal/v515/n7526/full/nature13915.html`.

[128] Charles L Kane and Eugene J Mele. "Z 2 topological order and the quantum spin Hall effect". In: *Physical review letters* 95.14 (2005), p. 146802. URL: `https://journals.aps.org/prl/abstract/10.1103/PhysRevLett.95.146802`.

[129] Colin J. Kennedy et al. "Observation of Bose-Einstein condensation in a strong synthetic magnetic field". In: *Nat Phys* 11 (2015), pp. 859–864. URL: `http://dx.doi.org/10.1038/nphys3421`.

[130] C. W. von Keyserlingk, Vedika Khemani, and S. L. Sondhi. "Absolute stability and spatiotemporal long-range order in Floquet systems". In: *Phys. Rev. B* 94 (8 Aug. 2016), p. 085112. DOI: `10.1103/PhysRevB.94.085112`. URL: `http://link.aps.org/doi/10.1103/PhysRevB.94.085112`.

[131] C. W. von Keyserlingk and S. L. Sondhi. "Phase structure of one-dimensional interacting Floquet systems. I. Abelian symmetry-protected topological phases". In: *Phys. Rev. B* 93 (24 June 2016), p. 245145. DOI: `10.1103/PhysRevB.93.245145`. URL: `http://link.aps.org/doi/10.1103/PhysRevB.93.245145`.

[132] C. W. von Keyserlingk and S. L. Sondhi. "Phase structure of one-dimensional interacting Floquet systems. II. Symmetry-broken phases". In: *Phys. Rev. B* 93 (24 June 2016), p. 245146. DOI: `10.1103/PhysRevB.93.245146`. URL: `http://link.aps.org/doi/10.1103/PhysRevB.93.245146`.

[133] Vedika Khemani et al. "Phase Structure of Driven Quantum Systems". In: *Phys. Rev. Lett.* 116 (25 June 2016), p. 250401. DOI: `10.1103/PhysRevLett.116.250401`. URL: `http://link.aps.org/doi/10.1103/PhysRevLett.116.250401`.

[134] S. Kirkpatrick and B. Selman. "Critical Behavior in the Satisfiability of Random Boolean Expressions". In: *Science* 264 (1994), p. 1297. DOI: `10.1126/science.264.5163.1297`.

[135] A Yu Kitaev. "Unpaired Majorana fermions in quantum wires". In: *Physics-Uspekhi* 44.10S (2001), p. 131. URL: `http://stacks.iop.org/1063-7869/44/i=10S/a=S29`.

[136] A. Yu Kitaev, A. Shen, and M. N. Vyalyi. *Classical and Quantum Computation*. Vol. 47. Graduate Studies in Mathematics, American Mathematical Society, 2002.

[137] Alexei Kitaev. "A Simple Model of Quantum Holography". In: (2015). URL: `http://online.kitp.ucsb.edu/online/entangled15/kitaev/`.

[138] Takuya Kitagawa et al. "Topological characterization of periodically driven quantum systems". In: *Physical Review B* 82.23 (Dec. 2010), p. 235114. DOI: `10.1103/PhysRevB.82.235114`. URL: `http://link.aps.org/doi/10.1103/PhysRevB.82.235114` (visited on 11/03/2015).

[139] Jonathan Kohler et al. "Negative-Mass Instability of the Spin and Motion of an Atomic Gas Driven by Optical Cavity Backaction". In: *Phys. Rev. Lett.* 120 (1 Jan. 2018), p. 013601. DOI: `10.1103/PhysRevLett.120.013601`. URL: `https://link.aps.org/doi/10.1103/PhysRevLett.120.013601`.

[140] Alicia J Kollar et al. "Supermode density-wave polariton condensation with a Bose-Einstein condensate in a multimode cavity". In: *Nature Communications* 8 (Feb. 2017), p. 14386. URL: `https://doi.org/10.1038/ncomms14386`.

[141] Ronen M. Kroeze et al. "Spinor Self-Ordering of a Quantum Gas in a Cavity". In: *Phys. Rev. Lett.* 121 (16 Oct. 2018), p. 163601. DOI: `10.1103/PhysRevLett.121.163601`. URL: `https://link.aps.org/doi/10.1103/PhysRevLett.121.163601`.

[142] Tomotaka Kuwahara, Takashi Mori, and Keiji Saito. "Floquet-Magnus theory and generic transient dynamics in periodically driven many-body quantum systems". In: *Annals of Physics* 367 (2016), pp. 96–124. ISSN: 0003-4916. DOI: `http://dx.doi.org/10.1016/j.aop.2016.01.012`. URL: `http://www.sciencedirect.com/science/article/pii/S0003491616000142`.

[143] Henning Labuhn et al. "Tunable two-dimensional arrays of single Rydberg atoms for realizing quantum Ising models". In: *Nature* 534.7609 (2016), pp. 667–670. URL: `http://www.nature.com/nature/journal/v534/n7609/full/nature18274.html`.

[144] M. Landini et al. "Formation of a Spin Texture in a Quantum Gas Coupled to a Cavity". In: *Phys. Rev. Lett.* 120 (22 May 2018), p. 223602. DOI: `10.1103/PhysRevLett.120.223602`. URL: `https://link.aps.org/doi/10.1103/PhysRevLett.120.223602`.

[145] A I Larkin and Yu N Ovchinnikov. "Quasiclassical Method in the Theory of Superconductivity". In: *JETP* 28.6 (1969), pp. 1200–1205.

[146] C R Laumann et al. "Phase transitions and random quantum satisfiability". In: *Quant. Inf. and Comp.* 10.1 (2009), pp. 0001–0015. URL: `http://arxiv.org/abs/0903.1904v1`.

[147] C.R. Laumann et al. "Product, generic, and random generic quantum satisfiability". In: *Physical Review A* 81.062345 (2010). DOI: `10.1103/PhysRevA.81.062345`.

[148] Achilleas Lazarides, Arnab Das, and Roderich Moessner. "Equilibrium states of generic quantum systems subject to periodic driving". In: *Physical Review E* 90.1 (July 2014), p. 012110. DOI: `10.1103/PhysRevE.90.012110`. URL: `http://link.aps.org/doi/10.1103/PhysRevE.90.012110` (visited on 11/03/2015).

[149] Jongmin Lee et al. "Demonstration of the Jaynes-Cummings ladder with Rydberg-dressed atoms". In: *arXiv preprint arXiv:1609.03940* (2016). URL: `https://arxiv.org/abs/1609.03940`.

[150] Tony E. Lee, Yogesh N. Joglekar, and Philip Richerme. "String order via Floquet interactions in atomic systems". In: *Phys. Rev. A* 94 (2 Aug. 2016), p. 023610. DOI: `10.1103/PhysRevA.94.023610`. URL: `http://link.aps.org/doi/10.1103/PhysRevA.94.023610`.

[151] Julian Léonard et al. "Supersolid formation in a quantum gas breaking a continuous translational symmetry". In: *Nature* 543 (Mar. 2017), p. 87. URL: `https://doi.org/10.1038/nature21067`.

[152] Ian D. Leroux, Monika H. Schleier-Smith, and Vladan Vuleti ć. "Implementation of Cavity Squeezing of a Collective Atomic Spin". In: *Phys. Rev. Lett.* 104 (7 Feb. 2010), p. 073602. DOI: `10.1103/PhysRevLett.104.073602`. URL: `https://link.aps.org/doi/10.1103/PhysRevLett.104.073602`.

[153] Brian J Lester et al. "Rapid Production of Uniformly Filled Arrays of Neutral Atoms". In: *Physical review letters* 115.7 (2015), p. 073003. URL: `http://journals.aps.org/prl/abstract/10.1103/PhysRevLett.115.073003`.

[154] R J Lewis-Swan et al. "Unifying scrambling, thermalization and entanglement through measurement of fidelity out-of-time-order correlators in the Dicke model". In: *Nature Communications* 10.1 (2019), p. 1581. ISSN: 2041-1723. DOI: `10.1038/s41467-019-09436-y`. URL: `https://doi.org/10.1038/s41467-019-09436-y`.

[155] Netanel H. Lindner, Gil Refael, and Victor Galitski. "Floquet topological insulator in semiconductor quantum wells". en. In: *Nature Physics* 7 (2011), pp. 490–495. ISSN: 1745-2473. DOI: `10.1038/nphys1926`. URL: `http://www.nature.com/nphys/journal/v7/n6/full/nphys1926.html`.

[156] Arjan F. van Loo et al. “Photon-Mediated Interactions Between Distant Artificial Atoms”. In: *Science* 342.6165 (2013), pp. 1494–1496. ISSN: 0036-8075. DOI: `10.1126/science.1244324`. URL: `https://science.sciencemag.org/content/342/6165/1494`.

[157] T. Luczak. “Component behavior near the critical point of the random graph process”. In: *Random Structures and Algorithms* 1.3 (1990), p. 287. DOI: `10.1002/rsa.3240010305`.

[158] David J. Luitz, Francois Huveneers, and Wojciech De Roeck. “How a Small Quantum Bath Can Thermalize Long Localized Chains”. In: *Phys. Rev. Lett.* 119 (15 Oct. 2017), p. 150602. DOI: `10.1103/PhysRevLett.119.150602`. URL: `https://link.aps.org/doi/10.1103/PhysRevLett.119.150602`.

[159] David J. Luitz, Nicolas Laflorencie, and Fabien Alet. “Many-body localization edge in the random-field Heisenberg chain”. In: *Phys. Rev. B* 91 (8 Feb. 2015), p. 081103. DOI: `10.1103/PhysRevB.91.081103`. URL: `https://link.aps.org/doi/10.1103/PhysRevB.91.081103`.

[160] Inna Lukyanenko, Phillip S Isaac, and Jon Links. “An integrable case of the p+ip pairing Hamiltonian interacting with its environment”. In: *Journal of Physics A: Mathematical and Theoretical* 49.8 (Jan. 2016), p. 084001. DOI: `10.1088/1751-8113/49/8/084001`. URL: `https://doi.org/10.1088%2F1751-8113%2F49%2F8%2F084001`.

[161] J Majer et al. “Coupling superconducting qubits via a cavity bus”. In: *Nature* 449 (Jan. 2007), pp. 443–447. URL: `http://dx.doi.org/10.1038/nature06184`.

[162] Juan Maldacena, Stephen H. Shenker, and Douglas Stanford. “A bound on chaos”. In: *Journal of High Energy Physics* 2016.8 (Aug. 2016), p. 106. ISSN: 1029-8479. DOI: `10.1007/JHEP08(2016)106`. URL: `http://link.springer.com/10.1007/JHEP08(2016)106`.

[163] Juan Maldacena and Douglas Stanford. “Remarks on the Sachdev-Ye-Kitaev model”. In: *Phys. Rev. D* 94 (10 Nov. 2016), p. 106002. DOI: `10.1103/PhysRevD.94.106002`. URL: `https://link.aps.org/doi/10.1103/PhysRevD.94.106002`.

[164] J. Marino and A. M. Rey. “A cavity-QED simulator of slow and fast scrambling”. In: (2018). arXiv: `1810.00866`. URL: `https://arxiv.org/abs/1810.00866`.

[165] Stuart J. Masson, M. D. Barrett, and Scott Parkins. “Cavity QED Engineering of Spin Dynamics and Squeezing in a Spinor Gas”. In: *Phys. Rev. Lett.* 119 (21 Nov. 2017), p. 213601. DOI: `10.1103/PhysRevLett.119.213601`. URL: `https://link.aps.org/doi/10.1103/PhysRevLett.119.213601`.

[166] P. Mazur. “Non-ergodicity of phase functions in certain systems”. In: *Physica* 43.4 (1969), pp. 533–545. ISSN: 0031-8914. DOI: `https://doi.org/10.1016/0031-8914(69)90185-2`. URL: `http://www.sciencedirect.com/science/article/pii/0031891469901852`.

[167] M. Mézard and A. Montanari. *Information, Physics, and Computation.* New York: Oxford Graduate Texts, 2009.

[168] Marc Mézard, Federico Ricci-Tersenghi, and Riccardo Zecchina. "Two solutions to diluted p-spin models and XORSAT problems". In: *Journal of Statistical Physics* 111.3-4 (2003), pp. 505–533. DOI: `10.1023/A:1022886412117`. (Visited on 01/19/2015).

[169] F. Mivehvar, H. Ritsch, and F. Piazza. "Cavity-Quantum-Electrodynamical Toolbox for Quantum Magnetism". In: *Phys. Rev. Lett.* 122 (11 Mar. 2019), p. 113603. DOI: `10.1103/PhysRevLett.122.113603`. URL: `https://link.aps.org/doi/10.1103/PhysRevLett.122.113603`.

[170] Farokh Mivehvar, Francesco Piazza, and Helmut Ritsch. "Disorder-Driven Density and Spin Self-Ordering of a Bose-Einstein Condensate in a Cavity". In: *Phys. Rev. Lett.* 119 (6 Aug. 2017), p. 063602. DOI: `10.1103/PhysRevLett.119.063602`. URL: `https://link.aps.org/doi/10.1103/PhysRevLett.119.063602`.

[171] Joel E Moore and Leon Balents. "Topological invariants of time-reversal-invariant band structures". In: *Physical Review B* 75.12 (2007), p. 121306. URL: `https://journals.aps.org/prb/abstract/10.1103/PhysRevB.75.121306`.

[172] Rose M. Morra et al. "Spin dynamics and the Haldane gap in the spin-1 quasi-one-dimensional antiferromagnet $CsNiCl_3$". In: *Phys. Rev. B* 38 (1 July 1988), pp. 543–555. DOI: `10.1103/PhysRevB.38.543`. URL: `http://link.aps.org/doi/10.1103/PhysRevB.38.543`.

[173] Rahul Nandkishore. "Many-body localization proximity effect". In: *Phys. Rev. B* 92 (24 Dec. 2015), p. 245141. DOI: `10.1103/PhysRevB.92.245141`. URL: `https://link.aps.org/doi/10.1103/PhysRevB.92.245141`.

[174] Rahul Nandkishore, Sarang Gopalakrishnan, and David A. Huse. "Spectral features of a many-body-localized system weakly coupled to a bath". In: *Phys. Rev. B* 90 (6 Aug. 2014), p. 064203. DOI: `10.1103/PhysRevB.90.064203`. URL: `https://link.aps.org/doi/10.1103/PhysRevB.90.064203`.

[175] Rahul Nandkishore and David A. Huse. "Many-Body Localization and Thermalization in Quantum Statistical Mechanics". In: *Annual Review of Condensed Matter Physics* 6.1 (2015), pp. 15–38. DOI: `10.1146/annurev-conmatphys-031214-014726`. URL: `http://dx.doi.org/10.1146/annurev-conmatphys-031214-014726` (visited on 11/03/2015).

[176] Matthew A. Norcia et al. "Cavity-mediated collective spin-exchange interactions in a strontium superradiant laser". In: *Science* 361.6399 (2018), pp. 259–262. ISSN: 0036-8075. DOI: `10.1126/science.aar3102`. URL: `http://science.sciencemag.org/content/361/6399/259`.

[177] Takashi Oka and Hideo Aoki. "Photovoltaic Hall effect in graphene". In: *Phys. Rev. B* 79 (8 Feb. 2009), p. 081406. DOI: `10.1103/PhysRevB.79.081406`. URL: `http://link.aps.org/doi/10.1103/PhysRevB.79.081406`.

[178] H K Owusu, K Wagh, and E A Yuzbashyan. "The link between integrability, level crossings and exact solution in quantum models". In: *Journal of Physics A: Mathematical and Theoretical* 42.3 (Dec. 2008), p. 035206. DOI: `10.1088/1751-8113/42/3/035206`. URL: `https://doi.org/10.1088%2F1751-8113%2F42%2F3%2F035206`.

[179] Arijeet Pal and David A. Huse. "Many-body localization phase transition". In: *Phys. Rev. B* 82 (17 Nov. 2010), p. 174411. DOI: `10.1103/PhysRevB.82.174411`. URL: `https://link.aps.org/doi/10.1103/PhysRevB.82.174411`.

[180] G. Parisi. "Toward a mean field theory for spin glasses". In: *Physics Letters A* 73.3 (1979), pp. 203–205. ISSN: 0375-9601. DOI: `https://doi.org/10.1016/0375-9601(79)90708-4`. URL: `http://www.sciencedirect.com/science/article/pii/0375960179907084`.

[181] Maxwell F Parsons et al. "Site-resolved measurement of the spin-correlation function in the Fermi-Hubbard model". In: *Science* 353.6305 (2016), pp. 1253–1256. URL: `http://science.sciencemag.org/content/353/6305/1253`.

[182] D Poilblanc et al. "Poissonvs.GOE Statistics in Integrable and Non-Integrable Quantum Hamiltonians". In: *Europhysics Letters (EPL)* 22.7 (June 1993), pp. 537–542. DOI: `10.1209/0295-5075/22/7/010`.

[183] Frank Pollmann et al. "Entanglement spectrum of a topological phase in one dimension". In: *Phys. Rev. B* 81 (6 Feb. 2010), p. 064439. DOI: `10.1103/PhysRevB.81.064439`. URL: `https://link.aps.org/doi/10.1103/PhysRevB.81.064439`.

[184] Pedro Ponte et al. "Many-Body Localization in Periodically Driven Systems". In: *Phys. Rev. Lett.* 114 (14 Apr. 2015), p. 140401. DOI: `10.1103/PhysRevLett.114.140401`. URL: `http://link.aps.org/doi/10.1103/PhysRevLett.114.140401`.

[185] Pedro Ponte et al. "Periodically driven ergodic and many-body localized quantum systems". In: *Annals of Physics* 353 (Feb. 2015), pp. 196–204. ISSN: 0003-4916. DOI: `10.1016/j.aop.2014.11.008`. URL: `http://www.sciencedirect.com/science/article/pii/S0003491614003212` (visited on 11/02/2015).

[186] I.-D. Potirniche et al. "Floquet Symmetry-Protected Topological Phases in Cold-Atom Systems". In: *Phys. Rev. Lett.* 119 (12 Sept. 2017), p. 123601. DOI: `10.1103/PhysRevLett.119.123601`.

[187] Ionut-Dragos Potirniche, Sumilan Banerjee, and Ehud Altman. "Exploration of the stability of many-body localization in d>1". In: *Phys. Rev. B* 99 (20 May 2019), p. 205149. DOI: `10.1103/PhysRevB.99.205149`. URL: `https://link.aps.org/doi/10.1103/PhysRevB.99.205149`.

[188] Ionut-Dragos Potirniche, C. R. Laumann, and S. L. Sondhi. "Classical-quantum mixing in the random 2-satisfiability problem". In: *Phys. Rev. A* 92 (4 Oct. 2015), p. 040301. DOI: `10.1103/PhysRevA.92.040301`. URL: `https://link.aps.org/doi/10.1103/PhysRevA.92.040301`.

[189] Andrew C. Potter, Takahiro Morimoto, and Ashvin Vishwanath. “Classification of Interacting Topological Floquet Phases in One Dimension”. In: *Phys. Rev. X* 6 (4 Oct. 2016), p. 041001. DOI: `10.1103/PhysRevX.6.041001`. URL: `http://link.aps.org/doi/10.1103/PhysRevX.6.041001`.

[190] G Pupillo et al. “Strongly correlated gases of Rydberg-dressed atoms: quantum and classical dynamics”. In: *Phys. Rev. Lett.* 104 (2010), p. 223002. URL: `https://journals.aps.org/prl/abstract/10.1103/PhysRevLett.104.223002`.

[191] Xiao-Liang Qi and Shou-Cheng Zhang. “Topological insulators and superconductors”. In: *Reviews of Modern Physics* 83.4 (2011), p. 1057. URL: `https://journals.aps.org/rmp/abstract/10.1103/RevModPhys.83.1057`.

[192] D. A. Rabson, B. N. Narozhny, and A. J. Millis. “Crossover from Poisson to Wigner-Dyson level statistics in spin chains with integrability breaking”. In: *Phys. Rev. B* 69 (5 Feb. 2004), p. 054403. DOI: `10.1103/PhysRevB.69.054403`. URL: `https://link.aps.org/doi/10.1103/PhysRevB.69.054403`.

[193] Mikael C Rechtsman et al. “Photonic Floquet topological insulators”. In: *Nature* 496.7444 (2013), pp. 196–200. URL: `https://www.nature.com/nature/journal/v496/n7444/full/nature12066.html`.

[194] Florentin Reiter and Anders S. Sørensen. “Effective operator formalism for open quantum systems”. In: *Phys. Rev. A* 85 (3 Mar. 2012), p. 032111. DOI: `10.1103/PhysRevA.85.032111`. URL: `https://link.aps.org/doi/10.1103/PhysRevA.85.032111`.

[195] Marcos Rigol, Vanja Dunjko, and Maxim Olshanii. “Thermalization and its mechanism for generic isolated quantum systems”. In: *Nature* 452 (Apr. 2008), p. 854. URL: `https://doi.org/10.1038/nature06838%20http://10.0.4.14/nature06838%20https://www.nature.com/articles/nature06838%7B%5C#%7Dsupplementary-information`.

[196] V. Ros, M. Müller, and A. Scardicchio. “Integrals of motion in the many-body localized phase”. In: *Nuclear Physics B* 891 (2015), pp. 420–465. ISSN: 0550-3213. DOI: `https://doi.org/10.1016/j.nuclphysb.2014.12.014`. URL: `http://www.sciencedirect.com/science/article/pii/S0550321314003836`.

[197] Rahul Roy and Fenner Harper. “Abelian Floquet symmetry-protected topological phases in one dimension”. In: *Phys. Rev. B* 94 (12 Sept. 2016), p. 125105. DOI: `10.1103/PhysRevB.94.125105`. URL: `http://link.aps.org/doi/10.1103/PhysRevB.94.125105`.

[198] Mark S. Rudner et al. “Anomalous Edge States and the Bulk-Edge Correspondence for Periodically Driven Two-Dimensional Systems”. In: *Physical Review X* 3 (July 2013), p. 031005. DOI: `10.1103/PhysRevX.3.031005`. URL: `http://link.aps.org/doi/10.1103/PhysRevX.3.031005` (visited on 11/03/2015).

[199] Angelo Russomanno and Emanuele G. Dalla Torre. “Kibble-Zurek scaling in periodically driven quantum systems”. In: *EPL (Europhysics Letters)* 115.3 (2016), p. 30006. URL: `http://stacks.iop.org/0295-5075/115/i=3/a=30006`.

[200] Subir Sachdev. “Bekenstein-Hawking entropy and strange metals”. In: *Physical Review X* 5.4 (2015), pp. 1–13. ISSN: 21603308. DOI: `10.1103/PhysRevX.5.041025`. eprint: `1506.05111`.

[201] Subir Sachdev and Jinwu Ye. “Gapless spin-fluid ground state in a random quantum Heisenberg magnet”. In: *Phys. Rev. Lett.* 70 (21 May 1993), pp. 3339–3342. DOI: `10.1103/PhysRevLett.70.3339`. URL: `https://link.aps.org/doi/10.1103/PhysRevLett.70.3339`.

[202] Jasen A. Scaramazza, B. Sriram Shastry, and Emil A. Yuzbashyan. “Integrable matrix theory: Level statistics”. In: *Phys. Rev. E* 94 (3 Sept. 2016), p. 032106. DOI: `10.1103/PhysRevE.94.032106`. URL: `https://link.aps.org/doi/10.1103/PhysRevE.94.032106`.

[203] Monika H. Schleier-Smith, Ian D. Leroux, and Vladan Vuleti ć. “Squeezing the collective spin of a dilute atomic ensemble by cavity feedback”. In: *Phys. Rev. A* 81 (2 Feb. 2010), p. 021804. DOI: `10.1103/PhysRevA.81.021804`. URL: `https://link.aps.org/doi/10.1103/PhysRevA.81.021804`.

[204] John Schliemann. “Spins coupled to a spin bath: From integrability to chaos”. In: *Phys. Rev. B* 81 (8 Feb. 2010), p. 081301. DOI: `10.1103/PhysRevB.81.081301`. URL: `https://link.aps.org/doi/10.1103/PhysRevB.81.081301`.

[205] J R Schmidt. “Singular point analysis of the Gaudin equations”. In: *Canadian Journal of Physics* 86.6 (2008), pp. 783–789. URL: `https://doi.org/10.1139/p08-008`.

[206] Jeanette Schmidt-Pruzan and Eli Shamir. “Component structure in the evolution of random hypergraphs”. English. In: *Combinatorica* 5.1 (1985), pp. 81–94. ISSN: 0209-9683. DOI: `10.1007/BF02579445`. URL: `http://dx.doi.org/10.1007/BF02579445`.

[207] T. Senthil. “Symmetry-Protected Topological Phases of Quantum Matter”. In: *Annual Review of Condensed Matter Physics* 6.1 (2015), pp. 299–324. DOI: `10.1146/annurev-conmatphys-031214-014740`. URL: `http://dx.doi.org/10.1146/annurev-conmatphys-031214-014740`.

[208] M. Serbyn, Z. Papic, and D. A. Abanin. “Criterion for Many-Body Localization-Delocalization Phase Transition”. In: *Phys. Rev. X* 5 (4 Dec. 2015), p. 041047. DOI: `10.1103/PhysRevX.5.041047`. URL: `https://link.aps.org/doi/10.1103/PhysRevX.5.041047`.

[209] Maksym Serbyn, Z. Papic, and Dmitry A. Abanin. “Thouless energy and multifractality across the many-body localization transition”. In: *Phys. Rev. B* 96 (10 Sept. 2017), p. 104201. DOI: `10.1103/PhysRevB.96.104201`. URL: `https://link.aps.org/doi/10.1103/PhysRevB.96.104201`.

[210] Maksym Serbyn, Z. Papic, and Dmitry A. Abanin. "Universal Slow Growth of Entanglement in Interacting Strongly Disordered Systems". In: *Phys. Rev. Lett.* 110 (26 June 2013), p. 260601. DOI: `10.1103/PhysRevLett.110.260601`. URL: `https://link.aps.org/doi/10.1103/PhysRevLett.110.260601`.

[211] Maksym Serbyn, Z. Papić, and Dmitry A. Abanin. "Local Conservation Laws and the Structure of the Many-Body Localized States". In: *Physical Review Letters* 111.12 (Sept. 2013), p. 127201. DOI: `10.1103/PhysRevLett.111.127201`. URL: `http://link.aps.org/doi/10.1103/PhysRevLett.111.127201` (visited on 11/02/2015).

[212] R. Shankar. "Renormalization-group approach to interacting fermions". In: *Rev. Mod. Phys.* 66 (1 Jan. 1994), pp. 129–192. DOI: `10.1103/RevModPhys.66.129`. URL: `https://link.aps.org/doi/10.1103/RevModPhys.66.129`.

[213] Stephen H. Shenker and Douglas Stanford. "Black holes and the butterfly effect". In: *Journal of High Energy Physics* 2014.3 (Mar. 2014), p. 67. ISSN: 1029-8479. DOI: `10.1007/JHEP03(2014)067`. URL: `http://link.springer.com/10.1007/JHEP03(2014)067`.

[214] David Sherrington and Scott Kirkpatrick. "Solvable Model of a Spin-Glass". In: *Phys. Rev. Lett.* 35 (26 Dec. 1975), pp. 1792–1796. DOI: `10.1103/PhysRevLett.35.1792`. URL: `https://link.aps.org/doi/10.1103/PhysRevLett.35.1792`.

[215] J. Sirker, R. G. Pereira, and I. Affleck. "Diffusion and Ballistic Transport in One-Dimensional Quantum Systems". In: *Phys. Rev. Lett.* 103 (21 Nov. 2009), p. 216602. DOI: `10.1103/PhysRevLett.103.216602`. URL: `https://link.aps.org/doi/10.1103/PhysRevLett.103.216602`.

[216] E. K. Sklyanin. "Separation of variables in the Gaudin model". In: *Journal of Soviet Mathematics* 47.2 (Oct. 1989), pp. 2473–2488. ISSN: 1573-8795. DOI: `10.1007/BF01840429`. URL: `https://doi.org/10.1007/BF01840429`.

[217] T. Skrypnyk. "New integrable Gaudin-type systems, classical r-matrices and quasi-graded Lie algebras". In: *Physics Letters A* 334.5 (2005), pp. 390–399. ISSN: 0375-9601. DOI: `https://doi.org/10.1016/j.physleta.2004.11.041`. URL: `http://www.sciencedirect.com/science/article/pii/S0375960104016391`.

[218] T. Skrypnyk. "Non-skew-symmetric classical r-matrices, algebraic Bethe ansatz, and BCS-type integrable systems". In: *Journal of Mathematical Physics* 50.3 (2009). DOI: `10.1063/1.3072912`. eprint: `https://doi.org/10.1063/1.3072912`. URL: `https://doi.org/10.1063/1.3072912`.

[219] T Skrypnyk. "Non-skew-symmetric classical r-matrices and integrable cases of the reduced BCS model". In: *Journal of Physics A: Mathematical and Theoretical* 42.47 (Nov. 2009), p. 472004. DOI: `10.1088/1751-8113/42/47/472004`. URL: `https://doi.org/10.1088%2F1751-8113%2F42%2F47%2F472004`.

[220] T. Skrypnyk. "Spin chains in magnetic field, non-skew-symmetric classical r-matrices and BCS-type integrable systems". In: *Nuclear Physics B* 806.3 (2009), pp. 504–528. ISSN: 0550-3213. DOI: `https://doi.org/10.1016/j.nuclphysb.2008.07.017`. URL: `http://www.sciencedirect.com/science/article/pii/S0550321308004008`.

[221] Anders Søndberg Sørensen and Klaus Mølmer. "Entangling atoms in bad cavities". In: *Phys. Rev. A* 66 (2 Aug. 2002), p. 022314. DOI: `10.1103/PhysRevA.66.022314`. URL: `https://link.aps.org/doi/10.1103/PhysRevA.66.022314`.

[222] Mark Srednicki. "Chaos and quantum thermalization". In: *Phys. Rev. E* 50 (2 Aug. 1994), pp. 888–901. DOI: `10.1103/PhysRevE.50.888`. URL: `https://link.aps.org/doi/10.1103/PhysRevE.50.888`.

[223] Mark Srednicki. "The approach to thermal equilibrium in quantized chaotic systems". In: *Journal of Physics A: Mathematical and General* 32.7 (1999), p. 1163. URL: `http://stacks.iop.org/0305-4470/32/i=7/a=007`.

[224] Dan M Stamper-Kurn. "Viewpoint: Shifting entropy elsewhere". In: *Physics* 2 (2009), p. 80. URL: `http://physics.aps.org/articles/v2/80`.

[225] Douglas Stanford and Edward Witten. "Fermionic localization of the schwarzian theory". In: *Journal of High Energy Physics* 2017.10 (Oct. 2017), p. 8. ISSN: 1029-8479. DOI: `10.1007/JHEP10(2017)008`. URL: `https://doi.org/10.1007/JHEP10(2017)008`.

[226] H.-J. Stöckmann and J. Stein. ""Quantum" chaos in billiards studied by microwave absorption". In: *Phys. Rev. Lett.* 64 (19 May 1990), pp. 2215–2218. DOI: `10.1103/PhysRevLett.64.2215`. URL: `https://link.aps.org/doi/10.1103/PhysRevLett.64.2215`.

[227] Philipp Strack and Subir Sachdev. "Dicke Quantum Spin Glass of Atoms and Photons". In: *Phys. Rev. Lett.* 107 (27 Dec. 2011), p. 277202. DOI: `10.1103/PhysRevLett.107.277202`. URL: `https://link.aps.org/doi/10.1103/PhysRevLett.107.277202`.

[228] M. Suzuki. "Ergodicity, constants of motion, and bounds for susceptibilities". In: *Physica* 51.2 (1971), pp. 277–291. ISSN: 0031-8914. DOI: `https://doi.org/10.1016/0031-8914(71)90226-6`. URL: `http://www.sciencedirect.com/science/article/pii/0031891471902266`.

[229] Brian Swingle and Nicole Yunger Halpern. "Resilience of scrambling measurements". In: *Phys. Rev. A* 97 (6 June 2018), p. 062113. DOI: `10.1103/PhysRevA.97.062113`. URL: `https://link.aps.org/doi/10.1103/PhysRevA.97.062113`.

[230] Brian Swingle et al. "Measuring the scrambling of quantum information". In: *Phys. Rev. A* 94 (4 Oct. 2016), p. 040302. DOI: `10.1103/PhysRevA.94.040302`. URL: `https://link.aps.org/doi/10.1103/PhysRevA.94.040302`.

[231] Manisha Thakurathi et al. "Floquet generation of Majorana end modes and topological invariants". In: *Phys. Rev. B* 88 (15 Oct. 2013), p. 155133. DOI: `10.1103/PhysRevB.88.155133`. URL: `http://link.aps.org/doi/10.1103/PhysRevB.88.155133`.

[232] Paraj Titum et al. "Disorder-Induced Floquet Topological Insulators". In: *Phys. Rev. Lett.* 114 (5 Feb. 2015), p. 056801. DOI: `10.1103/PhysRevLett.114.056801`. URL: `http://link.aps.org/doi/10.1103/PhysRevLett.114.056801`.

[233] A. M. Turner and A. Vishwanath. "Beyond Band Insulators: Topology of Semi-metals and Interacting Phases". In: *arXiv:1301.0330* (2013). URL: `https://arxiv.org/abs/1301.0330`.

[234] Ari M. Turner, Frank Pollmann, and Erez Berg. "Topological phases of one-dimensional fermions: An entanglement point of view". In: *Phys. Rev. B* 83 (7 Feb. 2011), p. 075102. DOI: `10.1103/PhysRevB.83.075102`. URL: `https://link.aps.org/doi/10.1103/PhysRevB.83.075102`.

[235] Benoît Vermersch et al. "Probing scrambling using statistical correlations between randomized measurements". In: (July 2018). arXiv: `quant-ph/1807.09087`. URL: `https://arxiv.org/abs/1807.09087`.

[236] Tamás Vicsek et al. "Novel Type of Phase Transition in a System of Self-Driven Particles". In: *Phys. Rev. Lett.* 75 (6 Aug. 1995), pp. 1226–1229. DOI: `10.1103/PhysRevLett.75.1226`. URL: `https://link.aps.org/doi/10.1103/PhysRevLett.75.1226`.

[237] Thibault Vogt et al. "Dipole Blockade at Forster Resonances in High Resolution Laser Excitation of Rydberg States of Cesium Atoms". In: *Phys. Rev. Lett.* 97 (8 Aug. 2006), p. 083003. DOI: `10.1103/PhysRevLett.97.083003`. URL: `http://link.aps.org/doi/10.1103/PhysRevLett.97.083003`.

[238] Ronen Vosk and Ehud Altman. "Many-Body Localization in One Dimension as a Dynamical Renormalization Group Fixed Point". In: *Phys. Rev. Lett.* 110 (6 Feb. 2013), p. 067204. DOI: `10.1103/PhysRevLett.110.067204`. URL: `https://link.aps.org/doi/10.1103/PhysRevLett.110.067204`.

[239] Y. H. Wang et al. "Observation of Floquet-Bloch States on the Surface of a Topological Insulator". In: *Science* 342.6157 (), pp. 453–457. URL: `http://science.sciencemag.org/content/342/6157/453`.

[240] Eugene P. Wigner. "Characteristics Vectors of Bordered Matrices with Infinite Dimensions II". In: *Annals of Mathematics* 65.2 (1957), pp. 203–207. ISSN: 0003486X. URL: `http://www.jstor.org/stable/1969956`.

[241] Kenneth G. Wilson. "The renormalization group: Critical phenomena and the Kondo problem". In: *Rev. Mod. Phys.* 47 (4 Oct. 1975), pp. 773–840. URL: `https://link.aps.org/doi/10.1103/RevModPhys.47.773`.

[242] Guangyong Xu et al. "Y_2BaNiO_5: A nearly ideal realization of the $S = 1$ Heisenberg chain with antiferromagnetic interactions". In: *Phys. Rev. B* 54 (10 Sept. 1996), R6827–R6830. DOI: `10.1103/PhysRevB.54.R6827`. URL: `http://link.aps.org/doi/10.1103/PhysRevB.54.R6827`.

[243] Zhenyu Xu et al. "Extreme Decoherence and Quantum Chaos". In: *Phys. Rev. Lett.* 122 (1 Jan. 2019), p. 014103. DOI: `10.1103/PhysRevLett.122.014103`. URL: `https://link.aps.org/doi/10.1103/PhysRevLett.122.014103`.

[244] N. Y. Yao et al. "Discrete Time Crystals: Rigidity, Criticality, and Realizations". In: *Phys. Rev. Lett.* 118 (3 Jan. 2017), p. 030401. DOI: `10.1103/PhysRevLett.118.030401`. URL: `https://link.aps.org/doi/10.1103/PhysRevLett.118.030401`.

[245] N. Y. Yao et al. "Many-Body Localization in Dipolar Systems". In: *Phys. Rev. Lett.* 113 (24 Dec. 2014), p. 243002. DOI: `10.1103/PhysRevLett.113.243002`. URL: `http://link.aps.org/doi/10.1103/PhysRevLett.113.243002`.

[246] N. Y. Yao et al. "Realizing Fractional Chern Insulators in Dipolar Spin Systems". In: *Phys. Rev. Lett.* 110 (18 Apr. 2013), p. 185302. DOI: `10.1103/PhysRevLett.110.185302`. URL: `http://link.aps.org/doi/10.1103/PhysRevLett.110.185302`.

[247] Norman Y. Yao, Chris R. Laumann, and Ashvin Vishwanath. "Many-body localization protected quantum state transfer". In: *arXiv:1508.06995 [cond-mat, physics:quant-ph]* (Aug. 2015). arXiv: 1508.06995. URL: `http://arxiv.org/abs/1508.06995` (visited on 11/02/2015).

[248] Johannes Zeiher et al. "Coherent many-body spin dynamics in a long-range interacting Ising chain". In: *arXiv preprint arXiv:1705.08372* (2017). URL: `https://arxiv.org/abs/1705.08372`.

[249] Johannes Zeiher et al. "Many-body interferometry of a Rydberg-dressed spin lattice". In: *Phys. Rev. X* 5 (3 Aug. 2015), p. 031015. DOI: `10.1103/PhysRevX.5.031015`. URL: `http://link.aps.org/doi/10.1103/PhysRevX.5.031015`.

[250] J. Zhang et al. "Observation of a discrete time crystal". In: *Nature* 543.21413 (2017), pp. 217–220. URL: `https://www.nature.com/articles/nature21413`.

[251] X. Zotos, F. Naef, and P. Prelovsek. "Transport and conservation laws". In: *Phys. Rev. B* 55 (17 May 1997), pp. 11029–11032. DOI: `10.1103/PhysRevB.55.11029`. URL: `https://link.aps.org/doi/10.1103/PhysRevB.55.11029`.